

**Development of nanostructured electrocatalysts using
electrochemical atomic layer deposition technique for the direct
liquid fuel cells**



By

Andile Cyril Mkhohlakali

A thesis submitted in fulfilment of the requirement for the degree of

Philosophiae Doctor,

in the department of Chemistry, Faculty of Science, University of the Western Cape,
South Africa

Supervisor: Prof Lindiwe Khotseng

Co-supervisors: Dr Xolile Fuku, and Dr Remegia MmalewaneModibedi

November 2019

Key words:

Nanostructured thin film

Underpotential deposition

Surface limited redox replacement

PdIr thin film

Oxidative Te-UPD

Pd-M based thin films analogues

Te-M thin film derivatives

Electrocatalysis

Alkaline direct liquid fuel cell

Ethanol oxidation



UNIVERSITY *of the*
WESTERN CAPE

Development of nanostructured electrocatalysts using electrochemical atomic layer deposition technique for the direct liquid fuel cells

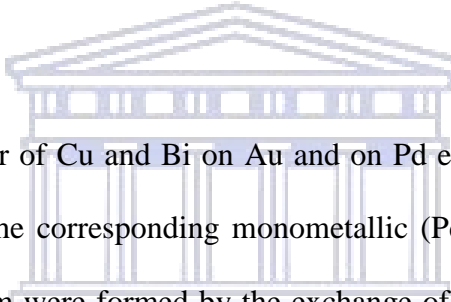
Andile Cyril Mkhohlakali

PhD Thesis, Department of Chemistry, University of the Western Cape, November 2019.

Abstract

The depletion of fossil fuel resources such as coal and the concern of climatic change arising from the emission of greenhouse gases (GHG) and global warming [1] lead to the identification of the 'hydrogen economy' as one of the renewable energy sources and possible futuristic energy conversion solution. Sources of hydrogen as fuel such as water through electrolysis and liquid organic fuel (Hydrogen carriers) have been found as potential game-changers and received increased attention, due to its low-carbon emission. With technological advances on bio-economy, ethanol has attracted tremendous amount of attention and resulted in the emergence of direct ethanol fuel cells (DEFCs) which does not only rely on Pt metal. However, the key drawback of alkaline DEFCs is the development of a high efficient anode electrocatalyst for complete oxidation of ethanol for the development of chemical energy conversion (fuel cell) devices. In this regard, nanostructured materials (NsM) thin films of PGMs have attracted great attention due to their unique properties and nanometre size (1-100 nm) as compared to bulk counterparts. In this study, E-ALD, which is an electrodeposition method, is recognized as a potential cost-effective method for electro-formation of group II-IV, IV-VI semiconductors with well-defined structures. However, there are limited reports on the electro-formation of Pd-based thin film electrocatalysts such as PdIr, Te-M (where M= Pd, BiPd, CuPd). The study reports on the design of a rare synthetic approach for the formation of nanostructured thin films of Pd, PdIr, Pd-M (M = Cu, Bi) and Te-M (M =Au, Pd, BiPd, CuPd) using E-ALD technique. The successful deposition of the resultant electrocatalysts was determined through different parameters such as

the number of cycles, time, deposition potential and concentration of a precursor solution. CV results showed Pd and PdIr voltammetric signatures confirming the successful utilization of Cu as the sacrificial metal for Pd and Ir ions. The resulting deposits were further characterized using a series of microscopic and spectroscopic techniques. X-ray techniques such as XRD, EDX and XPS were able to quantify and provide evidence for possible key composition of the deposited thin films. In addition, the composition and synergistic character of PdIr were determined using XPS, with $3d_{3/2}$ orbital of PdIr shifting to higher binding energy, indicating incorporation of Ir into Pd suggesting less availability of PdIr site for poisoning by EtOH intermediates. Scanning electron micrographs confirmed their structure and morphology. AFM determined the morphology and displayed higher roughness for PdIr ($S_a = 39.2$ nm) compared to Pd ($S_a = 33.7$ nm).



The electrochemical behavior of Cu and Bi on Au and on Pd electrodes was investigated using cyclic voltammetry (CV). The corresponding monometallic (Pd), bimetallic (CuPd, BiPd) and trimetallic (CuBiPd) thin-film were formed by the exchange of Pd for Cu-UPD adlayer followed by repetitive execution of reductive Bi-UPD and Cu-UPD. The deposition process was monitored by time-potential-current trace and CV. Further, the electrochemistry of tellurium (Te) on Au and various electrode surfaces such as Au, Pd, CuPd, BiPd was investigated using CVs and electrochemical impedance spectroscopy. Te showed overpotential deposition preference around -0.5 V to -0.6 V than UPD region (-0.2 to -0.38 V) vs. Ag/AgCl, due to its low experimental kinetics at UPD region. The large Rct (large arc) and small Rct (small arc) for Te-UPD and Te-OPD respectively corroborate with the CV revealing slow electron kinetics. The E-ALD cycles of oxidative Te-UPD (OX-Te-UPD) adlayer deposition on Au, Pd and other various electrode surfaces were formed. The acquired thin films were characterized using cyclic voltammetry (CVs) in acid media (0.1 M HClO₄) to determine the CV signature (redox features). All the corresponding Pd-M: (Pd, BiPd, CuPd and CuBiPd) deposits exhibited typical Pd voltammogram features, with

distinct current response profile at Pd-O region (0.46 V vs. Ag/AgCl). The structure and morphology of these thin films were further characterized using X-ray Diffraction (XRD), X-ray photoelectron Spectroscopy (XPS), Scanning Electron Microscopy-Energy Dispersive X-ray (SEM)-EDX, Atomic Force Microscopy (AFM). The M-Pd based thin films showed alloy formation phase and other thin films displayed some epitaxial relationship with preferred Au-Pd (111) substrate orientation using XRD. SEM-EDX exhibited nanoscale and conformal deposits, as well as the presence of a well distribution of each element which suggested successive atomic layer-by-layer deposition of elements. AFM revealed uniform grain distribution, with CuBiPd showing islands with the increased surface average ranging from bimetallic to trimetallic compounds, suggesting nucleation and 3D growth. EDX evidenced the presence of all deposited elements.

Interestingly some of the Te-M analogous exhibited nano dendritic (feather-like) microstructures with distinct branches size, outgrowing away from the nuclei. This has a strong agreement with the typical dendritic morphology common in Te-based compounds reported in a few existing literature studies. The dendritic structures are associated with most active sites for bifunctional mechanism and synergistic effect. EDX showed a highly dense Te distribution on both bimetallic and trimetallic compounds, suggesting alloys formation of deposited Te. The finding also supported by XRD as well, where the pattern exhibited positive 2θ shift and intense peaks at lower 2θ value.

All Pd-based thin films such as Pd, PdIr, CuPd, BiPd, CuBiPd, TePd, CuTePd, BiTePd were evaluated for electro-oxidation of 0.1M EtOH in 0.5M KOH containing solution. The addition of the second metal in the case of Ir on Pd improved electrocatalytic activity by 2 folds towards ethanol oxidation reaction (EOR). The catalytic activity of thin films towards the oxidation of ethanol in alkaline media was determined using CV. PdIr showed a more negative onset potential and higher current (-0.423V; 0.664 mA) than Pd (-0.402 V; 0.494 mA) thin film, indicating that

the bimetallic PdIr is more active than monometallic Pd. The electrochemical impedance spectroscopy (EIS) showed smaller $R_{ct} = 0.23 \text{ k}\Omega$ for PdIr than that of Pd; $R_{ct} = 14.8 \text{ k}\Omega$ when subjected to a fixed potential of -0.2 V . PdIr showed a higher i_f/i_b ratio of 1.094 than Pd ($i_f/i_b = 0.94$) indicating higher tolerance to poisoning by ethanol oxidation intermediates species than Pd. Moreover, chronoamperometry (CA) results confirmed that the addition of Ir to Pd improves the stability of the nanostructured PdIr film. The modification of Pd with Cu-UPD and Bi-UPD adlayers as catalytic promoters improved the electrocatalytic activity and fast electron kinetic transfer. The trimetallic (CuBiPd) compound showed higher activity and stability towards (EOR) than monometallic Pd and bimetallic counterparts. The indices (peak current and onset potential trend) used to evaluate the electrocatalytic performance has the follows trend: CuBiPd (1.35 mA, -0.45 V) > CuPd (0.6016 mA, -0.442 V) > BiPd (0.275 mA, -0.384 V) > Pd (0.186 mA, -0.35 V). Conclusively, incorporation of dual (CuBi) promoter species on Pd enhanced electron kinetics, evidenced by EIS possessing the diverse charge transfer resistance (R_{ct}): CuBiPd = $2.29 \text{ (k}\Omega)$ > CuPd = $2.98 \text{ (k}\Omega)$ > BiPd = $3.97 \text{ (k}\Omega)$ > Pd = $14.8 \text{ (k}\Omega)$. Te-M based thin films showed a remarkable electrocatalytic activity towards ethanol oxidation. The observed fascinating properties of the thin film formed by a low number (few minutes) of E-ALD cycles protocol, makes E-ALD technique a futuristic methodology to electroform thin film electrocatalysts. These results encourage the use of PdIr, Te-M and Pd-M based nanostructured thin films as anode electrocatalyst for application in alkaline direct ethanol fuel cells (ADEFCs).

Research outputs

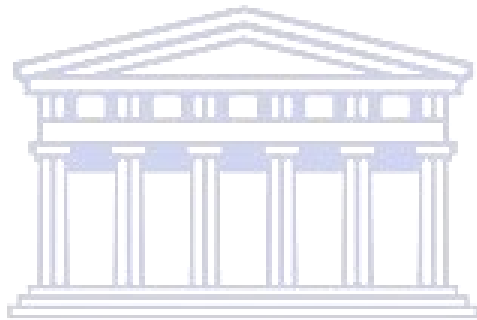
(i) List of Publication(s)

- **Andile C. Mkhohlakali**, X. Fuku, R. M. Modibedi, L.E. Khotseng , S.C Ray, M.K. Mathe. Electro synthesis and characterization of Pd, PdIr using electrochemical atomic layer deposition technique for ethanol oxidation in alkaline media, Applied Surface Science, (2020) 502 144-158.
- **Andile C. Mkhohlakali**, X. Fuku, R.M. Modibedi, L.E. Khotseng, M.K. Mathe. Electroformation of Pd-modified thin film electrocatalysts using E-ALD technique, Journal of Electrochemical Society, (Under review).
- **Andile C. Mkhohlakali**, X. Fuku, R.M. Modibedi, L.E. Khotseng, M.K. Mathe. Oxidative Te underpotential deposition on Pd-based electrode surface using E-ALD technique (draft).

(ii) Conferences/workshop attended

- **Poster Presentation:** 7th International Partnership for Hydrogen and Fuel Cells in the Economy (IPHE) 05-10 December 2018 University of Pretoria, Pretoria Republic of South Africa (RSA)-Best Poster award PhD category. **Title:** Electro-formation and characterization of Pd, PdIr using electrochemical atomic layer deposition technique for ethanol oxidation in alkaline media.
- **Oral Presentation:** 1st Korea-RSA Join workshop 05-07 August 2019, CSIR ICC, Pretoria South Africa. **Title:** Electrocatalysis on Pd dual-modified by foreign adatoms using E-ALD technique.
- **Oral Presentation:** SACI North (Young Chemists Symposium), University of Venda, Conference Centre, Thohoyandou, RSA (31 October 2019). **Title:** Automated electrosynthesis of Pd-based thin film using E-ALD technique for electrocatalysis.

- **Poster Presentation:** South African Nanoscience Initiative (SANi) conference (NYRS 2019 Symposium) 12 November 2019, University of Pretoria. **Title:** Electrosynthesis of Pd, PdIr using E-ALD technique for ethanol oxidation in alkaline electrolyte

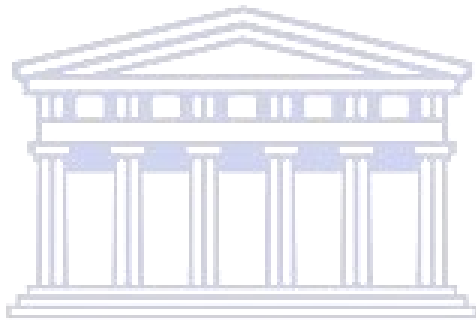


UNIVERSITY *of the*
WESTERN CAPE

Dedication

I dedicate this thesis to my parents Nozisile Bongiwe Mkhohlakali and my Father Zwel'gqithile

Dumisa Mkhohlakali and my elder brother Nceba Mkhohlakali



UNIVERSITY *of the*
WESTERN CAPE

Declaration

I declare that **Development of nanostructured thin film electrocatalysts using Electrochemical atomic layer Deposition technique for the direct liquid fuel cells** is my own work, and has not been submitted in any degree or examination in any other University and that all sources I have used or quoted have been indicated and acknowledged by means of complete references.

Andile Cyril Mkhohlakali

November 2019

Signed



UNIVERSITY *of the*
WESTERN CAPE

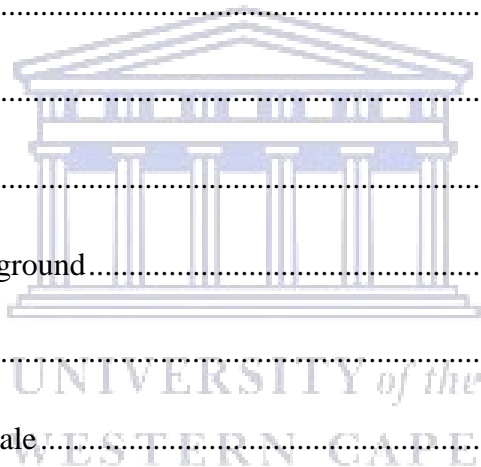
Acknowledgement

I would like to thank All Mighty God for the protection, strength, guidance and wisdom as well as life to live and for making this uphill journey possible.

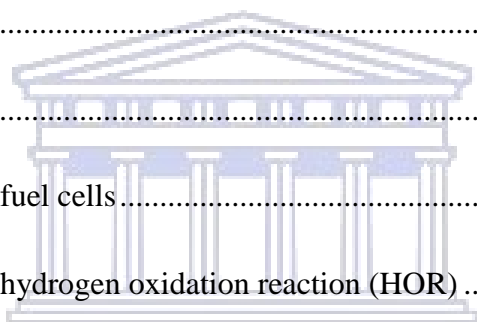
I would like to thank my supervisor Professor Lindiwe Khotseng for giving me an opportunity to work with her and her guidance during my journey. I also wish to extend my gratitude to my supervisors from CSIR Dr Mmalewane Modibedi and Dr Xolile Fuku for their unlimited guidance, patience with my mistakes, and for believing in me with this research project. Your role in this research is noticed and appreciated. A player-coach relationship with Dr Fuku with electrochemistry expertise as a whole has gone beyond the call of duty, I am grateful to work with you Sir. I appreciate the support from Smart Places: Energy Centre, Energy Materials manager, Dr. Mkhulu Mathe. I would also like to appreciate the fuel cell team under the Electrochemical Energy Technologies (EET) research group, Dr. Shakes Nonjola, Dr. Haitao Zheng, Ms. Nonhlahla Mphahlele, Ms. Nomthandazo Mabena, Ms. Mphoma Matseke, Ms. Thandiwe Maumau and Mr. Tshimangadzo Munonde for their kindness and support. I am so much grateful for the financial support from National Research Foundation-Professional Development Program (NRF-PDP) and the Council for Scientific and Industrial Research (CSIR), Scientia Pretoria. I am thankful for the support from the family, as the first graduate from the family, for not putting much pressure on me to let me continue with studies until PhD level. My mother Nozisile Bongiwe Mkhohlakali, thank you for your prayers sikhukukazi sakwa Zakumba ka Mbomboshe somzi ka Khumbuzile ka Dilesi ka Mkhohlakali. My Father Dumisa Mkhohlakali, for believing in me and always reminding me to focus. The unforgettable support from my elder brother Nceba Mkhohlakali from my first year of study. The fans, my siblings: Sinethemba Gan'zulu; Gcobani; Phiwe; Odidi; and Linge for making me feel like a warrior and a winner. My beautiful blessings from God, Libhongo Kuhle (son) and Ndalwentle (daughter) they were one of the reasons for me to wake up and go grind in my journey.

Contents

Key words	i
Abstract	ii
Research outputs	vi
Dedication	viii
Declaration	ix
Acknowledgement.....	x
List of figures	xx
List of abbreviation	xxix
Chapter 1	1
1. 0 Summary	1
1.1 Introduction and Background.....	1
1.2 Problem statement.....	7
1.3 Motivation and Rationale.....	8
1.4 Aims and objectives	9
1.5 Thesis outline and framework	11
References	14
Chapter 2.0	22
2.1 Literature review	22
Summary	22
2.1 Fuel cell overview	22
2.1.1 Fuel cells background.....	23

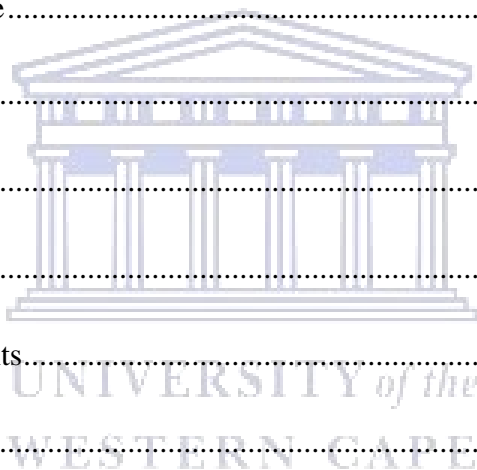


2.1.2 Components of fuels cell.....	23
2.1.3 Categories of fuel cell	24
2.1.3.1 Alkaline fuel cells.....	25
2.1.3.2 Phosphoric acid fuel cells (PAFCs)	27
2.1.3.3 Solid Oxide Fuel Cells (SOFCs)	28
2.1.3.4 Molten carbonate fuel cells (MCFCs).....	29
2.1.3.5 Polymer electrolyte membrane fuel cells (PEMFCs).....	30
2.1.3.6 Direct methanol fuel cells (DMFCs).....	32
2.2 Direct liquid fuel cell.....	33
2.3.1 Electrocatalysis.....	34
2.3.1.1 Electrocatalysis in fuel cells.....	35
2.3.1.2 Electrocatalysis in hydrogen oxidation reaction (HOR)	36
2.3.1.3 Electrocatalysis in ORR	38
2.3.1.4 The effect of foreign metal adatoms of electrocatalysis of ORR.....	40
2.3.1.5 Introduction of electrocatalysis in small liquid hydrocarbons (alcohols) molecules oxidation.....	41
2.3.2 General introduction on nanostructured thin films materials (NSMs) and nanotechnology	41
2.3.2. 1 Nanostructured materials in response to the fourth industrial revolution (4IR)	43
2.3.3. Fabrication methods of (NsMs).....	44
2.3.3.1 Physical vapour deposition (PVD) and Chemical vapour deposition (CVD).....	45
2.3.3.2 Molecular Beam Epitaxy (MBE)	45

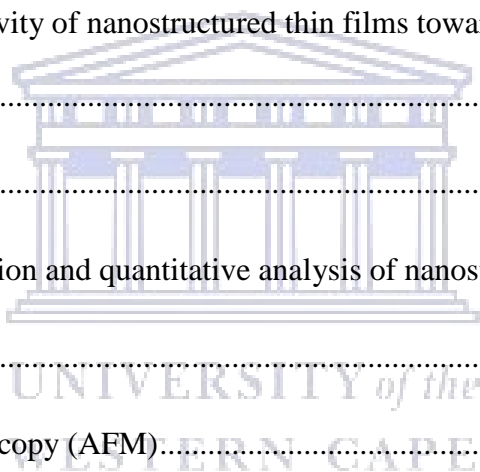


UNIVERSITY of the
WESTERN CAPE

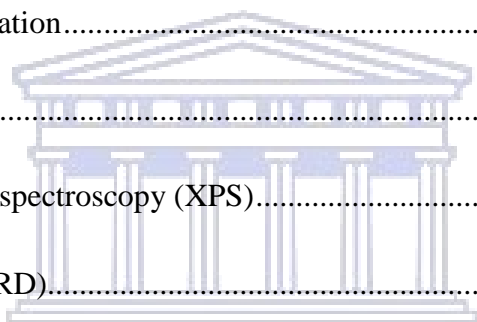
2.3.3.3 Pulsed Laser Deposition.....	46
2.3.3.4 Sputtering	46
2.3.3.5 Sol-gel synthesis.....	47
2.3.3.6 Atomic layer deposition (ALD)	47
2.3.3.7 Electrochemical deposition: Electrochemical atomic layer deposition (E-ALD) and Underpotential deposition (UPD)	48
2.4.1 Surface limited redox replacement: Prospects	51
2.4.2 Pourbaix diagrams on compounds formation.....	53
2.4.3 E-ALD and substrate.....	54
References	55
Chapter 3	75
3.0 Methodology	75
3.1.1 Materials and reagents.....	75
3.1.2 Precursor solutions	76
3.1.3 Electroformation of Pd-based nanostructured thin film through SLRR of Cu-UPD....	76
3.1.4 Electroformation of mono-metallic Pd nanostructured thin film via SLRR of Cu underpotential deposition	77
3.1.5 Electrodeposition of bimetallic PdIr thin film via SLRR Cu _{Upd}	78
3.2. Electrosynthesis of Pd-M (M= Cu, Bi): Pd surface Modification	79
3.2.1 Underpotential deposition of Bi on Au and Pd: CV profile	79
3.2.2 Underpotential deposition of Cu on Au and Pd: CV profile	79
3.2.3 Electrosynthesis of BiPd	80



3.2.4 Modification of Pd by mono Cu adlayer	80
3.3. Oxidative Te Underpotential deposition identification: CV profile	81
3.3. Electro-formation of Te-M thin film derivatives, (M = Au, Pd, BiPd, and CuPd)	81
3.3.1 Electro-formation of Te-M (M = Au) on Au substrate	81
3.3.2 Electroformation of Te-M, (M = Pd)	82
3.3.3: Electroformation of Te-M (M = BiPd)	82
3.3.4 Electro-formation of Te-M, (M = CuPd)	82
3.4.1 Electrochemical characterization of nanostructured thin films in 0.1 M HClO ₄	83
3.4.2 Electrochemical activity of nanostructured thin films towards KOH and EtOH oxidation	83
3.4.3 E-ALD set up	84
3.5. Physical characterization and quantitative analysis of nanostructured thin films.....	85
Microscopic analysis	85
3.5.2 Atomic force microscopy (AFM).....	85
Spectroscopic analysis.....	86
3.5.3 X-ray diffraction (XRD).....	86
3.5.4 X-ray photoelectron spectroscopy (XPS).....	86
3.6.1 Theory on characterization techniques.....	86
Electroanalytical techniques.....	86
The three electrochemical systems: Basic components	87
Working electrode	88
Reference electrode	89

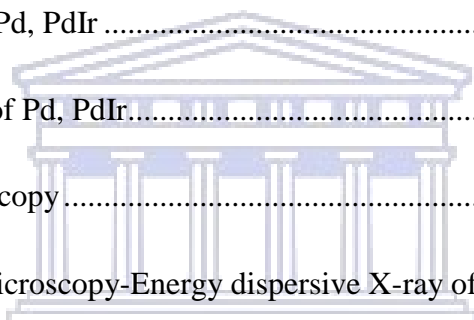


Counter/ Auxiliary electrode	89
Voltammetry.....	89
3.6.2 Cyclic voltammetry	90
3.6.3 Reversible systems	92
3.6.4 Quasi irreversible and irreversible systems.....	93
3.7.1 Chronoamperometry (CA)	94
3.7.2 Electrochemical impedance spectroscopy (EIS)	96
3.7.3 Equivalent or electric circuit elements	99
3.8.0 Physical characterization.....	100
Spectroscopic techniques	100
3.8.1 X-ray photoelectron spectroscopy (XPS).....	100
3.8.2 X-ray diffraction (XRD).....	102
3.8.3 Energy dispersion spectroscopy (EDS).....	104
3.9.0 Microscopic techniques.....	106
3.9.1 Scanning electron microscope (SEM).....	106
3.9.2 Atomic force microscopy (AFM).....	107
References	109
4.0 Chapter 4	114
4.0 Electrochemical deposition of monometallic Pd and bimetallic PdIr for ethanol oxidation	114
4.1 Introduction	114
4.2 Results and discussion.....	115



UNIVERSITY of the
WESTERN CAPE

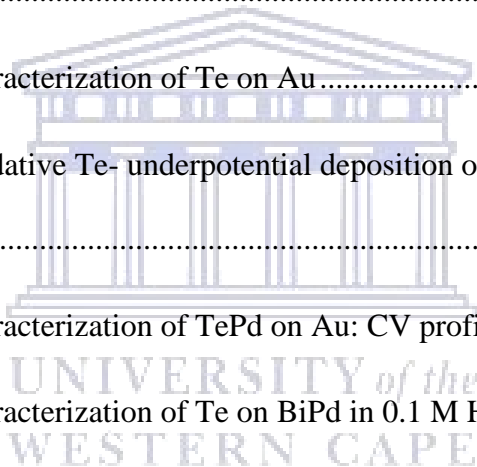
4.2.1 Cleaning and electrochemical characterization of gold (Au) substrate.....	115
4.2.2 Underpotential deposition of Copper (Cu) on Au: CV profile.....	116
4.2.3 Electrodeposition of Pd	118
4.2.4 Electrochemical characterization of Pd in acid (0.1 M HClO ₄).....	119
4.2.5 Electrodeposition of PdIr	120
4.2.6 Electrochemical characterization of PdIr in acid (0.1 M HClO ₄)	122
Spectroscopic and structural characterization of Pd, PdIr nanostructured thin films	123
4.2.7 X-ray photoelectron spectroscopy (XPS) of Pd, PdIr	123
4.2.8 X-ray diffraction of Pd, PdIr	126
4.3 Microscopic analysis of Pd, PdIr.....	128
4.3.1 Atomic force microscopy.....	128
4.3.2 Scanning electron microscopy-Energy dispersive X-ray of Pd, Ir, and PdIr thin films	130
4.4. Electrochemical characterization of Palladium-based thin film: Activity towards ethanol oxidation in alkaline media.....	131
4.4.1 Activity of Pd based thin film towards ethanol oxidation in alkaline media: Cyclic voltammetry (CV)	131
4.4.2 Electrochemical characterization of PdIr: Effect of scan rate of in KOH and ethanol oxidation.....	133
4.4.3 Chronoamperometry (CA) measurements of Pd, PdIr in 0.5 KOH + 0.1M EtOH...	135
4.4.4 Electrochemical impedance spectroscopy of Pd, PdIr based thin films towards EtOH oxidation.....	136
4.4.5 Sub conclusion	138



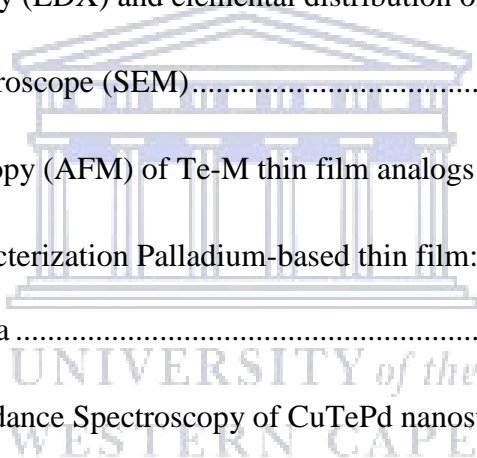
UNIVERSITY of the
WESTERN CAPE

References	139
Chapter 5	149
5.1 Introduction	149
5.2.1 Electrochemical characterization of Bi on Au: CV profile	150
5.2.2 Electrochemical characterization of Bi on palladium (Pd) surface	152
5.3 Electrochemical characterization of Cu on Pd electrode: CV profile	153
5.2.3 Electrochemical characterization of Pd-based electrodes in Bi ³⁺ solution: CV profile	154
5.2.4 E-ALD cycles of Pd modifications with foreign adatoms	156
5.3.1 Characterization of the Pd-M thin film, M= Cu and Bi in 0.1 M HClO ₄	158
5.3.2 Effect of potential and scan rate study of CuBiPd thin film in 0.1 M HClO ₄	159
5.4.1 X-ray diffraction of Pd-M based thin film.....	160
5.4.2 Scanning electron microscope (SEM) analysis of Pd-M based thin films.....	162
5.4.2 Energy dispersive X-ray analysis and elemental distribution of Pd-M based thin films	164
5.4.5 Atomic force microscopy (AFM) analysis bimetallic CuPd, BiPd, and CuBiPd	165
5.5. Electrochemical characterization Palladium-based thin film: Activity towards ethanol oxidation in alkaline media	169
5.5.1 Activity of Pd-M based thin film electrocatalysts towards ethanol oxidation in alkaline media: Cyclic voltammetry (CV).....	169
5.5.2 Scan rate dependence studies of CuBiPd catalyst	174
5.5.3 Chronoamperometric (CA) analysis of Pd-M based thin film in 0.5 KOH + 0.1M EtOH	175

5.5.4 Electrochemical impedance spectroscopy of Pd-M based thin film towards EtOH oxidation.....	177
5.5.6 Sub conclusion	179
References	180
Chapter 6	192
6.1 Electro-formation of nanostructured Te-based thin film (Te-M, where M= Pd, BiPd).....	192
6.2.0 Results and discussion.....	192
6.2.1 Identification of oxidative Te underpotential deposition (oxTe- _{UPD}) on Au, Pd, BiPd and CuPd: CV profiles	192
6.2.2 Electrochemical characterization of Te on Au.....	192
6.3.1 Identification of oxidative Te- underpotential deposition on Pd-covered Au: CV profile	196
6.3.2 Electrochemical characterization of TePd on Au: CV profile in 0.1 M HClO ₄	198
6.3.3 Electrochemical characterization of Te on BiPd in 0.1 M HClO ₄	200
6.4 X-ray diffraction of Te-M based nanostructured thin films, M = Pd, and BiPd electrodes	202
6.5 Scanning electron microscope (SEM)-energy dispersive x-ray (EDX) and elemental distribution of Te-M based thin films	203
6.6 Atomic force microscopy (AFM) of Te-M thin-film analogous.....	206
6.7 Electrochemical characterization Palladium-based thin film: Activity towards ethanol oxidation in alkaline media	208
6.8 Scan rate dependence study of BiTePd in 0.5 M KOH + 0.1 EtOH	212



6.9 Electrochemical Impedance Spectroscopy of Te-M nanostructured thin films	214
Sub conclusion	218
References	219
Chapter 7	230
7.0 Results and discussion.....	230
7.1 Electrochemical characterization of CuTePd in 0.1 HClO ₄	230
7.2 X-ray diffraction of CuTePd and its analogues Pd, TePd and CuPd nanostructured thin films.....	232
7.3 Energy dispersive x-ray (EDX) and elemental distribution of Te-M based thin films	233
7.4 Scanning electron microscope (SEM).....	234
7.5 Atomic force microscopy (AFM) of Te-M thin film analogs	235
7.6 Electrochemical characterization Palladium-based thin film: Activity towards ethanol oxidation in alkaline media	236
7.7 Electrochemical Impedance Spectroscopy of CuTePd nanostructured thin films and its derivatives	240
Sub-conclusion.....	243
8.1 Conclusion.....	248
8.2 Recommendations	250



List of figures

Figure s	Description	Page no
Figure 1.1:	Scheme 1.1: Research frame work.	(13)
Figure 2.1:	Schematic diagram of Alkaline Fuel cell.	(26)
Figure 2.2:	Schematic diagram for PAFCs operation.	(28)
Figure 2.3:	Schematic diagram of solid oxide fuel cell.	(29)
Figure 2.4:	Schematic diagram of MCFCs.as adopted from literature.	(30)
Figure 2.5:	Schematic diagram of PEMFCs, as adopted from literature.	(31)
Figure 2.6:	Schematic diagram for DMFCs.	(32)
Figure 2.7:	The illustration of electrocatalysis reaction (a) and the effect of catalyst in the chemical reaction (b).	(35)
Figure 2.8:	Volcano plot for electrocatalysis of hydrogen: log exchange current density of H ₂ reaction vs enthalpy oh H ₂ adsorption in various metals.	(37)
Figure 2.9:	Volcano curve showing trend in ORR activity as function of the oxygen binding energy.	(38)
Figure 2.10:	Schematic illustrating the relationship of potential (E/V) vs. current for UPD and OPD of Cu on Au.	(50)
Figure 2.11:	Schematic representation mechanism of surface limited redox replacement reaction.	(53)
Figure 2.12:	Pourbaix diagram of Cu, Te and BiTe in aqueous solution.	(54)

Figure 3.1: A typical potential-current time trace of Pd on Au recorded for two cycles and (b) generally schematic cartoon representing Pd SLRR of Cu-UPD. (78)

Figure 3.2: Picture of the up-pumping system, Potentiostat, and thin flow cell connected to a computer that have LABVIEW sequencer 4, Solution precursors, Thin flow cell and insert: thin flow cell. (85)

Figure 3.3: Illustration of three electrochemical cell consisting of three electrodes.(88)

Figure 3.4: A classical CV showing a current vs. potential and important anodic and cathodic parameters (a) and typical CV curve of Pd in a N₂ saturated 0.1M HClO₄ electrolyte, showing the important regions during anodic and cathodic scan at 25 °C. (91)

Figure 3.5: CV curves representing reversible (a) system and irreversible system (b) at various scan rates and Randles-Sevcik plot of peak current (I_p) versus square root of the scan rate ($v^{1/2}$). (92)

Figure 3.6: An example of chronoamperometric response as results of wave form perturbation (a) Typical experimental results of chronoamperometry of Pd in 0.5 M KOH + 0.1 M EtOH at applied biased potential of -0.2V for 3600s (1hr) duration, in which species in electroactive t₁ but reduced at diffusion-controlled rate at t₂. (95)

Figure 3.7: Illustration of amplitude of the sinusoidal potential, and the sinusoidal of the current resulting from the application of the potential. The phase difference (phase angle) between potential and current is highlighted. (97)

Figure 3.8: Typical example of Nyquist plot (a) and of PdIr in 0.5 M KOH + 0.1 M EtOH at 10-10⁴ Hz range at applied potential -0.2 V. (98)

Figure 3.9: Typical representation of Bode plot (a) and Bode plot of Pd in 0.5 M KOH + 0.1 M EtOH at $10\text{-}10^4$ Hz range at applied potential -0.2V (b). (99)

Figure 3.10: Schematic diagrams of typical XPS (a) and photoelectron line of PdIr/Au scan survey (b). (102)

Figure 3.11: Schematic diagram of XRD pattern (a) and spectra of typical single crystalline Au. (104)

Figure 3.12: Schematic of typical scanning electron microscope (SEM). (107)

Figure 3.13: Schematic diagram of AFM system (a), tip-sample separation curve, demonstrating the main interactions during AFM scanning (b). (108)

Figure 4.1: Cyclic voltammograms of bare Au substrate in 0.1 M HClO₄ at 10 mVs^{-1} scan rate. (116)

Figure 4.2: CV of Au in 0.1 mM CuSO₄ + 0.1 M HClO₄ at 10 mVs^{-1} . (117)

Figure 4.3: Time-potential-current trace of sequential layer-by layer deposition of Pd recorded for two cycles. (118)

Figure 4.4: CVs of Pd thin films deposited via SLRR on Au substrate in 0.1 M HClO₄. Scan rate: 30 mVs^{-1} . (119)

Figure 4.5: (a) Schematic representation of E-ALD cycle for the deposition of elements from their corresponding precursors, Cu-UPD on Au (111) substrate with its subsequent exchange for Pd and Ir at OCP, and (b) Time- potential-current trace of sequential layer-by layer deposition of Pd and PdIr recorded for two cycles. (121)

Figure 4.6: CVs of Pd and PdIr thin films deposited via SLRR on Au substrate in 0.1 M HClO₄. Scan rate: 30 mVs^{-1} . (123)

Figure 4.7: XPS spectra of (a) PdIr (b) Au 4f, (c) Pd 3d from monometallic Pd (black) and from bimetallic PdIr (red), (e) deconvoluted Pd 3d peak of PdIr, (d) XPS spectra of Ir 4f and (f) XPS spectra of O1S. (125)

Figure 4.8: XRD pattern of the whole Pd (a), PdIr thin films, and insert: magnified XRD pattern. (127)

Figure 4.9: AFM topography images of (a (i)) 2D and 3D (a (ii)) Pd topography (insert: zoomed Pd), (b (i)) 2D and (b (ii)) 3D of PdIr (insert (i): zoomed PdIr area), and their respective corresponding Texture profile (iii) and histogram (iv). (129)

Figure 4.10: SEM micrographs of (a) Au substrate (b) Ir, (c) Pd and (d) PdIr with corresponding EDX of (e) Pd and (f) PdIr. (131)

Figure 4.11: (a) and (b) illustrate cyclic voltammogram curves for Pd and PdIr thin films in 0.5 M KOH and 0.5 M KOH + 0.1 M EtOH respectively. (132)

Figure 4.12: (a) PdIr at various scan rates and (b) Randles-Sevcik plot. (134)

Figure 4.13: CA of Pd and PdIr at -0.2 V for 1 hour in 0.5 M KOH + 0.1M EtOH: insert, magnified CA from 3000s. (135)

Figure 4.14: (a) Nyquist plot of Pd (black) and PdIr (red), and insert: Randles-Sevcik circuit, and (b) their corresponding Bode plot. (137)

Figure 5.1: CVs of (a) Au in 0.2 mM Bi_2O_3 + 0.1 M HClO_4 at 10 mVs^{-1} . (151)

Figure 5.2: CV of Pd thin film in various cathodic limits potential (a), overlaid Au and Pd-covered Au (b) in solution of 0.2 mM Bi_2O_3 + 0.1 M HClO_4 at 10 mVs^{-1} . (152)

Figure 5.3: CVs of Pd thin film in 0.1 mM CuSO_4 + 0.1 M HClO_4 at 10 mVs^{-1} . (153)

Figure 5.4: CVs of CuPd thin film in 0.2 mM Bi₂O₃ + 0.1 M HClO₄ at 10 mVs⁻¹ scan rate. (155)

Figure 5.5: Potential-time-current trace of (a) CuPd and (b) BiPd recorded for two deposition cycles. (157)

Figure 5.6: CV of Pd-M based thin film in 0.1 M HClO₄ at 30 mVs⁻¹ scan rate. (159)

Figure 5.7: CuBiPd in 0.1 M HClO₄ at various potential window (a), scan rates (10, 20, 25, 30 and 40) mVs⁻¹, and Randles-Sevcik plot (c). (160)

Figure 5.8: (a) Whole XRD pattern of Au, Pd, BiPd, CuPd, and CuBiPd, magnified (111) plane: insert and (b) Magnified whole XRD pattern. (162)

Figure 5.9: Illustrates the low magnification SEM micrographs of Pd (a), CuPd(b), BiPd (c) and CuBiPd (d) and their corresponding high magnification: (inserts). (163)

Figure 5.10: The illustrate elemental of EDS and corresponding elemental mapping (insert) of (a) Pd, (b) BiPd and (c) CuPd, (d) CuBiPd. (165)

Figure 5.11: Reveals details of Atomic force microscopy (AFM) analysis for (a) Pd, (b) BiPd, (c) CuPd, and (d) CuBiPd. (167-168)

Figure 5.12: Illustration of reaction mechanisms of EtOH oxidation on Pd-based nano-structured thinfilm surface. (169)

Figure 5.13: CV of Pd, CuPd and BiPd and CuBiPd in 0.5 M KOH (a) and in 0.5 M KOH+ 0.1 M EtOH (b) at 30 mVs⁻¹. (170)

Figure 5.14: CVs of CuBiPd thin film in (a) 0.5 M KOH and (b) 0.5 KOH+ 0.1 M EtOH at various scan rates (10, 20, 25, 30, 40) mVs⁻¹. (175)

Figure 5.15: CA of Pd (black), BiPd (blue), CuPd (red), CuBiPd (dark green) and zoomed: insert in 0.5 KOH+ 0.1 M EtOH at fixed -0.2 V potential for an hour (3600s) duration.

(176)

Figure 5.16: (a) Nyquist plot and (b) the corresponding bode plot of Pd (black), CuPd (red), BiPd (blue), CuBiPd (dark green), insert (a) : Randles Sevcick circuit in 0.5 M KOH + 0.1 M EtOH at -0.2 V potential at 1×10^4 -1Hz frequency.

(177)

Figure 6.1: : (a) CV of Au in 0.5mM HTeO_2^+ + 0.1 M HClO_4 at 10 mVs^{-1} and (b) Nyquist plot at various bias cathodic limit potential.

(194)

Figure 6.2: Potential-current-time trace of Te-Au for (a) and CV in 0.1 M HClO_4 at 10 mVs^{-1} (b).

(196)

Figure 6.3: CV of Pd-covered Au at various cathodic limit potential (a), overlaid Pd-covered Au and bare Au (b) in solution of 0.5 mM HTeO_2^+ at 10 mVs^{-1} .

(197)

Figure 6.4: (a) Potential-current-time trace of TePd recorded for 2 cycles and (b) CV in 0.1 M HClO_4 at 30 mVs^{-1} .

(199)

Figure 6.5: (a) CV of BiPd-covered Au in 0.5 mM HTeO_2^+ + 0.1 M HClO_4 in 10 mVs^{-1} and of (b) BiTePd thin film analogues in 0.1 M HClO_4 at 30 mVs^{-1} .

(201)

Figure 6.6: XRD pattern of Au, Pd, and Te-M thin films, insert: Magnified (111) planes.

(203)

Figure 6.7: Reveals details of Atomic force microscopy (AFM) analysis for CuPd, TePd and BiPd on Au.

(205)

Figure 6.8 Illustrates the EDS and elemental distribution of (a) PdTe, (b) BiTePd and (c) CuTePd.

(206)

Figure 6.9: AFM topography (2D (i) and 3D (ii)) micrographs revealing details of Atomic Force Microscopy (AFM) analysis for (a) TePd, (b) CuTePd, (c) BiTePd thin films and corresponding height profile (iii) and Histogram (iv). (207)

Figure 6.10: CV of Pd, and Te-M thin film analogous in 0.5 M KOH at 30 mVs⁻¹ scan rate (209).

Figure 6.11: CV of Pd, Te-M based thin films in 0.5 M KOH + 0.1 M EtOH at 30 mVs⁻¹ scan rate. (210)

Figure 6.12: CA of Te-M based thin films in 0.5 M KOH +0.1 M EtOH for 1hour (3600s). (211)

Figure 6.13: Nyquist plot of Te-M analogous in 0.5 KOH + 0.1M EtOH at constant potential of -0.2 V at 1x10⁴ to 0.1 Hz frequency range, Randles-Sevcik circuit: insert. (214)

Figure 6.14: Bode plot of Te-M analogous in 0.5 KOH + 0.1 M EtOH at constant potential of -0.2 V. (216)

Figure 6.15: BiTePd thin film in 0.1M HClO₄ (a), 0.5 M KOH (b) and 0.5 M KOH + 0.1 M EtOH (c) at various scan rates (10, 20, 25, 30 and 40) mVs⁻¹ and corresponding Randles-Sevcik plot (c-f). (216)

Figure 7.1: CV of CuPd in 0.5 mM HTeO₂⁺ at 10 mVs⁻¹ in various cathodic limits (a) and CuTePd thin films derivative in 0.1 M HClO₄ at 30 mVs⁻¹ scan rate (b). (231)

Figure 7.2: XRD pattern of Au, Pd, CuPd TePd thin films (a) and CuTePd and its derivatives thin films, insert: Magnified (111) planes. (232)

Figure 7.3: Illustrates the EDX and corresponding elemental mapping (inserts) of (a) PdTe and CuTePd (b). (233)

Figure 7.4: Scanning electron microscope (SEM) analysis for TePd (a-b)) and CuTePd (c-d) on Au. (234)

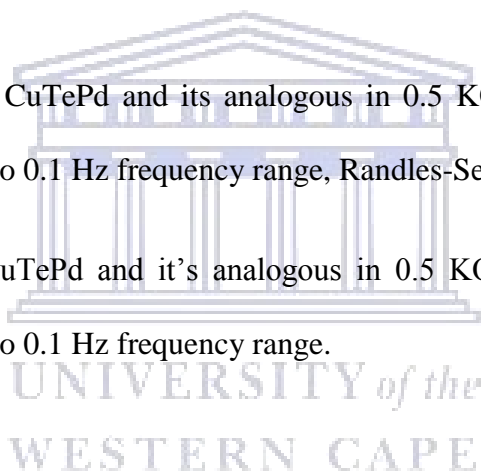
Figure 7.5: AFM topography (2D (i) and 3D (ii)) micrographs revealing details of Atomic Force Microscopy (AFM) analysis for (a) TePd, (b) CuTePd thin films and corresponding height profile (iii) and Histogram (iv). (236)

Figure 7.6: CV of CuTePd, CuPd, TePd and Pd in 0.5 M KOH (a) and 0.5 M KOH+ 0.1 M EtOH at 30 mVs⁻¹ scan rate. (238)

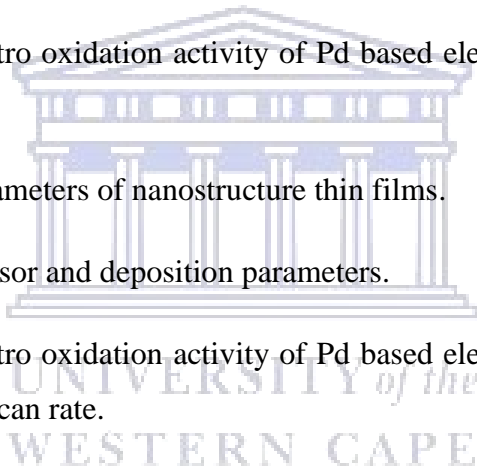
Figure 7.7: CA of CuTePd based thin films in 0.5 M KOH +0.1 M EtOH for 1hour (3600s). (239)

Figure 7.8: Nyquist plot of CuTePd and its analogous in 0.5 KOH + 0.1M EtOH at constant potential of -0.2 V at 1x10⁴ to 0.1 Hz frequency range, Randles-Sevcik circuit: insert.(241)

Figure 7.9: Bode plot of CuTePd and it's analogous in 0.5 KOH + 0.1M EtOH at constant potential of -0.2 V at 1x10⁴ to 0.1 Hz frequency range. (242)

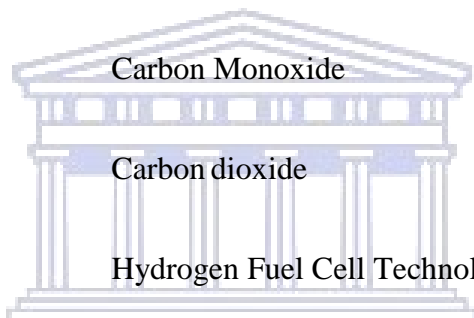


List of tables	Topic	Page no.
Tables		
Table 4.1:	Chemical states and Binding energy of Pd-based thin films.	(126).
Table 4.2:	Summary of electrochemical activity of Pd and PdIr electrocatalyst films towards EOR.	(137)
Table 4.3:	Summary of electrochemical activity of Pd and PdIr electrocatalyst films towards EOR.	(138)
Table 5.1:	Electrolyte precursor and deposition parameters.	(156)
Table 5.2:	Summary of electro oxidation activity of Pd based electrocatalyst towards ethanol in alkaline media.	(171)
Table 5.3:	Impedimetric parameters of nanostructure thin films.	(177)
Table 6.1:	Electrolyte precursor and deposition parameters.	(198)
Table 6.2:	Summary of electro oxidation activity of Pd based electrocatalyst towards ethanol in alkaline media at 30 mVs ⁻¹ scan rate.	(211)
Table 6.3:	Summary of some impedemetric parameter of Te-M based thin films in 0.5 KOH + 0.1 EtOH.	(217)
Table 7.1:	Summary of electro oxidation activity of Pd based electrocatalyst towards ethanol in alkaline media.	(238)
Table 7.2:	Summary of some impedemetric parameter of CuTePd based thin film in 0.5 KOH + 0.1 EtOH.	(242)



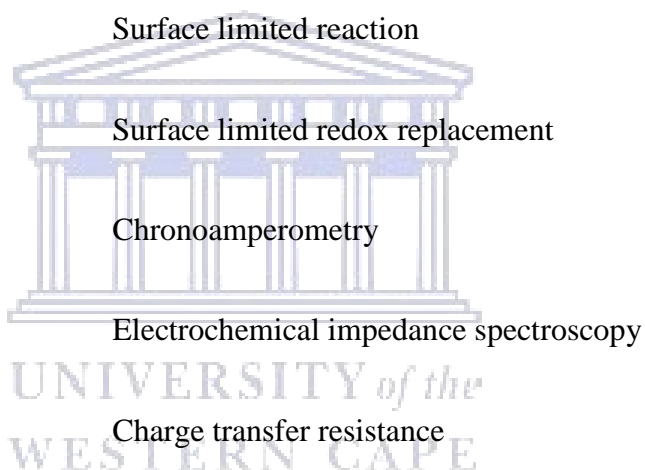
List of abbreviation

NsM	Nanostructure materials
AFC	Alkaline fuel cell
PGMs	Platinum Group Metals
HySA	Hydrogen South Africa
SANi	South African nanotechnology initiative
GHG	Green House Gases
CO	Carbon Monoxide
CO ₂	Carbon dioxide
HFCTs	Hydrogen Fuel Cell Technologies
PEMFC	Polymer Electrolyte Membrane Fuel Cell
DLFCs	Direct Liquid Fuel Cells
ADEFCS	Alkaline Direct Ethanol Fuel cell
DMFC	Direct Methanol Fuel Cell
PAFCs	Phosphoric acid fuel cells
SOFCs	Solid Oxide Fuel Cells SOFCs
MCFCs	Molten carbonate fuel cells MCFCs
CV	Cyclic voltammetry



UNIVERSITY of the
WESTERN CAPE

MBE	Molecular Beam Epitaxy
PVD	Physical Vapour disposition
CVD	Chemical Vapour Disposition
MOCVD	Molecular organic chemical vapour deposition
ALD	Atomic Layer Deposition
UPD	Underpotential deposition
E-ALD	Electrochemical atomic layer deposition
SLR	Surface limited reaction
SLRR	Surface limited redox replacement
CA	Chronoamperometry
EIS	Electrochemical impedance spectroscopy
R _{ct}	Charge transfer resistance
SEM	Scanning electron microscopy
EDS	Energy Dispersive X-ray spectroscopy
AFM	Atomic Force Spectroscopy
XRD	X-ray Diffraction
XPS	X-ray Photoelectron Spectroscopy

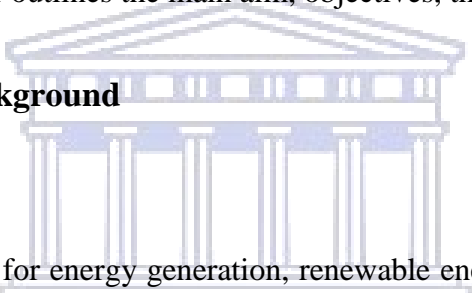


Chapter 1

1. 0 Summary

This chapter will give a general introduction of the technological developments that are devoted to mitigating fossil fuel use as energy conversion. It will explain terms, such as electrocatalysis, its background, and electrodeposition developments. A brief introduction on fuels and fuel cell categories will be given, and also addressing shortcomings associated with liquid fuels. The research problem and motivation will cover a brief description of the issues that need to be addressed. Lastly, the chapter outlines the main aim, objectives, thesis outline and research goals.

1.1 Introduction and Background



In quest to replace fossil fuel for energy generation, renewable energy technology emerges as an alternative replacement as a clean energy source. Fossil fuel such as oil (hydrocarbons), coal, and natural gas emit unwanted gases to the atmosphere and subsequently cause pollution and the greenhouse effect. Recently South African (SA) government signed a carbon tax bill to mitigate the high industrial usage of energy sources that emit poisonous gases to the atmosphere. SA' targets zero-carbon economy by 2030-2050, hence it is imperative to search for non-carbon energy sources. SA low-emission carbon development strategy (SALEDS 2050) and other countries considered to focus on low-carbon energy sources [5]. SA has positioned itself to be involved in the green economy using Platinum group metals (PGMs). SA remains as mining superpower house of PGMs which includes, Pt, Pd, Rh, and Ir. PGMs are key catalytic materials utilized in most fuel cell types. SA has around 88 % global PGMs with Zimbabwe holding 7 % and Russia 8 % [6] [7]. The South African Department of Science and Innovation has established

one of the national strategies, the hydrogen South Africa 'HySA' to develop the local technologies and skills for the development of hydrogen and fuel cell industry in the country. The programme has been in existence for more than 15 years, since its approval by the government in 2007 with a key goal of promoting the domestic-based PGMs catalysis value chain, which aims to supply 25 % of the catalyst demand for the global hydrogen fuel cell market by 2020.

Among other technologies, fuel cells attracted the most considerable attention because of its environmental friendliness as a power source. Fuel cell is an electrochemical device that converts the chemical energy of a fuel into direct current (DC), without resorting to a burning process [2], and with only water as a by-product in contrast to its counterparts (fossil fuel) [3]. The fuel may include pure hydrogen, liquid organic fuel (ethanol, methanol, formic acid) and is fed continuously to the anode where it is oxidized and split into electron and proton [10].

Fuel cell (FC) has emerged as non-emission technology of unwanted greenhouse gases (GHG), including nitrous oxide (NO_x), carbon dioxide (CO₂) and methane (CH₄). Research advances focus on technological development to stop the usage of fossil fuel. However, commercialization of the Polymer membrane electrolyte Fuel Cell (PEMFC) is hindered by the high cost and durability [11], hydrogen production and its infrastructure challenges such as, high-pressure storage to be stored and transported [12] and could cause explosions. These infrastructure issues of pure hydrogen gas [13] twisted the focus on more liquid-based hydrogen fuel carriers. Compared to hydrogen, liquid fuels are portable, easy to store and to transport, and have high energy density [14], [15]. Liquid fuels address the issue of hydrogen infrastructure, fossil fuel consumption and also have a high potential for application in fuel cell devices (Direct liquid fuel cells). Liquid organic fuels include alcohols, hydrocarbons, and inorganic liquids. This leads to the emerging of direct liquid fuel cells (DLFCs) which uses methanol, ethanol, ethylene glycol, glycerol, borohydrides, dimethyl ether, formic acid, and hydrazine as fuel [12]. DLFC is the kind

of device that directly converts the chemical energy of liquid organic molecules into electrical energy [16]. DLFC are classified according to the type of liquid fuel used, for an example, methanol is named direct methanol fuel cells (DMFCs), ethanol is direct ethanol fuel cells (DEFCs), glycerol is direct glycerol fuel cells (DGFCs), and so on [12]. Among DLFCs, DEFC has attracted most interest in liquid fuel cells, because ethanol (EtOH) as sustainable energy carrier, is regarded as renewable biofuel that possesses several advantages including; ease of storage liquid fuel, allowing storage in conventional tanks, high theoretical energy density (8.0 kW h kg^{-1}) in contrast to hydrogen (3.8 kW h kg^{-1}) fuel [12], [17], [18]. EtOH is a liquid hydrocarbon just like gasoline; it can be spread widely via the existing infrastructure unlike pure compressed or liquid hydrogen [19]. These factors of EtOH make ADEFCs more attractive in economic viability and environmental perspective. ADEFCs also address the issue of global warming crisis, because it does not emit greenhouse gases (GHG) [15]. However, the main drawback of ADEFCs is to develop a highly efficient electrocatalyst to completely oxidize ethanol and produce high power output [20]. In a complete EtOH oxidation of these typical fuels, EtOH oxidizes to give CO_2 yielding $12e^-$ [21], [22]. Nonetheless, the lack of complete oxidation in these fuels produces intermediates such as poisonous CO, acetaldehyde and acetic acid [12], [23]. For ethanol dihydroxyacetone, tartronic acid is produced and inhibits the performance of the fuel cell anode. It is very crucial to identify electrocatalysts that complete ethanol oxidation that is to cleave the C-C strong bond [19], [24].

Grubs developed fuel cells in 1963, where he initially investigated the term electrocatalysis. Electrocatalysis can be described as electrochemical surface reaction, in which metal electrode-electrolyte interface takes place. However, the term electrocatalysis existed before and was famous in a paper published by Horiuti and Polanyi [4]. A series of measurements have been done on various metal electrodes surface which marked the emergence of fuel cell technology. [26].

Nanostructured thin films of platinum group metals (PGMs) are playing a crucial role in most fuel cell devices [27]. The country has also considered PGMs thin film fabrication and their application in renewable and sustainable energy conversion, as a response and relevance to the Fourth Industrial Revolution (4IR) [28]. Among PGMs, Pd based nanostructured materials have shown increased attention due to the fast kinetics for the oxidation of small organic fuel, such as alcohol in alkaline media [29] and is relatively cheaper than Pt. However, Pd is readily poisoned by ethanol intermediates during ethanol oxidation reaction (EOR) [30], hence the consideration of embellishing its surface or forming an alloy with the second metal with electronic effect and bifunctional mechanism to improve Pd catalytic activity [22], [31]. The existing literature has been devoted to the development of PdM (M= Sn, Bi, CeO₂, Ni) to improve the activity and stability of Pd catalyst [32]. Modibedi et al., [33] reported PdSn and Pd-Ru-Sn catalysts using chemical reduction method and high electrocatalytic activity was achieved upon the introduction of the second metal on Pd. Chaudwury et.al [34] embellished Pd with copper using facile hydrothermal reduction method for oxidation of methanol in alkaline media for fuel cell application and showed an improved activity for methanol oxidation in alkaline media. Rostami and co-workers [35] reported an effect of Ni on PdCu using the facile electrochemical method and a promising electrocatalytic activity for direct ethanol fuel cell was obtained. Chen et al reported PdIr supported by carbon for formic acid electro-oxidation, where Ir formed Ir (OH) which can further oxidize CO_{ads} to CO₂) [9], [37].

On the other hand, nanostructured thin film electrocatalysts of PGMs-chalcogenides (PGM-E, where E = Se, Te, S) have also drawn increasing attention in recent years due to their relevance in catalysis and materials science. These chalcogenides include PGMs based compounds, primarily containing tellurium (Te), sulphur (S), oxygen (O) and selenium (Se) [38]. Particularly Te based chalcogenides such as binary-phase of Pt-Te system have been used for the manufacturing of semiconductors for photovoltaic cells, thermoelectric, and also frequently used

as cathode material in fuel cell application [39]. In addition, Te is a component on ternary mercury cadmium telluride (MCT - HgCdTe) semiconductor species which is considered as third-generation technology after GaAs [40]. Further, Te-based PGMs can be applied as anode electrocatalysts, because Te is an oxygen-containing species and has a promotional effect, during electro-oxidation of alcohols [41]. Recently, Haider reported ultra Pt thin film using SLRR of tellurium underpotential desposition (Te-upd) as sacrificial metals, and a rough deposit was obtained [43]. Huang et al., reported the formation of platinum telluride supported carbon PtTe_x/C, (in various x ratios) using polyol microwave method for oxidation of ethanol and high electrochemical activity was obtained [44][45]. Cai et al. reported PdTe_x/C using a microwave polyol method for oxidation of ethanol in alkaline media, and an improved electrochemical activity was achieved [41]. Yao et al. synthesized a stronger CO tolerating and high electrochemical activity PtIrTe towards methanol oxidation using wet chemical reduction method [46]. The existing literature demonstrates the importance of Te-based PGM chalcogenides in various electrochemical reactions. However, there are no reports on Pd based Te-chalcogenides thin films electrocatalysts prepared using E-ALD for ADEFC. Compared to other methods such as chemical vapour deposition (CVD), molecular beam epitaxy (MBE), sputtering, etc, E-ALD is a room temperature, vacuum free technique which form materials at atomic level in layer-by-layer (2D growth) [47] such as monometallic, bimetallic and trimetallic PGMs based compounds. This research, pursue the electroformation of PGMs based thin film electrocatalysts of well-defined structure using E-ALD technique for application in a direct liquid fuel cell (DLFCs).

There is a need to investigate the most efficient nanostructured thin film electrocatalyst for application in alkaline direct ethanol fuel cells (ADEFCs). The PGM based compounds at the nano-sized regime and high surface area with attracting properties have been produced by various methods including chemical reduction method using reducing agents, such as

microwave-assisted polyol, hydrothermal, solvothermal and thermal decomposition among others. The high quality of PGMs based thin films are produced by vapour deposition methods. The challenge facing the mentioned method is a lack of particles' conformal dispersion, control of structure and stoichiometry, as well as elemental composition of underlying particles.



UNIVERSITY *of the*
WESTERN CAPE

1.2 Problem statement

The dependency of fossil fuel for energy generation/conversion has become a major concern due to climatic changes. The development of alkaline direct ethanol fuel cells (ADEFCs) serves as a possible alternative fuel cell over PEMFCs since it is possible to use a variety of cheaper and abundant metal catalysts than Pt. However, incomplete oxidation of ethanol produces intermediates (carbonaceous species) that can poison the catalyst, and limit its performance. In this regard, new catalysts that have high potential to cleave the C-C bond to complete oxidation of ethanol must be developed. Furthermore, thin-film methodologies such as physical and chemical reduction methods, chemical vapor deposition (CVD) [11], molecular beam epitaxy (MBE), metalorganic chemical vapor deposition (MOCVD), physical vapor deposition (PVP) prepare high-quality thin films, however, they tend to form undesirable three dimensional (3D) crystal growth and they operate at high pressure-temperature conditions which results to layer interdiffusion [12],[13]. E-ALD could be an alternative method to fabricate thin film electrocatalysts because it produces nanostructures using the surface limited reaction of underpotential deposition (UPD) to controlled composition and crystal growth. E-ALD method operates in ambient conditions, and with controlled thickness, morphology, and composition.

E-ALD was first started with the formation of II-VI thin film semi-conductor, and further explored in the formation of III-VI and thereafter VI-VI nanofilm, superlattice, nanoclusters. The surface limited redox replacement reaction (SLRR) has made it possible for the application of E-ALD to electroform metal (PGMs) thin film electrocatalysts using Cu-UPD and Pb-UPD for fuel cell application [51]. Adzic reported the Pd surface modification using foreign adatoms for the oxidation of formic acid [52]. Sheridan reported Pd nanofilm on the Au substrate using Cu-UPD and the utilization of complexing agents [53]. There has been an extensive application of E-ALD for application in electrocatalysis. Recently Xaba et al reported Pd-based thin film formation on

Au using SLRR of Cu-UPD for application in the oxidation of alcohol in alkaline media [54]. Moreover, Mkhohlakali et al reported the bimetallic PdIr utilizing the Cu-UPD as the sacrificial metal for application in electrocatalysis of ethanol in alkaline media [55]. However, there are limited reports on PGMs-based chalcogenides reported using E-ALD.

In view of simplicity, the bimetallic and trimetallic metal catalyst of palladium-based thin films should be synthesized using E-ALD to achieve high electro-oxidation activity on high energy density liquid fuels such as ethanol in alkaline medium.

The modern fabrication of PGMs-based thin film electrocatalysts using E-ALD technique for fuel cell could be marked as a realization, response, and relevance to Africa/SA's fourth industrial revolution (4IR). Among PGMs, Pd is flexible and its alloy exhibits higher catalytic activity compared to Pt in alkaline media for DEFCs. Flexibility and activity of palladium and its alloys towards oxidation of alcohol in both acid and alkaline media have attracted this study. Furthermore, chalcogenide such as Te and p-nictides, Bi, act as promoters and further oxidize the carbonaceous species on Pd surface. In the preparation and fabrication of electrocatalyst, E-ALD is a preferred modern and viable technique. This typical method consumes a small amount of noble metal precursor solutions [56]. The technique creates highly uniform, conformal and quality thin films with a well-defined structure [57]. Part of this study also reports the originality (if not first time) use of E-ALD for the deposition of Ir and PdIr for EOR thus far. Furthermore, the study presents new interesting approach on Pd modified electrode surface by oxidative Te-UPD using E-ALD. The thin film prepared exhibited higher ethanol oxidation activity in alkaline media than Pd, which demonstrated the potential as a candidate catalyst for DEFCs.

1.3 Motivation and Rationale

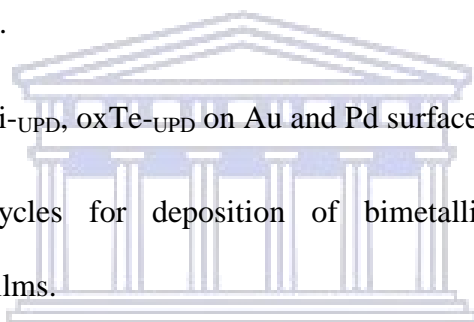
South African government has been a significant player in Hydrogen and fuel cell technologies (HFCTs) through the HySA programme, and been devoted to green energy technology research using PGMs beneficiation while targeting low-carbon energy utilization and global competitiveness by 2030. The largest PGMs reserves globally are mined in Pt belt known as Bushveld Complex in SA [58]. Biofuel based liquid fuel cell and metal-hydride systems for storage have played a significant role for hydrogen infrastructure and reduction of fossil fuel consumption. Hydrogen-fed PEMFC depends on expensive platinum (Pt) as the catalyst and pure hydrogen as fuel. The high energy density 8.0 kW h kg^{-1}) of liquid ethanol has triggered the research on alkaline direct ethanol fuel cells (DEFCs). SA' produces a million liters of ethanol annually preferring the sugarcane as feedstock. The electrochemical conversion (oxidation) of ethanol is occurring over the catalyst surface based on PGMs which gives high electrochemical activity with $12e^-$ more than that of hydrogen ($2e^-$) as compared to other transition metals. The incorporation of second metal particularly copper (Cu), antimony (Sb), lead (Pb), and bismuth (Bi) gained a wide attention as selective promoter species. Specifically Cu, Bi and Te adatoms are viewed as best candidates in this study due to less toxicity, high oxophilic character as compared to Sb and Pb and they could form hydroxyl at lower potential to further promote bifunctional mechanism and relatively enhance electrocatalytic activity. This research reports the development of PGMs-based thin film electrocatalysts for fuel cell application in line with the country's beneficiation strategies.

1.4 Aims and objectives

This research seeks to explore the use of E-ALD to design a low-cost nanostructured electrocatalyst for application in electro-oxidation of liquid fuels in alkaline media.

In order to achieve this aim, the following objectives must be met:

- To electroform mono, bi and trimetallic nanostructured Pd based thin films on Au substrate i.e., *Pd*, *PdIr*, *BiPd*, *CuPd*, *TePd*, *CuBiPd*, *BiTePd* and *CuTePd* via electrochemical surface limited reactions (SLR) approaches.
- Determine Cu-UPD as sacrificial metal on Au using cyclic voltammetry (CV).
- Develop E-ALD cycles for deposition of Pd and PdIr thin films.
- Electrochemical characterization of Pd and PdIr thin films using CV, CA and EIS.
- Physical characterization of mono metallic *Pd* and bimetallic *PdIr* thin films using XRD.
- Surface morphology and compositional analysis studies of *Pd* and *PdIr* using SEM, AFM, EDX and XPS.
- Determine Cu-UPD, Bi-UPD, oxTe-UPD on Au and Pd surface using CV.
- Develop E-ALD cycles for deposition of bimetallic M-Pd (M= Cu, Bi, Te) nanostructured thin films.
- Design E-ALD cycles for deposition of trimetallic *CuBiPd*, *BiTePd* and *CuTePd*.
- Electrochemical characterization of bimetallic and trimetallic nanostructured thin films using CV.
- Physical characterization of bimetallic and trimetallic thin films using XRD, The morphology and structure of M-Pd based thin films were determined using AFM, SEM and (EDX/EDS) for their corresponding composition.
- Electrochemical characterization of Pd-based thin film towards ethanol oxidation in alkaline media using electroanalytical techniques such as; CV, CA, and EIS.



UNIVERSITY OF
WESTERN CAPE

1.5 Thesis outline and framework

Chapter 1: This chapter will introduce the nanostructured thin film, their preparation, and application. It will touch on the importance of the study in line with technological developments. Application of the materials will be introduced focusing on Heterogeneous-(electro)-catalysis such as oxidation of some alcohols. Moreover, the chapter addresses the problem faced and elucidates the motivation and rationale.

Chapter 2: This chapter will focus on the literature on fuel cell types and their electrochemical reaction involved in each fuel cell type. The overview of nanostructured thin film materials and nanotechnological advances such as fourth industrial evolution will be given in this chapter. The overview of nanostructured materials and their application will be also summarized in a form of schematic charts. The fabrication methods of the nanostructured thin film will be reviewed and discussed. It will also narrow down on the importance of thermodynamic phenomena such as underpotential deposition and surface limited redox replacement. Lastly, the type and importance of substrate in electrocatalyst preparation will be outlined.

Chapter 3: This chapter will focus on methodology, experimental setup, chemicals and reagents that were used in the experiments. The details of the experiment and characterization that are going to be used will be highlighted in the chapter. The theory of characterization techniques will be also given in detail.

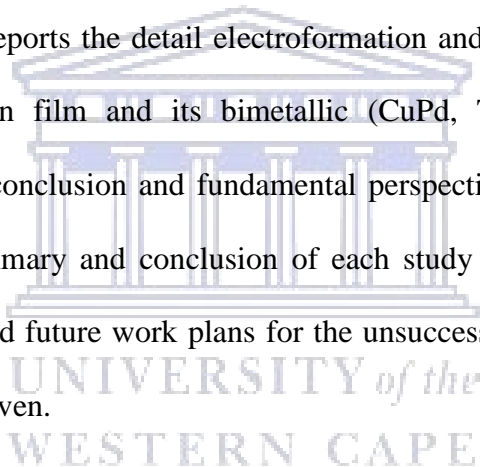
Chapter 4: This chapter details the electro-formation of monometallic Pd and bimetallic PdIr deposited on Au using the surface limited reaction of Cu underpotential deposition. The deposition cycles are also summarized in the form of a potential-current-time trace. The formation of compounds will be characterized and tested in a half-cell for ethanol oxidation in alkaline media. The content of this part of the work is published in a peer-reviewed journal.

Chapter 5: This chapter anecdote the Pd surface modification by adatoms of metal-UPD for the ethanol oxidation in alkaline medium. This chapter will be reported on the preparation and characterization of the nanostructured thin films electro-catalyst of M-Pd derivatives where M = Bi and Cu moieties to give the corresponding; monometallic (Pd), bimetallic (BiPd, CuPd) and trimetallic (CuBiPd) nanostructured thin films.

Chapter 6: This chapter will report the rare approach to oxidative Te underpotential deposition (OX-Te-UPD) on Au and Pd-covered Au and BiPd electrode. The nanostructured thin films reported herein, are Te-M analogous, where M= Au, Pd, BiPd. Electrochemical characterization of trimetallic BiTePd and its analogs nanostructured thin films will be discussed.

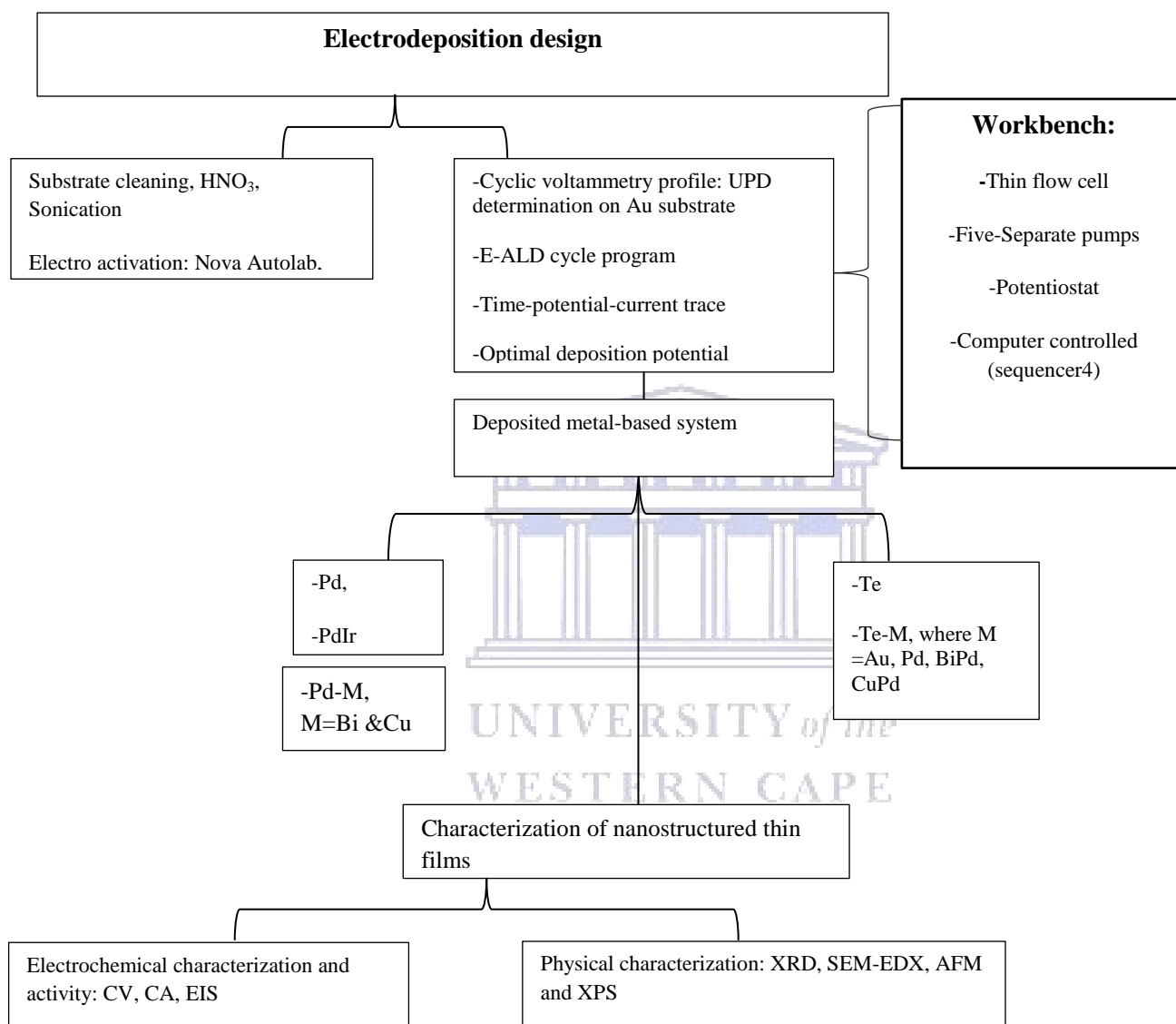
Chapter 7: This Chapter: reports the detail electroformation and characterization of trimetallic CuTePd nanostructured thin film and its bimetallic (CuPd, TePd) analogous compounds.

Chapter 8: Provide a key conclusion and fundamental perspectives on cogent findings on the entire thesis. Outlining summary and conclusion of each study or synthetic approach will be given. Recommendations and future work plans for the unsuccessful work possible solutions to and breakthroughs will be given.



Research frame work

This research frame work covers some of the general objectives of this work.



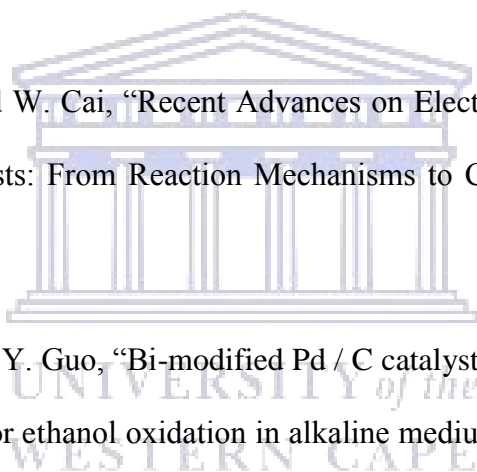
Scheme 1.1: Research frame work

References

- [1] A. C. Mkhohlakali and P. A. Ajibade, “Synthesis, Photo Physical Studies and Evaluation of Ruthenium (II) Complexes of Polypyridyl Ligands as Sensitizer for DSSCs,” *Int. J. Electrochem. Sci.*, vol. 10, pp. 9907–9918, 2015.
- [2] V. Venkatasamy, M. K. Mathe, S. M. Cox, U. Happek, and J. L. Stickney, “Optimization studies of HgSe thin film deposition by electrochemical atomic layer epitaxy (EC-ALE),” *Electrochim. Acta*, vol. 51, no. 21, pp. 4347–4351, 2006.
- [3] M. K. Mathe, S. M. Cox, V. Venkatasamy, U. Happek, and J. L. Stickney, “Formation of HgSe Thin Films Using Electrochemical Atomic Layer Epitaxy,” 2005.
- [4] R. G. Motsoeneng, R. M. Modibedi, M. K. Mathe, L. E. Khotseng, and K. I. Ozoemena, “The synthesis of PdPt / carbon paper via surface limited redox replacement reactions for oxygen reduction reaction,” *Int. J. Hydrogen Energy*, vol. 40, 2015.
- [5] B. Van Der Zwaan, G. Jan, T. Kober, F. D. Longa, and A. Van Der Laan, “An integrated assessment of pathways for low-carbon development in Africa,” *Energy Policy*, vol. 117, no. August 2017, pp. 387–395, 2018.
- [6] M. Trends, “PGE Production in Southern Africa, Part I : Production and Market Trends,” 2017.
- [7] B. J. Glaister and G. M. Mudd, “The environmental costs of platinum – PGM mining and sustainability : Is the glass half-full or half-empty ?,” *Miner. Eng.*, vol. 23, no. 5, pp. 438–450, 2010.

- [8] P. B. L. Chaurasia, Y. Ando, and T. Tanaka, "Regenerative fuel cell with chemical reactions," *Energy Convers. Manag.*, vol. 44, pp. 611–628, 2003.
- [9] S. J. Peighambaroust, S. Rowshanzamir, and M. Amjadi, *Review of the proton exchange membranes for fuel cell applications*, vol. 35, no. 17. Elsevier Ltd, 2010, pp. 9349–9384.
- [10] Y. Qiao and C. M. Li, "Nanostructured catalysts in fuel cells," pp. 4027–4036, 2011.
- [11] M. K. Mathe, T. Mkwizu, and M. Modibedi, "Electrocatalysis research for fuel cells and hydrogen production," *Energy Procedia*, vol. 29, pp. 401–408, 2012.
- [12] B. C. Ong, S. K. Kamarudin, and S. Basri, "Direct liquid fuel cells : A review," *Int. J. Hydrogen Energy*, vol. 42, no. 15, pp. 10142–10157, 2017.
- [13] "Hydrogen Fuel : Opportunities and Barriers," *J. Fuel Sci. Technol.*, vol. 6, 2009.
- [14] E. H. Yu, U. Krewer, and K. Scott, "Principles and Materials Aspects of Direct Alkaline Alcohol," pp. 1499–1528, 2010.
- [15] S. P. S. Badwal, S. Giddey, A. Kulkarni, J. Goel, and S. Basu, "Direct ethanol fuel cells for transport and stationary applications – A comprehensive review," *Appl. Energy*, vol. 145, pp. 80–103, 2015.
- [16] G. L. Soloveichik, "Liquid fuel cells," *Beilstein J. Nanotechnol.*, vol. 5, pp. 1399–1418, 2014.
- [17] R. M. Modibedi, T. Masombuka, and M. K. Mathe, "Carbon supported Pd-Sn and Pd-Ru-Sn Snanocatalysts for ethanol electro-oxidation in alkaline medium," *Int. J. Hydrogen Energy*, vol. 6, pp. 1–9, 2011.

- [18] H. Chen, Z. Xing, S. Zhu, L. Zhang, Q. Chang, J. Huang, W. Cai, N. Kang, C. Zhong, and M. Shao, "Palladium modified gold nanoparticles as electrocatalysts for ethanol electrooxidation," *J. Power Sources*, vol. 321, pp. 264–269, 2016.
- [19] J. Friedl and U. Stimming, "Model catalyst studies on hydrogen and ethanol oxidation for fuel cells," *Electrochim. Acta*, vol. 101, pp. 41–58, 2013.
- [20] K. A. Anna Zalineeva, Alexey Serov, Monica Padilla, Ulises Martinez and and P. B. A. Stève Baranton, Christophe Coutanceau, "Self-Supported Pd_xBi Catalysts for the Electrooxidation of Glycerol in Alkaline Media," *J. Am. Chem. Soc.*, vol. 136, pp. 3937–3945, 2014.
- [21] Y. Wang, S. Zou, and W. Cai, "Recent Advances on Electro-Oxidation of Ethanol on Pt- and Pd-Based Catalysts: From Reaction Mechanisms to Catalytic Materials," pp. 1507–1534, 2015.
- [22] J. Cai, Y. Huang, and Y. Guo, "Bi-modified Pd / C catalyst via irreversible adsorption and its catalytic activity for ethanol oxidation in alkaline medium," *Electrochim. Acta*, vol. 99, pp. 22–29, 2013.
- [23] G. L. Soloveichik, "Liquid fuel cells," *Beilstein J. Nanotechnol.*, vol. 5, pp. 1399–1418, 2014.
- [24] K. Artyushkova, B. Halevi, M. Padilla, P. Atanassov, and E. A. Baranova, "Mechanistic Study of Electrooxidation of Ethanol on PtSn Nanoparticles in Alkaline and Acid Media," *J. Electrochemical Soc.*, vol. 162, no. 6, pp. 345–351, 2015.
- [25] J. O. B. and Z. S. Minevski, "Electrocatalysis: Past, Present and future," *Electr. Acta*, vol. 39, no. 11, pp. 1471–1479, 1994.



- [26] S. Litster and G. Mclean, "PEM fuel cell electrodes," vol. 130, pp. 61–76, 2004.
- [27] Yan Qiao and Chang Ming Li, "Nanostructured catalysts in fuel cells," *J. Mater. Chem.*, vol. 21, no. 6, p. 062001, 2010.
- [28] M. Lee, J. J. Yun, A. Pyka, D. Won, F. Kodama, G. Schiuma, H. Park, J. Jeon, K. P. Id, and K. Jung, "How to Respond to the Fourth Industrial Revolution , or the Second Information Technology Revolution ? Dynamic New Combinations between Technology , Market , and Society through Open Innovation," *J. Open Innov. Technol. , Mark. Complex*, 2018.
- [29] R. Jana, S. Dhiman, and S. C. Peter, "Facile solvothermal synthesis of highly active and direct ethanol fuel cell applications Facile solvothermal synthesis of highly active and robust Pd_{1.87}Cu_{0.11}Sn electrocatalyst towards direct ethanol fuel cell applications," *Mater. Res. Express*, vol. 3, no. 8, pp. 1–9, 2016.
- [30] K. Ding, G. Yang, S. Wei, P. Mavinakuli, and Z. Guo, "Cyclic Voltammetric Preparation of Palladium Nanoparticles for Ethanol Oxidation Reaction," *Ind. Eng. Chem. Res.*, vol. 49, pp. 11415–11420, 2010.
- [31] C. Zhu and Y. Yang, "Surface voltammetric dealloying investigation on PdCu / C electrocatalysts toward ethanol oxidation in alkaline media," *J Nanopart Res*, vol. 20, p. 314, 2018.
- [32] T. Yang, Y. Ma, Q. Huang, G. Cao, S. Wan, N. Li, H. Zhao, X. Sun, and F. Yin, "Palladium – iridium nanowires for enhancement of electro-catalytic activity towards oxygen reduction reaction," *Electrochem. commun.*, vol. 59, pp. 95–99, 2015.

- [33] R. M. Modibedi, T. Mehlo, K. I. Ozoemena, and M. K. Mathe, "Preparation , characterisation and application of Pd / C nanocatalyst in passive alkaline direct ethanol fuel cells (ADEFC)," *Int. J. Hydrogen Energy*, vol. 40, no. 45, pp. 15605–15612, 2015.
- [34] S. kumar B. b Sreya Roy Chowdhury a, Parthasarathi Mukherjee a, "Palladium and palladium e copper alloy nano particles as superior catalyst for electrochemical oxidation of methanol for fuel cell applications," *Int. J. Hydrogen Energy*, vol. 41, no. 38, pp. 17072–17083, 2016.
- [35] H. Rostami, T. Abdollahi, P. Mehdipour, A. A. Rostami, and D. Farmanzadeh, "Effect of Ni addition on electrocatalytic activity of PdCu catalysts for ethanol electrooxidation : An experimental and theoretical study," *Int. J. Hydrogen Energy*, vol. 42, no. 39, pp. 24713–24725, 2017.
- [36] S. Yao, M. Wang, and M. Madou, "A pH Electrode Based on Melt-Oxidized Iridium Oxide," *J. Electrochem. Soc.*, vol. 4, pp. 29–36, 2001.
- [37] J. Chen, Y. Li, Z. Gao, G. Wang, J. Tian, C. Jiang, S. Zhu, and R. Wang, "Ultrahigh activity of Pd decorated Ir / C catalyst for formic acid electro-oxidation," *Electrochem. commun.* vol. 37, pp. 24–27, 2013.
- [38] B. S. Dey and V. K. Jain, "Platinum Group Metal Chalcogenides," *Platin. Met. Rev.*, vol. 2, no. 5, pp. 16–29, 2004.
- [39] J. Fernández-lodeiro, B. Rodríguez-gonzález, F. Novio, D. Ruiz-molina, J. L. Capelo, and A. A. Santos, "Synthesis and Characterization of PtTe₂ Multi-Crystallite Nanoparticles using Organotellurium Nanocomposites," *Sci. Rep.*, no. August, pp. 1–10, 2017.

- [40] E. Mori, C. K. Baker, J. R. Reynolds, and K. Rajeshwar, "Aqueous electrochemistry of tellurium at glassy carbon and gold. A combined voltammetry-oscillating quartz crystal microgravimetry study," *J. Electroanal. Chem.*, vol. 252, no. 2, pp. 441–451, 1988.
- [41] J. Cai, Y. Huang, and Y. Guo, "PdTe_x/C nanocatalysts with high catalytic activity for ethanol electro-oxidation in alkaline medium," *Appl. Catal. B Environ.*, vol. 150–151, pp. 230–237, 2014.
- [42] V. Venkatasamy, N. Jayaraju, S. M. Cox, C. Thambidurai, M. Mathe, and J. L. Stickney, "Deposition of HgTe by electrochemical atomic layer epitaxy (EC-ALE)," *J. Electroanalytical Chem.*, vol. 589, pp. 195–202, 2006.
- [43] F. Haidar, M. Maas, A. Piarristeguy, A. Pradel, S. Cavaliere, and M. Record, "Ultra-Thin Platinum Deposits by Surface-Limited Redox Replacement of Tellurium," *nanomaterials*, vol. 8, pp. 1–12, 2018.
- [44] M. Huang, L. Li, and Y. Guo, "Microwave heated polyol synthesis of Pt₃Te_x/C catalysts," *Electrochim. Acta*, vol. 54, pp. 3303–3308, 2009.
- [45] M. Huang, F. Wang, L. Li, and Y. Guo, "Short communication A novel binary Pt₃Te_x/C nanocatalyst for ethanol electro-oxidation," *J. Power*, vol. 178, pp. 48–52, 2008.
- [46] Y. Hao, Y. Yang, L. Hong, J. Yuan, L. Niu, and Y. Gui, "Facile Preparation of Ultralong Dendritic PtIrTe Nanotubes and Their High Electrocatalytic Activity on Methanol Oxidation," *Appl. Mater. Interfaces*, vol. 6, pp. 21986–21994, 2014.
- [47] V. Venkatasamy, N. Jayaraju, S. M. Cox, C. Thambidurai, and J. L. Stickney, "Studies of Hg_{1-x}Cd_xTe Formation by Electrochemical Atomic Layer Deposition and Investigations into Bandgap Engineering," pp. 720–725, 2007.

- [48] K.L. Choy, "Chemical vapour deposition of coatings," *Prog. Mater. Sci.*, vol. 48, pp. 57–170, 2003.
- [49] Y. Kim, J. L. Stickney, N. Jayaraju, D. Vairavapandian, Y. G. Kim, and D. Banga, "Electrochemical atomic layer deposition (E- ALD) of Pt nanofilms using SLRR cycles," *J. Electrochem. Soc.*, vol. 159, no. February 2015, pp. 616–622, 2012.
- [50] V. Venkatasamy, N. Jayaraju, S. M. Cox, C. Thambidurai, and J. L. Stickney, "Studies of Hg _{1-x} ... Cd x Te Formation by Electrochemical Atomic Layer Deposition and Investigations into Bandgap Engineering," *J. Electrochem. Soc.*, vol. 154, pp. 720–725, 2007.
- [51] M. Fayette, Y. Liu, D. Bertrand, J. Nutariya, N. Vasiljevic, and N. Dimitrov, "From Au to Pt via Surface Limited Redox Replacement of Pb UPD in One-Cell Configuration," *Langmuir*, vol. 27, pp. 5650–5658, 2011.
- [52] M. Studies, "Electrocatalysis on Surfaces Modified by Foreign Metal Adatoms," *Isr. J. Chem.*, vol. 18, pp. 166–181, 1979.
- [53] L. B. Sheridan, D. K. Gebregziabihier, J. L. Stickney, and D. B. Robinson, "Formation of palladium nanofilms using electrochemical atomic layer deposition (E-ALD) with chloride complexation," *Langmuir*, vol. 29, no. 5, pp. 1592–1600, 2013.
- [54] N. Xaba and R. M. Modibedi, "Pd , PdSn , PdBi , and PdBiSn Nanostructured Thin Films for the Electro-Oxidation of Ethanol in Alkaline Media," *Electrocatalysis*, pp. 11–16, 2019.
- [55] A. C. Mkhohlakali, X. Fuku, R. M. Modibedi, L. E. Khotseng, S. C. Ray, and M. K. Mathe, "Electrosynthesis and characterization of PdIr using electrochemical atomic layer

- deposition for ethanol oxidation in alkaline electrolyte,” *Appl. Surf. Sci.*, vol. 502, no. August 2019, pp. 144–158, 2019.
- [56] M. K. Mathe, S. M. Cox, V. Venkatasamy, U. Happek, and J. L. Stickney, “Formation of HgSe Thin Films Using Electrochemical Atomic Layer Epitaxy,” 2005.
- [57] V. Venkatasamy, I. Shao, Q. Huang, and J. L. Stickney, “ALD Approach toward Electrodeposition of Sb_2Te_3 for Phase-Change Memory Applications,” *J. Electrochemical Soc.*, vol. 155, pp. 693–698, 2008.
- [58] Y. Seo and S. Morimoto, “Analyzing Platinum and Palladium Consumption and Demand Forecast in Japan,” *resources*, vol. 6, pp. 1–13, 2017.



Chapter 2.0

2.1 Literature review

Summary

This chapter gives the literature survey, starting with an overview of fuel cells. General introduction on nanostructured material of Platinum group metals and their hybrid with non-PGMs towards application in electrocatalysis will be discussed in detail to be specific on oxidation of small organic molecules (SOMs). The general introduction on nanomaterials (nanostructured materials) will be given, including preparation, application (electrocatalysis) and contribution to the fourth industrial revolution (4IR). Introduction on thin film technology and basics concepts will be addressed in this chapter. The introduction of the top-down preparation/fabrication method of thin film will be given, with a detailed discussion on the bottom-up design of metal thin film methodologies. Electrodeposition of metal thin film will be discussed, singling out the details on electrochemical atomic layer deposition (E-ALD) to be specific.

UNIVERSITY of the
WESTERN CAPE

2.1 Fuel cell overview

The fuel cell is the electrochemical devices that chemical energy of Fuel (oxidant) and oxygen (reductant) direct to electrical energy. Hydrogen can be produced from various sources; pure hydrogen is produced from electrolysis of water that is the decomposition of water into hydrogen and oxygen gas through electrical current passed. Although pure hydrogen is a goal in fuel cell energy conversion, the storage and infrastructure is a critical issue. As a result of that, the realm is on sourcing hydrogen from hydrogen-based hydrocarbons such as methanol, ethanol, ethylene

glycol and borohydride. Many attempts are on oxidation of these hydrogen-rich molecules into a proton (H^+) and electron (current) for electrical energy generation. In fuel cell oxidation takes place on the anode (electrode catalyst) surface. Arguably electrode catalyst is the key/critical component in the fuel cell. The most commonly used anode electrocatalyst is precious platinum (Pt). The major drawback that inhibits fuel cell into commercialization is the carbon monoxide (CO) generated as reaction intermediate from organic fuel during electrochemical reaction at the anode [1],[2]. CO contaminate Pt-electrocatalyst surface active sites [3] and block hydrogen adsorption and electro-oxidation [4], and then resulting to fuel cell degradation. Fundamental research limits the barrier on fuel cell by considering parameters such as operating temperature, type of electrolyte, metal electrode electrocatalyst. So far the most considered efficient fuel cell is polymer electrolyte fuel cell (PEMFCs), with an efficiency of above 60-70 % at low temperature 50-80 °C [5], [6]. The polymer-based electrolyte used in this typical fuel cell is Nafion®, which is a perfluorinated polymer manufactured from DuPont company [7], [8]. The high cost of platinum and Nafion has resulted in intensive research of less noble metals to replace Pt metal with platinum-free catalyst [9], reduce Pt loading by coupling with less noble metal to make bimetal, which will relative reduce the cost. Several fuel cell types have emerged through consideration and attempts of replacing expensive Nafion [10], which were named according to mediator species employed.

2.1.1 Fuel cells background

2.1.2 Components of fuels cell

A fuel cell is mainly composed of major four components such as gas diffusion layer (GDL), anode/cathode catalyst layer (CL), proton exchange membrane (PEM), and substrate mostly carbon [11]. GDL is passage or porous for proton (H^+) and oxygen (air) to pass from cathode to anode [12]. Anode side is where the oxidation takes place in the fuel cell. Membranes in fuel are

electrolyte layers with the dimension of (10-100 μm), it is an ironically conductive, and electronically insulating material. The role for the membrane is the transportation of protons from anode side to cathode and water to anode but prevents oxygen from cathode to anode [13].

2.1.3 Categories of fuel cell

Fuel cells are classified according to the electrolyte employed in electrochemical reaction [14],[15], there is six categories of fuel cells; namely [16]. Electrolyte's function in the fuel cell, it conducts ions, rather than an electron and is sandwiched between the positive and negative electrode, which is cathode and anode respectively.

- Alkaline membrane Fuel Cells (AMFCs)
- Phosphoric acid fuel cells (PAFCs)
- Solid Oxide Fuel Cells (SOFCs)
- Molten carbonate fuel cells (MCFCs)
- Polymer Electrolyte Membrane fuel cell (PEMFCs)
- Direct Methanol Fuel Cells (DMFCs)

Table 2.1: Summarizes the fuel cell categories conditions and potential application [17], [18],[19], [20].

Fuel cell type	Type of electrolyte	Temperature (T°C)	Fuel source	Common use	Electrode reaction
Polymer electrolyte fuel cell	Polymer (Nafion)	50-120	Hydrogen	Automotive, Stationary	Anode $H_2 \rightarrow 2H^+ + 2e^-$ Cathode $e \frac{1}{2}O_2 + 2H^+ + e^- \rightarrow H_2O$
Direct methanol fuel cell	Nafion	50-120	Methanol	Portable devices, stationary	Anode $CH_3OH + H_2O \rightarrow CO_2 + 6H^+ + 6e^-$ Cathode $\frac{3}{2}O_2 + 6H^+ + 6e^- \rightarrow 3H_2O$
Alkaline fuel cell	Potassium hydroxide	50-200	Hydrogen, methanol, ethanol, Borohydride	Space shuttle, stationary	Anode $H_2 + 2HO^- \rightarrow H_2O + 2e^-$ Cathode $\frac{1}{2}O_2 + H_2O + 2e^- \rightarrow 2HO^-$

Phosphoric fuel cell	Phosphoric acid	1450-200	Hydrogen	Stationary, Automotive	Anode $H_2 \rightarrow 2H^+ + 2e^-$ Cathode $\frac{1}{2}O_2 + 2H^+ + e^- \rightarrow H_2O$
Solid oxide fuel cell	Yttria-stabilized zirconium	800-1000	Hydrogen, Hydrocarbons	Automotive, Home	Anode $2H_2 + O_2^{2-} \rightarrow H_2O + 2e^-$ Cathode $\frac{1}{2}O_2 + 2e^- \rightarrow O^{2-}$
Molten carbonate fuel cell	Molten carbonate	>650	Hydrogen, reformed hydrocarbons, syngas	Automotive	Anode $H_2 + 2CO_2^{2-} + 4e^- \rightarrow 2CO_2 + 2H_2O$ Cathode $O_2 + 2CO_2 + 4e^- \rightarrow 2CO_3$

2.1.3.1 Alkaline fuel cells

Alkaline fuel cells (AFCs) also known as Bacon fuel cell is among the oldest fuel cell technology, dating back 1960s and 1970s was used by National Aeronautics and Space Administration (NASA) in Apollo and Space shuttle programs [21]. Since the discovery of AFCs, the interest has increased because of its simplicity, facile kinetic at the cathode and anode, possibility of using non noble metal, low cost compared to other fuel cell types[22],[23],[24]. This type of fuel cell uses aqueous hydroxides such as potassium hydroxide as electrolyte[17], sodium hydroxide is also possible but has some disadvantages, and was the first fuel cell technology to put into practical service. The use of alkaline medium has benefited AFCs popularity due to high efficiency, and a wider selection of electrocatalyst and fuels [18]. The operating temperature of this typical fuel cell is wide as 50-200 °C, and have the highest efficiency obtained is 70 % [19], [20] with fast oxygen kinetic reaction. **Figure 2.1** shows the schematic diagram.

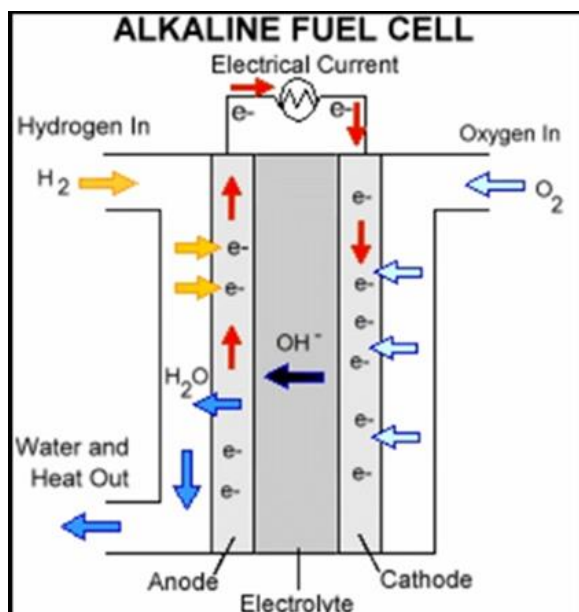
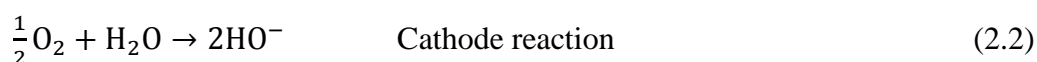


Figure 2.1: Schematic diagram of Alkaline Fuel cell [28].

There are many electrocatalysts used in AFCs, both noble and non-noble, such as Nickel (Ni) and silver (Ag) [21], Platinum, Iron (Fe III), Al(III), PtRu (III) and Pd [22]. Another advantage of this typical fuel cell is wide range of using fuel sources, such as ethanol, methanol, and sodium borohydride. Among the metal used in AFCs, nickel is the most used and active electrocatalyst.

The electrochemical reaction at anode, cathode and the overall reaction is as follows;

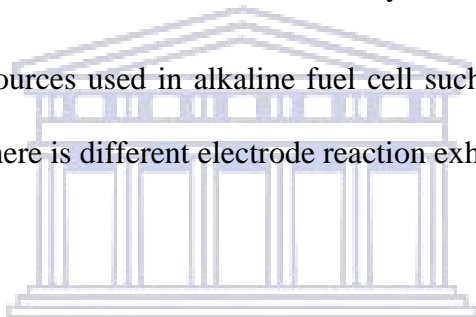


Equation 2.1 and **2.2** revealing the anode, cathode, overall cell reaction in alkaline fuel cell

The drawbacks associated with AFCs of electrolyte and electrocatalyst degradation is caused by formation of Pt poisoning CO, possible formation of carbonate (CO_3^{2-})\bicarbonate (HCO_3^-) on reaction of OH^- from alkaline medium with CO_2 contamination in the oxidant gas (air) stream [23] or from reformat of fuel source (Varcoe and Slade, 2005). The major limitation is

precipitation of carbonate (CO_3^{2-}) anion with mobile cation (K^+) to form K_2CO_3 solid crystals⁴⁰ which block gas diffusion layer [19], increase the viscosity of mass transport which results to degradation of the cell [33],[42]. This typical fuel has expensive choices (i) to avoid CO_2 contaminated air or fuel source by employing partial scrubbing, (ii) by using pure hydrogen and oxygen. As a result of that, the expenses of AFCs CO_2 free operation have impeded the development of these fuel cells for general application. To overcome these shortcoming Pd - based electrocatalysts was well reported by many researchers as good, alternative metal catalysts in alkaline media (typical KOH) and also Pd is not rare compared to Pt-based catalysts [33], [34]. And also the replacement of liquid potassium hydroxide as electrolyte [35] with solid polymeric electrolyte, would be a solution to the issue of carbonate crystal formation.

There are numerous Fuel sources used in alkaline fuel cell such as ethanol, methanol, sodium borohydride [36] are used, there is different electrode reaction exhibited,



2.1.3.2 Phosphoric acid fuel cells (PAFCs)

PAFCs are fuel cell devices that phosphoric acid (H_3PO_4) solution as electrolyte (Sotouchi and Hagiwara). They employ platinum as catalyst, porous carbon as support and operate at around 220°C with an efficiency of 75-80 %. This typical fuel cell has broadened its choice for use due to the high tolerance of about 15000 ppm CO [38]. However, the use of only precious metal platinum catalyst has limited its popularity.

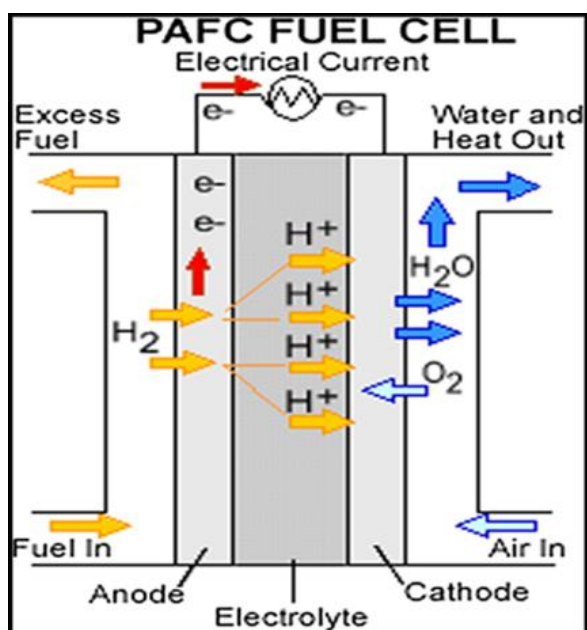
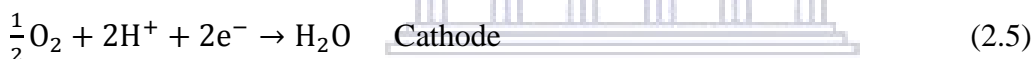


Figure 2.2 : Schematic diagram for PAFCs operation [28].

The electrochemical reactions of PAFCs occur on highly supported Pt-catalyst with carbon:



Equation 2.4 to 2.6 reveals anode, cathode and overall reactions in PAFCs

2.1.3.3 Solid Oxide Fuel Cells (SOFCs)

SOFCs (yttria zirconium) is the high temperature (100 °C) type of fuel cell device that appears to be one of most promising technology to provide efficient and clean energy generation because it only produces water as a by-product. It can be widely employed with power generator systems, both auxiliary power source in vehicles or aircraft and in-residence applications [39]. This type of fuel cell was invented in the 1930s by a Swiss scientist Emil Baur and his co-worker H. Preis ceramic starting materials such as zirconium, yttrium, cerium, lanthanum and tungsten oxide

[40],[41], uses yttria-stabilized zirconium as solid electrolyte at temperature range of 800-1000 °C operation [42]. SOFCs suppresses other fuel cell types, due to the capability of converting carbon monoxide and hydrogen through internal reforming at high temperatures and not limited by the Carnot cycle [42],[43],[44]. The shortcomings related to this typical fuel cell, s the high-temperature operations, as result of that many attempts have been made to lower temperature as they increase the cost of resources [45].

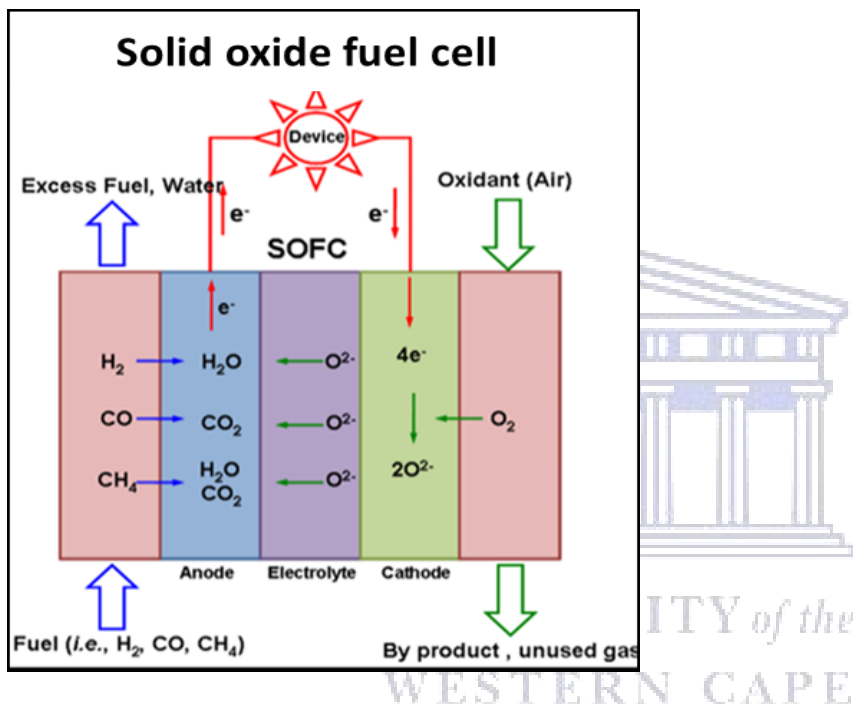
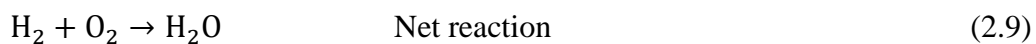
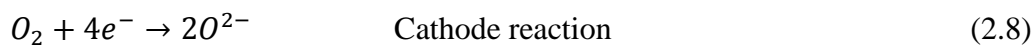
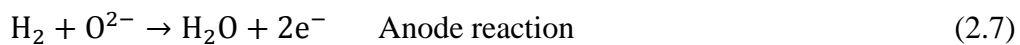


Figure 2.3 : Schematic diagram of solid oxide fuel cell [46].



2.1.3.4 Molten carbonate fuel cells (MCFCs)

MFC is one of the high-temperature devices that use molten carbonates as the electrolyte. This typical fuel cell was developed for natural gas, electrical and military applications, at a temperature range of 600-1000 °C with an efficiency of up to 85 %. It was developed in the

1950s in the Netherlands, by Dutch scientists G. H. J Broers and J.A.A Katelaar using a mixture of alkali metal carbonates salts such as lithium, sodium and potassium carbonates. Sources of fuel are hydrogen, reformed hydrocarbons (methane and methanol), and syngas. This typical fuel cell (MCFCs) has an operating temperature of 650 °C, it has many advantages compared to other fuel cell devices; such advantages are it does not need precious metal for oxidation; carbon monoxide is also a fuel source, high efficiency of up to 85 %.

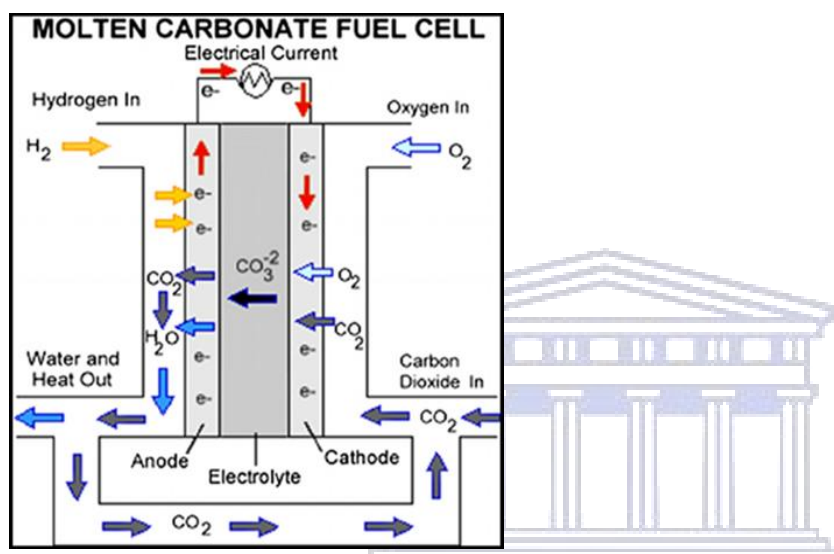
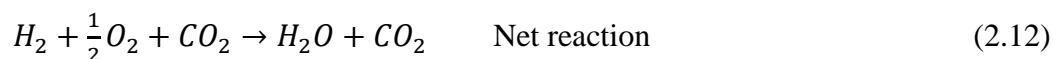


Figure 2.4: Schematic diagram of MCFCs as adopted from literature [28].



Equation (2.10 to 2.12) illustrate anode, cathode and overall in MCFCs

2.1.3.5 Polymer electrolyte membrane fuel cells (PEMFCs)

Polymer electrolyte membrane fuel cells also known as proton exchange membrane fuel cells (PEMFCs) are considered to be the most popular fuel cell type compared to other fuel cells [47].

PEMFCs is considered as promising zero-emission fuel cell and is suitable for transportation,

stationary and portable devices application [15], [48]. The first PEMFCs were applied in 1960 as auxiliary Gemini space flight, [48],[49], recently it has gained remarkable attention because of its wide application in a portable device, automotive and stationery application [50],[51]. This typical fuel cell has a low operating temperature range of 50-100 °C with an efficiency of 70 %. It uses classes of solid polymer electrolytes membranes such a Nafion (perfluorosulfonic acid), polyvinylidene-flouride (PVDF), polyether ether ketone (PEEK), polytetrafluoroethylene (PTFE). The most used membrane as proton conductor in PEMFCs is typically Nafion 20. Nafion was developed by Walther Grot of DuPont by modification of Teflon, a polytetra fluoro ethylene (PTFE) by adding a hanging sulphonic acid group. Nafion has been used as a benchmark for polymer membranes electrolytes development for PEMFCs, due to the good characteristic such as stability that arises because of Teflon backbone and proton conductivity from sulphonic acid group. It has an inverted micelle structure because of hydrophobic Teflon backbone structure and hydrophilic sulphonic acid group, this protects electrode catalyst from water flooding in PEMFCs and transfer of proton to the cathode side.

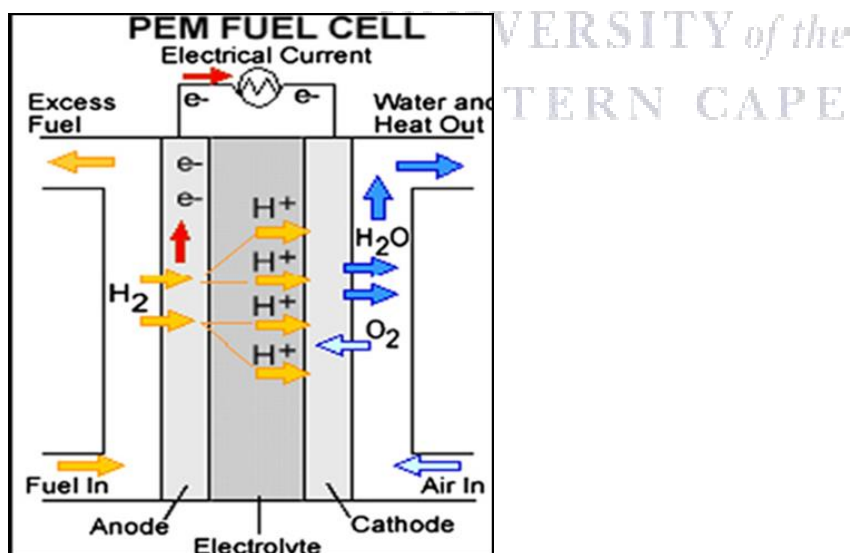
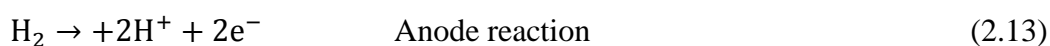
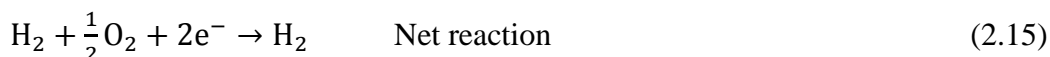
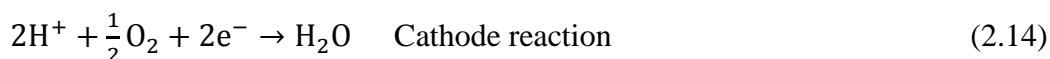


Figure 2.5: Schematic diagram of PEMFCs, as adopted from the literature [15].





Equation 2.13 to 2.15 showing the anode, cathode reactions in PEMFCs

The drawback associated with PEMFCs is that it employs expensive precious Platinum as electrocatalyst [52]. Also when the source of fuel is a hydrocarbon, or alcohol the carbon monoxide formed as intermediate contaminate Pt active site and block the electrooxidation [53]. Another shortcoming is the high cost of the Nafion® electrolyte membrane and its complexity in the assembling of the fuel cell.

2.1.3.6 Direct methanol fuel cells (DMFCs)

Direct methanol fuel cell (DMFC) is the further development or analog of PEMFCs but uses methanol as a fuel source. Methanol as fuel has high energy density [54] and has emerged to overcome the challenges of pure hydrogen are storage, distribution, and infrastructure [55]. DMFCs are promising portable fuel cell devices [56] with 55 % efficiency at low operating temperature range 30-80 °C [57].

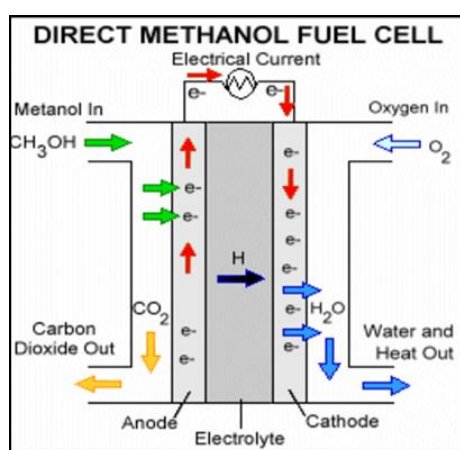
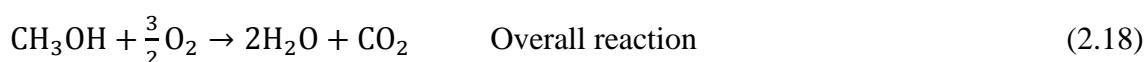
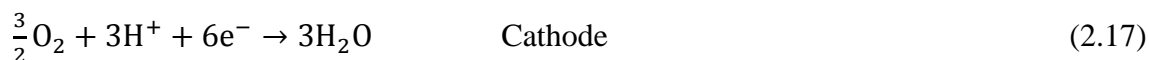


Figure 2.6: Schematic diagram for DMFC [28].

In this typical fuel cell device, methanol is fed at anode side where electro-oxidation takes place and reduction of oxygen at the cathode side. The basic electrochemical reaction in DMFC is given below;



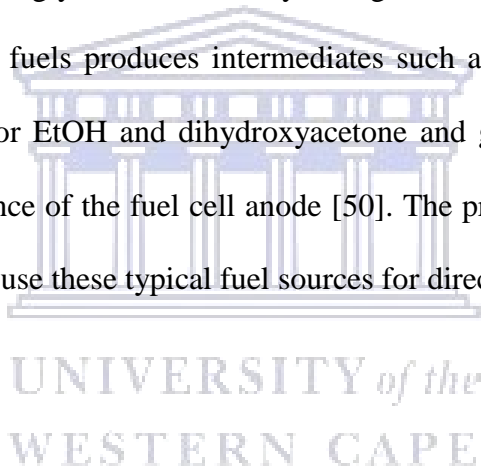
Equation 2.13 to 2.18 reals anode, cathode reactions and overall in DMFC

The drawbacks for commercialization of DMFCs are (i) Methanol cross over from anode side through PEM to cathode side (ii) Slow electro-kinetic of methanol oxidation results in low output power and fuel cell degradation, (iii) Expensive membrane and catalyst

2.2 Direct liquid fuel cell

In the last three to four-decade, Liquid fuels have been classified as conventional gasoline or petroleum and diesel from produced from the coal (non-renewable source) and are being utilized in the internal combustion engines. The recent emerging liquid fuel and most studied are organic (alcohols) which can also act oxygenate in the alcohol-gasoline blend and have been estimated to have 30% higher efficiency as compared to gasoline especially in alcohol designed engines. Amongst, the most studied is ethanol and because of possessing combustion characteristics such as; clean-burning, high burning-octane efficiency, and high theoretical density. These characteristics lead to the emerging of a clean biofuel-based direct liquid fuel cell. In addition, due to the complex reforming process for hydrogen and problematic storage and transportation of the pure hydrogen gas [58]. Thhe research has recently focused on organic liquid –feed fuels because of ethanol simple structure, safe and easy to handle, small cartridge and ease of storage [59] [60], transportation and obvious high theoretical energy density and efficiency as compared

to pure hydrogen [61], [62]. These properties drive the development of direct ethanol fuel cell (DEFC) which is the subcategory of DLFCs. Other Liquid-feed fuels include various small organic molecules (alcohols), and inorganic liquids (sodium borohydrides) and some acids at room temperature and pressure [59],[63]. DLFCs are classified according to the type of liquid-feed fuel, for instance, methanol is named direct methanol fuel cells (DMFCs), glycerol is (DGFCs), and so on [59]. EtOH and glycerol are considered as promising and possible fuels for liquid fuel cells because of several advantages over methanol such as low toxicity large quantity production from biomass materials [59], and glycerol is an odorless, less expensive bi-product during biodiesel production [64]. Incomplete oxidation of these typical fuels, EtOH oxidizes to CO_2 yielding $12e^-$ [65], and glycerol to CO_3^{2-} yielding $14e^-$ [53]. Nonetheless, the lack of complete oxidation in these fuels produces intermediates such as poisonous CO, acetaldehyde and acetic acid [59], [63] for EtOH and dihydroxyacetone and glyceric acid for glycerol [53] which inhibits the performance of the fuel cell anode [50]. The properties of EtOH and glycerol have motivated this study to use these typical fuel sources for direct liquid fuel cells.



2.3.1 Electrocatalysis

It has been explained in chemical catalysis and conventional catalysis that, when the reaction is being catalyzed take place at the electrode surface, such process is referred to as electrocatalysis. Electrocatalysis can be divided into two categories, depending on electrode (catalyst) nature (phase); into Homogenous electrocatalysis and Heterogeneous electrocatalysis. In the case of homogeneous electrocatalysis, both the electrode and reactant are in the same phase, commonly dissolved in the bulk phase and such processes at the interface do not influence chemical steps involved in it [66]. Electrocatalysis mostly described as a heterogeneous type of, which involved

in a chemical reaction occurring in an electrochemical cell at the surface of the electrode or being electrode itself, which is at the electrode interface [57]. Heterogeneous electro-(catalysis) may also be defined as a branch of electrocatalysis concerned with the study of reactions involving reactants species that shuttle electron through an electrolyte-electrode (catalyst) interface.

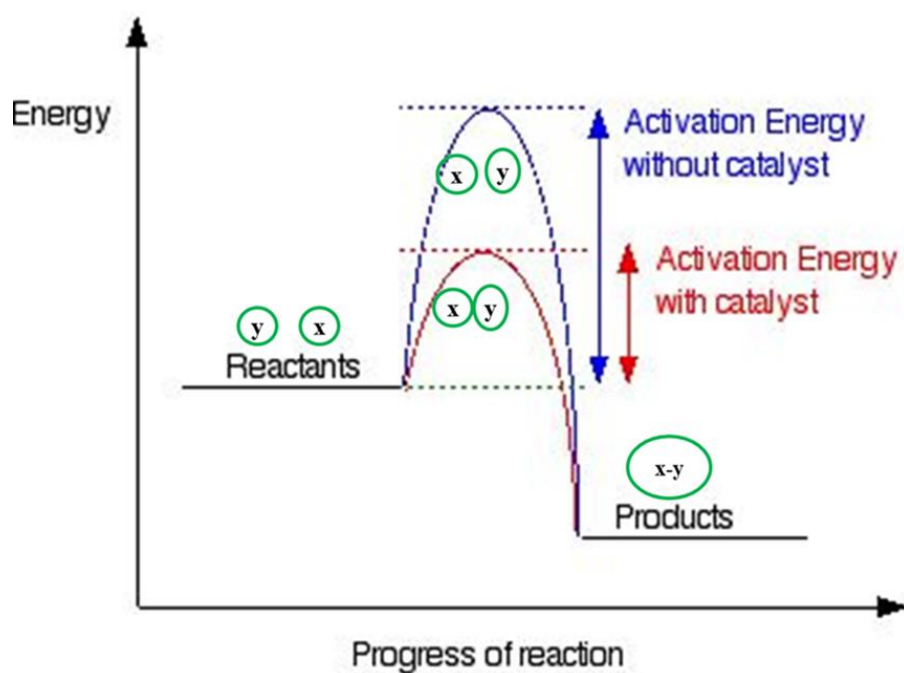


Figure 2.7: The illustration of electrocatalysis reaction and the effect of a catalyst in the chemical reaction.

2.3.1.1 Electrocatalysis in fuel cells

Electrocatalyst by definition is a catalyst that participates in an electrochemical reaction to modify and accelerates the rate of a chemical reaction without itself being consumed. Platinum group metals (PGMs) gained remarkable attention in catalysis due to their unique properties. Among the PGMs Platinum (Pt) and Palladium (Pd) are the most popular and widely used catalyst because of its high catalytic activity, and stability to name the few, however, its use has been inhibited due to its less abundance and high cost. Electrocatalyst plays a critical if

fuel cell, at electrode surface where fuel and electrolyte contact, increase the kinetics of electro-oxidation. Among PGMs palladium (Pd) has considered as alternative because of its durability, active and not rare compared to platinum. Palladium is a popular electrocatalyst in an alkaline fuel cell as it is active compared to platinum in an alkaline medium. Pd and Pd alloy outperformed alloys of Pt and Pd alloys in most oxidation-reduction reactions, especially in alcohol oxidation in alkaline medium. This typical metal is less affected or poisoned by reformate from hydrocarbon and alcohol as a source of fuel in a fuel cell, as results of that are superior metal and most investigated metal recently.

2.3.1.2 Electrocatalysis in hydrogen oxidation reaction (HOR)

The hydrogen oxidation reaction is one of the most important reactions in electrocatalysis and has been a subject of extensive investigation over the last century [68],[69]. PGMs such as Pd, Pt, Ir, Rh, Os are the most imperative catalyst for electrochemical oxidation of hydrogen, these metals correspond to optimal hydrogen binding energy and exhibit the highest activity in the volcano plot. The volcano curve on these metals was plotted and displayed in **Figure 2.8** to correlate the catalytic activity as a function of exchange current and hydrogen adsorption enthalpy on the metal surface.

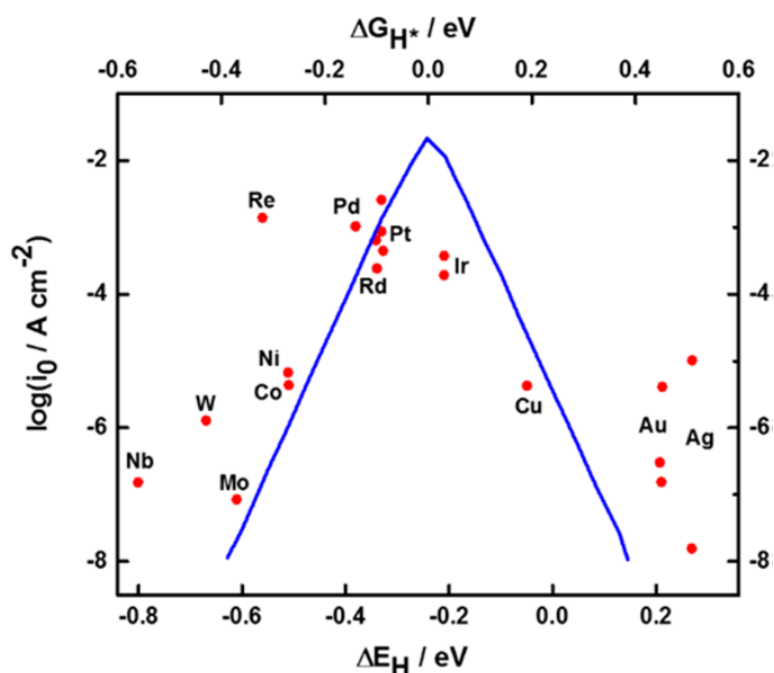
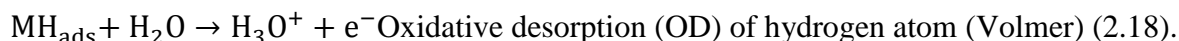
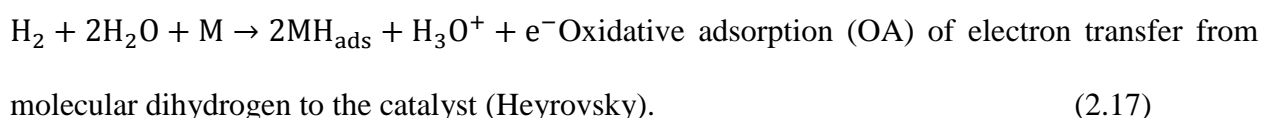


Figure 2.8: Volcano plot for electrocatalysis of hydrogen: log exchange current density of H_2 reaction vs enthalpy of H_2 adsorption in various metals.

It can be seen that the reaction is readily taking place on Pt and Pd are by initial hydrogen adsorption. It can be then oxidizing through the following mechanism;



Where M represents the elemental catalyst, the rate-determining step changes depending on the catalyst used. The Pt catalyst amount can be reduced without affecting its activity and CO intermediate tolerance, alloying with other transition metal was extensively investigated. Hydrogen oxidation reaction takes place at potential regarded at the combination of Tafel, Heyrovsky, and Volmer.

2.3.1.3 Electrocatalysis in ORR

Oxygen reduction reaction (ORR) remains the most important reaction in many electrochemical energy conversion and storage applications, such as fuel cells and metal-air batteries. ORR is most vital in fuel cells for the cathodic reaction.

Among PGMs, Pt (most preferred acidic condition) remains the most important and active in electrochemical catalytic and it shows stability for thousands of operation hours in acidic and corrosive conditions of a PEMFCs electrode surface. Norsk and co-workers generated an ORR volcano plot to illustrate the activities of various metals catalysts as a function of O₂ binding energy. The plot indicates that Pt and Pd based elemental catalysts are the best catalysts for ORR.

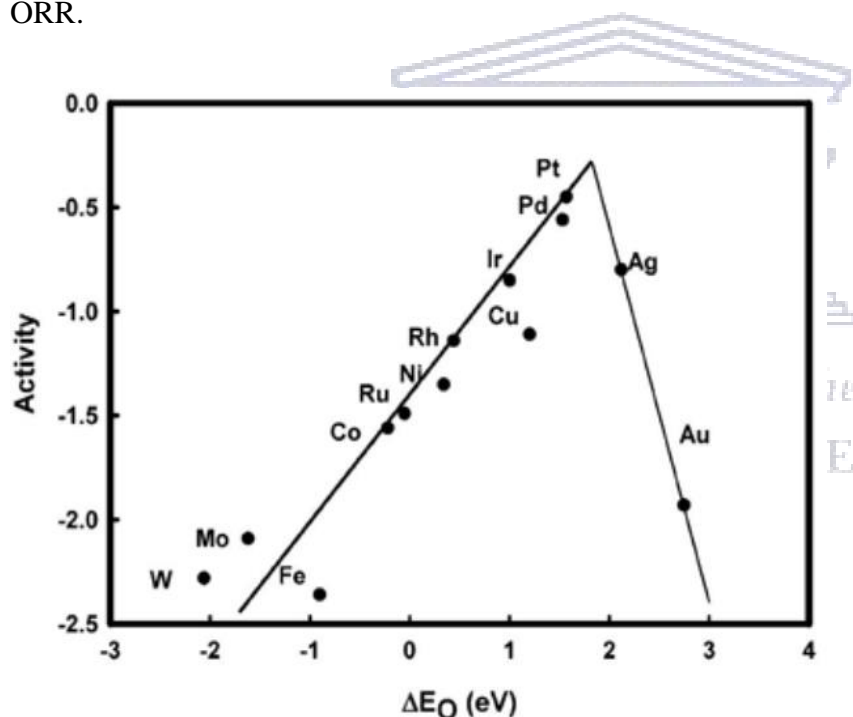


Figure 2.9: Volcano curve showing the trend in ORR activity as a function of the oxygen-binding energy.

Norsk and core-workers studied density functional theory (DFT) calculation and Sabatier analysis to support the use of Pt and their alloys as electrocatalysts for ORR in order to improve the metal electrode performance. It is well known that PGMs and their alloys exhibit the best

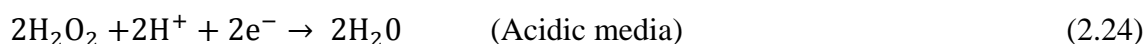
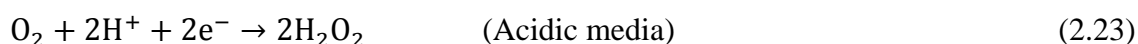
electrocatalytic activity towards ORR. ORR is strongly influenced by the effect of metal UPD layers such as Pb, Tl, Bi, Te, and these layers cause the positive and negative catalytic effect depending on the kind of the substrate. Kokkinidis and core-workers reported modification of Pt with foreign adatoms such as Pb, Cu for the ORR in acidic media [70], [71]. It is well known that ORR is a multi-step reaction pathway that involves several reaction mechanisms during the reaction. Such mechanism involves occurring by two overall pathways; (i) "Direct" four electrons reduction (with each O₂ molecule) and (ii) "peroxide" formation pathway as an intermediate for acid solutions.

However, peroxide intermediate can further undergo reduction as expressed in reaction (2.24)

These two overall reaction pathways can be expressed as follows;

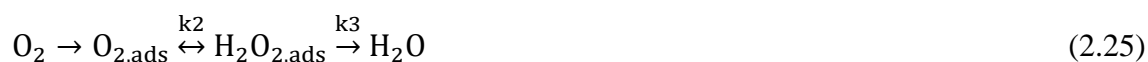


Peroxide formation as the final product takes place on less active metal electrodes. The same pathways are operative in alkaline solutions but at a distinguished set of potentials involving solution intermediates and products determined by certain pH of the solution. The peroxide pathway in alkaline and in acidic electrolyte respectively can be expressed as **Equation 2.21** and **2.22**;



These mechanisms of ORR on Pt-based catalyst been the most frequently studied and are

summarized in **Equation 2.25** as follows;



How the ORR proceeds depends on the adsorption mode which is manifested by the overpotential (activation energy), O_2 can react with two platinum atoms and form (Pt-OO-Pt) 1.2 peroxy-dimetal complex via four-electron (Yeager's model) pathway as displayed in the following diagram (**Figure 2.9**), is the On the other hand, O_2 can react with a metal atom (M-OO) to form superoxo-metal complex which results to the formation of two electrons (Pauling's model) pathway yielding H_2O_2 . The sluggish of ORR is ascribed to the cleavage of O-O of oxygen. The improvement of slow kinetics of oxygen reduction reaction at low temperature and pressure has been done through the addition of second metals such as (Ni, Fe, Cu, Ag) transition metal [72].

2.3.1.4 The effect of foreign metal adatoms of electrocatalysis of ORR

The catalytic reaction on Au, GC, and Pt have been studied, and the change in electrocatalytic from two systems (A-OO) to four-electron pathway upon addition of foreign adlayer is recognized by the decrease in overpotential [72]. K. Kokkidinis and co-workers reported the addition of metal adatoms such as Tl, Pb and Bi adlayers on Au and GC [73]. The foreign metal adlayer on the electrocatalytic surface (metal electrode) of noble (precious) metals cause a remarkable effect on electrocatalytic reaction such as ORR and oxidation of small alcohol molecules [73], [74]. In ORR metal surface modified by foreign adatoms deviates and shifts the half-wave potential of O_2 to a high positive value and an approximate doubling of the diffusion-limited current density [70]. This is more likely due to change from the two-electron pathway to the four-electron pathway induced by metal adlayer. This has been reported in several modified metal surfaces such as Pt, Au, Pd by foreign metal adlayer namely Pb, Sb, Bi, Tl [75].

2.3.1.5 Introduction of electrocatalysis in small liquid hydrocarbons (alcohols) molecules oxidation

Another famous electrode- (electrochemical) reaction like ORR and HOR is the oxidation of small liquid hydrocarbon (alcohol) fuels. These fuels include C1-C2 organic fuels such as formic acid, methanol, and ethanol and are the most extensively studied in electrochemical reactions. However, the accumulations of poisoning species on catalyst surface which arise from lack of C-C bond scissoring become the barrier [6], [9]. The bottle-neck associated with oxidation of small organic molecules (SOMs) is the poisoning of the noble metal catalytic surface by by-products, thus, inhibiting the electrocatalytic activity. Approaches to the enhancement of electrocatalytic activities on noble metal during oxidation of SOMs such as formic acid and ethanol oxidation are being developed. In the past two decades, there has been a fundamental investigation devoted to the several electrocatalysis on the metal substrate mostly on PGMs, modified by heavy transition metals adatoms deposited at UPD [73]. It has been found that modification of the metal surface by foreign metal adatoms (ads) "metallic electrode-adatoms system" enhance the catalytic activity and selectivity [76]. Foreign metal UPD on a catalyst surface act "third body" effect [60], electronic effect and bifunctional mechanism for the oxidation of small organic fuels for fuel cell application [73].

2.3.2 General introduction on nanostructured thin films materials (NSMs) and nanotechnology

Nanomaterials of nanostructured thin films have been extensively studied and been a heartthrob in many fields such as photo electronic, photovoltaic, electronic, medicinal, thermoelectric, corrosion electrocatalysis to name the few [78], [80]. These nanomaterials have unique

properties that differ significantly from those of a large scale (bulk) material [81],[83]. Those properties include magnetism, optical, heat, and fusion) enable them for many applications due to manipulation of the metal bulk material into the billionth meter (10^{-9} m) dimension [84], [85]. The nanometres concept was first proposed by Richards Zsigmondy, the 1925 Nobel Laureates in chemistry, as he measured gold colloids using a microscope. Researcher's efforts have devoted to finding applications on the nanoscale (nanostructured materials) which involves healthcare (biotechnology), water purification, energy storage (battery and capacitors) and energy conversion (fuel cells) [83], [86]. The utilization of atomic and molecular scale materials is the most paramount in chemical and electrical energy conversion due to its cost-effect practices to mitigate the use of fossil fuel. The existence of nanoscale objects/ materials have been there in ancient years, exists in nature due to biological processes such as protein units assembly, macromolecules, quasi inorganic systems (shells and bones) and photosynthesis. Also, nano clay minerals such as vermiculite, montmorillonite, kaolinite to name few existed in nature (natural nanoparticles) [87], [88]. Recently the manipulation of materials at nanometre scale become famous, this grabbed the attention in ‘Nanoscience’ and ‘Nanotechnology’. Nanotechnology term coined by Norio Taniguchi in 1974 [89], is referred to as the type of applied science, studying the ability to observe, measure, manipulate and produce materials at a nanometre regime [90]. The materials of nanoscale (2D) ever since known with size ranging from below 100 nm. The activities of ‘Nanotechnology’ involve science and engineering that deals with the formation of 2D and 3D nanodevices. Nanostructured metal thin film has played a critical role in the effectiveness of industrial catalysis due to its high surface area, good conductivity for low polarization [9]. Nanotechnology has developed a great interest in nanostructured materials (NsM) thin film material of noble metal-based chalcogenides due to their application in both academic and industrial. The size of the nanomaterials influences the electrocatalytic activity due to an enhanced surface area and electric properties in contrast to the bulk material counterparts

[9]. These nanomaterials are produced by two main approaches such as top-down and bottom-up approaches targeting near-atomic levels [91]. Both of these approaches imply the building on nanomaterial from bulk (in case of top-down) and self-assembly of atoms or molecules (in bottom-up).

2.3.2. 1 Nanostructured materials in response to the fourth industrial revolution (4IR)

The history of nanotechnology dates back from 1959, first introduced by Richards Feynman a Noble laureate in 1959 at the annual meeting of American physical science society at the California Institute of technology. Nanostructured materials (NsM) as the driving force of nanotechnology, holds the futuristic technological developments, next technology generation such as the fourth industrial revolution (4IR) [92],[93]. The NsM and nanotechnology are also recognized as the gate to the (4 IR) and a next big technology which may contribute to the next industrial revolution (what is known as 'secrete on (superconducting) 5IR) [94]. The concept of 4IR was first proposed by the CEO of the World Economic Forum (WEF) Prof Klaus Schwab in Davos. The WEF has identified nanostructured materials as an enabling technology for the fourth industrial revolution (industry 4.0).

Ever since the discovery of C60 (fullerenes), nanotubes (NTs) and nanodiamonds (NDs), carbon-based nanomaterials possess a diameter of around 0.15 nm ('carbon atom, C-C length) have been marked as next material to contribute in industrial revolution prospects (development). Recently, Europe opened research and development Manchester institute (R&D) to pursue more work on graphene for application in electronics, biosensor, and energy storage to name the few. This work pursues to respond on 4IR and for the next industrial revolution. In South Africa, 2002 department of Science and Innovation (DSI), South African National Initiative, Mintek and

Council for Scientific and Industrial Research (CSIR, Pretoria) have played a pivotal role in contributing to nanotechnology and manufacturing on nanomaterials. Recently the University of Johannesburg installed a robust atomic layer deposition technique (ALD, The Picosum R-200 Advance) for lab-scale and scale-up single-wafer for research and industrial application respectively. This technology is the first time in the African continent, which empowers the realization of Africa and response in the industry 4.0. ALD's ever-growing capabilities for fabricating new properties nanostructured thin films for use in superconductors such as thallium nitride (TlN), tantalum nitride (TaN), Niobium nitride (NbN) based thin films as well as electrocatalysts based on Pt, Pd, TiO₂ and Al₂O₃ coatings to name the few. In the past decade, many PGMs-based electrocatalyst and chalcogenides were electro-formed at CSIR using the lab-scale electrochemical atomic layer deposition (E-ALD). This technique produced high quality and performing thin films at ambient conditions, with the use of small precursor solution as compared to a conventional vacuum-based ALD and it will further be explained in **section 2.4**.

2.3.3. Fabrication methods of (NsMs)

Nanofabrication has been a critical research discipline in the past twenty years and has formed wide range applications in improvising material properties, sensitive clinical diagnostics, improving efficiency electron shuttling within the materials, generating high energy density.

These nano/thin films are produced by two main approaches, such as the top-down approach and the bottom-up approach technique [91], [95]. Top-down consists of lithographic methods which imply the building of nanomaterial from bulk to the desired nanoscale, by means of etching with both chemical and mechanical [96]. It consists of numerous synthetic approaches as nano lithology, photo lithology, soft lithology, colloidal lithology, non-contact printing, and scanning

lithology. In the case of the bottom-up approach it implies electrosynthesis of nanostructured material from the molecular/atomic scale by means of self-assembly of atoms and molecules [97]. The bottom-up approach has been known for a very long time by chemists for making a conformal nanoscale material/ nanostructures with a small defect. The latter method is the most commonly used nanofabrication technique for nanofilm growth because it creates small defects and self-control structure than top-down [97]. The bottom-up approach includes physical vapour, chemical vapour deposition (CVD), molecular beam epitaxy (MBE) [98], atomic layer deposition (ALD) [99] and electrochemical atomic layer deposition (E-ALD).

2.3.3.1 Physical vapour deposition (PVD) and Chemical vapour deposition (CVD)

Chemical Vapour Deposition (CVD) and PVD refer to the class of techniques in which solid grown/produced by the reaction of gaseous materials sources yielding a product [84]. It is widely used for the advanced manufacturing technology for surface coating currently enjoying intense development. It is a chemical process used to produce high-purity, high-performance thin films of a large variety of materials [100]. In a typical CVD process, the reactant gases enter the reaction chamber/system and the substrate exposed to one or more volatile precursors, which react and/or decompose on the substrate surface to produce the desired deposit. CVD poses advantages such as Metallic thin film materials formations that have been increased significantly by PVD and CVD [101].

2.3.3.2 Molecular Beam Epitaxy (MBE)

Molecular beam epitaxy (MBE) is an epitaxial method suitable for the preparation of high quality metallic thin film with controlled growth and composition in a nanoscale [102]. The term first mentioned in 1960s; known as vapour phase epitaxy along with its analogues such as vapour phase epitaxy (VPE), metalorganic vapour epitaxy (MOCVE). It employs ultra-high vacuum (UHV, $\sim 10^{-10}$ Torr) environment to allow precise control of stoichiometry [103], [104], growth

conditions high purity and real-time. It distinguishes its self from other evaporation crystal growth techniques by employing an atomic and molecular beam in UHV to allow precise thin film growth conditions. The deposition principle of MBE uses both liquid and solid precursors similar to thermal evaporation. In this case, high purity element is contained in a fusion cell. Many classes of material have been synthesized by MBE, such as semiconductors of III-Vs, II-VI, IV-VIs and their oxides [105],[106]. Flulop et al use MBE to grow layer-by-layer thermoelectric (BiTe) compounds on a substrate [107]. There is a report on high-quality Cu thin film formation and ultrathin integrated thin film (UL fabricated using MBE [108]. Huang et al reported an epitaxial growth of Te on graphene substrate [109]. The technique was also used to deposit Pd oxide single-crystalline thin film by Nanao et al [110]. The bottleneck associated with this technique is the heat-induced interdiffusion of the adjacent layers due to high pressure and temperature operation [111] and it requires an expensive precursor [112].

2.3.3.3 Pulsed Laser Deposition

Pulse laser deposition (PLD) is a technique that is suitable for preparing various types of a metallic thin film for application in electrocatalysis and formation of metal oxide for photocatalytic materials [113]. PLD is a conceptionally simple technique, which involves the collection on a nearby substrate of material eject from a pulse laser-irradiation target [100].

2.3.3.4 Sputtering

Sputtering is the technique in which the material is released from the source at a lower temperature than evaporation. The sources used in this method include ion beam accelerator, plasma and magnetron source. This technique can form a quality deposit at a lower substrate temperature. Delique V. et al [114] deposited Au containing oxygen (AuOx) on a silicon

substrate at room temperature by reactive magnetron sputtering under Ar/O₂ plasma. The use of charged ions from the source limits mixing; the ion can be directed to a specific site, for instance, the positive argon ions move towards the cathode at high momentum and hit target. The momentum of atoms at the target surface is dictated by argon ions and it comes out as vapour and condenses at the substrate surface. Salcedo et.al reported Pd thin films deposited by this method on sappier (Al₂O₃) substrate at 3.5mbar at various temperatures (473 K, 523 K, and 573 K) [115]. Ramirez et.al also deposited Pd nanostructures on HOPG using this method for application in DMFCs, and high performance was obtained [116]. This technique suffers to shortcoming such as control over the particle's morphology and energy consumption for injection of the electron is high

2.3.3.5 Sol-gel synthesis

The development of sol-gel process date back in 150 years ago, The sol-gel process is a promising method for preparation on nanomaterials that can disperse uniform and large surface area on gel matric such as silica [117]. It is an interesting alternative synthesis route for the preparation of nan-sized particles (forms, fibers), a porous system using inexpensive equipment [118],[119]. Among another deposition method, it is a considerable technique due to homogeneity, composition and mild processing conditions [120]. It is prepared from a metal-organic precursor suspended in a liquid hydrocarbon (alcohol). Researchers have been used this technique for the preparation of Platinum-based binary nanomaterials to create stable silica-gel PtAg nanoparticles.

2.3.3.6 Atomic layer deposition (ALD)

Atomic layer deposition (ALD) is classified as a subclass of CVD, and is known to be invented in the 1970s by Sutola Tuomo a scientist in Finland at Helsinki University of Technology who developed a thin film using ALD a general class of chemical vapour deposition technique [121]. Typical method using surface limited replacement reaction phenomena to form layer by layer process[75],[76]. In 1960 there was research on ALE, molecular layering by .W.B Aleskoskii in Lannigrand Institute of technology a former “soviet union” who reported a basic principle of ALD deposited TiCl_4 and GeCl_4 [77] precursors. Ever since then scientist have shown an interest in the formation of thin-film, semiconductor using ALD. Although ALD/ALE known to be born in 1977 where a Finland scientist Tuomo Suntola in Helsinki University of Technology reported thin film growth by ALD surface limited reaction. ALD is a general vapor phase/molecular beam epitaxy (MBE) technique that produces metal thin film from their metal oxide precursor and subsequent and subsequent gas-solid reaction on substrate surface [121], [124].

2.3.3.7 Electrochemical deposition: Electrochemical atomic layer deposition (E-ALD) and Underpotential deposition (UPD)

Electrodeposition of thin film material also known as electroplating has been known as used for fabrication of metallic mirrors, corrosion-resistant surfaces, among other things. Electrodeposition chamber comprised of electrolyte-containing metal ion precursor, electrode/substrate on which the desired deposition takes place, and a counter electrode. Among electrodeposition methods, the electrochemical atomic layer deposition (E-ALD) method found to be feasible [125], low cost, low temperature, and pressure condition during its operation and it also use the small concentration of precursor solutions [126], [127]. E-ALD was found by Stickney in the 1970s using silver (Ag) on single-crystal gold Au (111) and has identified as an efficient, potential method for fabrication of electrocatalysts because it produces small nanoparticle, well dispersed, stable and self-controlled thin film epitaxial layers. It is an

electrochemical version of atomic layer deposition (ALD) in which underpotential deposition (UPD) is involved [128]. The deposition of metal (M) atom on a foreign substrate (S) is extensively studied in electrochemical reactions for many years because of its fundamental and practical significance in electrocatalysis. It is also important due to its wide variety in many electrochemical reactions such as charge transfer, adsorption, surface diffusion, nucleation and growth, and double-layer changes. Among the electrochemical method, cyclic voltammetry plays the most important role in characterizing metal atoms deposited on the foreign metal substrate.

There are two crucial important terms in electrodeposition methodology, underpotential and overpotential deposition (OPD & UPD) respectively in line with redox properties of metal on foreign substrate. UPD is a phenomenon in which metal is deposited on the foreign metal substrate at the potential that is more positive than its Nernstian equilibrium potential. Where OPD is referred to as the potential that is more negative to that of bulk deposition (Nernstian equilibrium deposition potential). The metal deposition (reduction) and dissolution (oxidation) processes at the electrode surface (solution electrode interface) can be represented by this following simple equation. Electrochemical deposition (electrodeposition) can be expressed by a typical reduction expression of metal ions (M_n^{+}) because metal ions reduce on a conductive surface by gaining electrons during deposition [129]. The metal electrodeposition reaction can be written as $M^{Z+} + ze^{-} \rightarrow M_{(s)}$. The equilibrium at which reduction (deposition) and oxidation (dissolution) of metal (M) bulk is given by Nernst equation: $E_{cell} = E^{\circ} + \frac{RT}{zF} \ln \frac{a_{M^{Z+}}}{a_M}$, where E_{cell} is the equilibrium potential, E° is the standard potential, z is the number of electrons transferred, a is the activities (referred to as concentrations) and R, T, F are gas constant, temperature in (Kelvin, K) and Faraday (F) constant. In deposition or formation of monolayer or UPD on a foreign metal substrate, it occurs at the potential that is more positive than predicted by Nernst equilibrium potential. There are two requirements of for underpotential deposition, i.e.

Overvoltage must be greater than zero ($\eta > 0$) and actual potential (E°) is more positive than potential predicted Nernst equilibrium $E \gg E_{M^{2+}/M_{(bulk)}}$, the **equation (3)** below is being used to calculate the overpotential (η).

$$\text{For peak potential } E_{P=} E_{\frac{1}{2}} - 109 \frac{RT}{nF} = \frac{28.5}{mV} \text{ at } 25^\circ \text{C} \quad (2.16)$$

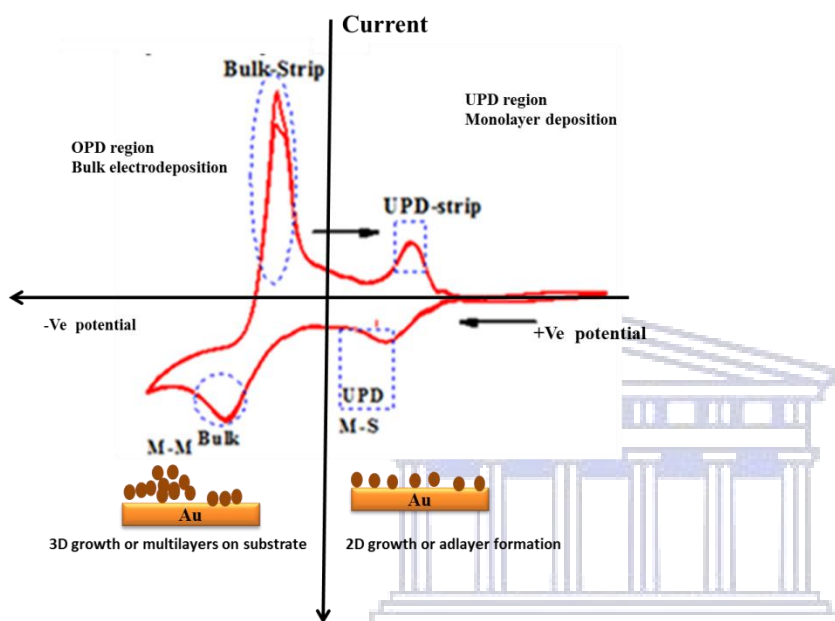


Figure 2.10: Schematic illustrating the relationship of potential (E/V) vs. current for UPD and OPD of Cu on Au.

Figure 2.10 presents the typical UPD is self-confined reaction and it provides adlayer deposition of metal onto the foreign metal substrate (S) at potentials more positive with respect to the reduction potential. OPD is not self-limited and favors 3D growth of multi-layered metal (bulk) deposition. The UPD phenomenon plays a significant role in monolayer deposits and has gained attention in electro crystallization, surface chemistry, and catalyst design to name the few. The UPD phenomenon refers to deposition potential dependent on the metal atomic layer onto a foreign metal substrate at a potential which is more positive than predicted by reversible Nernst equilibrium potential [130]. The main idea of the UPD phenomenon is to modify

electrodeposition processes, is to the metal deposit at the atomic level, layer by layer. UPD involves reaction of adatoms (metal ion) - electrode (substrate) M-S interaction rather than adatom-adatom (M-M) interaction [80],[81]. This implies that Adatom-adatom interaction favors bulk metal deposition [133] (overpotential deposition). UPD is determined by binding energy between metal-substrate and metal atoms with the metal of the same type as explained by Kolb in 1974 [134]. UPD used to limit deposition to a monolayer. UPD is a surface-limited phenomenon so that the resulting deposition is generally limited to an atomic layer. In simple terms UPD is opposite of OPD, it is also defined at potential proceeds that (Equilibrium) occurs at potential positive to that predicted by Nernst equilibrium potential. Underpotential deposition can occur in various condition pathways that is reductive UPD and oxidative UPD, classically UPD on metal surface is generally reductive UPD, a metal on a foreign substrate at potential positive to that predicted by Nernst equilibrium, the second UPD pathway is a reduction of hydrogen ions on metal surface or lattice to hydrogen atom, (H^+/H^2) for an example hydrogen adsorption/desorption wave (region) on the platinum and palladium surface. In the case of oxidative UPD condition, where a reduced species/element is re-oxidized or re-reduced, at potential before/positive for that species to be reduced. Oxidative UPD, denoted by the following equation, the examples of metal/non-metal species going to oxidative UPD are I on Au, initial oxidation of copper oxide, Te on Au (Te^{-2}) from reduced species Te(0), sulphur on Au and Arsenic on Au [135], [136]. UPD has been used to investigate the initial stages of compounds formation such as II-IV, III-VI, and IV-VI semiconductors. B.W Gregory has used the UPD to probe the initial electroformation of CdTe on various substrates such as Cu, Pt, and Au [137].

2.4.1 Surface limited redox replacement: Prospects

Surface limited redox replacement protocol employs the underpotential deposition to deposit an

atomic monolayer at a time. It has been widely used for many applications such as the formation of nanostructured metal thin film, metal semi-conductor. It also has been utilized for many technological applications such as printed circuit board (PCB), extractive hydrometallurgy, anticorrosion, coating, and ultra-large-scale integrated (ULSI). Historically, SLRR used for ultrathin film formation was brought forward by Brankovic et al [138], [139] for the formation of electrocatalyst for fuel cell application. The Pt, Pd monolayers and Ag bilayer were deposited by replacement of pre-deposited Cu on Au (111) substrate. In recent work by Mkwizu and co-workers employed numerous SLRR (2 successive steps; UPD and redox replacement) cycles to deposit multilayers of bimetallic Ru and Pt monolayers on the different conducting substrate [140], [141], [142] using electrochemical atomic layer deposition (E-ALD) for application in the fuel cell. Following these early works Domistroy, used Pb-UPD.

It has been found that PGMS ultrathin films can be grown using SLRR protocol using various UPD mediators either less noble metal such as Cu, Pd, Tl, Zn, Co, or monometallic system (H-UPD). Fayette was the first to utilize SLRR protocol via non-metallic mediator species (H-UPD) sacrificial non-metal for the formation of Pt ultrathin film on Au [143]. Subsequently, Achri et al reported Pd ultrathin film on Au substrate using H-UPD sacrificial mediator species, and there were up to eight Pd monolayer thin film was grown [144]. In 2011 Fayette et al developed SLRR protocol of Pb-UPD sacrificial metal for the formation of Pt thin film on Au, and a free contamination thin film was obtained using one cell configuration [145]. Several SLRR protocols using less noble metals sacrificial metals was explored extensively, recently SLRR of Zn-UPD sacrificial metal was used for the fabrication of Cobalt (Co) on ruthenium substrate and it was found to be the potential replacement of conventional Cu-UPD [146]. Duajotis et al. studied and reported SLRR of Thallium UPD sacrificial metal on a silver polycrystalline substrate [147].

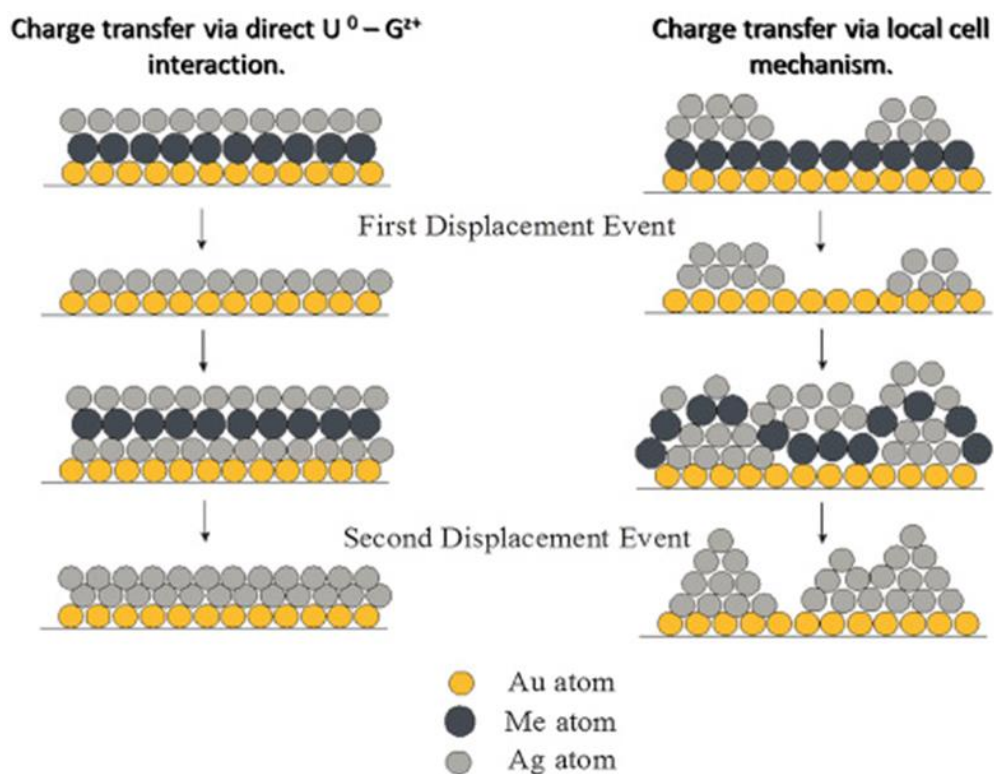


Figure 2.11: Schematic representation mechanism of surface limited redox replacement reaction [72], [148], [149].

2.4.2 Pourbaix diagrams on compounds formation

The electrochemical (thermodynamic) stability and dominating species of each element to be electrodeposited are normally predicted by the potential-pH (Pourbaix) diagram. This is a plot of the potential of each element as a function of pH. This diagram was established by Marcel Pourbaix, in his atlas as electrode potential-pH diagram which offers the visual thermodynamic stability of species such as stable oxides, hydroxide, and oxyhydroxides of a specific metal. Each element is stable and has a unique region. Such regions are known as, passivation, oxide formation, where intersect. The elemental Pourbaix diagram discusses the electrochemical stability zone for an element as a function of pH and potential. Through comparing the Pourbaix diagram for a compound's constituents indicates the probabilities of forming stable compounds. The conditions where both elements overlap and exist in their elemental state is a good insight of where to begin to form the corresponding compound. However, the free energy of the compound

should be taken into account as well as it can be increasing the conditions under which the compound formation might take place. By considering UPD as the surface compound formation and consider free energy should modified Pourbaix diagram can be constructed and expanded.

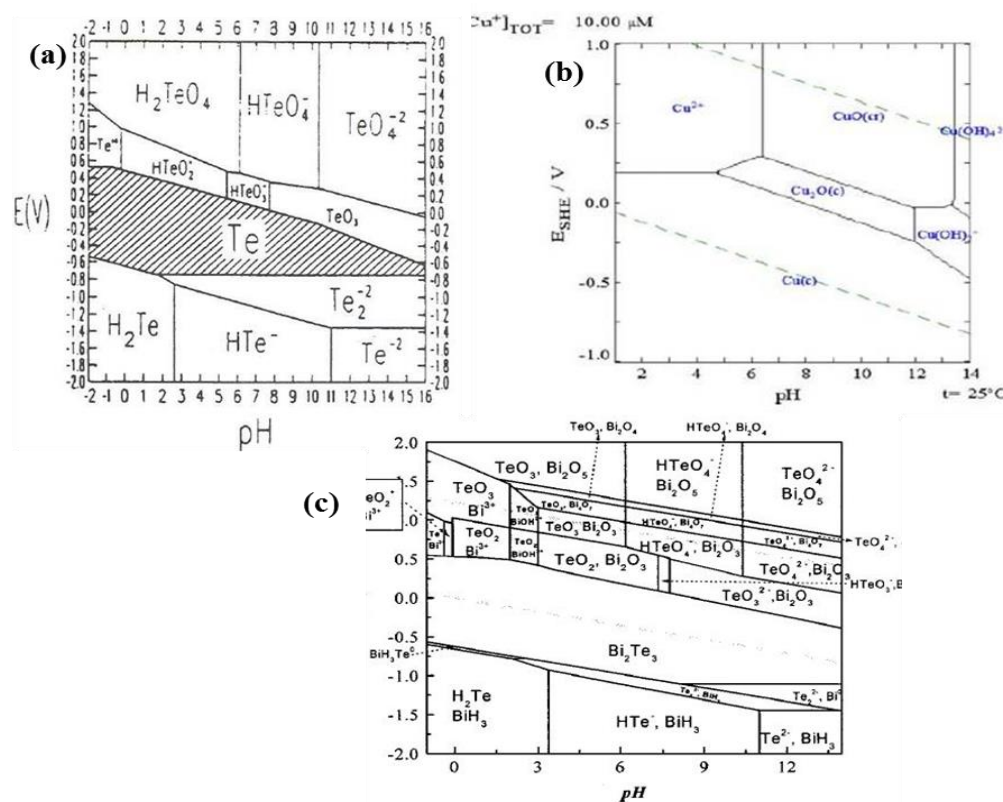


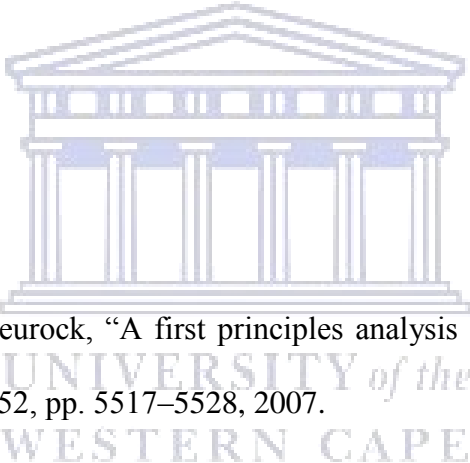
Figure 2.12: Pourbaix diagram of Te (a), Cu (b) and BiTe (c) [150]

2.4.3 E-ALD and substrate

In catalysis support or substrate plays a crucial role in the performance of electrocatalyst. It increases conductivity, stability, improvement of dispersion of the deposited catalyst [151]. The substrate is classically defined as inert electrical conductive support onto which material/ catalyst of interest can be deposited [152]. The choice of the substrate in catalysis is a vital preliminary step in accurately evaluating electrochemically active materials, including electrocatalyst, photoelectrodes. There is wide research on the selection of appropriate substrate in catalysis and photoelectrodes to probe the electrochemically active support. There are two categories of

electrochemically inert substrates such as Indium doped tin oxide, fluorine doped tin oxide, aluminum-doped zinc oxide and opaque conductive substrate which include carbonaceous glassy carbon (GC), highly oriented pyrolytic graphite (HOPG). Stainless steel 304 and gold (Au) [153]. Arvia et al reported electrodeposition of noble metal on HOPG using electrochemical technique [154]. Hsu et al obtained a high catalytic activity towards ethanol oxidation using PtSn layers on GC substrate [155]. Another emerging paramount important step into selecting the substrate is reported by B.W Gregory as a potential window (where non-faradaic is taking place) to observe a definite UPDs of the depositing metal [137]. Due to inertness, stability, strong mechanical support and wide potential window, Au has been considered as the best conductive substrate.

References

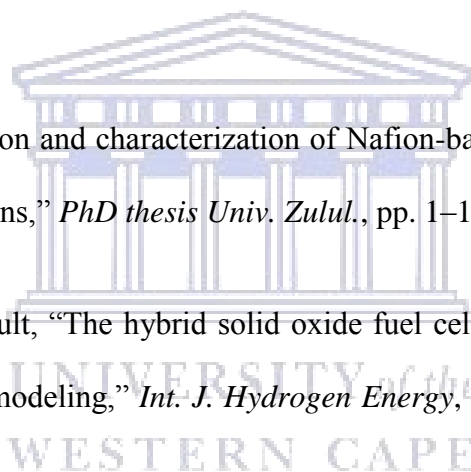
- 
- [1] M. J. Janik and M. Neurock, "A first principles analysis of the electro-oxidation of CO over Pt (1 1 1)," vol. 52, pp. 5517–5528, 2007.
- [2] E. Antolini, "Pt-Ni and Pt-M-Ni (M = Ru, Sn) anode catalysts for low-temperature acidic direct alcohol fuel cells: A review," *Energies*, vol. 10, no. 1, pp. 1–20, 2017.
- [3] P. Inkaew, W. Zhou, and C. Korzeniewski, "CO monolayer oxidation at Pt(1 0 0) probed by potential step measurements in comparison to Pt(1 1 1) and Pt nanoparticle catalyst," *J. Electroanal. Chem.*, vol. 614, no. 1–2, pp. 93–100, 2008.
- [4] B. N. Grgur, C. A. Lucas, and P. N. Ross, "Surface Chemistry of CO on Pt (1 0 0) - Bimetallic Surfaces : Displacement Effects," no. 100, pp. 1998–2005, 2005.

- [5] P. Molla-Abbasi, M. S. Asgari, and M. M. Hassani Sadrabadi, "Improving the Performance of Nafion®-Based Fuel Cell Membranes by Introducing Histidine Functionalized Carbon Nanotubes," *J. Macromol. Sci. Part B*, vol. 56, no. 4, pp. 234–244, 2017.
- [6] N. P. Cele and S. S. Ray, "Effect of multiwalled carbon nanotube loading on the properties of Nafion® membranes," *J. Mater. Res.*, vol. 30, no. 01, pp. 66–78, 2015.
- [7] D. B. Spry and M. D. Fayer, "Proton transfer and proton concentrations in protonated nafion fuel cell membranes," *J. Phys. Chem. B*, vol. 113, no. 30, pp. 10210–10221, 2009.
- [8] N. Cele and S. S. Ray, "Recent progress on nafion-based nanocomposite membranes for fuel cell applications," *Macromol. Mater. Eng.*, vol. 294, no. 11, pp. 719–738, 2009.
- [9] Yan Qiao and Chang Ming Li, "Nanostructured catalysts in fuel cells," *J. Mater. Chem.*, vol. 21, no. 6, p. 062001, 2010.
- [10] S. L. Chen, A. B. Bocarsly, and J. Benziger, "Nafion-layered sulfonated polysulfone fuel cell membranes," *J. Power Sources*, vol. 152, no. 1–2, pp. 27–33, 2005.
- [11] S. M. Haile, "Fuel cell materials and components," *Acta Mater.*, vol. 51, no. 19, pp. 5981–6000, 2003.
- [12] S. Litster and G. Mclean, "PEM fuel cell electrodes," vol. 130, pp. 61–76, 2004.
- [13] S. M. Haile, "Materials for fuel cells," *Mater. Today*, vol. 6, no. 3, pp. 24–29, 2003.
- [14] N. Sammes, R. Bove, and K. Stahl, "Phosphoric acid fuel cells: Fundamentals and applications," vol. 8, pp. 372–378, 2004.

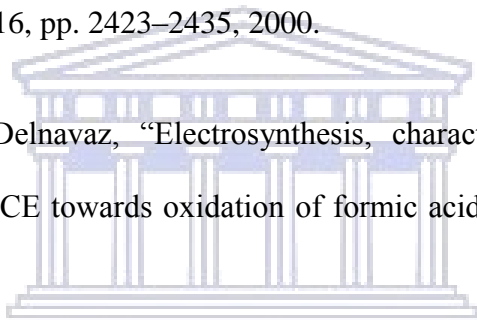
- [15] Y. Wang, K. S. Chen, J. Mishler, S. C. Cho, and X. C. Adroher, "A review of polymer electrolyte membrane fuel cells: Technology, applications, and needs on fundamental research," *Appl. Energy*, vol. 88, no. 4, pp. 981–1007, 2011.
- [16] O. P. Sahu and S. Basu, "Direct Alcohol Alkaline Fuel Cell as Future Prospectus," vol. 1, no. 1, pp. 43–52, 2014.
- [17] A. Kirubakaran, S. Jain, and R. K. Nema, "A review on fuel cell technologies and power electronic interface," *Renew. Sustain. Energy Rev.*, vol. 13, pp. 2430–2440, 2009.
- [18] C. A. C. Sequeira, D. S. P. Cardoso, M. Martins, and L. Amaral, "Novel materials for fuel cells operating on liquid fuels," *AIMS Energy*, vol. 5, no. May, pp. 458–481, 2017.
- [19] F. Bidault, D. J. L. Brett, P. H. Middleton, and N. P. Brandon, "Review of gas diffusion cathodes for alkaline fuel cells," *J. Power Sources*, vol. 187, no. 1, pp. 39–48, 2009.
- [20] F. Bidault, "Development of Alkaline Fuel Cell Gas Diffusion Cathodes using new Substrate Materials," no. March, pp. 1–150, 2010.
- [21] A. Verma and S. Basu, "Direct alkaline fuel cell for multiple liquid fuels: Anode electrode studies," vol. 174, pp. 180–185, 2007.
- [22] J. Yang, Y. Xie, R. Wang, B. Jiang, C. Tian, G. Mu, J. Yin, B. Wang, and H. Fu, "Synergistic Effect of Tungsten Carbide and Palladium on Graphene for Promoted Ethanol Electrooxidation," *Applied Materials & Interfaces* 2013.
- [23] M. Ünlü, D. Abbott, N. Ramaswamy, X. Ren, S. Mukerjee, and P. A. Kohl, "Analysis of Double Layer and Adsorption Effects at the Alkaline Polymer Electrolyte-Electrode Interface," *J. Electrochem. Soc.*, vol. 158, no. 11, p. B1423, 2011.

- [24] E. H. Yu and K. Scott, "Development of direct methanol alkaline fuel cells using anion exchange membranes," vol. 137, pp. 248–256, 2004.
- [25] D. Gaurava, A. Verma, D. K. Sharma, and S. Basu, "Development of a direct alcohol alkaline fuel cell stack," *Fuel Cells*, vol. 10, no. 4, pp. 591–596, 2010.
- [26] B. Y. S. Lin, D. W. Kirk, and S. J. Thorpe, "Performance of alkaline fuel cells: A possible future energy system," *J. Power Sources*, vol. 161, no. 1, pp. 474–483, 2006.
- [27] N. Scott, F. Andrieux, R. Dawson, H. Sutherland, and G. Lewis, "Direct Fuel Oxidation Alkaline Fuel Cells; The Kinetics of Borohydride Oxidation," *Chem. Eng.*, vol. 41, pp. 247–252, 2014.
- [28] H. Vaghari, H. Jafarizadeh-malmiri, A. Berenjian, and N. Anarjan, "Recent advances in application of chitosan in fuel cells," *Sustain. Chem. Process.*, vol. 1, no. 1, p. 1, 2013.
- [29] N. Wagner, M. Schulze, and E. Gülzow, "Long term investigations of silver cathodes for alkaline fuel cells," *J. Power Sources*, vol. 127, no. 1–2, pp. 264–272, 2004.
- [30] A. Verma and S. Basu, "Direct use of alcohols and sodium borohydride as fuel in an alkaline fuel cell," vol. 145, pp. 282–285, 2005.
- [31] G. McLean and T. Niet, "An assessment of alkaline fuel cell technology," *Int. J. ...*, vol. 27, pp. 507–526, 2002.
- [32] J. R. Varcoe and R. C. T. Slade, "Prospects for alkaline anion-exchange membranes in low temperature fuel cells," *Fuel Cells*, vol. 5, no. 2, pp. 187–200, 2005.
- [33] J. Liu, J. Ye, C. Xu, S. P. Jiang, and Y. Tong, "Kinetics of ethanol electrooxidation at Pd electrodeposited on Ti," *Electrochem. commun.*, vol. 9, no. 9, pp. 2334–2339, 2007.

- [34] R. M. Modibedi, T. Mehlo, K. I. Ozoemena, and M. K. Mathe, "Preparation , characterisation and application of Pd / C nanocatalyst in passive alkaline direct ethanol fuel cells (ADEFC)," *Int. J. Hydrogen Energy*, vol. 40, no. 45, pp. 15605–15612, 2015.
- [35] S. Mekhilef, R. Saidur, and A. Safari, "Comparative study of different fuel cell technologies," *Renew. Sustain. Energy Rev.*, vol. 16, no. 1, pp. 981–989, 2012.
- [36] A. Verma and S. Basu, "Experimental evaluation and mathematical modeling of a direct alkaline fuel cell," vol. 168, pp. 200–210, 2007.
- [37] H. Sotouchi and A. Hagiwara, "SA NE M SC PL O E – C EO AP LS TE S PL O E –," vol. II.
- [38] N. P. Cele, "Preparation and characterization of Nafion-based nanocomposite membranes for fuel cell applications," *PhD thesis Univ. Zulul.*, pp. 1–172, 2010.
- [39] P. Chinda and P. Brault, "The hybrid solid oxide fuel cell (SOFC) and gas turbine (GT) systems steady state modeling," *Int. J. Hydrogen Energy*, vol. 37, no. 11, pp. 9237–9248, 2012.
- [40] A. B. Stambouli and E. Traversa, "Solid oxide fuel cells (SOFCs): A review of an environmentally clean and efficient source of energy," *Renew. Sustain. Energy Rev.*, vol. 6, no. 5, pp. 433–455, 2002.
- [41] V. M. Ortiz-Martnez, M. J. Salar-Garc, A. P. de los Ros, F. J. Hernndez-Fernndez, and L. J. Egea, J. A. Lozano, "Developments in microbial fuel cell modeling," *Chem. Eng. J.*, vol. 271, pp. 50–60, 2015.
- [42] S. C. Singhal, "Solid Oxide Fuel Cells," *Electrochem. Soc. Interface*, pp. 41–44, 2007.



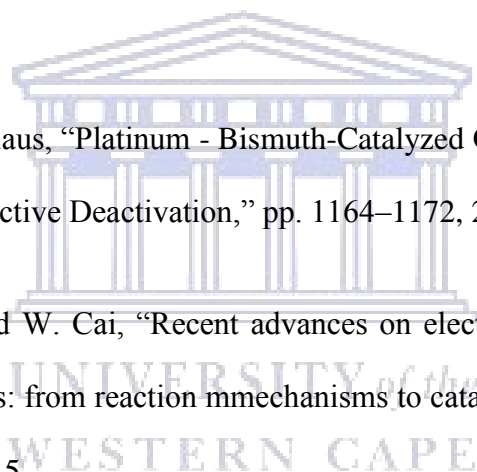
- [43] S. P. Jiang and S. H. Chan, "A review of anode materials development in solid oxide fuel cells," *J. Mater. Sci.*, vol. 39, no. 14, pp. 4405–4439, 2004.
- [44] N. Laosiripojana, W. Wiyaratn, W. Kiatkittipong, A. Arpornwichanop, A. Soottitantawat, and S. Assabumrungrat, "Reviews on solid oxide fuel cell technology," *Eng. J.*, vol. 13, no. 1, pp. 65–83, 2009.
- [45] A. Tarancn, "Strategies for lowering solid oxide fuel cells operating temperature," *Energies*, vol. 2, no. 4, pp. 1130–1150, 2009.
- [46] O. Yamamoto, "Solid oxide fuel cells: fundamental aspects and prospects," *Electrochim. Acta*, vol. 45, no. 15–16, pp. 2423–2435, 2000.
- [47] B. Habibi and N. Delnavaz, "Electrosynthesis, characterization and electrocatalytic properties of Pt–Sn/CCE towards oxidation of formic acid," *RSC Adv.*, vol. 2, no. 4, pp. 1609–1617, 2012.
- [48] K. Jiao and X. Li, "Water transport in polymer electrolyte membrane fuel cells," *Prog. Energy Combust. Sci.*, vol. 37, no. 3, pp. 221–291, 2011.
- [49] L. Gu, N. Luo, and G. H. Miley, "Cathode electrocatalyst selection and deposition for a direct borohydride / hydrogen peroxide fuel cell," vol. 173, pp. 77–85, 2007.
- [50] H. Kim, N. P. Subramanian, and B. N. Popov, "Preparation of PEM fuel cell electrodes using pulse electrodeposition," *J. Power Sources*, vol. 138, , pp. 14–24, 2004.
- [51] N. Rajalakshmi and K. S. Dhathathreyan, "Nanostructured platinum catalyst layer prepared by pulsed electrodeposition for use in PEM fuel cells," *Int. J. Hydrogen Energy*, vol. 33, no. 20, pp. 5672–5677, 2008.



UNIVERSITY of the
WESTERN CAPE

- [52] S. D. Thompson, L. R. Jordan, and M. Forsyth, "Platinum electrodeposition for polymer electrolyte membrane fuel cells," *Electrochim. Acta*, vol. 46, no. 10–11, pp. 1657–1663, 2001.
- [53] E. Habibi and H. Razmi, "Glycerol electrooxidation on Pd , Pt and Au nanoparticles supported on carbon ceramic electrode in alkaline media," *Int. J. Hydrogen Energy*, vol. 37, no. 22, pp. 16800–16809, 2012.
- [54] Y. Na, F. Zenith, and U. Krewer, "Increasing fuel efficiency of direct methanol fuel cell systems with feedforward control of the operating concentration," *Energies*, vol. 8, no. 9, pp. 10409–10429, 2015.
- [55] H. Liu, C. Song, L. Zhang, J. Zhang, H. Wang, and D. P. Wilkinson, "A review of anode catalysis in the direct methanol fuel cell," *J. Power Sources*, vol. 155, no. 2, pp. 95–110, 2006.
- [56] S. K. Kamarudin, F. Achmad, and W. R. W. Daud, "Overview on the application of direct methanol fuel cell (DMFC) for portable electronic devices," *Int. J. Hydrogen Energy*, vol. 34, no. 16, pp. 6902–6916, 2009.
- [57] S. Basri, S. K. Kamarudin, W. R. W. Daud, and Z. Yaakub, "Nanocatalyst for direct methanol fuel cell (DMFC)," *Int. J. Hydrogen Energy*, vol. 35, no. 15, pp. 7957–7970, 2010.
- [58] J. Friedl and U. Stimming, "Model catalyst studies on hydrogen and ethanol oxidation for fuel cells," *Electrochim. Acta*, vol. 101, pp. 41–58, 2013.
- [59] B. C. Ong, S. K. Kamarudin, and S. Basri, "Direct liquid fuel cells : A review," *Int. J. Hydrogen Energy*, vol. 42, no. 15, pp. 10142–10157, 2017.

- [60] G. L. Soloveichik, "Liquid fuel cells," *Beilstein J. Nanotechnol.*, vol. 5, pp. 1399–1418, 2014.
- [61] E. H. Yu, U. Krewer, and K. Scott, "Principles and Materials Aspects of Direct Alkaline Alcohol," pp. 1499–1528, 2010.
- [62] S. P. S. Badwal, S. Giddey, A. Kulkarni, J. Goel, and S. Basu, "Direct ethanol fuel cells for transport and stationary applications – A comprehensive review," *Appl. Energy*, vol. 145, pp. 80–103, 2015.
- [63] G. L. Soloveichik, "Liquid fuel cells," *Beilstein J. Nanotechnol.*, vol. 5, pp. 1399–1418, 2014.
- [64] A. Brandner and P. Claus, "Platinum - Bismuth-Catalyzed Oxidation of Glycerol: Kinetics and the Origin of Selective Deactivation," pp. 1164–1172, 2010.
- [65] Y. Wang, S. Zou, and W. Cai, "Recent advances on electro-oxidation of ethanol on Pt- and Pd-based catalysts: from reaction mechanisms to catalytic materials," *Catalysts*, vol. 5, pp. 1507–1534, 2015.
- [66] A. Wieckowski and M. Neurock, "Contrast and synergy between electrocatalysis and heterogeneous catalysis," *Adv. Phys. Chem.*, vol. 2011, pp. 1–18, 2011.
- [67] G. Q. Lu and A. Wieckowski, "Heterogeneous electrocatalysis: A core field of interfacial science," *Curr. Opin. Colloid Interface Sci.*, vol. 5, no. 1–2, pp. 95–100, 2000.
- [68] S. Henning, J. Herranz, and H. A. Gasteiger, "for the Oxidation of Hydrogen in Alkaline Electrolyte," vol. 162, no. 1, pp. 178–189, 2015.



- [69] A. E. Von Mengershausen, N. V Almeida, M. N. Barzola, J. O. Zerbino, S. M. Esquenoni, and M. G. Sustersic, "Comparative Study of Hydrogen Electrooxidation on Gold and Platinum in Solutions Containing Perchlorate Ion," no. May, pp. 55–59, 2014.
- [70] S. A. Sequoia, G. Kokkinidis, and G. Papanastasiou, "Some specific features of the catalytic role of UPD foreign metal adatoms and water on the anodic oxidation of absolute methanol on Pt," *J. Electroanal. Chem.*, vol. 221, pp. 175–186, 1987.
- [71] E. S. S. A and G. Kokkinidis, "Underpotential deposition and electrocatalysis," *J. Electroanal. Chem.*, vol. 201, pp. 217–236, 1986.
- [72] A. Papaderakis, I. Mintsouli, J. Georgieva, and S. Sotiropoulos, "Electrocatalysts Prepared by Galvanic Replacement," *Catalysts*, no. 2, 2017.
- [73] G. Kokkinidis, "Underpotential deposition and electrocatalysis," *J. Electroanal. Chem.*, vol. 201, pp. 217–236, 1986.
- [74] A. Kelaidopoulou, E. Abelidou, and G. Kokkinidis, "Electrocatalytic oxidation of methanol and formic acid on dispersed electrodes: Pt, Pt ± Sn and Pt / M (upd) in poly (2-hydroxy-3-aminophenazine)," pp. 1255–1261, 1999.
- [75] E. Herrero and J. M. Feliu, "Formic acid electrooxidation on thallium modified platinum single crystal electrodes a b," *J. Electroanal. Chem.*, vol. 800, pp. 82–88, 2017.
- [76] R. R. Adzic, "Electrocatalysis on Surfaces Modified by Foreign Metal Adatoms," *Isr. J. Chem.*, vol. 18, pp. 166–181, 1979.

- [77] L. Wang, X. Cao, Y. Wang, and Q. Li, "Sb Surface Modification of Pd by Mimetic Underpotential Deposition for Formic Acid Oxidation," *Catalyst*, vol. 5, pp. 1388–1398, 2015.
- [78] M. J. Pitkethly, "Nanomaterials – the driving force," *Mater. Today*, vol. 7, no. 12, pp. 20–29, 2004.
- [79] O. A. Petrii, "Related content Electrosynthesis of nanostructures and nanomaterials," *Russian Chem. Review*, vol. 84, pp. 159-193 .2015.
- [80] J. Thomas, V. S. Saji, and J. Thomas, "Nano-materials for corrosion control Nanomaterials for corrosion control," *Curr. Sci.*, vol. 92, no. April, pp. 1–51, 2014.
- [81] J. Liao, W. Ding, S. Tao, Y. Nie, W. Li, G. Wu, S. Chen, and L. Li, "Carbon supported IrM (M = Fe , Ni , Co) alloy nanoparticles for the catalysis of hydrogen oxidation in acidic and alkaline medium article (Special Issue on Electrocatalysis Transformation) Carbon supported IrM (M = Fe , Ni , Co) alloy nanoparticles," *Chinese J. Catal.*, vol. 37, no. July, pp. 1142–1148, 2016.
- [82] B. S. Dey and V. K. Jain, "Platinum Group Metal Chalcogenides," *Platin. Met. Rev.*, vol. 2, no. 5, pp. 16–29, 2004.
- [83] Y. Zhang, Q. Zhou, J. Zhu, Q. Yan, S. X. Dou, and W. Sun, "Nanostructured Metal Chalcogenides for Energy Storage and Electrocatalysis," *Adv. Funct. Mater.*, vol. 27, no. 35, pp. 1–34, 2017.
- [84] K.L. Choy, "Chemical vapour deposition of coatings," *Prog. Mater. Sci.*, vol. 48, pp. 57–170, 2003.

- [85] F.-R. R. Carrera-Carritos, C. Salazar-Hernandez, I.R. Galindo-Esquivel, "Effect of the Reduction Temperature of PdAg Nanoparticles during the Polyol Process in the Ethanol Electrooxidation Reaction," *J. Nanomater.*, vol. 2018, 2018.
- [86] G. Zangari, "Electrodeposition of Alloys and Compounds in the Era of Microelectronics and Energy Conversion Technology," pp. 195–218, 2015.
- [87] S. Griffin, M. I. Masood, M. J. Nasim, M. Sarfraz, A. P. Ebokaiwe, K. Schäfer, C. M. Keck, and C. Jacob, "Natural Nanoparticles : A Particular Matter Inspired by Nature," *antioxidants*, vol. 7, pp. 1–21, 2018.
- [88] K. N. Islam, A. B. Z. Zuki, M. E. Ali, M. Zobir, B. Hussein, M. M. Noordin, M. Y. Loqman, H. Wahid, M. A. Hakim, S. Bee, and A. Hamid, "Facile Synthesis of Calcium Carbonate Nanoparticles from Cockle Shells," vol. 2012, no. 1, 2012.
- [89] I. Khan, K. Saeed, and I. Khan, "Nanoparticles : Properties , applications and toxicities," *Arab. J. Chem.*, 2017.
- [90] J. E. Hulla, S. C. Sahu, and A. W. Hayes, "Nanotechnology : History and future," vol. 34, no. 12, pp. 1318–1321, 2015.
- [91] G. A. Ozin, K. Hou, B. V. Lotsch, L. Cademartiri, D. P. Puzzo, F. Scotognella, A. Ghadimi, and J. Thomson, "Nanofabrication by self-assembly," *Mater. Today*, vol. 12, no. 5, pp. 12–23, 2009.
- [92] S. Rai and A. Rai, "Review : Nanotechnology - The secret of fifth industrial revolution and the future of next generation," vol. 7, no. 2, pp. 61–66, 2015.

- [93] M. Lee, J. J. Yun, A. Pyka, D. Won, F. Kodama, G. Schiuma, H. Park, J. Jeon, K. P. Id, and K. Jung, “How to Respond to the Fourth Industrial Revolution , or the Second Information Technology Revolution ? Dynamic New Combinations between Technology , Market , and Society through Open Innovation,” *J. Open Innov. Technol. , Mark. Complex*, 2018.
- [94] Y. Liao, E. Rocha, F. Deschamps, and G. Brezinski, “The impact of the fourth industrial revolution : a cross-country / region comparison,” vol. 5411, 2018.
- [95] G. M. Whitesides and B. Grzybowski, “Self-assembly at all scales.,” *Sci. (New York, NY)*, vol. 295, no. 5564, pp. 2418–2421, 2002.
- [96] A. Biswas, I. S. Bayer, A. S. Biris, T. Wang, E. Dervishi, and F. Faupel, “Advances in top-down and bottom-up surface nanofabrication: Techniques, applications & future prospects,” *Adv. Colloid Interface Sci.*, vol. 170, no. 1–2, pp. 2–27, 2012.
- [97] R. Thiruvengadathan, V. Korampally, A. Ghosh, N. Chanda, K. Gangopadhyay, and S. Gangopadhyay, “Nanomaterial processing using self-assembly-bottom-up chemical and biological approaches,” *Reports Prog. Phys.*, vol. 76, no. 6, 2013.
- [98] B. D. Gates, Q. Xu, M. Stewart, D. Ryan, C. G. Willson, and G. M. Whitesides, “New approaches to nanofabrication: Molding, printing, and other techniques,” *Chem. Rev.*, vol. 105, no. 4, pp. 1171–1196, 2005.
- [99] J. Lu, J. W. Elam, and P. C. Stair, “Atomic layer deposition - Sequential self-limiting surface reactions for advanced catalyst ‘bottom-up’ synthesis,” *Surf. Sci. Rep.*, vol. 71, no. 2, pp. 410–472, 2016.

- [100] O. O. Abegunde, E. T. Akinlabi, O. P. Oladijo, S. Akinlabi, and A. U. Ude, "Overview of thin film deposition techniques," *AIMS Mater. Sci.*, vol. 6, no. 2, pp. 174–199, 2019.
- [101] R. Messier, "Thin Film Deposition Processes," *MRS Bull.*, vol. 13, no. 11, pp. 18–21, 1988.
- [102] D. Banga, B. Perdue, and J. Stickney, "Electrodeposition of a PbTe / CdTe superlattice by electrochemical atomic layer deposition (E-ALD)," *J. Electroanal. Chem.*, vol. 716, pp. 129–135, 2014.
- [103] G. Biasiol and L. Sorba, "Molecular Beam Epitaxy : Principles and," *Cryst. growth Mater. energy Prod. energy Sav. Appl.*, pp. 66–83, 2001.
- [104] B. W. Gregory and J. L. Stickney, "Electrochemical atomic layer epitaxy (ECALE)," vol. 300, pp. 543–561, 1991.
- [105] K. Varazo, M. D. Lay, T. A. Sorenson, and J. L. Stickney, "Formation of the first monolayers of CdTe on Au(111) by electrochemical atomic layer epitaxy (EC-ALE): Studied by LEED, Auger, XPS, and in-situ STM," *J. Electroanal. Chem.*, vol. 522, no. 1, pp. 104–114, 2002.
- [106] R. Vaidyanathan, J. L. Stickney, and U. Happek, "Quantum confinement in PbSe thin films electrodeposited by electrochemical atomic layer epitaxy (EC-ALE)," *Electrochem. commun.*, vol. 49, pp. 1321–1326, 2004.
- [107] A. Fülöp, Y. Song, S. Charpentier, P. Shi, M. Ekström, L. Galletti, R. Arpaia, T. Bauch, F. Lombardi, and S. Wang, "Phase transition of bismuth telluride thin films grown by MBE," *Appl. Phys. Express*, vol. 7, no. 4, 2014.

- [108] S. Lee, J. Y. Kim, T. W. Lee, W. K. Kim, B. S. Kim, J. H. Park, J. S. Bae, Y. C. Cho, J. Kim, M. W. Oh, C. S. Hwang, and S. Y. Jeong, "Fabrication of high-quality single-crystal Cu thin films using radio-frequency sputtering," *Sci. Rep.*, vol. 4, pp. 1–6, 2014.
- [109] X. Huang, J. Guan, Z. Lin, B. Liu, S. Xing, W. Wang, and J. Guo, "Epitaxial Growth and Band Structure of Te Film on Graphene," *Nano Lett.*, vol. 17, no. 8, pp. 4619–4623, 2017.
- [110] Y. Nanao, A. Ikeda, M. Naito, H. Yamamoto, K. Kumakura, and Y. Krockenberger, "Molecular beam epitaxy of Nd₂PdO₄ thin films," *AIP Adv.*, vol. 7, no. 7, 2017.
- [111] M. Bic and H. Ko, "Selective Electrodeposition and Growth Mechanism of Thermoelectric Bismuth-Based Binary and Ternary Thin Films," *J. Phys. Chem. C*, vol. 114, pp. 8256–8263, 2010.
- [112] D. O. Banga, R. Vaidyanathan, L. Xuehai, J. L. Stickney, S. Cox, and U. Happeck, "Formation of PbTe nanofilms by electrochemical atomic layer deposition (ALD)," *Electrochim. Acta*, vol. 53, pp. 6988–6994, 2008.
- [113] J. Huotari, V. Kekkonen, J. Puustinen, J. Liimatainen, and J. Lappalainen, "Pulsed Laser Deposition for Improved Metal-oxide Gas Sensing Layers," *Procedia Eng.*, vol. 168, pp. 1066–1069, 2016.
- [114] V. Dolique, A. Thomann, E. Millon, A. Petit, P. Brault, V. Dolique, A. Thomann, E. Millon, A. Petit, and P. Brault, "About the key factors driving the resistivity of AuOx thin films grown by reactive magnetron sputtering," 2014.
- [115] F. A. P. and H. R. K.L. Salcedo, C.A. Rodriguez, "Morphological study of palladium thin films deposited by sputtering," *J. Phys. Conf. Ser.*, vol. 274, 2011.

- [116] L. Arroyo-Ramírez, Y. Figueroa, D. Rodríguez, W. Otaño, and C. R. Cabrera, "Palladium nanostructures synthesis by sputtering deposition on HOPG surfaces," *ECS Trans.*, vol. 28, no. 7, pp. 1–7, 2010.
- [117] S. M. A. L. I. Andrabi, M. A. Shah, and K. P. Road, "A Study of Catalyst Preparation Methods for Synthesis of Carbon Nanotubes," vol. 5, no. 1, pp. 1–7, 2016.
- [118] R. L. S. Mello, F. I. Mattos-Costa, H. de las M. Villullas, and L. O. de S. Bilhões, "Preparation and electrochemical characterization of Pt nanoparticles dispersed on niobium oxide," *Eclética química*, vol. 28, no. 2, pp. 69–76, 2003.
- [119] S. V. Ingale, P. B. Wagh, D. Bandyopadhyay, I. K. Singh, R. Tewari, and S. C. Gupta, "Synthesis of nanosized platinum based catalyst using sol-gel process," *IOP Conf. Ser. Mater. Sci. Eng.*, vol. 73, p. 012076, 2015.
- [120] F. Chekin, S. Bagheri, and S. B. A. Hamid, "Synthesis and spectroscopic characterization of palladium-doped titanium dioxide catalyst," *Bull. Mater. Sci.*, vol. 38, no. 2, pp. 461–465, 2015.
- [121] R. L. Puurunen, "A short history of atomic layer deposition: Tuomo Suntola's atomic layer epitaxy," *Chem. Vap. Depos.*, vol. 20, no. 10–12, pp. 332–344, 2014.
- [122] N. P. Dasgupta, J. F. MacK, M. C. Langston, A. Bousetta, and F. B. Prinz, "Design of an atomic layer deposition reactor for hydrogen sulfide compatibility," *Rev. Sci. Instrum.*, vol. 81, no. 4, pp. 1–6, 2010.
- [123] C. Travis and R. Adomaitis, "Dynamic modeling for the design and cyclic operation of an atomic layer deposition (ALD) reactor," *Processes*, vol. 1, no. 2, pp. 128–152, 2013.

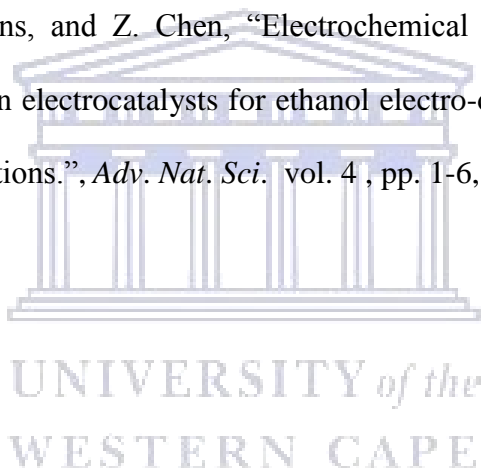
- [124] Y. Wu, D. Döhler, M. Barr, E. Oks, M. Wolf, L. Santinacci, and J. Bachmann, "Atomic Layer Deposition from Dissolved Precursors," *Nano Lett.*, vol. 15, no. 10, pp. 6379–6385, 2015.
- [125] R. W. Johnson, A. Hultqvist, and S. F. Bent, "A brief review of atomic layer deposition : from fundamentals to applications," *Biochem. Pharmacol.*, vol. 17, no. 5, pp. 236–246, 2014.
- [126] R. M. Modibedi, E. K. Louw, M. K. Mathe, and K. I. Ozoemena, "The Electrochemical Atomic Layer Deposition of Pt and Pd Nanoparticles on Ni Foam for the Electro Oxidation of Alcohols.," *ECS Trans.*, vol. 50, no. 21, pp. 9–18, 2013.
- [127] M. K. Mathe, S. M. Cox, V. Venkatasamy, U. Happek, and J. L. Stickney, "Formation of HgSe Thin Films Using Electrochemical Atomic Layer Epitaxy," *J. Electroche. Soc.* vol. 152 , pp 7511-7555, 2005.
- [128] C. Thambidurai, D. K. Gebregziabiher, X. Liang, Q. Zhang, V. Ivanova, P. Haumesser, and J. L. Stickney, "E-ALD of Cu Nanofilms on Ru / Ta Wafers Using Surface Limited Redox Replacement," *J. Electrochem. Soc.*, vol. 152, pp. 466–471, 2010.
- [129] D. Gokcen, S. Bae, and S. R. Brankovic, "Reaction kinetics of metal deposition via surface limited red-ox replacement of underpotentially deposited metal monolayers," *Electrochim. Acta*, vol. 56, no. 16, pp. 5545–5553, 2011.
- [130] V. Sudha and M. V. Sangaranarayanan, "Underpotential deposition of metals – Progress and prospects in modelling," *J. Chem. Sci.*, vol. 117, no. 3, pp. 207–218, 2005.

- [131] M. Nishizawa, T. Sunagawa, and H. Yoneyama, "Underpotential Deposition of Copper on Gold Electrodes through Self-Assembled Monolayers of Propanethiol," vol. 7463, no. c, pp. 5215–5217, 1997.
- [132] T. Goric, "Reactions of Copper on the Au (111) surface in the underpotential deposition region from chloride solutions," *Langmuir*, vol. 17, no. 11, pp. 4347–4351, 2001.
- [133] G. K. Jennings and P. E. Laibinis, "Underpotentially deposited metal layers of silver provide enhanced stability to self-assembled alkanethiol monolayers on gold," vol. 7463, no. 11, pp. 6173–6175, 1996.
- [134] D. M. Kolb, M. Przasnyski, and H. Gerischer, "Underpotential deposition of metals and work function differences," *J. Electroanal. Chem.*, vol. 54, no. 1, pp. 25–38, 1974.
- [135] J. S. B.M. Huang, L.P. Colletti, B.W. Gregory, J.L. Anderson, "Preliminary Studies of the use of an Automated Flow-Cell Electrochemical System for the Formation of CdTe Thin Film by Electrochemical Atomic Layer Epitaxy," pp. 3007–3016, 1995.
- [136] W. D. Suggs and J. L. Stickney, "Characterization of Atomic Layers of Tellurium Electrodeposited," *J. Phys. Chem.*, vol. 95, no. 5, pp. 10056–10064, 1991.
- [137] B. W. Gregory, M. L. Norton, and J. L. Stickney, "Thin-layer electrochemical studies of the underpotential deposition of cadmium and tellurium on polycrystalline Au, Pt and Cu electrodes," *J. Electroanal. Chem.*, vol. 293, no. 1–2, pp. 85–101, 1990.
- [138] J. Y. Kim, Y. Kim, and J. L. Stickney, "Cu nanofilm formation by electrochemical atomic layer deposition (ALD) in the presence of chloride ions," *J. Electroanalytical Chem.*, vol. 621, pp. 205–213.

- [139] T. S. Mkwizu and I. Cukrowski, "Physico – chemical Modelling of Adlayer Phase Formation via Surface – limited Reactions of Copper in Relation to Sequential Electrodeposition of Multilayered Platinum on Crystalline Gold," *Electr. Acta*, vol. 147, pp. 432–441, 2014.
- [140] R. M. Modibedi, M. K. Mathe, R. G. Motsoeneng, L. E. Khotseng, K. I. Ozoemena, and E. K. Louw, "Electro-deposition of Pd on Carbon paper and Ni foam via surface limited redox-replacement reaction for oxygen reduction reaction," *Electrochim. Acta*, vol. 128, no. May, pp. 406–411, 2014.
- [141] T. S. Mkwizu, M. K. Mathe, and I. Cukrowski, "Electrodeposition of multilayered bimetallic nanoclusters of ruthenium and platinum via surface-limited redox-replacement reactions for electrocatalytic applications," *Langmuir*, vol. 26, no. 1, pp. 570–580, 2010.
- [142] T. S. Mkwizu and I. Cukrowski, "Physico-chemical modelling of adlayer phase formation via surface-limited reactions of copper in relation to sequential electrodeposition of multilayered platinum on crystalline gold," *Electrochim. Acta*, vol. 147, pp. 432–441, 2014.
- [143] J. Nutariya, M. Fayette, N. Dimitrov, and N. Vasiljevic, "Electrochimica Acta Growth of Pt by surface limited redox replacement of underpotentially deposited hydrogen," *Electrochim. Acta*, vol. 112, pp. 813–823, 2013.
- [144] I. Achari, S. Ambrozik, and N. Dimitrov, "Electrochemical Atomic Layer Deposition of Pd Ultrathin Films by Surface Limited Redox Replacement of Underpotentially Deposited H in a Single Cell," *J. Phys. Chem. C*, vol. 121, pp. 4404–4411, 2017.

- [145] M. Fayette, Y. Liu, D. Bertrand, J. Nutariya, N. Vasiljevic, and N. Dimitrov, "From Au to Pt via Surface Limited Redox Replacement of Pb UPD in One-Cell Configuration," *Langmuir*, vol. 27, pp. 5650–5658, 2011.
- [146] K. Venkatraman, Y. Dordi, and R. Akolkar, "Electrochemical Atomic Layer Deposition of Cobalt Enabled by the Surface-Limited Redox Replacement of Underpotentially," *J. Electrochemical Soc.*, vol. 164, no. 2, pp. 104–109, 2017.
- [147] V. Daujotis and E. Gaidamauskas, "Effect of anions on the underpotential deposition of thallium (I) on polycrystalline silver," *J. Electroanalytical Chem.*, vol. 446, pp. 151–157, 1998.
- [148] N. Dimitrov, "Electrochimica Acta Recent Advances in the Growth of Metals , Alloys , and Multilayers by Surface Limited Redox Replacement (SLRR) Based Approaches," *Electrochim. Acta*, vol. 209, pp. 599–622, 2016.
- [149] T. S. Mkwizu and I. Cukrowski, "Physico – chemical Modelling of Adlayer Phase Formation via Surface – limited Reactions of Copper in Relation to Sequential Electrodeposition of Multilayered Platinum on Crystalline Gold," *Electrochim. Acta*, vol. 147, pp. 432–441, 2014.
- [150] A. M. Stacy, "Insights into the Electrodeposition of Bi₂Te₃ Insights into the Electrodeposition of Bi₂Te₃," *J. Electrochem. Soc.*, vol 149, pp 546-554 , 2002.
- [151] J. Lu, J. W. Elam, and P. C. Stair, "Synthesis and Stabilization of Supported Metal Catalysts by Atomic Layer Deposition," *Acc. Chem. Res.* vol. 46, pp 1805-1815 8, 2013.

- [152] R. G. Motsoeneng, R. M. Modibedi, M. K. Mathe, L. E. Khotseng, and K. I. Ozoemena, “The synthesis of PdPt / carbon paper via surface limited redox replacement reactions for oxygen reduction reaction,” *Int. J. Hydrogen Energy*, vol. 40, pp 16734-16744, 2015.
- [153] J. D. Benck, B. A. Pinaud, Y. Gorlin, and T. F. Jaramillo, “Substrate Selection for Fundamental Studies of Electrocatalysts and Photoelectrodes : Inert Potential Windows in Acidic , Neutral , and Basic Electrolyte,” *Plos One*, vol. 9, pp 1-3, 2014.
- [154] A. J. Arvia, R. C. Salvarezza, and W. E. Triaca, “Noble Metal Surfaces and Electrocatalysis . Review and Perspectives,” vol. 143, pp. 133–143, 2004.
- [155] R. S. Hsu, D. Higgins, and Z. Chen, “Electrochemical and surface characteristics of carbon-supported PtSn electrocatalysts for ethanol electro-oxidation : possible application for inkjet ink formulations.”, *Adv. Nat. Sci.* vol. 4 , pp. 1-6, 2013.



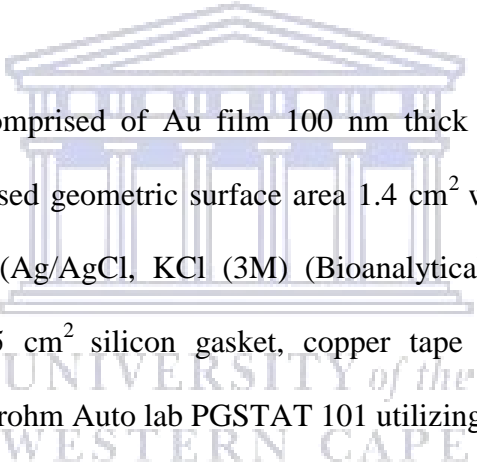
Chapter 3

Summary

This chapter describes the various electroanalytical techniques employed, detailed research methods and general experimental procedures for the electrochemical atomic layer deposition on the gold substrate as well as electrochemical characterization, microscopic and spectroscopic characterization of the synthesized thin film.

3.0 Methodology

3.1.1 Materials and reagents



The gold (Au) substrate, comprised of Au film 100 nm thick film on glass, with 5 nm Ti adhesion layer with an exposed geometric surface area 1.4 cm^2 was used as working electrode (WE), Reference electrode (Ag/AgCl, KCl (3M) (Bioanalytical Systems, Inc). The counter electrode (Gold wire). 1.45 cm^2 silicon gasket, copper tape as WE connector, Auto lab Potentiostat/Galvanostat Metrohm Auto lab PGSTAT 101 utilizing software NOVA 2.1.1 for CV data, electrochemical thin flow cell, Plexiglas box peristaltic pump. Perchloric acid (HClO_4 , 70 % (Merc, Suprapur), Sulphuric acid, 98 % (Associated Chemical Enterprise, ACE), Nitric acid 65 %, (Merc, Suprapur), Copper(II) sulphate pentahydrate, $\text{CuSO}_4 \cdot 5\text{H}_2\text{O}$ ACS reagent, $\geq 98 \%$ were supplied by Sigma Aldrich, Acetone (ACS), PdCl_2 (from Sigma Aldrich), TeO_2 (Sigma Aldrich), Bi_2O_3 (Sigma Aldrich) Bi_2O_3 (from Sigma Aldrich). The measurements of pH were obtained using Thermo Scientific Orion star A221, and star A321, portable pH meter). All chemicals were pure, analytical grade was used without further purification without any further purification.

3.1.2 Precursor solutions

All chemical solutions in this research were prepared using ultrapure water with $18.2 \mu\text{Scm}^{-1}$ conductivity and were deaerated for 1 hour with compressed nitrogen (N_2) gas supplied by Afrox (South Africa) before each experiment resume. The precursor solutions were; (i) Cu solution prepared was $1\text{mM CuSO}_4 + 0.1\text{M H}_2\text{SO}_4$, pH (1.4), (ii) Bi solution consisted of $0.2 \text{mM Bi}_2\text{O}_3$ in 0.1M HClO_4 , (iii) Pd solution prepared was composed of 1mM PdCl_2 solution in $0.1\text{M H}_2\text{SO}_4$ pH (1.2), (iv) Te prepared was $0.5 \text{mM HTeO}_2 + 0.1\text{M HClO}_4$.

3.1.3 Electroformation of Pd-based nanostructured thin film through SLRR of Cu-UPD

Before the electrodeposition gold (Au) substrate was cleaned through immersion in hot nitric acid (HNO_3 conc) for 30 min, followed by ultrapure water, then acetone and ultrapure water to remove any contaminants. The substrate was further taken for an ultra-sonication bath for 3 min and was rinsed again with ultrapure water before the assembly of the electrochemical thin flow cell. Au substrate was further electrochemically cleaned/ activated with nitrogen saturated aqueous solution of 0.1M HClO_4 (70 %), pH 1.12 and $0.1 \text{M H}_2\text{SO}_4$ (98 %) pH 1.02 by cycling from +1.7 to -0.5 V potential (upper and lower vertex respectively) until a CV's (25 cycles) were stable. In 1 L volumetric flask, a solution of 0.1M of perchloric acid (HClO_4) and 0.1M sulphuric acid (H_2SO_4) as blank solution/ background electrolytes (BE) solution was prepared. A single peristaltic pump connected to three electrode-cells (flow cell) was used to pump solution onto a thin flow cell connected to the egress of a cell. The electrode/electrolyte interface study and inert potential window were examined using CV. Cyclic voltammograms of Au are carried out at different scan rate, and potentials are reported versus Ag/AgCl (3 M KCl) as reference electrode.

3.1.4 Electroformation of mono-metallic Pd nanostructured thin film via SLRR of Cu underpotential deposition

The deposition process of Pd is shown in **Figure 1 (Chapter 4)** with time-potential-current plot recorded for two SLRR cycles to optimize time and potential for E-ALD cycles. Pd was deposited using SLRR of Cu-_{UPD} metal on Au as reported in literature [1],[3]. The E-ALD cycle for monometallic Pd was electro-formed by a number of steps as (i) Cu solution was filled into the thin flow cell at OCP for 10s, (ii) The solution was held quiescent to allow Cu deposition at $UPD = 0.18\text{ V}$ for 10s, (iii) Then Pd solution was filled into the thin flow cell at OCP for 15s to allow exchange of Cu-_{UPD} for Pd, (iv) Lastly, BE was pumped onto the electrochemical thin flow cell at OCP to rinse the excess Pd. The repetitive alternated cycle for Pd deposition was executed for fifteen times to form a required deposit. The time-potential-current trace of layer-by-layer deposition of Pd was recorded for two cycles and is illustrated in **Figure 3.2** and discussed in the discussion section.

The potential-current time trace of Pd in **Figure 3.1 (a)** recorded for two E-ALD cycles. This trace was used to monitor the deposition steps and cycles, in which it monitors the stripping current which is referred to as monolayer or bulk stripping at the triggered potential. The reductive current correlates to UPD and OPD depending on the potential set. Lastly, the trace gives an insight on the time required to form the coverage of deposit. Sheridan et al [3] have reported the trace of Pd SLRR of Cu-_{UPD}. The corresponding schematic cartoon displays the general mechanism for reductive Cu-_{UPD} and SLRR at OCP as demonstrated in literature [4], [5], [6], [7]. In this research, the potential-current-trace for mono Pd deposition is discussed in discussion section **Chapter 4 to 7**, and other trace for modification of Pd on Au.

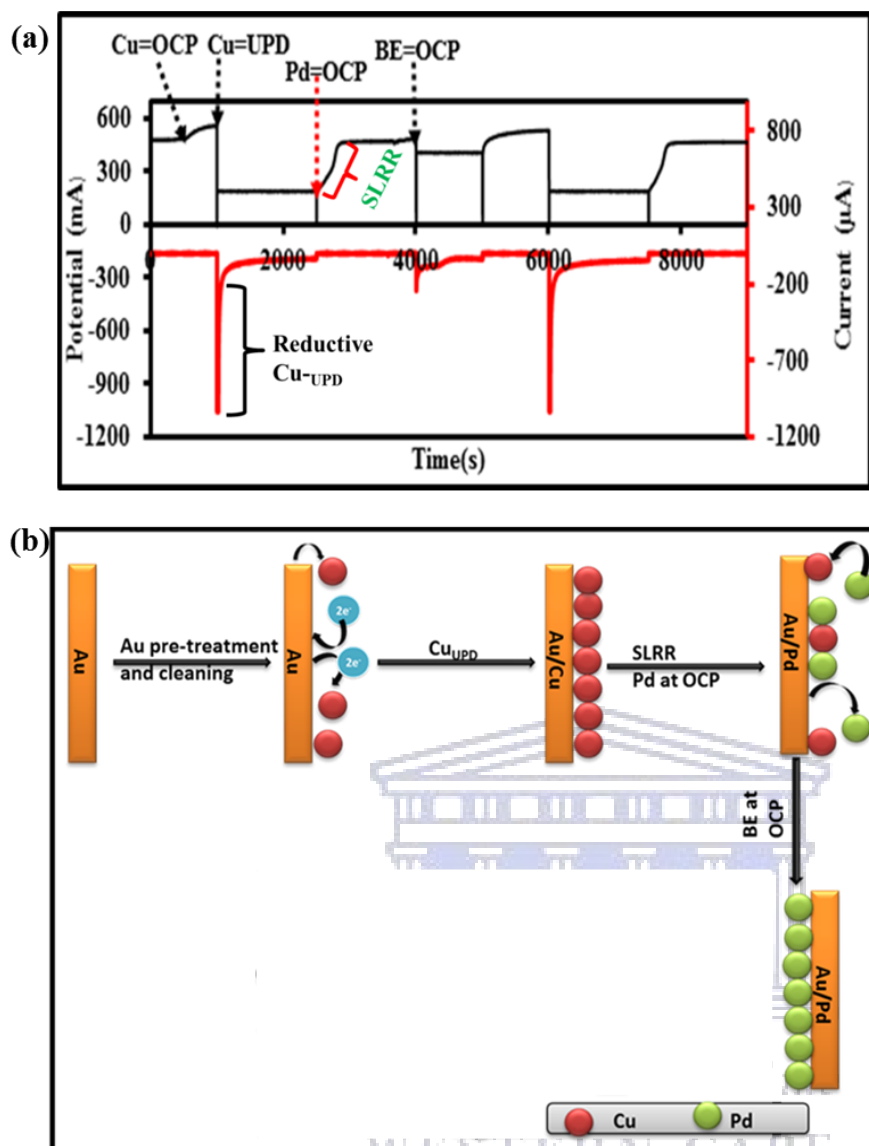


Figure 3.1: (a) A typical potential-current-time plot of Pd on Au recorded for two cycles and (b) generally schematic cartoon illustrating Pd SLRR of Cu-UPD.

3.1.5 Electrodeposition of bimetallic PdIr thin film via SLRR Cu_{UPD}

The SLRR cycle for PdIr was formed by alternated repeating excursion of Pd and Ir steps as (i) Cu solution was flow into the cell at OCP for 10s, (ii) The solution was held constant, with no flow to allow Cu deposition at UPD = 0.18 V for 10s, (iii) Then Pd solution was filled into the

thin flow cell at OCP for 15s to allow exchange of Cu UPD for Pd, (iv) Cu solution was filled into the thin flow cell at OCP for 10s, (ii) The solution was held quiescent to allow Cu deposition at UPD = 0.18 V for 10s, (iii) Then Ir solution was filled into the thin flow cell at OCP for 15s to allow exchange of Cu UPD for Ir. Finally BE was filled into the thin flow cell at OCP to rinse the excess Pd and Ir. The deposition cycle was repeated 15 times to form a required deposit. Potential-current time-trace of sequential layer-by-layer deposition of PdIr recorded for two cycles is illustrated in **Chapter 4, section 4.2.5, Figure 4. 4.**

3.2. Electrosynthesis of Pd-M (M= Cu, Bi): Pd surface Modification

3.2.1 Underpotential deposition of Bi on Au and Pd: CV profile

Prior the deposition, cyclic voltammetry (CV) profile of Au substrate in of solution of 0.2 Mm Bi₂O₃ in 0.1M HClO₄ was investigated to identify optimal UPD potential for programming the E-ALD cycles. The optimal underpotential deposition (UPD) was identified using cyclic voltammetry at 10 mVs⁻¹. The UPD of the desired depositing metal precursor was obtained from CV. Generally, UPD values are identified and used for the initial deposition cycle [8]. The CV profile of Pd in the above solution was also probed to identify the optimal Cu-UPD and Bi-UPD for respective corresponding (CuPd, BiPd) deposits. The CVs are illustrated in **Figure 5.1** and **Figure 5.2 (b)**. The E-ALD cycles set are presented below in section **3.8.4.1** and **3.8.4.2** respectively.

3.2.2 Underpotential deposition of Cu on Au and Pd: CV profile

Underpotential deposition (UPD) of depositing metal precursor is very crucial to set the E-ALD cycle program The UPD of Cu²⁺ solution on Au and Pd substrate was obtained from CV and was

depicted in **Figure 4.2 (Chapter 4)** and **Figure 5.3 (Chapter 5)** respectively. Generally, UPD values are identified and used for the initial deposition cycle [8].

The electroformation of Pd-M (M= Bi, Cu) for corresponding bimetallic BiPd, CuPd and trimetallic CuBiPd.

3.2.3 Electrosynthesis of BiPd

E-ALD cycle1 for BiPd deposition on Au is as follows (i) Fill Cu solution into the thin flow cell at OCP, Hold the Cu solution quiescent to allow Cu deposition at $UPD = 0.18V$, (ii) Fill Pd solution at OCP for 15s to exchange Cu_{-UPD} for Pd, (iii) then fill BE solution at OCP for 5s these steps were repeated 15 times to make cycle 1 (period 1). Subsequently (i) Bi solution was filled into the thin flow cell as $0.18 V$ for 10s, (ii) Bi solution was held quiescent to allow deposition at $UPD = 0.150 V$ for 10s, (iii) then BE solution was flushed into the thin flow cell for 10s, and cycling steps were repeated 15 times to obtain the deposit.

3.2.4 Modification of Pd by mono Cu adlayer

E-ALD cycles for CuPd was done as follows (i) Fill Cu solution into the thin flow cell at OCP for 10s, (ii) Hold quiescent to allow Cu deposition at $UPD = 180 V$ for 10s, (iii) Fill Pd solution into the cell at OCP for 15s, (iv) BE rinse for 5s, these steps were repeated 15 times. The second cycles was as follows (i) Flush Cu solution at OCP for 10s, (ii) hold static to allow Cu deposition for 10s, (iii) BE rinse at OCP for 5s. These steps were repeated for 15 times, and the time-potential-current trace depicts the steps as demonstrated in **Figure 5.5 (b) Chapter 5**. The CuPd thin film formed was immersed in $0.1M HClO_4$ and was scanned from -0.2 to various anodic potential limit ($+1.0, +1.2, +1.4$) V at $30 mVs^{-1}$ to the identity of Pd or Cu redox feature on Au as shown in **Figure 5.6, Chapter 5**.

3.4.5 Modification of Pd by (CuBi) adlayer

E-ALD cycle for CuBiPd deposition on Au is as follows (i) Fill Cu solution into the thin flow cell at OCP for 10s, (ii) Hold quiescent to allow Cu deposition at UPD = 180 V for 10s, (iii) Fill Pd solution into the cell at OCP for 15s. These steps were repeated as 15 times for a required deposit. Subsequently Cu solution was filled into the thin flow cell at OCP, Hold the Cu solution quiescent to allow at UPD = 0.189 V for 10s, (iii) Fill Bi solution at OCP for 10s, then the solution was held for 10s to allow deposition at UPD= 0.189 V, (iv) Fill BE solution at OCP for 10s. These sequential steps were repeated for 15 times to acquire the desired deposit.

3.3. Oxidative Te Underpotential deposition identification: CV profile

This sub-section details the oxidative Te underpotential deposition on metal electrode (M) such as bare Au, Pd-covered Au, CuPd-covered Au and BiPd-covered Au. It is paramount important to investigate the optimal ox Te-_{UPD} on Au and Pd-covered Au to programme the E-ALD cycles. It was investigated using CVs through immersion of Metal electrode in 0.5 mM HTeO₂⁺ in 0.1 M HClO₄. The potential was started from 1.0 V to various cathodic window potentials to obtain redox couple of Te using CV (See section 6.2 Chapter 6, Figure 6.1 (a)).

3.3. Electro-formation of Te-M thin film derivatives, (M = Au, Pd, BiPd, and CuPd)

3.3.1 Electro-formation of Te-M (M = Au) on Au substrate

E-ALD cycle for Te on Au deposition on Au is as follows (i) Fill Te solution into the thin flow cell at OCP, hold the Te solution quiescent to allow Te deposition at OPD = -0.5 V, (iii) Fill BE solution at -0.6 V to re-reduce excess Te(0) leaving atomic Te layer through oxidative underpotential deposition. Finally, BE was filled into the cell at OCP. These steps were repeated 15 times for a required deposit. The time-potential-current trace for Te thin films on Au is illustrated (see Chapter 6, Figure 6.2 (a-b)).

3.3.2 Electroformation of Te-M, (M = Pd)

E-ALD cycle for TePd deposition on Au is as follows (i) Fill Cu $2+$ solution at OCP for 10s, (ii) Solution was held for 10s to allow Cu to deposit at UPD = +0.18 V, (ii) Subsequently, Pd solution was allowed to flow at OCP for 10s, (iii) the BE electrolyte was filled at OCP, (iv) Te solution into the thin flow cell at OCP, Hold the Te solution quiescent to allow Te deposition at OPD = -0.5 V, (iii) Fill BE solution at -0.6 V to re-reduce excess Te(0) leaving atomic Te layer through oxidative Te underpotential deposition ($oxTe_{-UPD}$). These steps were repeated like 15 times for a required deposit. The time-potential-current trace and CV for TePd thin films on Au is illustrated in **Figure 6.4 (a-b)** (see **Chapter 6**).

3.3.3: Electroformation of Te-M (M = BiPd)

E-ALD cycle¹ for BiTePd deposition on Au is as follows (i) Fill Cu solution into the thin flow cell at OCP, Hold the Cu solution quiescent to allow Cu deposition at UPD = 0.18 V, (ii) Fill Pd solution at OCP for 15s to exchange Cu_{-UPD} for Pd, (iii) then fill BE solution at OCP for 5s these steps were repeated 15 times to make cycle 1 (period 1). Subsequently (i) Bi solution was filled into the thin flow cell as 0.18 V for 10s, (ii) Bi solution was held quiescent to allow deposition at UPD = 0.150 V for 10s, (iii) BE solution was flushed into the thin flow cell for 10s, (iv) Fill Te solution at OCP (v) Te solution was held quiescent for 10s to allow deposition at -0.55 V (v) The BE solution was flushed into the thin flow cell at -0.6V to reduce the excess Te(0). The cycling steps were repeated 15 times to make cycles of the required deposit.

3.3.4 Electro-formation of Te-M, (M = CuPd)

E-ALD cycle¹ for CuTePd deposition on Au as (i) Fill Cu solution into the thin flow cell at OCP, Hold the Cu solution quiescent to permit Cu deposition at UPD = 0.18 V, (ii) Fill Pd solution at OCP for 15s to exchange Cu_{-UPD} for Pd, (iii) then fill BE solution at OCP for 5s these steps were repeated 15 times to make cycle 1 (period 1). Subsequently, (iv) Fill Te solution at

OCP for 10s, (v) then Te solution was held quiescent for 10s to allow deposition at -0.5 V, (vi) Flow BE into the cell at OCP, Finally (vii) Flow Cu solution into the thin flow cell at set potential (Cu = 0.19 V) for 10s, (viii) at solution was held constant to allow deposition at UPD = 0.1890 V for 10s, (viii) BE solution was flushed at OCP into the thin flow cell for 10s. The cycling steps were repeated 15 times to make cycle the required deposit.

3.4.1 Electrochemical characterization of nanostructured thin films in 0.1 M HClO₄

All the nanostructured thin films were immersed solution of 0.1 M HClO₄ immediately after the E-ALD cycle to confirm the formation of thin film by examining the redox feature. Cyclic voltammetry was used to examine the redox features, by scanning the thin film from 1.0 to -0.2V at scan rate of 30 mVs⁻¹ depending on a desired potential window of thin film. The cyclic voltammetric characteristics on nanostructured thin film is displayed and explained in discussion in the corresponding sections in **Chapter 4, Chapter 5, 6 and 7.**

3.4.2 Electrochemical activity of nanostructured thin films towards KOH and EtOH oxidation

All the nanostructured thin films activity towards ethanol (EtOH) oxidation reaction (EOR) were tested through immersion in nitrogen (N₂) gas saturated 0.5 M KOH + 0.1 M EtOH electrolyte solution. Cyclic voltammetry (CVs) and chronoamperometric results were used to obtain electrochemical activity and stability. CVs were cycled between -1.0 to +0. 2V at a scan rate of 30 mVs⁻¹. The electrochemical stability was evaluated for 1 hour (3600s) duration. Furthermore, electron kinetic transfer reaction of as-synthesized nanostructured thin film electrocatalyst was evaluated using electrochemical impedance spectroscopy, the results were presented using Nyquist and Bode plot using selected potential -0.2V from CV at 1x10⁴ to 0.1Hz frequency range. The results are discussed in the discussion section, in **Chapter 4 to Chapter 7.**

3.4 3 E-ALD set up

The workbench was composed of the special sophisticated instrument, apparatus used in this research for electroformation nanostructured Pd-thin film in accordance to the previous literature [9-11], the this technique is referred to as Electrochemical atomic layer deposition technique (E-ALD).

The E-ALD instrument is comprised of the components that are computer-controlled a Laboratory Virtual Instrument Engineering Workbench (LABVIEW) program with Sequencer 4 software. The software could allow a cycle program that makes up a specific sequence for a specific compound formation [9]. These components consist of piston pumps (supplied by Metrohm, Switzerland), multi-valve system, Potentiostat PGSTAT 30 (from Eco Chemie, Autolab, Netherlands). Up to 5 different electrolytes solution could be pumped into the thin flow cell independently. The auxiliary electrode was a gold wire, the reference electrode is connected on egress of thin flow cell and working electrode (WE) was wire-gold substrate (Au) connected on copper wire attached on working surface substrate and counter electrode (CE) was gold wire as reported in literature [10], [11]. The most working electron is embedded on an assembled electrochemical thin flow cell (as displayed in **Figure 3.2:** insert). The area of WE and the thickness of the deposits is controlled by the assembled rubber gasket.

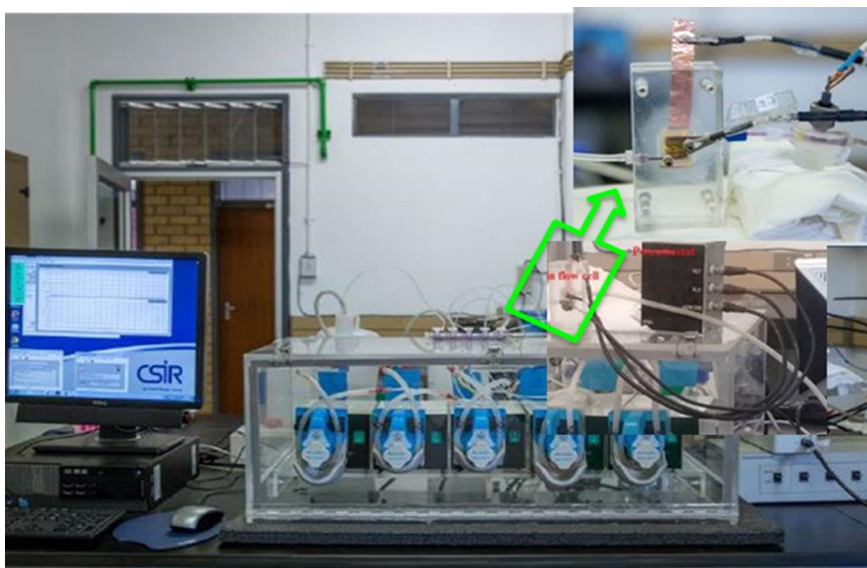


Figure 3.2: Picture of the up-pumping system, Potentiostat, and thin flow cell connected to a computer that has LABVIEW sequencer 4, Solution precursors, thin flow cell and insert: thin flow cell.

3.5. Physical characterization and quantitative analysis of nanostructured thin films

Microscopic analysis

3.5.1 Scanning electron-microscope- energy dispersive x-ray (SEM-EDX)

Scanning electron microscopy (SEM, Auriga Cobra FIB FE-SEM, Germany) coupled with Energy dispersive X-Ray spectroscopy (EDX) at the accelerating voltage of 15 kV was used for estimating the bulk composition of the thin films.

3.5.2 Atomic force microscopy (AFM)

The morphology and topography of the thin film was examined using atomic force microscopy (AFM) was carried out using Agilent Technologies AC Mode III instrument in ambient tapping mode using a model RTESPW tip (Veeco Manufacturing, Inc.).

Spectroscopic analysis

3.5.3 X-ray diffraction (XRD)

The XRD measurements were done on a Rigaku Ultima IV X-ray DI powder diffractometer using Cu-K α radiation operating at 40 kV (diffraction wavelength $\lambda = 0.15406$ nm) to determine the structure of the thin films. Diffractograms were recorded in the 2θ range of 10-90° with the step size of 0.02 speed, scan time 2s per step.

3.5.4 X-ray photoelectron spectroscopy (XPS)

X-ray photoelectron spectroscopy (XPS) measurements were performed at room temperature using KRATOS-SUPRA spectrometer with monochromatic Al K α radiation possessing excitation energy, $h\nu = 1486.6$ eV and base pressure 1.2×10^{-9} Torr at UNISA (Florida Science Campus).

3.6.1 Theory on characterization techniques

Electroanalytical techniques

Electrochemical techniques involve the use of electrodes to study the chemical changes accompanied or transformation that occurs on the electrodes or follows the transformation of adsorbed/ dissolved species in solution in the form of ionic or electronic transfer between the anode solution interfaces. In general, all electrochemically-induced properties involve the changes in (a) Potentiostat, (b) produces current or accumulation of charge over time (t). Electrochemical techniques such as cyclic voltammetry (CV), differential pulse polarography (DPV), chronoamperometry (CA), electrochemical impedance spectroscopy (EIS) and

polarography are also useful into supplying the supporting information for physical characterization with physical and chemical properties.

The three electrochemical systems: Basic components

The modern electrochemical system for voltammetric measurements is composed of an external source the Potentiostat, an electrochemical cell, and a computer. The cell is used to generate voltage and current from the chemical reaction or induce chemical reactions by the input of electrochemical signals. The role of external source Potentiostat is to apply the optimal and accurate controlled potential and monitor the current produced. The three electrochemical cell systems where measurements are carried out comprised of a working electrode, reference electrode, and counter or auxiliary electrode immersed in the analyte and non-reacting electrolyte known as supporting electrolyte. The working electrode is where the deposition or reaction occurs, in this system voltage is carefully regulated between the working electrode and the reference electrode, while the current passes the working electrode and counter electrode. **Figure 3.2** shows three electrochemical cell.



UNIVERSITY *of the*
WESTERN CAPE

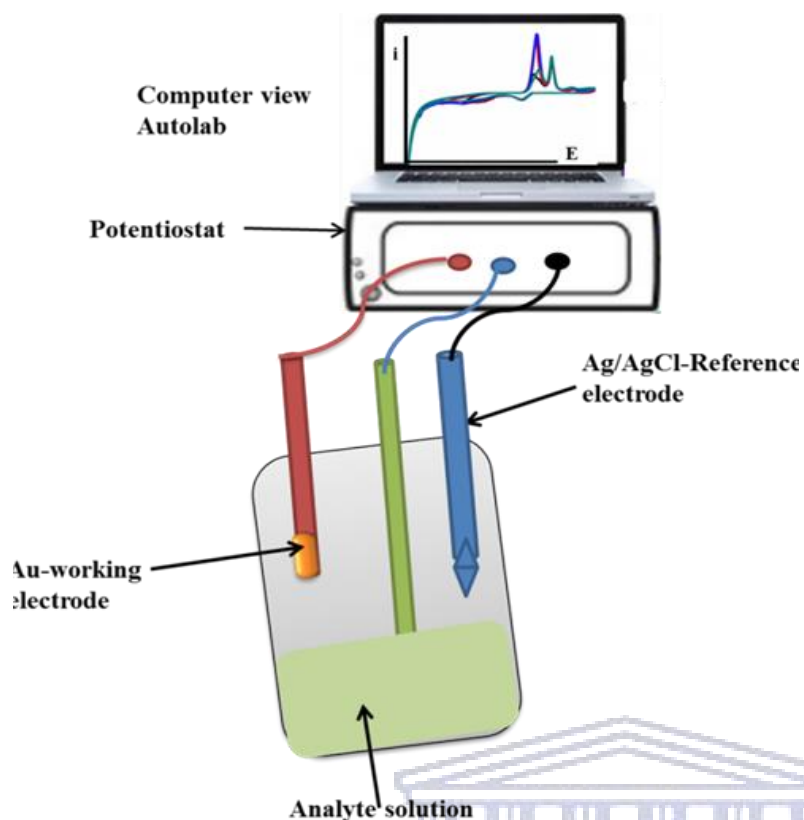


Figure 3.3: Illustration of three electrode electrochemical cell consisting of three electrodes.

Working electrode

The working electrode (WE) at which electrochemical phenomena such as chemical adsorption or deposition investigated takes place. The potential of WE varied linearly with time. The WE serves as a transducer in electrochemical and bioelectrochemical. Most materials used for working electrodes includes, noble metals: Gold (Au) or Platinum, a carbon material such as pyrolytic graphite (HOPGC), glassy carbon (GC), carbon paste, diamonds, to name the few. In this work, Au- coated glass (Evaporated metal film 50 Å Ti: 1, 000 Å Au) was used as a substrate for deposited catalyst (working electrode).

Reference electrode

This is the electrode with a constant and known potential throughout the experiment. Its potential is taken as a reference against which the potential of another electrode is measured. This electrode is mostly given the distance of the electrodes in the electrochemical cell. The commonly used reference electrode for aqueous solution are saturated standard calomel electrode (sat'd SCE, (sat'd $\text{Hg}_2\text{Cl}_2/\text{Hg}$)), saturated silver/silver chloride (Ag/AgCl (sat'd, $\text{KCl}(3\text{M})$) [12]. The most commonly used reference electrode system composed of silver immersed in potassium chloride solution Ag/AgCl (sat'd), KCl (xM), where normally concentration (x = 3-5 M) ranges. Among these reference electrodes, Ag/AgCl reference electrode has an advantage that they can be used in temperature greater than 60°C , with fewer chances to contaminate the analyte solution (and is used in the electrochemical cell in this research).

Counter/ Auxiliary electrode

The counter electrode in many voltammetric methods, the analytic reaction at the electrode surface occurs a very short period and rarely produces any appreciable changes in bulk concentration species, thus isolation of CE from the sample. In the electrochemical cell, (CE) acts as sink for electron so that the current can be passed from the external circuit through the cell. CE can be any convenient metal electrode because its electrochemical properties do not affect the behavior of the electrode under the study. In a most electrochemical cell, CE consists of metallic foil or wire of platinum although gold and carbonaceous electrodes may also be used [13].

Voltammetry

Voltammetry as a branch of electrochemistry established from the discovery of polarography in the 1920s by a chemist from Czechoslovakian, Jaroslav Heyrovsky. Voltammetric technique

based experimental evaluation works on the effect that current (i) flowing through the system is a function of potential applied (E_{app}) across the electrode. The common characteristic of all voltammetric techniques is that they involve the application of an (E) to an electrode and the monitoring of the resulting current (i) flowing through the electrochemical cell. In many cases the applied potential is varied or the current is monitored over a period of time (t). All voltammetry techniques parameters can be described as some function of applied potential (E_{app}), current (i) response, and time (t). They are considered active techniques (as opposed to passive techniques such as potentiometry) because the E_{app} forces a change in the concentration of an electroactive species at the electrode surface by electrochemically reducing or oxidizing it. Voltammetry is one of those basic experimental methods that measure the kinetics of the electrode process, such as current density as a function of time, while the potential is varied [14].

3.6.2 Cyclic voltammetry

Cyclic voltammetry (CV) is the most studied and widely used voltammetric techniques in modern electrochemistry for obtaining quantitative information about electrochemical reactions. It intensively measures the kinetics of electrode process: Current density as a function of time, I_p (t) which is measured as a function of time-varying potential $E_p(t)$ [15][16]. The potential (E_p) is applied between two limits (V_1 and V_2), by scanning from initial point (V_1) to final (V_2) point and back to (V_1) at constant speed $v = \frac{dE}{dt}$ during the experiment [16]. The importance of CV results begins with its ability to rapidly provide considerable information on the thermodynamic of the redox process and the kinetics in electrode-electrolyte (heterogeneous) electron transfer and on coupled chemical reactions and adsorption process [16].

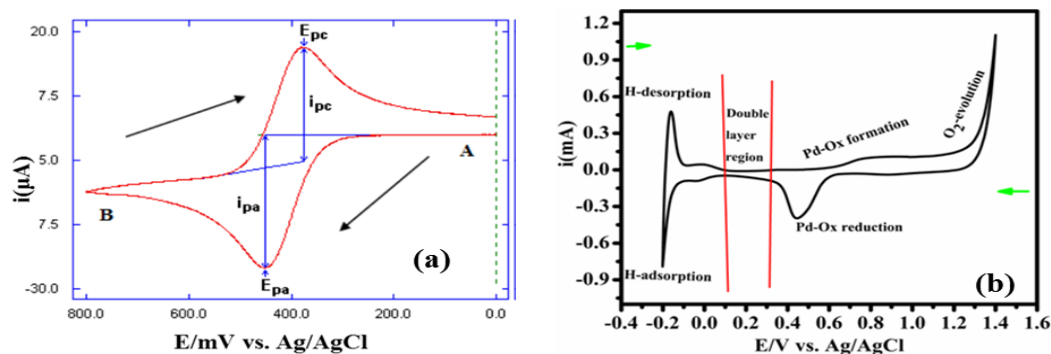


Figure 3.4: A classical CV showing a current vs. potential and important anodic and cathodic parameters (a) and typical CV curve of Pd in a N_2 saturated 0.1M HClO_4 electrolyte, showing the important regions during an anodic and cathodic scan at 25°C .

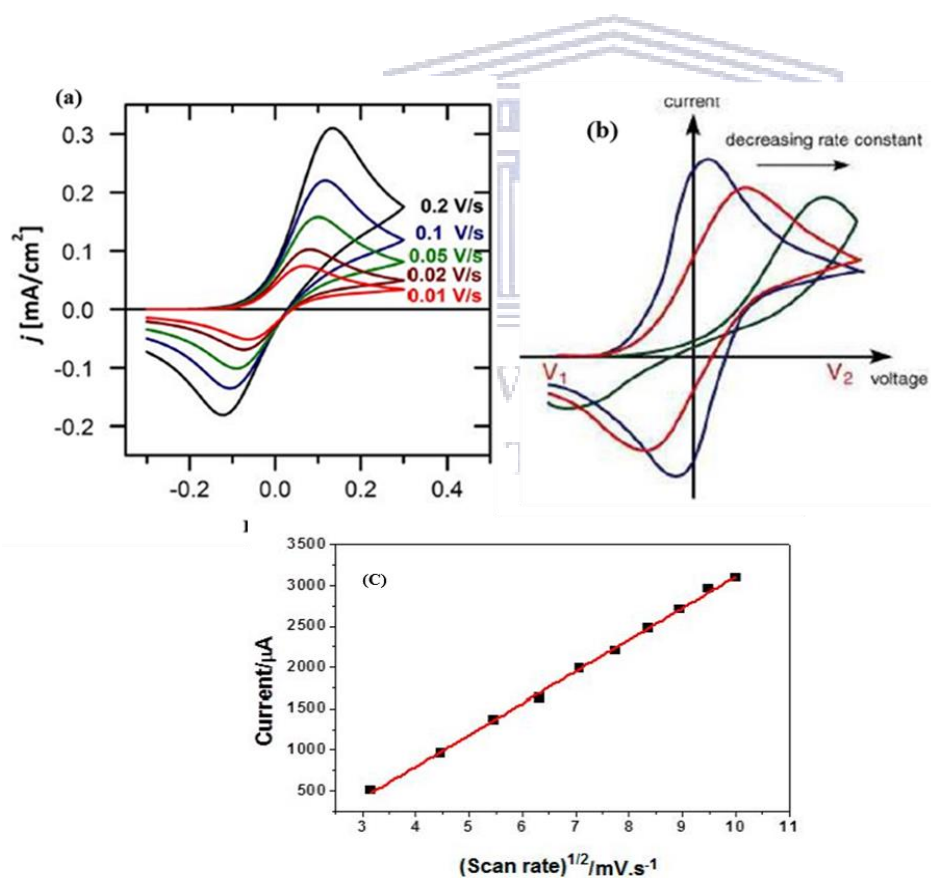


Figure 3.5: CV curves representing reversible (a) system and irreversible system (b) at various scan rates and Randles-Sevcik plot of peak current (i_p) versus square root of the scan rate ($v^{1/2}$) [15], [17].

The techniques are usually performed using the three-electrode configuration system whereby the potential relative to the reference electrode is scanned at the working electrode while the produced current is flowing through the counter electrode or auxiliary electrode is monitored in a stationary solution. When the peak current is plotted against the square root of the scan rate, with I_p as the y-axis and $v^{1/2}$ as the x-axis, often called a Randles-Sevcik plot, a straight line is obtained that passes through the origin and the slope of the linear plot can be used to determine the concentration of the analyte (C_0) if the diffusion coefficient D is known.

3.6.3 Reversible systems

The peak current response for a reversible system is given by the following equation (**Equation (3.1)**), known as Randles-Sevcik equation.

According to the Randles-Sevcik equation, in a reversible reaction, the concentration is related to the peak current response and can be calculated at 25 °C utilizing the following equation;

$$I_p = 2.69 \times 10^5 n^3 A D^{1/2} v^{1/2} C \quad (3.1)$$

Where I_p is the peak current response in (Amperes, A), n is the number of electrons transferred in the electrochemical reaction, D is the diffusion coefficient (cm^2/s), A is the active electrode area.

In cyclic voltammetry, the reversible system obeys some specific rules of criteria such as proportionality between peak current and concentration, and scan rate. These rules are elaborated as follows;

- The peak potential E_{pa} , E_{pc} is independent of the scan rate, meaning to remain constant with a position as scan rate increases or changes.

- The ratio of cathodic current (I_{pc}) passed during the reduction and anodic (I_{pa}) passed during the oxidation, is almost equal ($I_{pa} = I_{pc}$) or near unity ($\frac{I_{p,c}}{I_{p,a}} = 1$).
- The formal potential (E°) should be positioned half distance between E_{pa} and E_{pc} so that $E^\circ = \frac{E_{pa} + E_{pc}}{2}$. Peak current response is directly proportional to the root of the scan rate ($v^{1/2}$).
- The separation between the peaks potential E_{pa} , E_{pc} is equal to 59 mV/n for the n-electron couple at 25 °C or $|E_{pa} - E_{pc}|$ would be 59 mV for 1 electron process and 30 mV for the two-electron process.

3.6.4 Quasi irreversible and irreversible systems

For irreversible system, individual oxidation and reduction peaks are reduced in size and separated widely. Irreversible systems are characterized by a shift of peak potential with the scan rate:

$$I_p = (2.99 \times 10^5) n (\alpha n_a)^{1/2} A C_0 D^{1/2} v^{1/2} \quad (3.3)$$

The most vital characteristic of a cyclic voltammogram of an irreversible system is the total absence of a reverse peak. For totally irreversible systems, the peak potential shifts with the scan rate. In addition, the individual peaks are reduced in size and widely separated as shown in

Figure 3.5 (b). Irreversible systems are characterized by a shift of the peak potential with the scan rate:

$$E_p = E^\circ - \frac{RT}{\alpha n_a F} \left[0.78 - \ln \left(\frac{K^0}{D^2} \right) + \ln \ln \left(\frac{\alpha n_a F v}{RT} \right) \right] \quad (3.4)$$

Where K^0 is the heterogeneous rate constant and α is the transfer coefficient and n_a is the number of electrons involved in the charge-transfer step. Thus, E_p occurs at higher potentials than E° , with the over-potential related to K^0 and α . In a case where E_p is independent of K^0 , the shift of

the peak potential could be compensated by an appropriate change of the scan rate. The peak potential and the half-peak potential (at 25 °C) will differ by 48/ αn mV. Therefore, when αn decreases, the voltammogram could become more drawn out. Equation 3.9 also allows for the calculation of the heterogeneous rate constant, K^0 , if the values of E^0 and D are known.

Nicholson and Shain's equation is commonly used to analyze irreversible and quasi irreversible systems. According to Nicholson and Shain equation, the peak current can be expressed as;

$$I_p = (2.69 \times 10^6) \alpha n^{1/2} A C D^{1/2} \nu^{1/2} \quad (3.5)$$

Where I_p is a peak current (in ampere, A), ν is the rate at which potential is scanned (scan rate in Vs^{-1}), A is the area of the electrode, D is the diffusion coefficient in (cm^2s^{-1}) of the electroactive reactant species during appropriated voltammetric scan, n is the electron stoichiometry, C is the concentration in $mol\ cm^{-3}$ of the reactant species in the bulk electrolyte, α is the charge transfer coefficient. For a quasi-irreversible system, the current is controlled by mass transfer.

3.7.1 Chronoamperometry (CA)

Chronoamperometry (CA) is one of the electrochemical methods in which a step potential is applied and the current, (A) is measured as a function of time, $t(s)$ [12]. CA can, therefore, be employed to measure current time dependence for the diffusion-controlled process occurring at an electrode [18]. The current (i)-time(s) response consists of two components (i) the current of charging the double-layer and the other (ii) ascribed to the electron transfer reaction with the electrode/electroactive species. These electroanalytical techniques possess a few advantages over CV, such as determining diffusion coefficient, kinetics, and mechanisms in one single experiment.

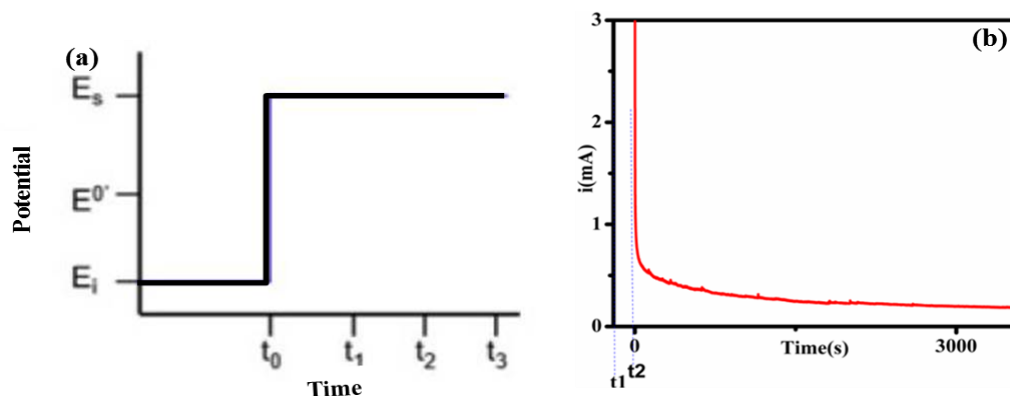


Figure 3.6: An example of chronoamperometric response as results of waveform perturbation (a) Typical experimental results of chronoamperometry of Pd in 0.5 M KOH + 0.1 M EtOH at the applied biased potential of -0.2V for 3600S (1hr) duration, in which species is electroactive at \$t_2\$ but reduced at the diffusion-controlled rate at \$t_2\$.

The current response drops over a period of time, due to the diffusion barrier of the electrode surface.

The surface is, rate constant and diffusion thickness can be measured with CA, using the Cottrell equation for the diffusion limiting current as explained in literature [18], [19].

$$i_t = \frac{nFA C_0 D_0^{1/2}}{\pi^{1/2} t^{1/2}} \quad (3.6)$$

According to the relationship between current and potential, the Cottrell equation can calculate the diffusion coefficient and bulk concentration.

Where \$i_t = n\$ is the number of electron transferred in the electrochemical reactions, \$F\$ = Faraday constant (96,485 C/equivalent), \$A\$ is an active electrode area (cm²), \$C_0\$ is the initial bulk concentration (mol.cm⁻³) of oxygen in the electrolyte, \$D\$ is the diffusion coefficient (cm² .s⁻¹), \$t\$ is the time in seconds (s) [18].

3.7.2 Electrochemical impedance spectroscopy (EIS)

The electrochemical impedance spectroscopy (EIS) is an inexpensive, fast and invasive technique for measurement in bio-sensor, corrosion, battery, and fuel cell development, and physical characterization. In energy materials, it provides mechanistic and kinetic information widely in batteries, fuel cells, and corrosion inhibitors. EIS is based on the measurement of current in response to an applied potential perturbation in a form of sine wave [20] and is displayed in **Figure 3.5**. ESI is also used for the evaluation of electron transfer properties of the modified surface and understanding of chemical transformation [21]. Theoretical, impedance measurements can be used to inspect any intrinsic properties of nanomaterials such as nanoparticle's and nano film's solution interface. The measure of current is linearly proportional to the applied potential as shown in **Equation 3.7**:

$$V(f) = I(f) \times Z(f) \quad (3.7)$$

Which is ohm law ($V = IR$) with fundamental differences, such as (i) in place of an alternating resistance R , the impedance Z is used, (ii) when an alternating potential is applied, the value of impedance depends on the frequency at which potential oscillate. EIS employs the alternating current (AC) instead of direct current (DC) to induce electrochemical reactions on an electrode-electrolyte interface. It measures the impedance between the current and potential at the fixed DC potential during the frequency (f) scan with a constant applied superimposed AC signal of small amplitude. EIS data mostly obtained by analyzing through fitting it to a Randles equivalent circuit, each physical process in the electrochemical cell, for example, electrolyte resistance and polarization resistance, has characteristic impedance behavior and can be considered as an electric component or a simple electrical circuit. The obtained data from EIS is represented using the Bode plot (**Figure 3.9**) and the Nyquist plot (**Figure 3.8**). The Bode is the representative plot of frequency, as x-axis against the logarithm of real impedance as y^1 -axis, and phase angle y^2 -

axis [22]. Its plot is a plot log magnitude of impedance and phase angle versus the log of frequency [23] [24].

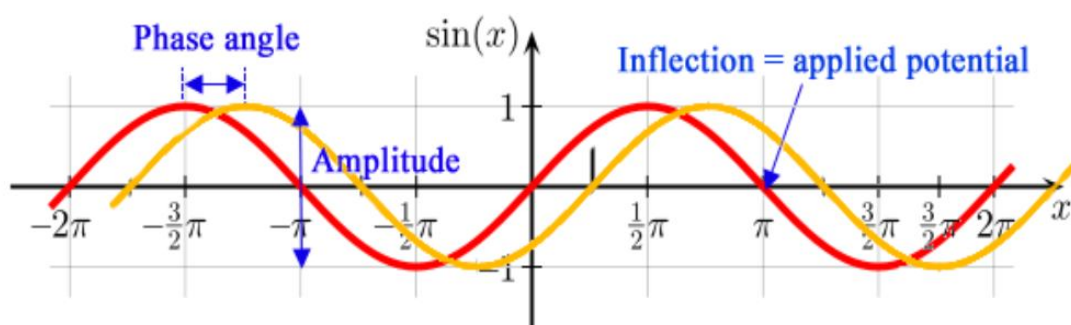


Figure 3.7: Illustration of the amplitude of the sinusoidal potential, and the sinusoidal of the current resulting from the application of the potential. The phase difference (phase angle) between potential and current is highlighted [20].

The four specialized elements used for EIS includes ohmic resistance (solution resistance, R_s), capacitance or inductance (cd or R_{ct}), constant phase element (CPE and Warburg (W)

The total impedance from the Nyquist plot is plotted as a function of frequency and is expressed with real frequency (x-axis) imaginary frequency (y-axis) as the following Equation;

$$Z'(j\omega) = \frac{E(j\omega)}{I(j\omega)} = Z''(\omega) + jZ'(\omega) \quad (3.8)$$

Where $Z'(\omega)$ and $Z''(\omega)$ are real and imaginary terms respectively.

The capacitor as denoted as (C) is an ability of an electrochemical system to retain or store the charge.

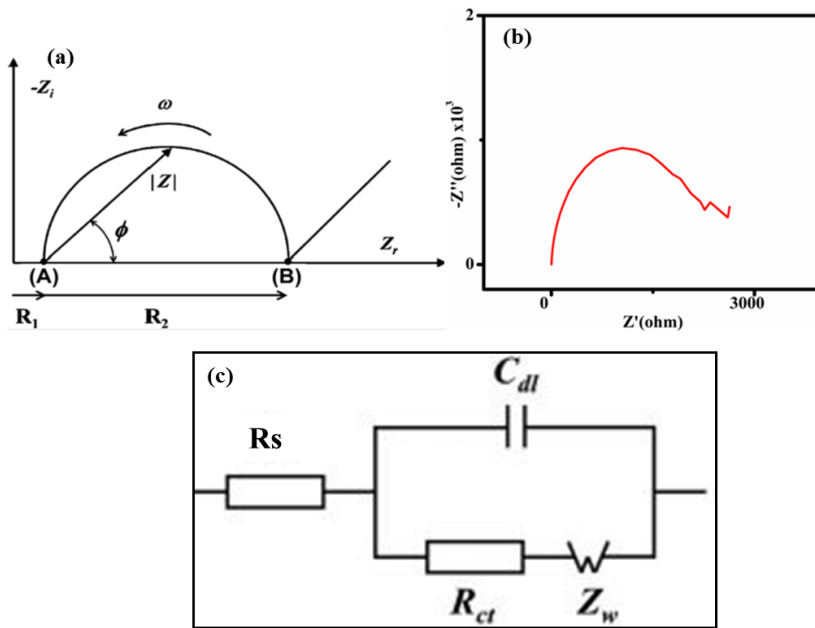


Figure 3.8: Typical example of Nyquist plot (a), of PdIr in 0.5 M KOH + 0.1 M EtOH at 10^{-10} to 10^4 Hz range at applied potential -0.2V and classical equivalent circuit (c).

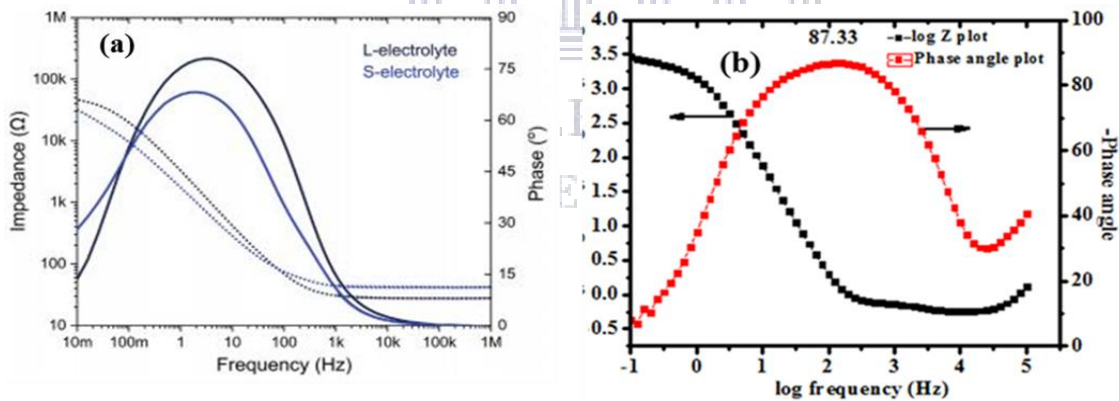


Figure 3.9: Typical representation of Bode plot (a) [25] and Bode plot of Pd in 0.5 M KOH + 0.1 M EtOH at 10^{-10} to 10^4 Hz range at applied potential -0.2V (b).

The phase angle gives direct information about the frequency. The maximum phase angle as a function of frequency is used to calculate the double-layer capacitance is expressed in the following equation;

$$\omega_{\theta\max} = \left(\frac{1 + \frac{R_{ct}}{R_{sol}}}{R_{ct}D_{cl}} \right) \quad (3.9)$$

The analysis of both Bode and Nyquist plot is highly recommended to conclusively study the electrochemical process at the electrode-electrolyte interface.

3.7.3 Equivalent or electric circuit elements

In general, electric circuit elements can be considered as simple impedance to a sinusoidal perturbation. The impedance is mostly containing several time constants but often only a portion of one or more of their semi-circle appears. The total impedance composed of contributions of the solution electrolyte, the electrode-solution interface and the electrochemical reactions proceeding on the working electrode surface.

In order to represent any electrochemical cell with an equivalent circuit that consists of resistance and capacitance and also considers at least these following corresponding terms: the resistance of the electrolyte solution (R_s), the electrochemical double-layer, expressible as double-layer capacitance (C_{dl}); and the impedance of the faradaic charge-transfer process of Warburg. The specific contributions to the resistance are solution resistance (R_s), the charge transfer resistance (R_{ct}), Warburg while contributions to capacitance are constant phase element (CPE), and capacitor (C).

For the equivalent circuit, in general, R_s is simply the Ohmic resistance of the electrolyte solution given as;

$$R_s = \rho \frac{l}{A} \quad (3.10)$$

Where ρ is an electrical conductivity/ resistivity of the solution and A is a bound area and l length carrying a uniform current. While the Rct can be expressed as;

$$R_{ct} = \frac{RT}{nFI_0} \quad (3.11)$$

Where I_0 is an exchange current density, n is a number of electrons transferred and F = Faraday constant = 98,487 C/mol⁻¹. Warburg is only characterized as linear proportion at an angle of 45° and a slope of -0.5 in the Bode plot and 1 in Nyquist plot. The resistance in Warburg is associated with the diffusion of ions across the electrode/electrolyte interface. This impedance is associated with the difficulty of mass transport of electroactive species. The capacitor as denoted as (C) in the equivalent circuit, represents the ability of the electrochemical system to retain or store charge. A capacitor has no real part of the impedance, so the Nyquist plot of the real capacitor would be just a straight line on y or Z-axis with no semi-circle formed, while the Bode plot would have a slope -1 with phase angle -90, and it can be expressed as Equation follow;

$$Z_{(o)} = Z'' = \frac{1}{j\omega C} \text{ or in the logarithm form of } \log Z = -\log_{j\omega C} \quad (3.12)$$

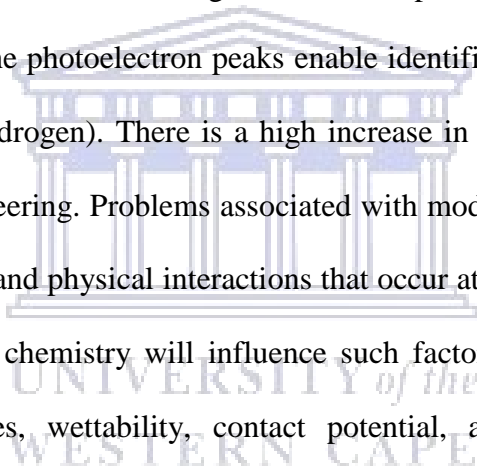
Where Z is the imaginary value, Z' is Z real impedance, C is a capacitance and ω is the frequency. Among the equivalent circuit elements, there is a constant phase element which is a non-intuitive equivalent circuit element that was invented while investigating or looking at the response of the real-world system.

3.8.0 Physical characterization

Spectroscopic techniques

3.8.1 X-ray photoelectron spectroscopy (XPS)

X-ray photoelectron spectroscopy (XPS) is a technique that analyzes the surface chemistry of a material. This technique gives information (measure) the elemental composition, empirical formula, chemical state and electron state of elements within the material of study. The wavelength of rays is about 1\AA , has an energy range of about 12-15 keV. The interaction of the ray radiation with the sample can provide a high-resolution structure and compositional information on the atomic scale. XPS spectra are acquired by irradiating a solid surface with a beam of X-rays and in parallel measuring the kinetic energy and electrons that are emitted from the top 1 - 10 nm of the material being analyzed. A photoelectron spectrum is acquired by counting ejected electrons over a wide range of electron kinetic energies, **Figure 3.10**. Peaks are observed in the spectrum from atoms emitting electrons of a particular characteristic energy. The energies and intensities of the photoelectron peaks enable identification and quantification of all surface elements (except hydrogen). There is a high increase in material performance as is the importance of surface engineering. Problems associated with modern materials can be solved by understanding the chemical and physical interactions that occur at the surface or the interfaces of a material's layers. Surface chemistry will influence such factors as corrosion rates, catalytic activity, adhesive properties, wettability, contact potential, and failure mechanisms. The material's surface is the point of interaction with the external environment and other materials. Therefore, surface modification can be used in a wide variety of applications to alter or improve the performance and behavior of a material. XPS can be used to analyze the surface chemistry of material after an applied treatment such as fracturing, cutting or scraping. From non-stick cookware coatings to thin-film electronics and bio-active surfaces, XPS is the standard tool for surface material characterization.



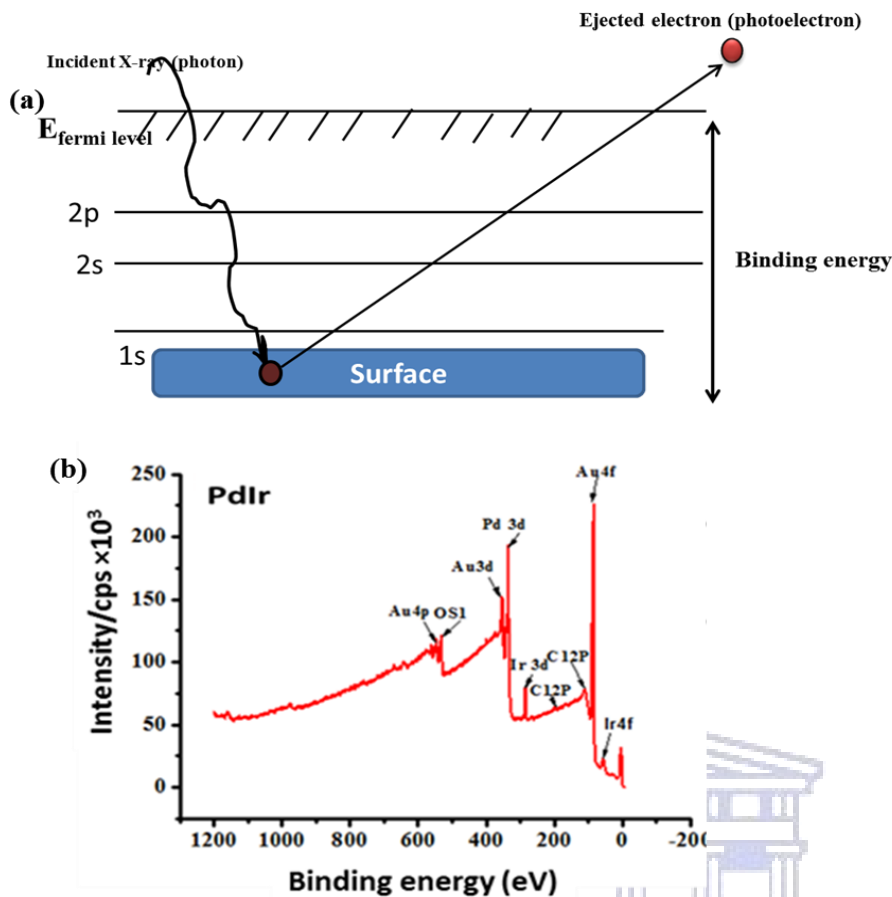


Figure 3.10: Schematic diagram of typical XPS (a) and photoelectron line of PdIr/Au scan survey (b).

3.8.2 X-ray diffraction (XRD)

X-ray diffraction (XRD) is electromagnetic (monochromatic) radiations with a wavelength ranging from 10^{-2} to 10 nm and photon energy between 100 eV- 1000 keV. It is known to be invented by W.H Bragg, Sir and W. L Braggs, the son to delineate why the cleavage faces of crystal appear to reflect X-ray beams at a certain incident angle (theta, 2θ). Diffraction of rays is produced when incoming (incident) rays are in contact with a sample and producing constructive interference which provides Bragg law. Bragg's law denotes the relationship between the wavelength (λ) of the rays and the sample diffraction angle. The Bragg's law can be expressed as following equation (20), XRD spectroscopy is a flexible non-destructive technique that reveals detailed information about the chemical composition and crystallographic structure of natural

and synthetic compounds. A crystalline lattice is a regular three-dimensional distribution (cubic, rhombic) of atoms in space. The atoms are arranged in such a manner that they form a series of parallel planes separated from one another by a distance (d), which varies according to the nature of the material. When a monochromatic x-ray beam with a wavelength λ is projected onto a crystalline material at an angle θ , diffraction occurs only when the distance traveled by the rays reflected from successive planes differs by a complete number of wavelengths as shown in **Equation 3.13**.

$$n\lambda = 2d\sin \theta \quad (3.13)$$

By varying the angle θ , the Bragg's law conditions are satisfied by different d-spacing in polycrystalline materials. Plotting the angular positions and intensities of the resultant diffracted peaks of radiation produces a pattern, which is a representative of the sample where a mixture of different phases is present. The incorporation of an individual pattern then brings about a diffractogram. Now based on the principle of X-ray diffraction, a wealth of structural, physical and chemical information about the material being investigated can, therefore, be acquired. The following Scherer equation given below can be used quantitatively for the determination of average particle size as mentioned above, using;

$$D = \frac{0.9\lambda}{\beta \cos \theta} \quad (3.14)$$

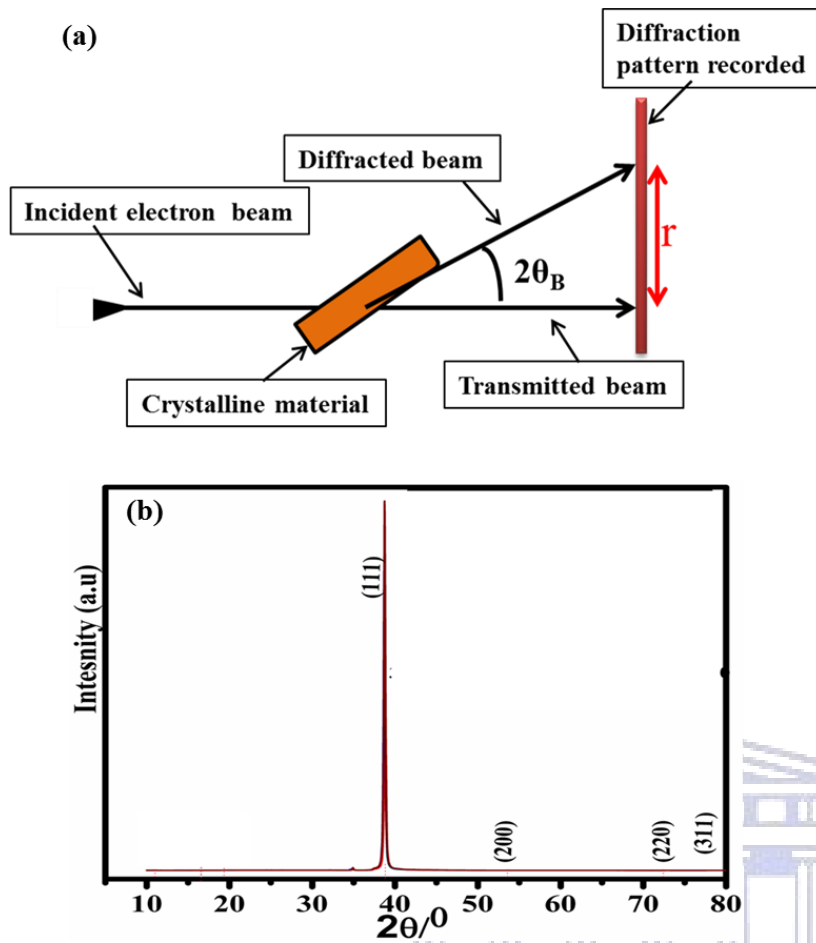
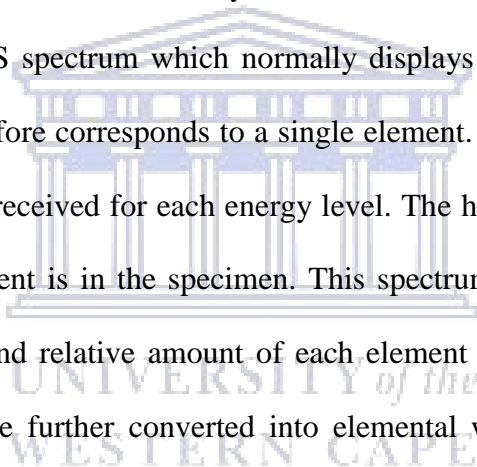


Figure 3.11: Schematic diagram of the XRD pattern (a) and spectra of typical single-crystalline Au.

3.8.3 Energy dispersion spectroscopy (EDS)

Energy Dispersive X-ray spectroscopy (EDS) analysis is sometimes referred to also as Energy-dispersive X-ray spectroscopy analysis (EDX) is a technique that is mostly used for qualitative analysis and also providing semi-quantitative results. EDS is a technique that is based on the collection and energy dispersion of characteristic X-rays. It is a technique used for identifying the elemental composition of the specimen, or an area of study. The EDS is equipped with a typical SEM to allow an elemental or chemical analysis of a sample, otherwise, it cannot operate on its own without SEM [26], [27]. During EDX Analysis, the specimen is bombarded with an

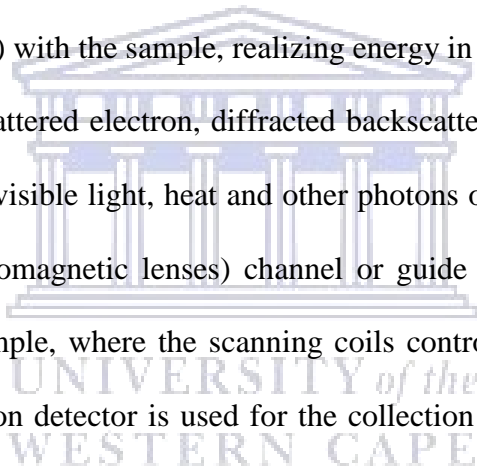
electron beam inside the scanning electron microscope. When atoms of any material are being ionized by high radiation, they emit the X-ray electron must give up some of its energy by emitting an X-ray. The bombarding electrons collide with the specimen atoms' electrons, knocking some of them off in the process. A position vacated by an ejected inner shell electron is eventually occupied by a higher-energy electron from an outer shell. The amount of energy released by the transferring electron depends on which shell it is transferring from, as well as which shell it is transferring to. Furthermore, the atom of every element releases X-rays with unique amounts of energy during the transferring process. Thus, by measuring the amounts of energy present in the X-rays being released by a specimen during electron beam bombardment, the identity of the atom from which the X-ray was emitted can be established. The output of EDS analysis is, in the EDS spectrum which normally displays peaks. Each of these peaks is unique to an atom and therefore corresponds to a single element. The EDS spectrum is a plot of how frequently an X-ray is received for each energy level. The higher a peak in a spectrum, the more concentrated the element is in the specimen. This spectrum consists of a series of peaks representative of the type and relative amount of each element in the sample. The number of counts in each peak may be further converted into elemental weight concentration either by comparison with standards or by standardless calculation. Accuracy is nominally in the range of 4-5 % and detection limits are 100-200 ppm for isolated elements with atomic number greater than 11, 1-2% wt. for low atomic number elements and overlapped peaks. An EDX spectrum plot not only identifies the element corresponding to each of its peaks but the type of X-ray to which it corresponds as well. For example, a peak corresponding to the amount of energy possessed by X-rays emitted by an electron in the L-shell going down to the K-shell is identified as a K-alpha peak. The peak corresponding to X-rays emitted by M-shell electrons going to the K-shell is identified as a K-Beta peak.



3.9.0 Microscopic techniques

3.9.1 Scanning electron microscope (SEM)

A scanning electron microscope is the most popular and classical technique for obtaining information in detail about the physical nature and surface of the sample. This technique uses a high energy beam of the electron that contact and interacts with the sample of analysis [26]. The operation of the SEM is under vacuum (10^{-6} torr), varied electric field, it needs a cooling system and constant power supply. The source of a high energy beam of the electron is a gun and the sample is placed on a mobile stage. This shower of electron formed through the field emission or thermionic emission mechanism in the gun [26], [27]. These electrons (primary) deaccelerate when they collide (in-elastic) with the sample, realizing energy in various types of signal, such as secondary electrons, backscattered electron, diffracted backscattered electrons, Auger electrons, X-ray fluorescence photon, visible light, heat and other photons of different energies [26]. A set of focusing magnets (electromagnetic lenses) channel or guide the high beam of electrons to raster the surface of the sample, where the scanning coils control the spot size of the electron beam. The secondary electron detector is used for the collection of electrons and be utilized in image formation. The topography image and morphology with differentiable contrast is produced through the secondary and backscattered electron which was formed during the inelastic collision between electrons and nucleus of the sample. X-ray signals are also produced and used for elemental composition and phase identification of materials on the surface of atoms [27].



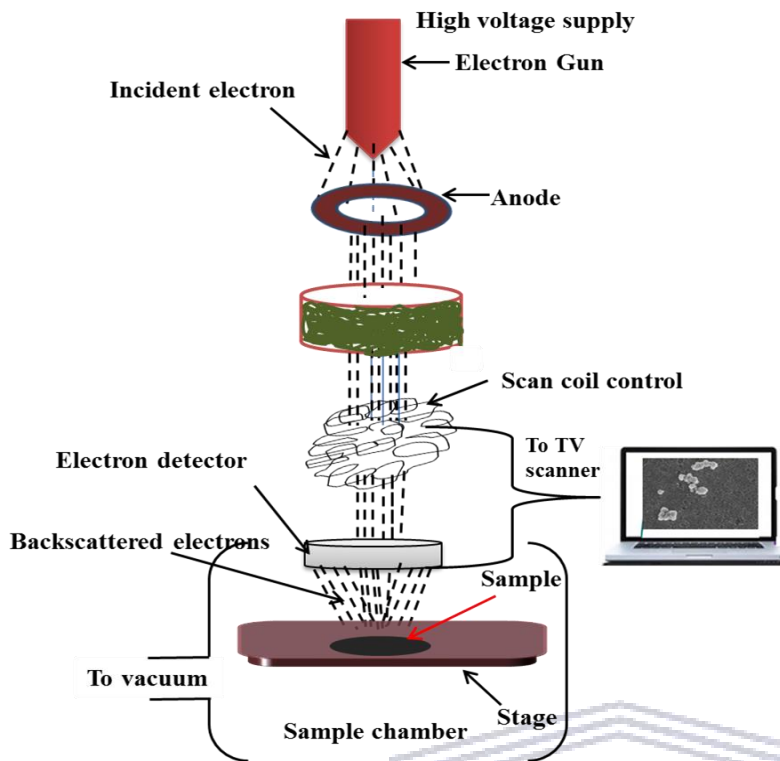


Figure 3.12: Schematic of a typical scanning electron microscope (SEM).

3.9.2 Atomic force microscopy (AFM)

The Atomic Force Microscope is an instrument that can analyze and characterize samples at the microscope level from 100nm to $<1\mu\text{m}$. Since the AFM was invented by Gerd Binnig in 1986, the technique played a crucial role in the nano-scale level [28], [29]. The techniques have been utilized in several research disciplines including chemistry, engineering, and biology to name the few. This microscopic technique is basically used for imaging surface topography using attractive and repulsive interaction forces between a few atoms attached at the tip of the cantilever and sample surface [28], [30]. In AFM cantilever is being used as a probe to measure the force or potential energy between the tip (about 100 \AA) and sample, and was made of gold foil attached diamond tip to it in the first experiment. Recently cantilever is made of silicon (Si), silica (SiO_2) and silicon nitride (Si_3N_4) with 100-200 μm long and 1 μm thick [30] by using the micro matching technique. The cantilever systems are operated in three various loop modes as illustrated in **Figure 3.13 (b)**, including (i) Non-contact mode, (ii) static or contact mode and (iii)

tapping mode [29], [31]. The static or contact mode, which is the one used in this research, acquires sample attributes by monitoring interaction forces while the cantilever tip remains in contact with the target specimen, at the repulsive forces. While the non-contact mode is based to probe electric, magnetic or atomic force by moving cantilever slightly away from the specimen surface and oscillating the cantilever at or close natural resonance, at the attracting forces [30], [32]. Alternatively, the tapping mode working principle collection of the qualities of both contact and no-contact mode such as the presence of attracting and repulsive forces or ionic forces by collecting sample data and oscillating cantilever tip at or close to its natural resonance frequency while allowing cantilever tip to impact the target sample for a short time.

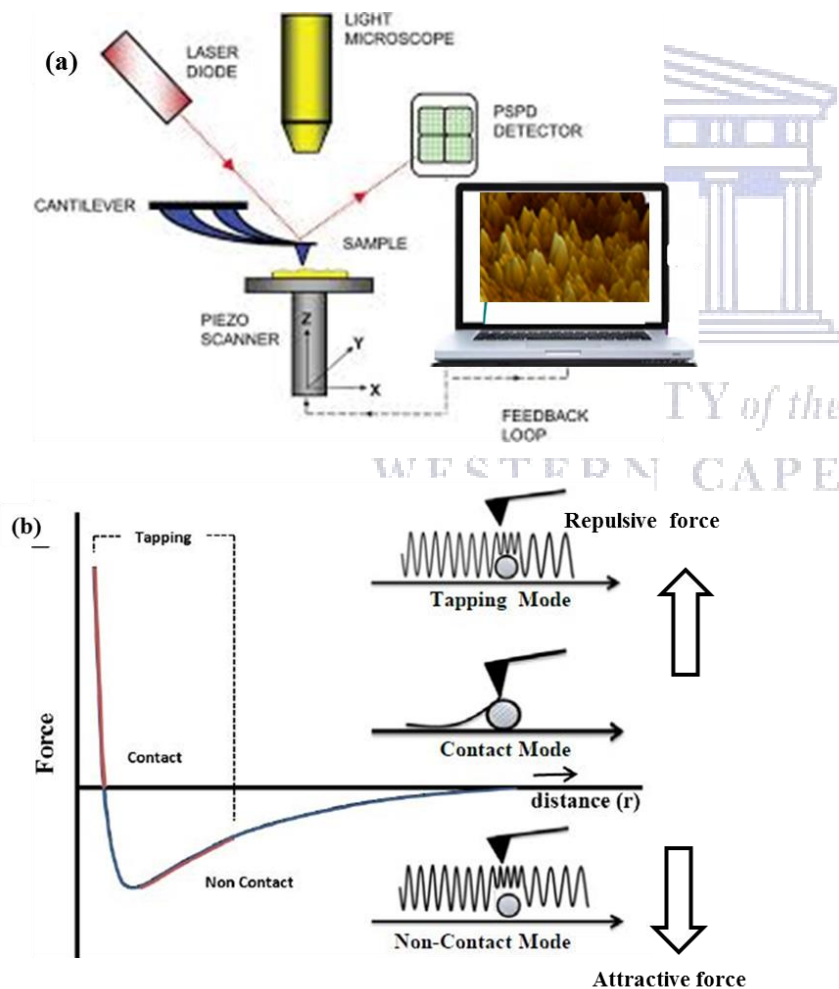
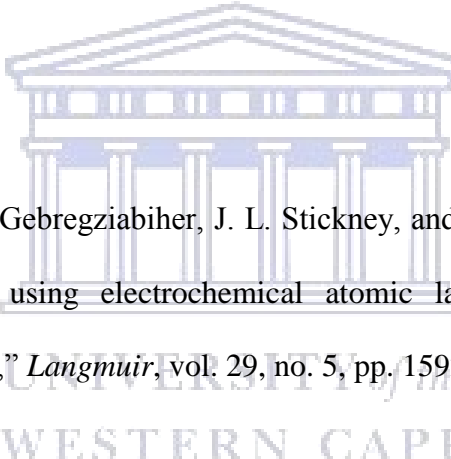


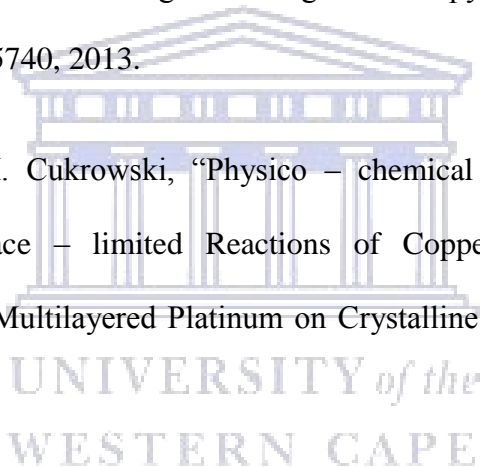
Figure 3.13: Schematic diagram of the AFM system (a), tip-sample separation curve, demonstrating the main interactions during AFM scanning.

The sharp tip is attached at the end of the cantilever and is used to scan the specimen surface [28], the sample position or held on a piezoelectric micropositioner which moves either z- (vertical) direction or x-y-(laterally) direction. The interaction between the sample surface and the probe tip may be van der Waals or of a short-range chemical, magnetic or electrostatic [32]. The working principle is as; during the AFM's cantilever tip scanning some forces either attract or repel the tip. The image resulted in a topographical representation of the sample being imaged. AFM provides more deposits as compared to the microscopic techniques. Notably, in contrast to SEM, it possesses many advantages such the height measurement, and unobstructed surface feature.

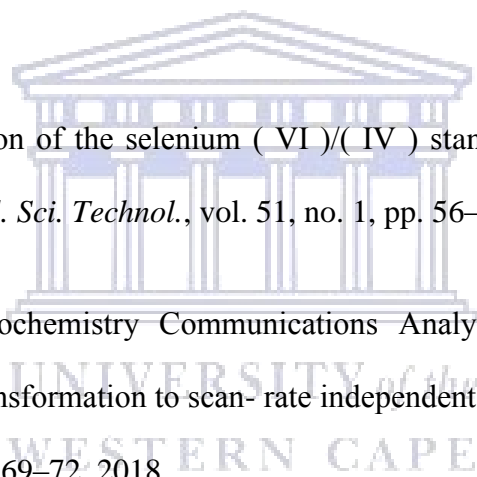
References

- 
- [1] L. B. Sheridan, D. K. Gebregziabiher, J. L. Stickney, and D. B. Robinson, "Formation of palladium nanofilms using electrochemical atomic layer deposition (E-ALD) with chloride complexation," *Langmuir*, vol. 29, no. 5, pp. 1592–1600, 2013.
- [2] T. S. Mkwizu and I. Cukrowski, "Physico-chemical modelling of adlayer phase formation via surface-limited reactions of copper in relation to sequential electrodeposition of multilayered platinum on crystalline gold," *Electrochim. Acta*, vol. 147, pp. 432–441, 2014.
- [3] L. B. Sheridan, D. K. Gebregziabiher, J. L. Stickney, and D. B. Robinson, "Formation of Palladium Nano films Using Electrochemical Atomic Layer Deposition (E-ALD) with Chloride Complexation," *Langmuir*, vol. 29, pp. 1592–1600, 2013.
- [4] A. C. Mkhohlakali, X. Fuku, R. M. Modibedi, L. E. Khotseng, S. C. Ray, and M. K. Mathe, "Electrosynthesis and characterization of PdIr using electrochemical atomic layer

- deposition for ethanol oxidation in alkaline electrolyte,” *Appl. Surf. Sci.*, vol. 502, no. August 2019, pp. 144–158, 2019.
- [5] S. Henning, J. Herranz, and H. A. Gasteiger, “Bulk-Palladium and Palladium-on-Gold Electrocatalysts for the Oxidation of Hydrogen in Alkaline Electrolyte,” *J. Electrochem. Soc.*, vol. 162, no. 1, pp. F178–F189, 2014.
- [6] L. B. Sheridan, Y. Kim, B. R. Perdue, K. Jagannathan, J. L. Stickney, and D. B. Robinson, “Hydrogen Adsorption, Absorption, and Desorption at Palladium Nanofilms formed on Au(111) by Electrochemical Atomic Layer Deposition (E-ALD): Studies using Voltammetry and In Situ Scanning Tunneling Microscopy,” *J. Phys. Chem. C*, vol. 117, no. 11, pp. 15728–15740, 2013.
- [7] T. S. Mkwizu and I. Cukrowski, “Physico – chemical Modelling of Adlayer Phase Formation via Surface – limited Reactions of Copper in Relation to Sequential Electrodeposition of Multilayered Platinum on Crystalline Gold,” *Electr. Acta*, vol. 147, pp. 432–441, 2014.
- [8] V. Venkatasamy, N. Jayaraju, S. M. Cox, C. Thambidurai, M. Mathe, and J. L. Stickney, “Deposition of HgTe by electrochemical atomic layer epitaxy (EC-ALE),” *J. Electroanal. Chem.*, vol. 589, pp. 195–202, 2006.
- [9] L. B. Sheridan, J. Czerwiniski, N. Jayaraju, D. K. Gebregziabher, J. L. Stickney, D. B. Robinson, and M. P. Soriaga, “Electrochemical Atomic Layer Deposition (E-ALD) of Palladium Nanofilms by Surface Limited Redox Replacement (SLRR), with EDTA Complexation,” *Electrocatalysis*, vol. 3, no. 2, pp. 96–107, 2012.

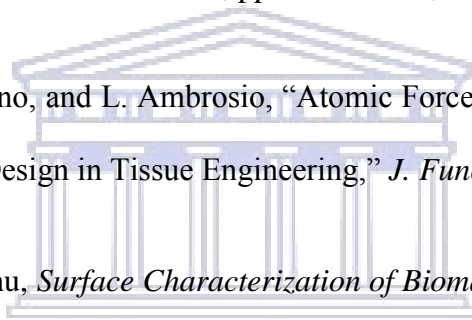


- [10] D. Banga, B. Perdue, and J. Stickney, "Formation of $\text{CuIn} (1-x) \text{Ga} x \text{Se}_2$ (CIGS) by Electrochemical Atomic Layer Deposition (ALD)," vol. 161, no. 4, pp. 141–146, 2014.
- [11] D. Banga, B. Perdue, and J. Stickney, "A Electrodeposition of a $\text{PbTe} / \text{CdTe}$ superlattice by electrochemical atomic layer deposition (E-ALD)," *J. Electroanalytical Chem.*, vol. 716, pp. 129–135, 2014.
- [12] A. J. Bard, L. R. Faulkner, and Swain, *Electrochemical Methods: Fundamentals and Application*. 2001.
- [13] S. P. Kounaves, "Voltammetric Techniques," *Handb. Instrum. Tech. Anal. Chem.*, pp. 709–726.
- [14] R. Doi, "Determination of the selenium (VI)/(IV) standard redox potential by cyclic voltammetry," *J. Nucl. Sci. Technol.*, vol. 51, no. 1, pp. 56–63, 2017.
- [15] T. Pajkossy, "Electrochemistry Communications Analysis of quasi-reversible cyclic voltammograms : Transformation to scan- rate independent form," *Electrochem. commun.*, vol. 90, no. April, pp. 69–72, 2018.
- [16] S. Vesztergom, "Electrochimica Acta Analysis of voltammograms of quasi-reversible redox systems : Transformation to potential program invariant form," *Electrochim. Acta*, vol. 297, pp. 1121–1129, 2019.
- [17] M. Masikini, S. N. Mailu, A. Tsegaye, N. Njomo, K. M. Molapo, C. O. Ikpo, C. E. Sunday, C. Rassie, L. Wilson, P. G. L. Baker, and E. I. Iwuoha, "A Fumonisin Immunosenor Based on Polyanilino-Carbon Nanotubes Doped with Palladium Telluride Quantum Dots," *Sensrs*, vol. 15, pp. 529–546, 2015.



- [18] V. Ag and L. Box, "Chronoamperometric Investigations of the Electrode – Electrolyte Interface of a Commercial High Temperature PEM FuelCell," *Fuel Cells*, vol. 6, no. 6, pp. 983–992, 2010.
- [19] B. Rezaei, *Chapter 2 - Electrochemical detection techniques in biosensor applications*. 2019, pp. 11–43.
- [20] L. Bardini, "an introduction to electrochemical spectroscopy.," no. July 2015, 2018.
- [21] F. Hernandez and H. Baltruschat, "Electrochemical Characterization of Gold Stepped Surfaces Modified with Pd," *Langmuir*, vol. 520, no. 25, pp. 4877–4884, 2006.
- [22] V. G. Celante, "Electrodeposition of copper from spent Li-ion batteries by electrochemical quartz crystal microbalance and impedance spectroscopy techniques Electrodeposition of copper from spent Li-ion batteries by electrochemical quartz crystal microbalance and impedan," *J. Appl. Electrochem.*, vol. 40, no. January 2017, pp. 233–239, 2009.
- [23] Richard C . Alkire and Dieter M. Kolb, *Advances in Electrochemical Science and engineering*, vol. 8. 2002.
- [24] K. Ding, Y. Zhao, L. Liu, Y. Cao, Q. Wang, H. Gu, X. Yan, and Z. Guo, "Pt-Ni bimetallic composite nanocatalysts prepared by using multi-walled carbon nanotubes as reductants for ethanol oxidation reaction," *Int. J. Hydrogen Energy*, vol. 39, no. 31, pp. 17622–17633, 2014.
- [25] S. E. E. Profile and S. E. E. Profile, "Solid electrolyte containing a colorless redox couple for electrochromic device Solar Energy Materials and Solar Cells Solid electrolyte containing a colorless redox couple for electrochromic device," *Sol. Energy Mater. Sol. Cells*, vol. 196, no. 314407, pp. 9–15, 2019.

- [26] S. Nasrazadani and S. Hassani, *Chapter 2 - Modern analytical techniques in failure analysis of aerospace, chemical, and oil and gas industries*. Elsevier Ltd., 2016, pp. 39–54.
- [27] M. Scimeca, S. Bischetti, H. K. Lamsira, R. Bonfiglio, and E. Bonanno, “Energy Dispersive X-ray (EDX) microanalysis: A powerful tool in biomedical research and diagnosis,” vol. 62, 2018.
- [28] B. Y. O. P. Ayton, A. R. C. Hampneys, M. E. H. Omer, and B. Bs, “Feedback-induced instability in tapping mode atomic force microscopy: theory and experiment,” *Proceeding R. Soc. A*, vol. 467, no. December 2010, pp. 1801–1822, 2011.
- [29] M. Marrese, V. Guarino, and L. Ambrosio, “Atomic Force Microscopy: A Powerful Tool to Address Scaffold Design in Tissue Engineering,” *J. Funct. Biomater.*, vol. 8, p. 7, 2017.
- [30] H. Wang and P. K. Chu, *Surface Characterization of Biomaterials*. Elsevier, pp. 105–174.
- [31] N. Jalili and K. Laxminarayana, “A review of atomic force microscopy imaging systems: application to molecular metrology and biological sciences,” *Mechatronics*, vol. 14, pp. 907–945, 2004.
- [32] Y. Seo and W. Jhe, “Atomic force microscopy and,” 2008.



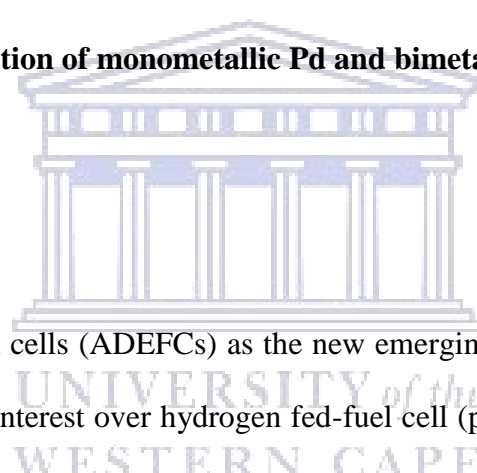
UNIVERSITY of the
WESTERN CAPE

4.0 Chapter 4

This chapter outlines results, based on electrochemical characterization, physical characterization and a subsequent application for ethanol oxidation in alkaline media. The underpotential deposition study of Cu on Au as a substrate will be discussed to select the optimal deposition potential. The electro-synthesis and characterization of Pd, PdIr thin film using electrochemical atomic layer deposition is highlighted in this chapter and the time-potential trace for Pd and PdIr deposition which is used to obtain optimal time and deposition potential of the elements will also be mentioned.

4.0 Electrochemical deposition of monometallic Pd and bimetallic PdIr for ethanol oxidation

4.1 Introduction



Alkaline direct ethanol fuel cells (ADEFCs) as the new emerging renewable energy source that has attracted a tremendous interest over hydrogen fed-fuel cell (proton exchange membrane fuel cells (PEMFCs)) due to notable higher theoretical energy density of ethanol (EtOH) over hydrogen. EtOH liquid hydrocarbon (fuel source), allowing storage in conventional tanks, high theoretical energy density (8.0 kW h kg^{-1}) in contrast to hydrogen (3.8 kW h kg^{-1}) fuel [1]. However, the main barrier of ADEFCs EtOH is to design an efficient anode electrocatalyst for complete oxidation of ethanol to use it for chemical energy conversion (fuel cell) device application. Pd-based materials at nano-sized scale are the most frequently used for ethanol oxidation reaction (EOR) and a high electrochemical activity has been obtained, varying from monometallic to bimetallic electrocatalyst. The fast kinetic, high electrochemical activity and stability of bimetallic based compounds compared to monometallic Pd-based compounds have predominantly assigned the bi-functional effect or electronic effect [2], [3].

4.2 Results and discussion

4.2.1 Cleaning and electrochemical characterization of gold (Au) substrate

Au is considered to possess a wide double layer region, where no faradaic reaction occurs [4]. The region mostly occurs in a potential region between -0.09 to 0.6 V of thoroughly cleaned substrate immersed in an aqueous acid solution of an acid. The typically clean substrate is depicted in **Figure 4.1**, furthermore, in this region the current response is almost zero [5]. Only perchlorate ion (ClO^-) adsorbed on the substrate in the inner/outer Helmholtz (double layer) region [6], [7]. As displayed in **Figure 4.1**, the CV peaks exhibit a polycrystalline characteristic with a dominant single-crystalline peak as described in the literature [8]. During anodic scanning from -0.2 Au forms oxide (Au_2O_3) around 1.2 V and 0.9 V respectively (see **Figure 4.1 (a)**) similar and consistent previous studies [9],[10],[11],[12]. On the cathodic sweeping direction, Au_2O_3 was reduced from Au^{3+} to Au (0) at around 0.9 V [13]. The reduction reaction of hydrated Au which may be represented as Au (OH)₃, has a formal standard potential, $E^\circ = 1.45$ V according to the literature [14] and maybe expressed as follow;



At higher negative potential, from -0.1 to -0.2, a negligible hydrogen evolution was observed, which is similar to observation as in literature [15].

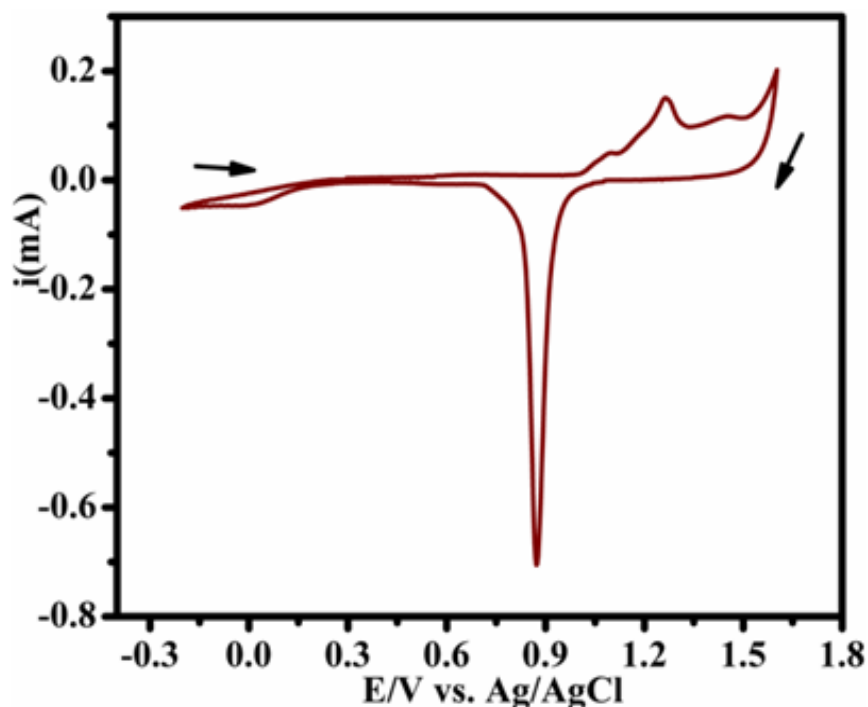


Figure 4. 1: Cyclic voltammograms of bare Au substrate in 0.1 M HClO₄ at 10 mVs⁻¹ scan rate.

4.2.2 Underpotential deposition of Copper (Cu) on Au: CV profile

The CV shown in **Figure 4.2** is obtained from the Au substrate in 1 mM CuSO₄ + 0.1M HClO₄. There are two well-defined peak pairs, one a reductive peak around 0.180 V and the other around -0.099 V during the cathodic scan, and they are associated with UPD and bulk (overpotential deposition-OPD) respectively as indicated in the CV. On the subsequent anodic scanning, the stripping peaks at + 0.01 V and + 0.28 V corresponds to oxidation of bulk and UPD respectively. The peak height of Cu-UPD and its corresponding stripping ascribed to strong Cu metal adatoms and substrate (M-S) interaction [16] which signifies Cu-UPD is bound on a foreign substrate [17], whereas M-M occurs at OPD region [17] which indicates the strong interaction on the metal itself.

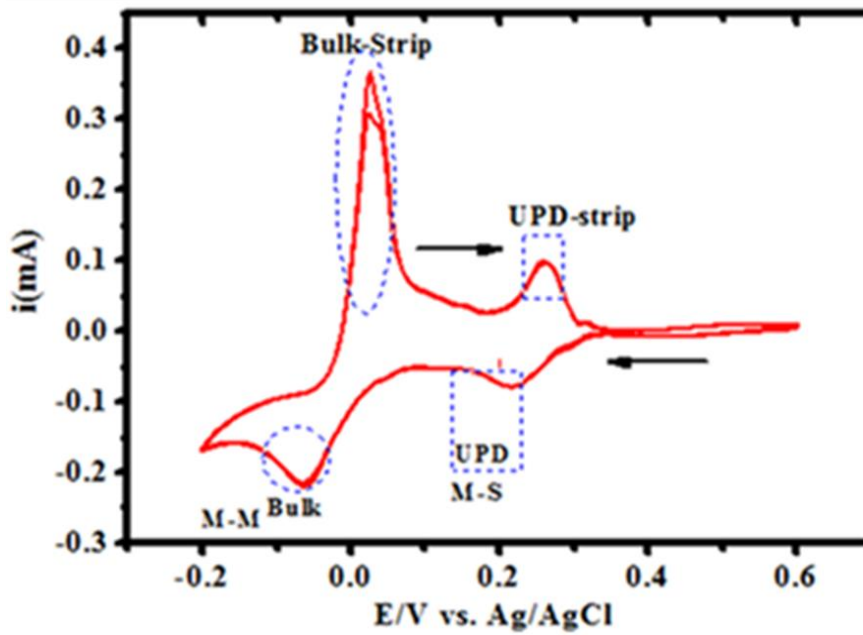


Figure 4. 2: CV of Au in 0.1 mM CuSO₄ + 0.1 M HClO₄

The standard (Nernst equilibrium) reduction reaction of Cu²⁺ can be expressed with the following equation;



The deposition of a Cu-_{UPD}, which occurs prior (positive) to Nernst positive potential can be expressed as in **Equation 4.3**, while OPD **Equation 4.4** occur past Nernst equilibrium potential as denoted in the following two equations;



The shape of the CVs and peaks assignment are similar and consistent to those reported in the literature [18],[19],[20],[21],[22],[23].

4.2.3 Electrodeposition of Pd

The deposition cycles for Pd are summarized in **Figure 4.3** with time-potential- current trace recorded for two SLRR cycles to optimize time and potential for E-ALD cycles. Pd was deposited via SLRR of Cu-UPD metal. The behavior of Cu-UPD as a sacrificial metal is relatively well understood in literature and has been reported for the deposition of noble Ag, Pt, and Pd metals on Au [8], [24]. In this work, during the deposition of Cu at UPD = 0.18 V, the reductive current response of -1000 μA was observed indicating the formation of Cu-adlayer. There was a potential drift from 0.250 to 0.420 V (stop potential) during Pd at OCP. The stopping potential (0.420 V) was set in the program (sequencer 4) to trigger the OCP. Although the potential was set, there was a shift to more positive potential up to 0.586 V which is the formation of the Pd-O layer, which is in strong agreement with CV results in Figure 4.3. The E-ALD cycle for Pd was explained in (section 3.4, Chapter 3) adopting procedure from the literature [18], [24]–[27].

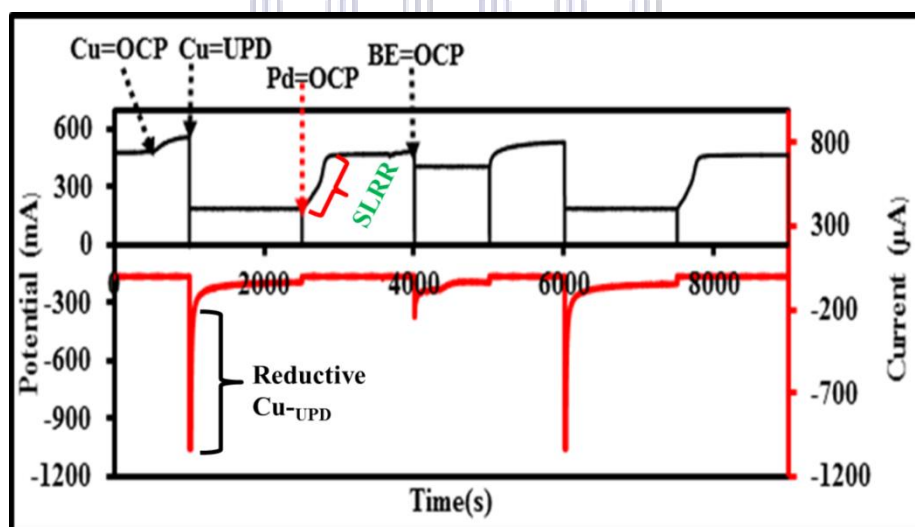


Figure 4.3: Time- a potential-current trace of sequential layer-by-layer deposition of Pd recorded for two cycles.



4.2.4 Electrochemical characterization of Pd in acid (0.1 M HClO₄)

Typical cyclic voltammogram signatures depicted before and after carrying out E-ALD cycles are shown in **Figure 4.4**. An activated Au CV profiles are illustrated in **Figure 4.1** confirming the characteristic features of Au (111) at the potential window between -0.2 and +1.4 V in 0.1 M HClO₄. The Au-oxide formation was observed around +1.2 V vs. Ag/AgCl during anodic scanning direction [15]. For comparison purposes and surface coverage investigation, CVs of Pd and Au are overlaid. During the subsequent cathodic sweeping direction, the prominent peak at +0.9 V (peak 'a') is ascribed to Au oxide reduction and around -0.1 and -0.2 V region (peak 'c') is due to hydrogen evolution [21]. The CV confirms the Pd coverage and its characteristic features in acidic medium. In addition, the disappearance of Au-oxide reduction (peak a) around +0.9 V and the emerging of Pd-O reduction peak b and its corresponding oxidation (peak 'b') verifies that Pd fully covered Au substrate. At higher negative potential around -0.18 V, peak 'c' is due to hydrogen adsorption-desorption as observed in cathodic and anodic sweeping. The shape and assignment of peaks are similar and consistent with the literature [24], [25], [28], [29].

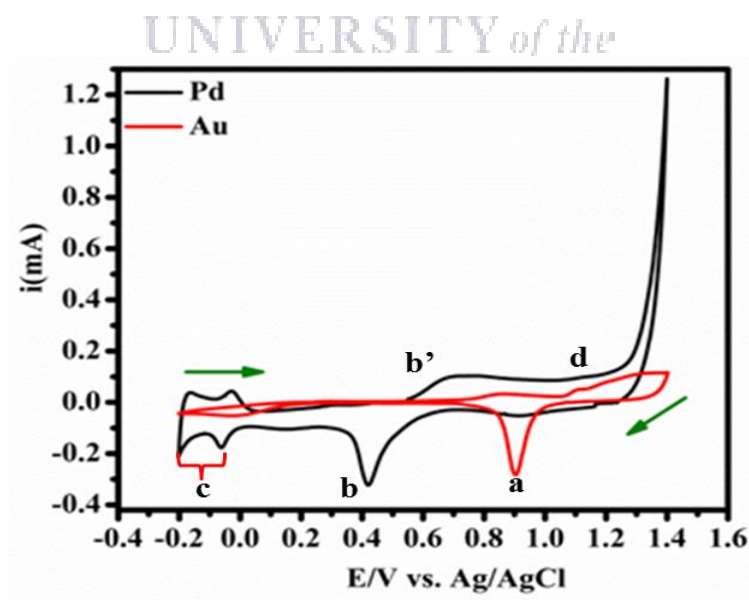
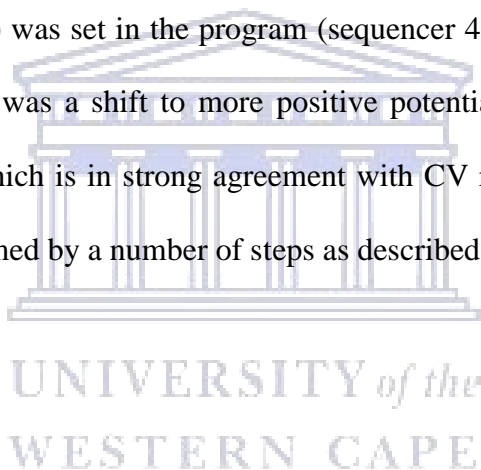


Figure 4.4: CVs of Pd thin films deposited via SLRR on Au substrate in 0.1 M HClO₄. Scan rate: 30 mVs⁻¹.

4.2.5 Electrodeposition of PdIr

The deposition cycles for PdIr summarized as displayed in **Figure 4.5 (b)** with time-potential-current trace recorded for two SLRR cycles to optimize time and potential for the E-ALD cycles programme. The deposition process of PdIr is shown as a schematic diagram in **Figure 4.5 (a)**. PdIr was deposited via SLRR of Cu-UPD metal. The behavior of Cu-UPD as a sacrificial metal is relatively well understood in literature and has been reported for the deposition of noble Ag, Pt, and Pd metals on Au [8],[24] . In this work, during the deposition of Cu at UPD = 0.18 V, the reductive current response of -1000 μ A was observed indicating the formation of Cu-adlayer. There was a potential drift from 0.250 to 0.420 V (stop potential) during Pd and Ir flow at OCP. The stop potential (0.420 V) was set in the program (sequencer 4) to trigger the OCP. Although the potential was set, there was a shift to more positive potential up to 0.586 V which is the formation of Pd-O layer, which is in strong agreement with CV results in (**Figure 4.6**). The E-ALD cycle for PdIr was formed by a number of steps as described in detail (**Section 3.3 Chapter 3.33**).



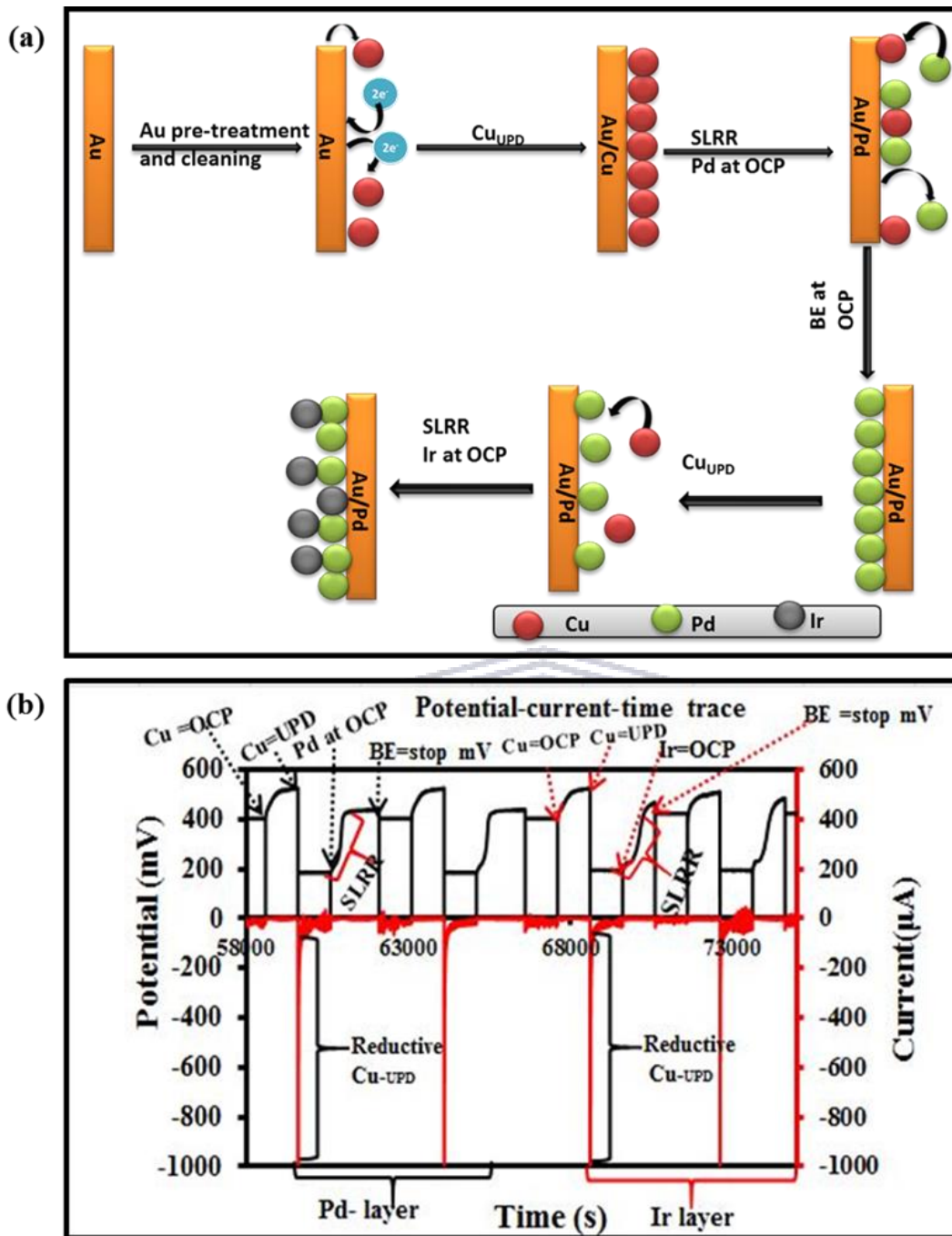


Figure 4.5: (a) Schematic representation of E-ALD cycle for the deposition of elements from their corresponding precursors, Cu-UPD on Au (111) substrate with its subsequent exchange for Pd and Ir at OCP, and (b) Time- the potential-current trace of sequential layer-by-layer deposition of Pd and PdIr recorded for two cycles.

4.2.6 Electrochemical characterization of PdIr in acid (0.1 M HClO₄)

CVs of monometallic Pd and bimetallic PdIr were overlaid to contrast and are displayed in **Figure 4.6** were studied in order to determine the effect of Ir on Pd. The acquired voltammogram features of PdIr and Pd are similar to those observed in previous studies [30]. CVs for both Pd and PdIr exhibited characteristic voltammogram features of Pd [24], [29]. However, there is a difference in Pd peak current and potential shift after Ir deposition. During cathodic scanning Pd-O peak shifted to a more positive potential. As cathodic scan proceeds between 0 and -0.2 V vs. Ag/AgCl the peak current associated with hydrogen adsorption-desorption ($H_{ads-desp}$) region on the surface of Pd [31],[32], is smaller for bimetallic PdIr which suggest that some Pd atoms are replaced by the metallic Ir and formed a PdIr thin film. The CVs of PdIr reveals that Ir on Pd crystal lattice inhibited the hydrogen adsorption (Pd-Hydride bond) [33]. During the anodic scanning direction, the onset curve Pd-oxide formation at +0.6 to +0.98 V, the peak current is higher for bimetallic PdIr which is due to the addition of Ir on the Pd surface. The increased peak current at this region is attributed to Ir redox couples, Ir(0) to Ir(IV) via Ir(III) around +0.8 V as an intermediate redox process [34],[35],[36]. This region is known as the formation of Iridium oxide film (IROFs)-Ir (Ir IIII)-oxide layer in a form of Ir(OH)₃ [47].

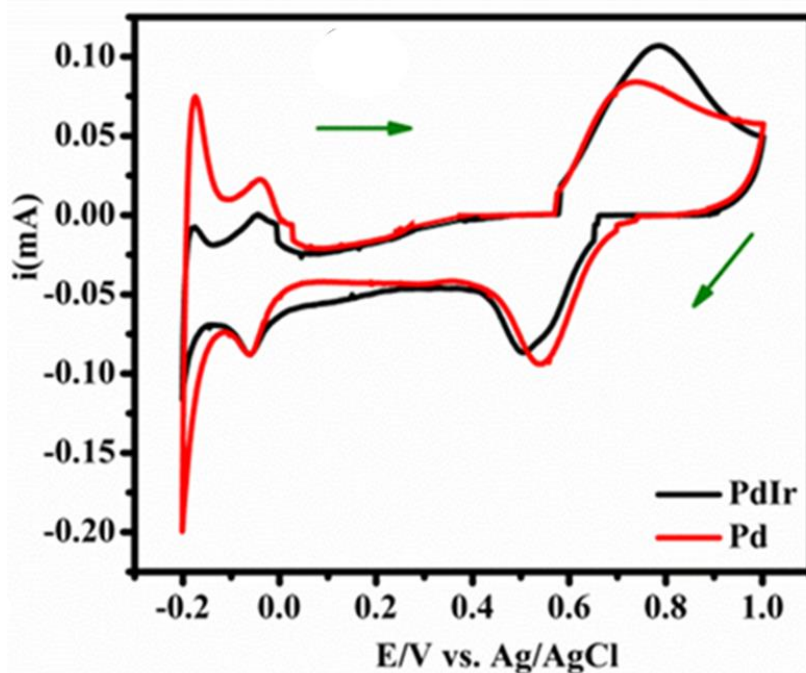


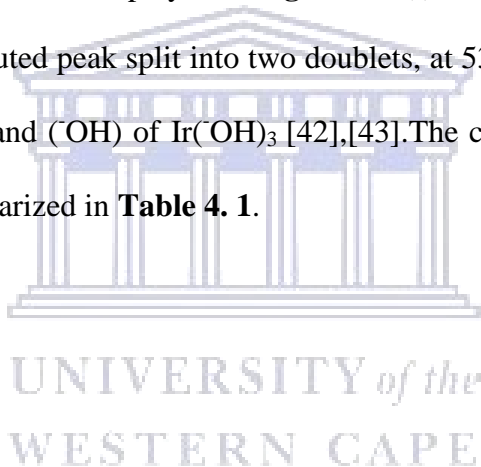
Figure 4.6 CVs of Pd and PdIr thin films deposited via SLRR on the Au substrate in 0.1 M HClO₄. Scan rate: 30 mVs⁻¹.

Spectroscopic and structural characterization of Pd, PdIr nanostructured thin films

4.2.7 X-ray photoelectron spectroscopy (XPS) of Pd, PdIr

XPS was employed to investigate the surface composition, surface chemical state and electronic structure of the monometallic Pd and bimetallic PdIr thin film. **Figure 4.7 (a)** displays the wide XPS spectra and the positions of the main peaks characteristic as the main composition of monometallic Pd and bimetallic PdIr on the Au substrate. The Au 4f spectra in **Figure 4.7 (b)** shows the position of Au photoelectron lines that exhibit the doublet binding energy of 88.01 and 84.2 eV which are attributed to Au 4f_{7/2} and Au 4f_{5/2} metallic state of Au substrate. **Figure 4.7 (c)** displays two asymmetrical peak of Pd 3d at high energy band (Pd 3d_{3/2} = 340.86 eV) and low energy band (Pd 3d_{5/2} = 335.8 eV) for PdIr on Au; and Pd_{3/2} = 340.558 eV, Pd 3d_{5/2} = 335.32 eV) for Pd on Au, which corresponds to the presence of metallic Pd [38], [39] which is in strong agreement with the previous reports [40],[41]. A slight shift in binding energy ($\Delta E = \sim 0.3$ eV) on

PdIr relative to Pd was observed indicating the least effect on electronic structure of Pd upon addition of Ir. This shift also suggests that the electron charge transfer from Ir to Pd, in the d-band center, resulting to Pd d-band shifts upwards (high energies) upon addition of Ir. This upward shift could be the reason for less carbonaceous species (ethanol intermediates) on the surface of Pd. This corroborates with CV (i_f/i_b ratio) (**Figure 4.11**) and CA results (**Figure 4.13**). After the deconvolution process of Pd 3d peaks, each peak split into doublet corresponding to Pd⁰ and Pd²⁺ moieties as shown in **Figure 4.7 (e)**. **Figure 4.7 (d)** shows Ir 4f spectrum at low energy band (57.6 eV,) and its deconvoluted peaks, exhibited Ir (III) and Ir (IV) chemical state at 57.25 eV and 58.48 respectively [42]. The O1S photoelectron line at high energy resolution (532 eV) and its deconvoluted peaks are displayed in **Figure 4.7 (f)** and could be attributed to Ir(OH)₃ from IROFS, with deconvoluted peak split into two doublets, at 531.496 eV and 533.1 eV which are ascribed to O²⁻ of IrO₂ and (OH) of Ir(OH)₃ [42],[43]. The chemical states and moieties of the prepared films are summarized in **Table 4. 1**.



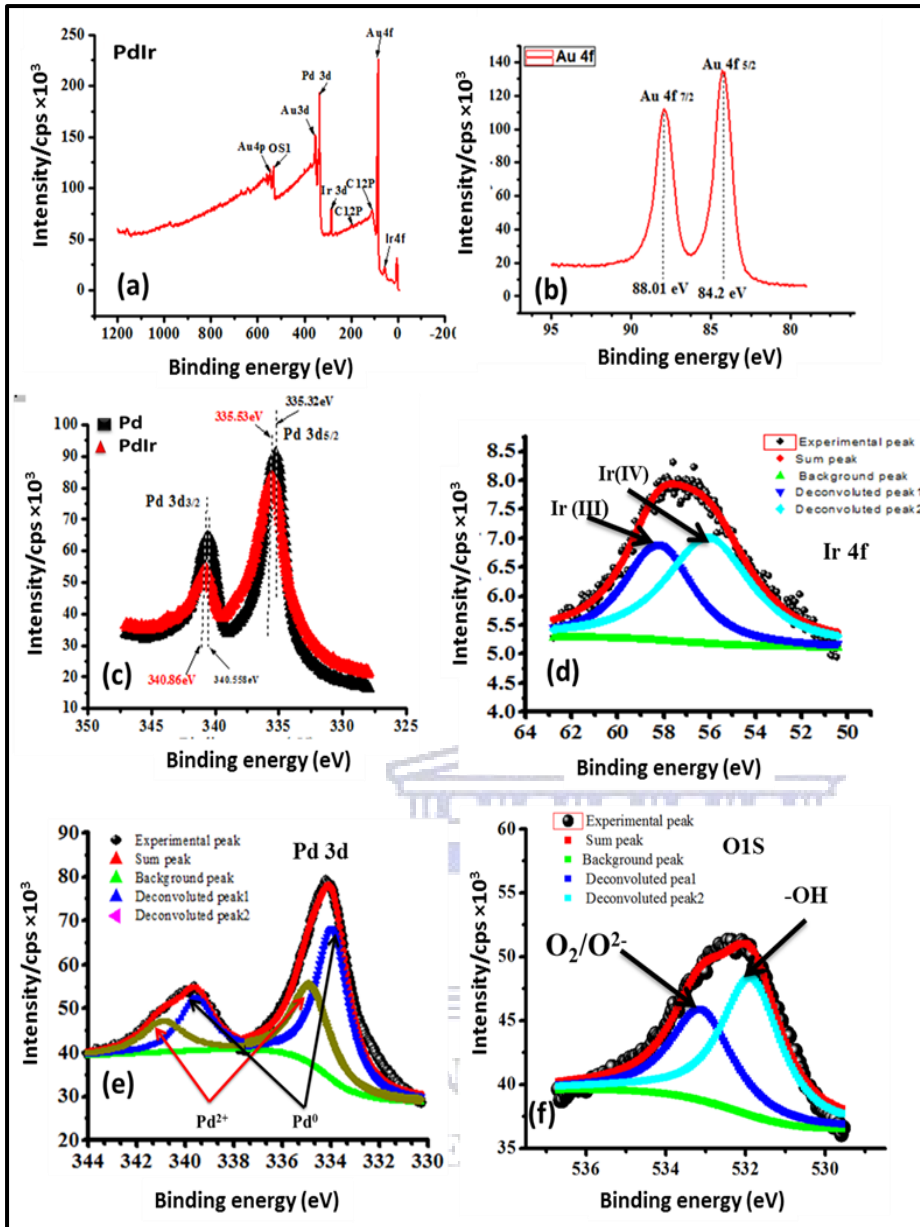


Figure 4.7: XPS spectra of (a) PdIr (b) Au 4f, (c) Pd 3d from monometallic Pd (black) and bimetallic PdIr (red), (e) deconvoluted Pd 3d peak of PdIr, (d) XPS spectra of Ir 4f and (f) XPS spectra of O1S.

Table 4.1: Chemical states and Binding energy of Pd-based thin films

Thin film	Species	Binding energy(eV)	Moiety	Intensity (10 ³ cps)
Pd on Au	Pd 3d _{5/2}	343.5	Pd ⁰	85
		333.5	Pd ²⁺ /Pd(O)	80
	Pd 3d _{3/2}	333.1	Pd ⁰	84.4
			Pd ²⁺ /Pd(O)	79.2
PdIr on Au	Pd 3d _{5/2}	335.3413	Pd ⁰	71.360
		336.353	Pd ²⁺ /Pd(O)	58.140
	Pd 3d _{3/2}		Pd ⁰	55.212
			Pd ²⁺ /Pd(O)	49.453
	Ir4f	57.25	Ir(III)	7.058
		58.48	Ir(IV)	6.785
	O1s	533.16	O ²⁻ of IrO ₂	8.5
		531.599	(OH)of Ir(OH) ₃	8.0

4.2.8 X-ray diffraction of Pd, PdIr

XRD patterns of Pd and PdIr thin film on the Au substrate are displayed in **Figure 4.8**. The four main diffraction peaks situated at 38.97°, 51°, 77°, and 80.5° are attributed to the indexed (111), (200), (220), and (311) reflection planes which are characteristic of face-centered cubic (fcc) of metallic Pd [40]. The pattern for bare Au exhibits polycrystalline features with notable Au (111) crystallite which in accordance to the CV curve (see **Figure 4.1**), and the shape and assignment of the pattern peaks are consistently reported in the literature [40]. Both Pd and PdIr shows (fcc)

characteristic features, however, PdIr showing a shift to higher 2θ value (clearly observed at (200) plane), indicating strong interaction with Pd, weakening Pd-H bond in accordance to lower binding energy induced by second metal adlayer as described by [33],[45]. This interaction may be due to insertion of Ir into Pd crystal lattice [46], [47], indicating some alloy formation [48] resulting to Pd(fcc) lattice contraction [3],[49], and also is in good agreement CVs (see **Figure 4.6**) and XPS results (see **Figure 4.7 (e)**). The additional strong diffraction peak at low 2θ (26°) value is likely due to an elemental Ir, indicating Ir SLRR of Cu-UPD on Pd-covered Au as it also well pronounced in EDS results (see **Figure 4.10 (f)**). This strong peak is parallel to a prominent Pd/Au (111) preferred orientation, which is likely ascribed to the existence of some epitaxial relationship between Ir and substrate.

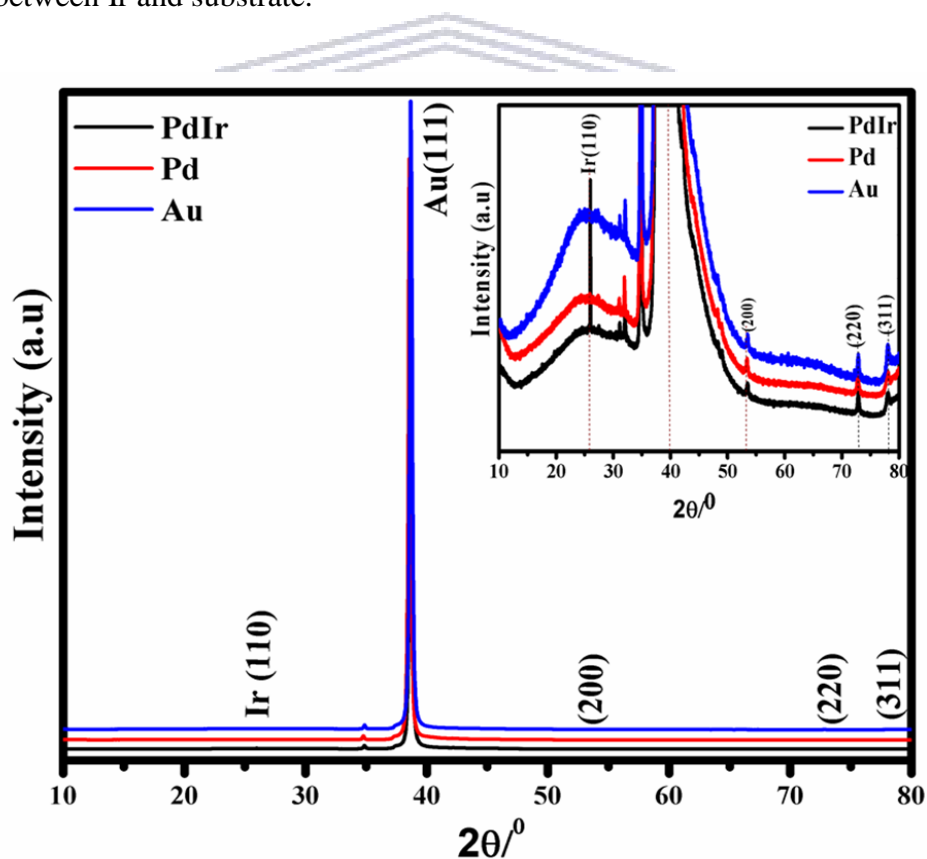


Figure 4.8: EDX spectra of Pd (a), (b) PdIr thin films, and (c) XRD patterns of the corresponding thin films, insert: magnified XRD pattern.

4.3 Microscopic analysis of Pd, PdIr

4.3.1 Atomic force microscopy

Figure 4.9 reveals details of Atomic force microscopy (AFM) analysis for Pd and PdIr on Au. AFM was used to establish the surface morphology, surface texture and topographic information of the thin films. **Figure 4.9 (A)** and **(B)** depicts 2D AFM topographic images of Pd/Au thin film, Au substrate (insert) and **Figure 4.9 (B)** PdIr thin film while their corresponding 3D images of Pd, PdIr displayed in **Figure 4.9 (C)** and **(D)**, respectively. AFM micrographs quantify average roughness (Ra) and root mean square roughness (Rq)/(r.m.q) of the prepared thin films. It can be seen that the Au substrate has the pinholes attributable to sintering. Monometallic Pd and bimetallic PdIr clearly distinguish each other by their roughness; Pd= (Sa= 33.7 nm, Sq= 39.9 nm) and PdIr= (Sa= 39.2 nm, Sq= 45.5 nm) which corresponds to improved crystallinity upon addition of Ir on Pd. The calculations from the cross-section area revealed that most particles have a height between 25-42 nm and 50-120 nm for monometallic and bimetallic nanostructures respectively. The texture profiles of Pd and PdIr are illustrated in **Figure 4.9 (E)** and **(F)** respectively, whilst their corresponding histogram for grain distribution is displayed in **Figure 4.9 (G)** and **(H)** respectively. The increased roughness on bimetallic PdIr can be pinpointed to improved crystallinity, the addition of second element (Ir) and consequent increase in grain size. PdIr showed a rough surface and evenly distributed grains due to Pd and its neighboring Ir nanostructures [48], [50] as seen in **Figure 4.9 B**. The round white grains could be attributed to oxidized Ir, which is in agreement with EDS and XPS results which revealed IrOx oxides (IROFs) formation on surface of binary PdIr thin film, and the AFM micrographs are similar to and are as described in literature [38],[44],[51],[52].

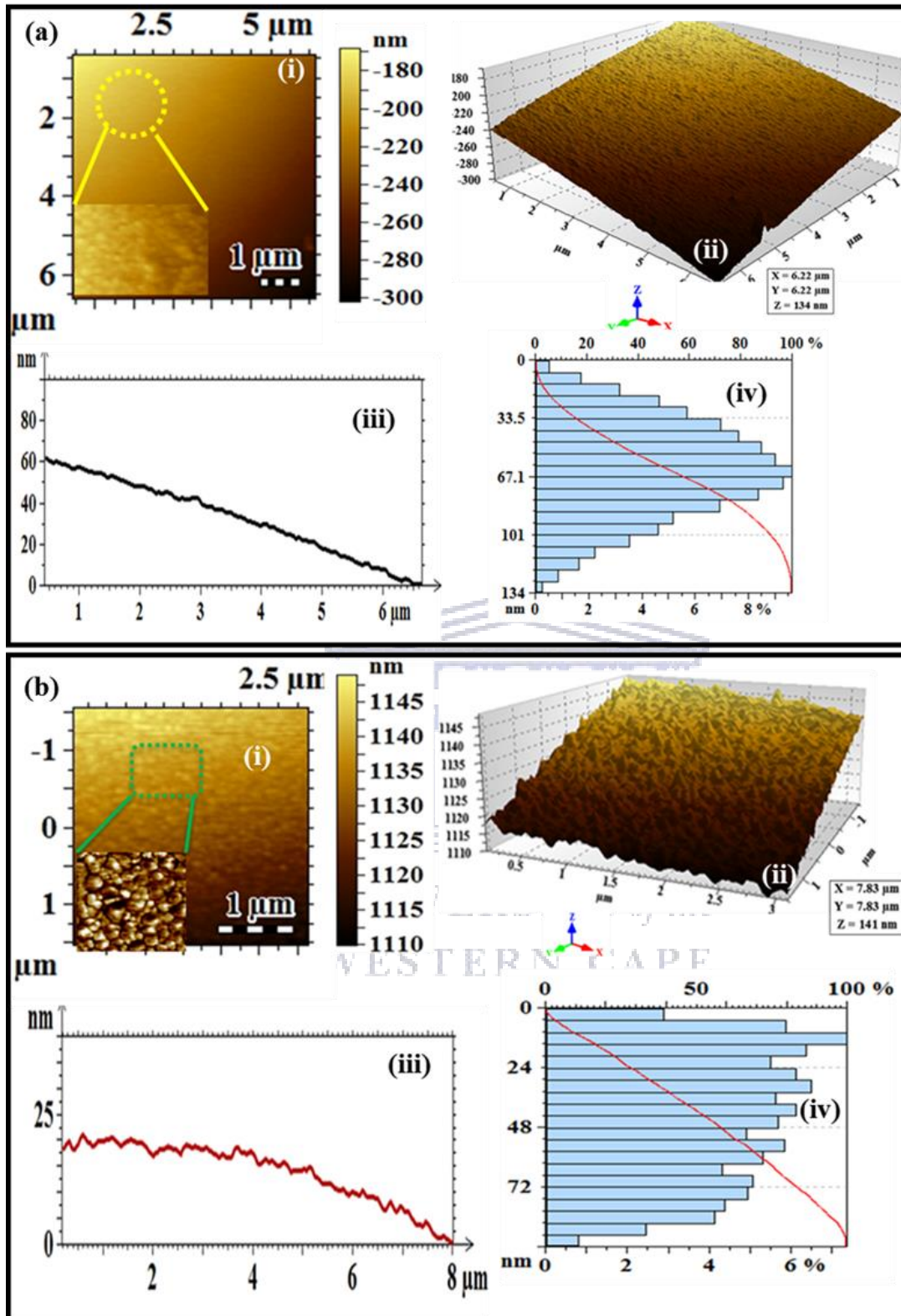
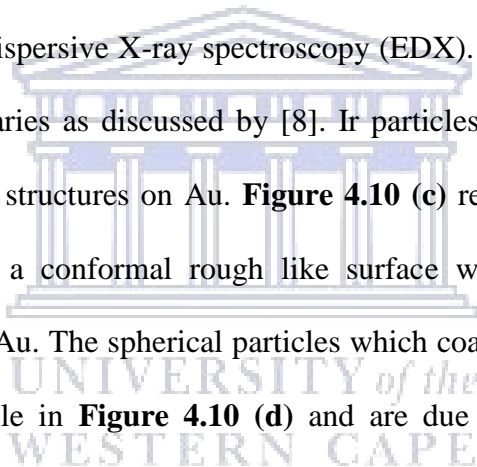


Figure 4.9: AFM topography images of (a (i)) 2D and 3D (a (ii)) Pd topography (insert: zoomed Pd), (b (i)) 2D and (b (ii)) 3D of PdIr (insert (i): zoomed PdIr area), and their respective corresponding Texture profile (iii) and histogram (iv).

The grains formed island humps, and this is probably due to agglomeration of nanostructures of Pd and Ir formation which could result in 3D growth that is ascribed to consecutive deposition cycles of alternated Pd and Ir deposits. The texture profile and histogram of Pd and PdIr thin films show a define grains formation, and they reveal an inhomogeneity surface. The histogram shows that the nanostructures of the thin films are evenly-distributed (40-163 nm and up to 85 %) for PdIr, and (16 nm -82 nm up to 85 %) for Pd.

4.3.2 Scanning electron microscopy-Energy dispersive X-ray of Pd, Ir, and PdIr thin films

Figure 4.10 illustrates the scanning electron microscopy (SEM) images of monometallic Ir, Pd and bimetallic PdIr deposited on the Au substrate. Their corresponding elemental composition was obtained from energy-dispersive X-ray spectroscopy (EDX). **Figure 4.10 (a)** shows distinct particles of Au with boundaries as discussed by [8]. Ir particles in **Figure 4.10 (b)** illustrated spherical and rhombohedral structures on Au. **Figure 4.10 (c)** reveals that Au morphology has been distorted and formed a conformal rough like surface which could correspond to the deposition growth of Pd on Au. The spherical particles which coalesced with the block of grains forming an island are visible in **Figure 4.10 (d)** and are due to PdIr. The arrangements of particles formed microspheres and islands which correspond to Pd nanostructures agglomerating with the neighboring Ir particles. The EDX patterns in **Figure 4.10 (e)** and **(f)** confirm the presence of both metallic Pd and Ir on Au. EDX detected no Cu in all thin films, which proves the exchange of Cu-UPD for noble metal (Pd and Ir) during the SLRR step.



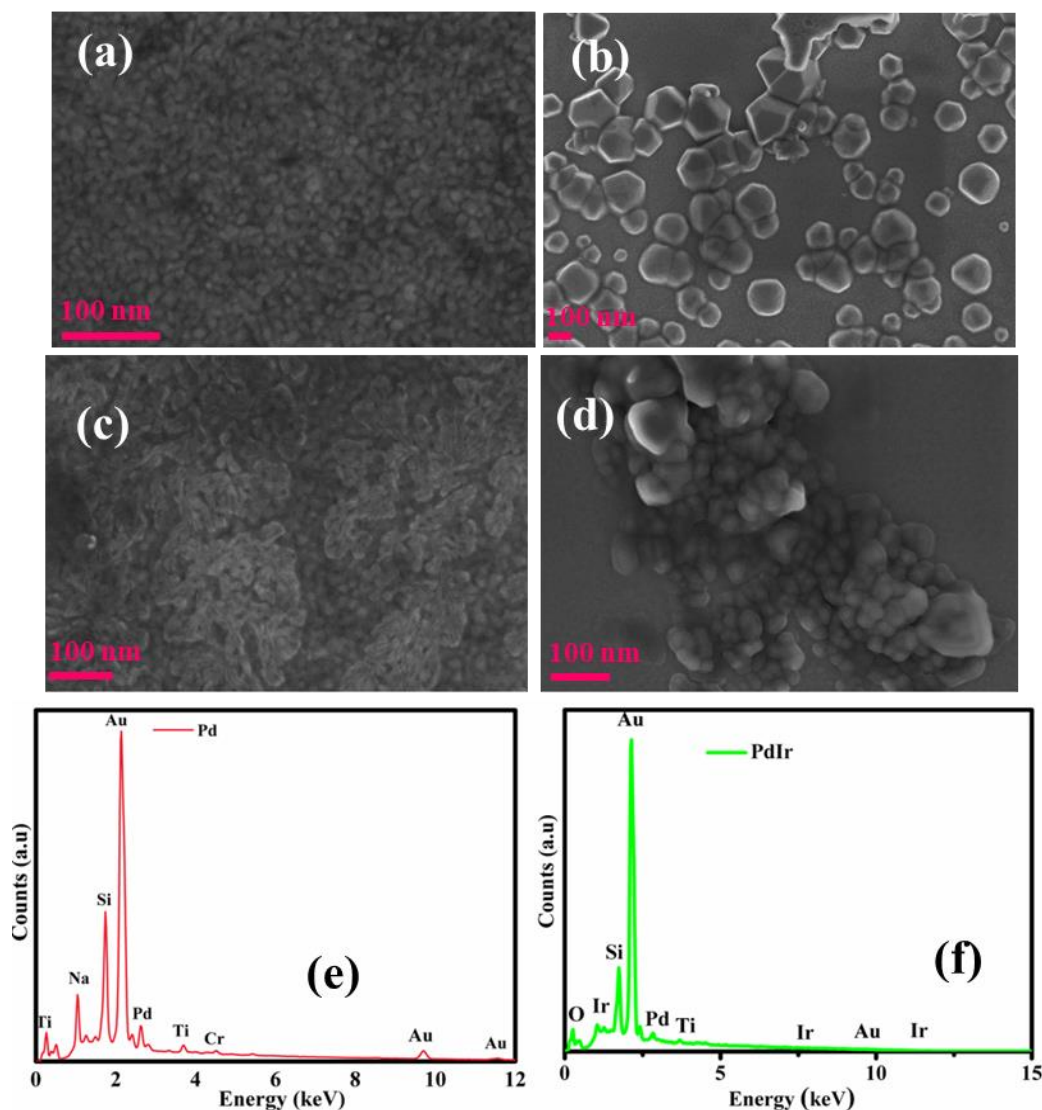


Figure 4.10: SEM micrographs of (a) Au substrate (b) Ir, (c) Pd and (d) PdIr with corresponding EDX of (e) Pd and (f) PdIr.

4.4. Electrochemical characterization of Palladium-based thin film: Activity towards ethanol oxidation in alkaline media

4.4.1 Activity of Pd based thin film towards ethanol oxidation in alkaline media: Cyclic voltammetry (CV)

Cyclic voltammetry (CV) was used to probe the electrocatalytic activity of Pd and PdIr thin film catalysts. In this experiment, an electrolyte solution of 0.1 M EtOH + 0.5 M KOH was prepared

using ultrapure water and was deaerated for 1 hour before use. During the experiment, N_2 gas was allowed to flow over the solution. Using a single peristaltic pump, a solution was flushed onto the surface of each thin film electrocatalyst.

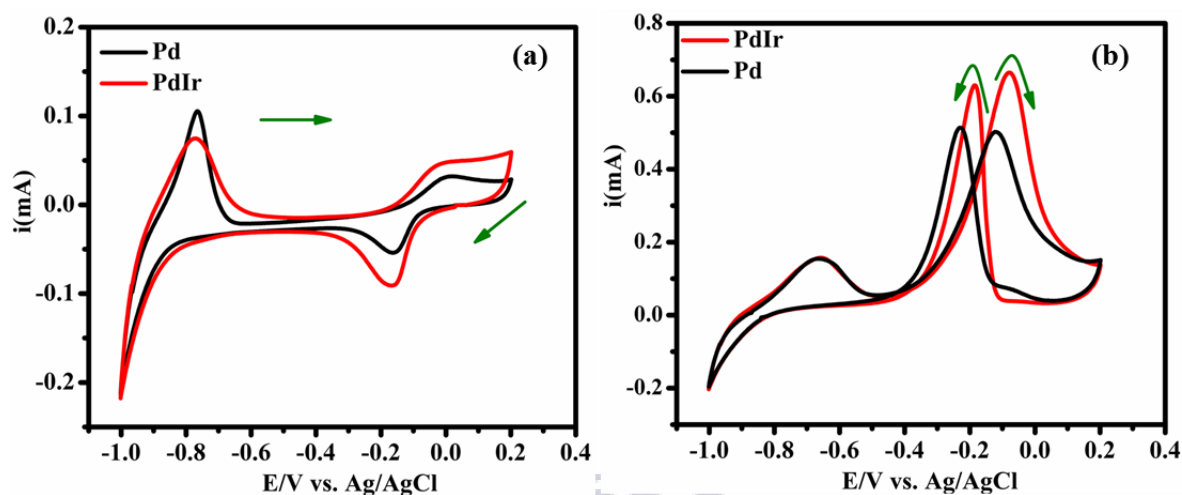


Figure 4.11: (a) and (b) illustrate cyclic voltammogram curves for Pd and PdIr thin films in 0.5 M KOH and 0.5 M KOH + 0.1 M EtOH respectively.

Figure 4.11 Sweeping in a potential range of -1.0 to +0.2 V CVs shows features of Pd in alkaline solution. During cathodic sweeping direction all CVs exhibit prominent peaks at -0.2 to -0.18 V and -0.83 V to -0.99 V potential ranges, which are ascribed to reduction/ dissociation of Pd-O and hydrogen adsorption/desorption features respectively. During the anodic scanning direction both CV depicts onset oxidation at around -0.1 V to +0.05 V which is attributed to the formation of the Pd-O/Pd-OH layer [53]. These three voltammogram distinguish themselves with the following changes (i) The current response for Pd-O reduction and Pd-O formation peak current is higher for bimetallic PdIr and shifted to more positive potential range respective to that of monometallic Pd, (ii) PdIr evidence increase in concentration of hydroxyl by the presence of IROFs species on the Pd surface [54]. This finding also suggests that more PdIr particles are dispersed on Au compared to its counterparts (Pd), suggesting electron interaction between Ir and Pd [55]. All of these changes corroborate the significant addition of Ir on the Pd surface. At

high negative potential region, the hydrogen absorption and desorption is observed during cathodic and anodic scanning direction respectively. The peak around -0.198 V is due to the reduction of Pd-O/Pd-OH [56]. The prominent peak current decrease for $H_{\text{adsp}}/H_{\text{desp}}$ of upon the ethanol solution translates to the hindrance of $H_{\text{ads}}/H_{\text{des}}$ ethoxy group on the Pd surface during the positive sweeping direction as displayed in **Figure 4.11 (b)**. The onset oxidation of ethanol is found around -0.42 V vs. Ag/AgCl and maximum peak current centered at -0.06 V, 0.47 mA current, and -0.05 V at 0.32 mA for Pd and PdIr, respectively. During cathodic scanning, Pd (II) oxide was electro-reduced at a low potential region which is also re-oxidation of any remaining carbonaceous species [57], [58]. The ratio of forward peak current to backward peak current is around 0.48 mA which may suggest the poisoning of Pd active surface sites. **Figure 4.11 (b)** shows the overlaid bimetallic PdIr and monometallic Pd thin film in a solution of 0.5 M KOH + 0.1 M EtOH, during the anodic sweeping direction. It was observed from the ratio of forward peak current (i_f/i_b) to reverse peak current that the bimetallic PdIr shows excellent tolerance to poisoning by ethanol intermediates species. This was ascribed to the addition of IROFs on the surface of Pd, assisting to complete the oxidation and be resistant upon poisoning. The small peak at the high negative potential in both catalysts is due to the high concentration of KOH versus low concentration of ethanol, there for the shoulder curve probably attributed to the hydroxyl group from 0.5 M KOH solution.

4.4.2 Electrochemical characterization of PdIr: Effect of scan rate of in KOH and ethanol oxidation

The effect of scan rate on the electrochemistry of Pd and PdIr thin film was studied in 0.5 M KOH+0.1M EtOH as displayed by CV in **Figure 4.12 (a)** and Randles-Sevcik plot (**Figure 4.12 (b)**), where the chosen scan rates were (10, 15, 25, and 30) mVs^{-1} .

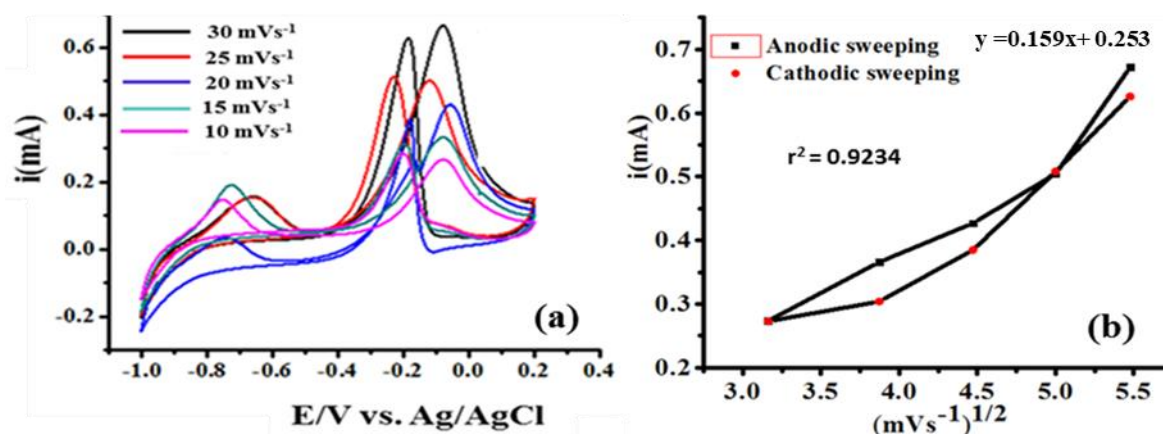


Figure 4.12: (a) CVs of PdIr in 5 KOH + 0.1M EtOH in at various scan rates and (b) Randles-Sevcik plot.

The electrode current response has been evaluated by observing a change in anodic and cathodic peak currents. The forward (oxidation) peak current showed an increase with scan rate and the potential shift was also observed. This increase of peak current with the square root of the scan rate shows the stability of electrocatalysts and reveals a diffusion-controlled electrocatalytic process [59]. However, the slight difference in peak potential was calculated to be $\Delta E > 0.59$ V, suggesting an irreversible electrochemical reaction process on the electrode-electrolyte interface. According to results obtained from using the Randles-Sevcik equation, PdIr possesses fast kinetics for the electrochemical reaction for EtOH oxidation in 0.5 M KOH. In addition, the slope with correlation coefficient ($r^2 = 0.92$) may suggest that the reaction is diffusion-controlled electrochemical process. To confirm the electron mobility, the diffusion coefficient (D) and surface coverage was calculated using the by Randles-Sevcik (**Equation. 4.6**) and Laviron (**Equation 4.7**). The values were found to be $1.334 \times 10^{-5} \text{ cm}^2 \text{ s}^{-1}$, and $1.441 \times 10^{-3} \text{ mol cm}^{-2}$ respectively. The finding suggests the monolayer coverage for PdIr electrode. The units in equations are as explained in **Chapter 3 (section 3.3.2)** for reversible and quasi-reversible reaction.

$$I_p = (2.99 \times 10^5) n (\alpha n_a)^{1/2} A C_0 D^{1/2} \nu^{1/2} \quad (4.6)$$

$$\frac{I_p}{v} = \frac{n^2 F^2 A \Gamma}{4RT} \quad (4.7)$$

4.4.3 Chronoamperometry (CA) measurements of Pd, PdIr in 0.5 KOH + 0.1M EtOH

The long-term stability of electrocatalysts was further tested using a chrono amperometric test.

Figure 4.13 display the chrono amperograms curves of Pd (i) and PdIr (ii) thin film in 0.5M KOH containing 0.1M EtOH solution to probe the current stability and poisoning within 3600s (1hour) at fixed potential -0.2 V. The CA's shows a high current response in the first few minutes of electrocatalysts. However, the bimetallic PdIr showed a higher current response and remained high throughout the reaction. The initial high current response is ascribed to available active sites of the electrocatalyst, and the sharp decay is due to the accumulation of CO- intermediates of ethanol [60]. PdIr is more resistant to poisoning corresponding to the addition of Ir which causes the bifunctional mechanism. The CA results corroborate with CVs (**Figure 4.11 (b)**) where PdIr showed I_f/i_b ratio which translates to tolerance to the poisoning of the electrocatalyst.

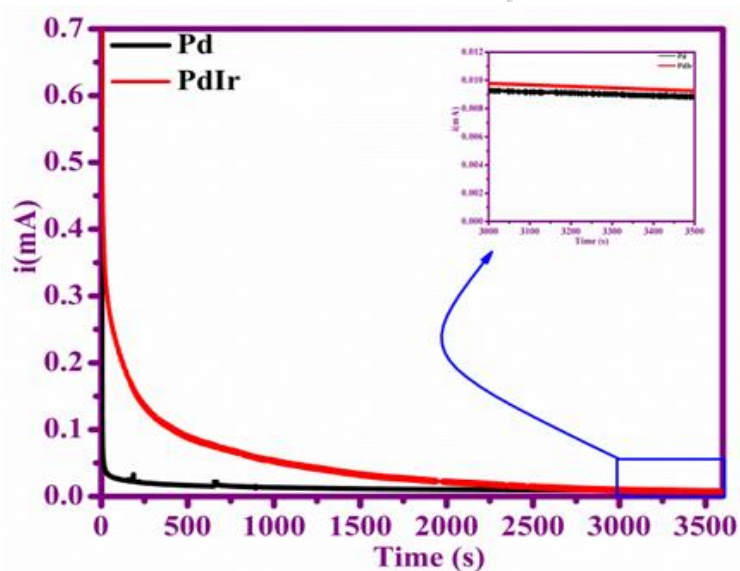


Figure 4.13: CA of Pd and PdIr at -0.2 V for 1 hour in 0.5 M KOH + 0.1M EtOH.

4.4.4 Electrochemical impedance spectroscopy of Pd, PdIr based thin films towards EtOH oxidation

Figure 4.14 represents the Nyquist plot (a) and Bode plot (b) of Pd and PdIr in 0.5 M + 0.1 M EtOH solution at -0.2 V applied potential. To clearly interpret the impedance results, the Randles' equivalent circuit $R_s (R_{ct} CPE)$ is used to fit and simulate the electrochemical parameters, where R_s is solution resistance of the electrolyte, R_{ct} is a charge transfer and CPE a constant phase element. R_{ct} is related to reaction kinetic, and it can be observed that PdIr has a smaller R_{ct} compared to a monometallic Pd thin film which suggests a faster electron transfer and higher activity for EOR. The R_{ct} value for PdIr = 2.32 (k Ω); Pd = 14.5 (k Ω) which suggests that the bimetallic PdIr is more a conducting system than the monometallic Pd on Au system. Using the equivalent circuit fit elements, the exchange current and time constant value was calculated using **Equation 4.5**;

$$i_0 = R_t \frac{RT}{nFR_{ct}} \quad (4.6 \text{ (a)})$$

$$\tau = R_{ct} \times CPE \quad (4.7 \text{ (b)})$$

Where i_0 = exchange current, n is a number of electrons transferred, CPE is a distributive element that models a double layer capacitance (Cdl), τ is a time constant value [59]. Pd thin film electrocatalyst gave a smaller exchange current and larger time constant value, while PdIr gave a larger exchange current value and smaller time constant value. Additionally, the rate of electron transfer (k_{et}) during ethanol oxidation on the Pd surface is slow or sluggish compared to that of bimetallic PdIr hence a larger R_{ct} . The Bode plot further investigates the electric properties of the catalyst, and the results obtained from the plot corroborate with the Nyquist plot as the bimetallic PdIr shows a higher phase angle = 84° (metallic value); the semi-metallic value of Pd = 74°. The higher phase angle corresponds to higher conductivity of PdIr compared to that of Pd,

since the phase angle of pure conductor/ more capacitive system should show a phase angle that is close to 90° [60], [61], [62], [63]. Furthermore, the total impedance $\log |Z|$ data for Pd and higher total impedance of 3.48Ω for PdIr at low-frequency value. These EIS results have a strong agreement with results obtained from the CVs (**Figure 4.11 (b)**) and CA (**Figure 4.13**) where bimetallic PdIr exhibited higher peak current for EOR. Also, the decrease in R_{ct} and higher phase angle of PdIr are attributed to higher conductivity and electrocatalytic activity and make it a good candidate for electron transfer reactions. **Table 4.2** and **4.3** shows the summary of electrochemical activity and impedance metric parameters of Pd and PdIr electrocatalyst films towards EOR

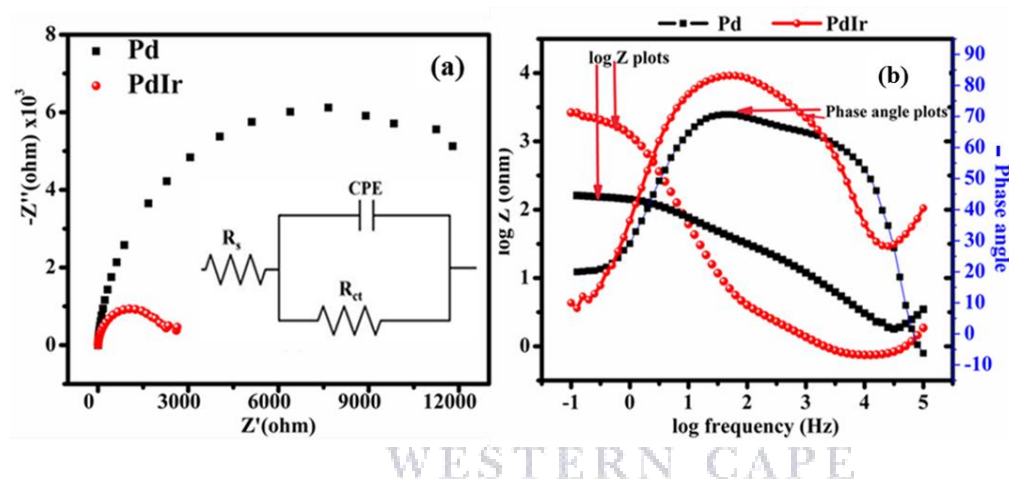


Figure 4.14: (a) Nyquist plot of Pd (black) and PdIr (red), and insert: Randles Sevcick circuit, and (b) their corresponding Bode plot.

Table 4.2 Summary of electrochemical activity of Pd and PdIr electrocatalyst films towards EOR.

Thin films	I_f (mA)	I_b (mA)	Onset potential (V)	I_f/I_b ratio
Pd	0.494	0.521	-0.402	0.94
PdIr	0.334	0.625	-0.423	1.065

Table 4.3: Electrochemical impedimetric data of Pd and PdIr towards EOR measurements

Thin films	R_s (Ω)	R_{ct} ($k\Omega$)	N	CPE (F)	Φ ($^\circ$)
Pd	7.33E3	14.9	0.87	40.8	74
PdIr	7.98	2.32	0.929	7.74	85

4.4.5 Sub conclusion

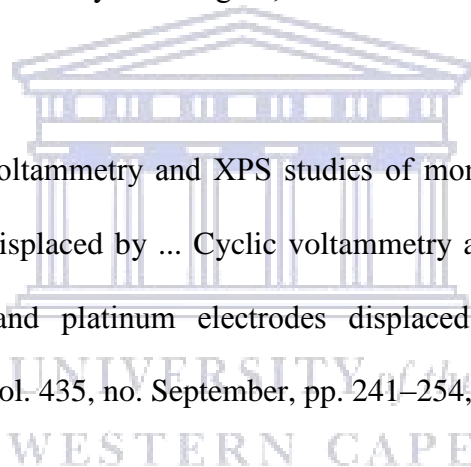
Electrochemical atomic layer deposition was successfully used to deposit monometallic Pd and bimetallic PdIr thin film electrocatalyst. The thin films were successfully electrodeposited on Au via SLRR of Cu-UPD followed by SLRR for Pd and Ir. Pd and PdIr deposits formed were up to 15 cycles, and the deposition processes were studied using (CV) method and were monitored with time-potential-current curves. AFM showed that the addition of Ir on Pd increased the surface roughness and evenly-distribution of grains. XPS spectra confirmed the formation of monometallic Pd and bimetallic PdIr. Bimetallic PdIr showed about 2 folds higher stability, conductivity and electrocatalytic activity towards the oxidation of ethanol and improved tolerance to poisoning by ethanol intermediates when compared to monometallic Pd. The electron transfer kinetics of electrocatalysts was confirmed using EIS. PdIr showed higher kinetics and electric conductivity than Pd as confirmed by R_{ct} values of 2.9 and 14.8 ($k\Omega$), respectively. It means that, the bimetallic electrocatalyst displays characteristic of higher film conductivity, improved corrosion resistance and higher electrocatalytic behavior towards electrooxidation of ethanol. The more negative onset potential and higher oxidation current on

PdIr than Pd for ethanol oxidation reaction (EOR) in alkaline electrolyte indicates that PdIr is the best candidate catalyst for ADEFCs.

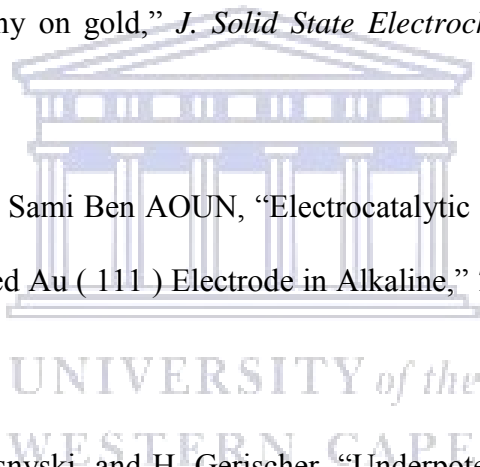
References

- [1] R. M. Modibedi, T. Masombuka, and M. K. Mathe, "Carbon supported Pd-Sn and Pd-Ru-Sn Snanocatalysts for ethanol electro-oxidation in alkaline medium," *Int. J. Hydrogen Energy*, vol. 6, pp. 1–9, 2011.
- [2] W. Xu, S. Zhu, Z. Li, Z. Cui, and X. Yang, "Preparation of Nanoporous Pd / CuO by Dealloying and Their Electrocatalysis for Methanol in Alkaline Condition Preparation of Nanoporous Pd / CuO by Dealloying and Their Electrocatalysis for Methanol in Alkaline Condition," *J. Electrochem. Soc.*, vol. 161, no. October 2014, pp. 1474–1480, 2014.
- [3] C. Zhu and Y. Yang, "Surface voltammetric dealloying investigation on PdCu/C electrocatalysts toward ethanol oxidation in alkaline media," *J Nanopart Res*, vol. 20, p. 314, 2018.
- [4] M. Cappadonia, U. Linke, K. M. Robinson, and U. Stimming, "Anion effects on the cyclic voltammetry of copper underpotential deposition on Au (100)," *J. Electroanal. Chem.*, vol. 405, pp. 227–232, 1996.
- [5] J. Perez, E. R. Gonzalez, and H. M. Villullas, "Hydrogen Evolution Reaction on Gold Single-Crystal Electrodes in Acid Solutions," *J. Phys. Chem. B*, vol. 102, no. 52, pp. 10931–10935, 1998.

- [6] M. Kasuya, T. Sogawa, T. Masuda, T. Kamijo, K. Uosaki, and K. Kurihara, "Anion Adsorption on Gold Electrodes Studied by Electrochemical Surface Forces Measurement," *J. Phys. Chem. C*, vol. 120, pp. 15986–15992, 2016.
- [7] U. E. Zhumaev, A. S. Lai, I. V Pobelov, A. Kuzume, A. V Rudnev, and T. Wandlowski, "Quantifying perchlorate adsorption on Au (111) electrodes," *Electrochim. Acta*, vol. 146, pp. 112–118, 2014.
- [8] T. S. Mkwizu and I. Cukrowski, "Physico-chemical modelling of adlayer phase formation via surface-limited reactions of copper in relation to sequential electrodeposition of multilayered platinum on crystalline gold," *Electrochim. Acta*, vol. 147, pp. 432–441, 2014.
- [9] C. Alonso, "Cyclic voltammetry and XPS studies of monolayers deposited on gold and platinum electrodes displaced by ... Cyclic voltammetry and XPS studies of monolayers deposited on gold and platinum electrodes displaced by mercaptopyridines .," *J. Electroanal. Chem.*, vol. 435, no. September, pp. 241–254, 1997.
- [10] T. S. Mkwizu, M. K. Mathe, and I. Cukrowski, "Multilayered Nanoclusters of Platinum and Gold : Insights on Electrodeposition Pathways, Electrocatalysis , Surface and Bulk Compositional Properties Multilayered Nanoclusters of Platinum and Gold : Insights on Electrodeposition Pathways , Electrocatalys," *J. Electrochem. Soc.*, vol. 160, no. February 2016, pp. 529–546, 2013.
- [11] L. . B. and P. F. Ngent, "The Electrochemistry of Gold : I The Redox Behaviour of the Metal in," *Gold Bull.*, vol. 30, pp. 43–53, 1997.



- [12] D. W. Suggs and J. L. Stickney, "Characterization of atomic layers of tellurium electrodeposited on the low-index planes of gold," *J. Phys. Chem.*, vol. 95, no. 5, pp. 10056–10064, 1991.
- [13] N. P. Finkelstein and R. D. Hancock, "A New Approach to the Chemistry of Gold," pp. 2–7.
- [14] W. Zhang, A. D. Bas, E. Ghali, and Y. Choi, "Passive behavior of gold in sulfuric acid medium," *Trans. Nonferrous Met. Soc. China*, vol. 25, no. 6, pp. 2037–2046, 2015.
- [15] Y. Chen, L. Wang, A. Pradel, A. Merlen, and M. Ribes, "Underpotential deposition of selenium and antimony on gold," *J. Solid State Electrochem.*, vol. 19, pp. 2399–2411, 2015.
- [16] I. T. Zakerya Dursun, Sami Ben AOUN, "Electrocatalytic Oxidation of D-Glucose Using a Cd ad-atom-Modified Au (111) Electrode in Alkaline," *Turk J Chem*, vol. 32, pp. 423–430, 2008.
- [17] D. M. Kolb, M. Przasnyski, and H. Gerischer, "Underpotential deposition of metals and work function differences," *J. Electroanal. Chem.*, vol. 54, no. 1, pp. 25–38, 1974.
- [18] N. Xaba and R. M. Modibedi, "Pd , PdSn , PdBi , and PdBiSn Nanostructured Thin Films for the Electro-Oxidation of Ethanol in Alkaline Media," *Electrocatalysis*, pp. 11–16, 2019.
- [19] Z. Yazar and S. Abac, "Characterization of CuTe nanofilms grown by underpotential deposition based on an electrochemical codeposition technique," *J. Solid State Electrochem.*, vol. 21, pp. 1417–1430, 2017.



- [20] Y. Kim, J. Y. Kim, D. Vairavapandian, and J. L. Stickney, "Platinum nanofilm Formation by EC-ALE via Redox Replacement of UPD Copper: Studies Using in-Situ Scanning Tunneling Microscopy," *J. Phys. Chem. B*, vol. 110, pp. 17998–18006, 2006.
- [21] J. Aldana-González, J. Olvera-García, M. G. Montes De Oca, M. Romero-Romo, M. T. Ramírez-Silva, and M. Palomar-Pardavé, "Electrochemical quantification of the electroactive surface area of Au nanoparticles supported onto an ITO electrode by means of Cu upd," *Electrochem. commun.*, vol. 56, pp. 70–74, 2015.
- [22] W. Z. and D. K. M.H. Holzle, "The influence of steps on the deposition of Cu onto Au(111)," *Electrochim. Acta*, vol. 40, no. 95, pp. 1237–1247, 1995.
- [23] A. Kuzume, E. Herrero, J. M. Feliu, R. J. Nichols, and D. J. Schiffrin, "Copper underpotential deposition at high index single crystal surfaces of Au," *J. Electroanalytical Chem.*, vol. 570, pp. 157–161, 2004.
- [24] L. B. Sheridan, D. K. Gebregziabihier, J. L. Stickney, and D. B. Robinson, "Formation of palladium nanofilms using electrochemical atomic layer deposition (E-ALD) with chloride complexation," *Langmuir*, vol. 29, no. 5, pp. 1592–1600, 2013.
- [25] L. B. Sheridan, J. Czerwiniski, N. Jayaraju, D. K. Gebregziabihier, J. L. Stickney, D. B. Robinson, and M. P. Soriaga, "Electrochemical Atomic Layer Deposition (E-ALD) of Palladium Nanofilms by Surface Limited Redox Replacement (SLRR), with EDTA Complexation," *Electrocatalysis*, vol. 3, no. 2, pp. 96–107, 2012.
- [26] R. G. Motsoeneng, R. M. Modibedi, M. K. Mathe, L. E. Khotseng, and K. I. Ozoemena, "The synthesis of PdPt / carbon paper via surface limited redox replacement reactions for oxygen reduction reaction," *Int. J. Hydrogen Energy*, vol. 40, 2015.

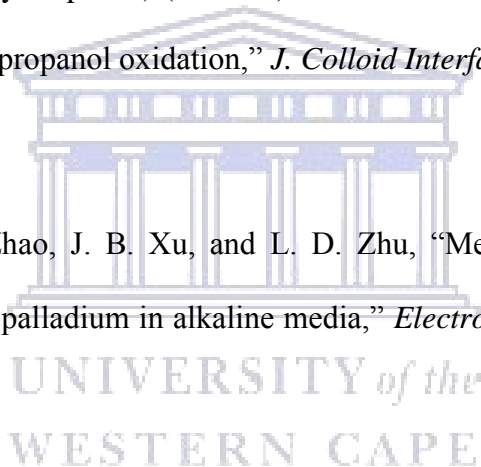
- [27] R. M. Modibedi, E. K. Louw, M. K. Mathe, and K. I. Ozoemena, "The Electrochemical Atomic Layer Deposition of Pt and Pd Nanoparticles on Ni Foam for the Electro Oxidation of Alcohols.," *ECS Trans.*, vol. 50, no. 21, pp. 9–18, 2013.
- [28] Z. Al, M. P. Mercer, and N. Vasiljevic, "Surface Limited Redox Replacement Deposition of Platinum Ultrathin Films on Gold: Thickness and Structure Dependent Activity towards the Carbon Monoxide and Formic Acid Oxidation reactions," *Electrochim. Acta*, vol. 210, pp. 520–529, 2016.
- [29] S. Henning, J. Herranz, and H. A. Gasteiger, "Bulk-Palladium and Palladium-on-Gold Electrocatalysts for the Oxidation of Hydrogen in Alkaline Electrolyte," *J. Electrochem. Soc.*, vol. 162, no. 1, pp. F178–F189, 2014.
- [30] I. Achari, S. Ambrozik, and N. Dimitrov, "Electrochemical Atomic Layer Deposition of Pd Ultrathin Films by Surface Limited Redox Replacement of Underpotentially Deposited H in a Single Cell," *J. Phys. Chem. C*, vol. 121, pp. 4404–4411, 2017.
- [31] K. Ding, G. Yang, S. Wei, P. Mavinakuli, and Z. Guo, "Cyclic Voltammetric Preparation of Palladium Nanoparticles for Ethanol Oxidation Reaction," *Ind. Eng. Chem. Res.*, vol. 49, pp. 11415–11420, 2010.
- [32] R. M. Modibedi, T. Mehlo, K. I. Ozoemena, and M. K. Mathe, "Preparation , characterisation and application of Pd / C nanocatalyst in passive alkaline direct ethanol fuel cells (ADEFC)," *Int. J. Hydrogen Energy*, vol. 40, no. 45, pp. 15605–15612, 2015.
- [33] C. Zlotea, F. Morfin, T. S. Nguyen, N. T. Nguyen, J. Nelayah, C. Ricolleau, M. Latroche, and L. Piccolo, "Nanoalloying bulk-immiscible iridium and palladium inhibits hydride

- formation and promotes catalytic performances,” *Nanoscale*, vol. 6, no. 17, pp. 9955–9959, 2014.
- [34] Kazusuke Yamanaka, “Anodically electrodeposited iridium oxide films (AEIROF) from alkaline solutions for electrochromic display device.” pp. 632–637, 1989.
- [35] I. Valsiunas and K. Juodkazis, “Iridium Anodic Oxidation to Ir (III) and Ir (IV) Hydrous Oxides,” *Electroanalysis*, vol. 17, no. Iii, pp. 947–952, 2005.
- [36] G. Stalnionis, K. Juodkazis, and J. Juodkazyte, “EQCM Study of Iridium Anodic Oxidation in H₂SO₄ and KOH Solutions,” *Electroanalysis*, vol. 17, pp. 1734–1739, 2005.
- [37] T. Reier, M. Oezaslan, and P. Strasser, “Electrocatalytic Oxygen Evolution Reaction (OER) on Ru, Ir, and Pt Catalysts: A Comparative Study of Nanoparticles and Bulk Materials,” *ACS Catal.*, vol. 2, pp. 1765–1772, 2012.
- [38] S. S. Maluf, A. L. Gobbi, and P. A. P. Nascente, “XPS and atomic force microscopy analyses of thin Au and Cu films on Pd,” *Surf. Interface Anal.*, vol. 36, pp. 931–934, 2004.
- [39] J. Cai, Y. Huang, and Y. Guo, “Bi-modified Pd / C catalyst via irreversible adsorption and its catalytic activity for ethanol oxidation in alkaline medium,” *Electrochim. Acta*, vol. 99, pp. 22–29, 2013.
- [40] F. Gao, Y. Zhang, P. Song, J. Wang, C. Wang, J. Guo, and Y. Du, “Self-template construction of Sub-24 nm Pd e Ag hollow nanodendrites as highly efficient electrocatalysts for ethylene glycol oxidation,” *J. Power Source*, vol. 418, no. August 2018, pp. 186–192, 2019.

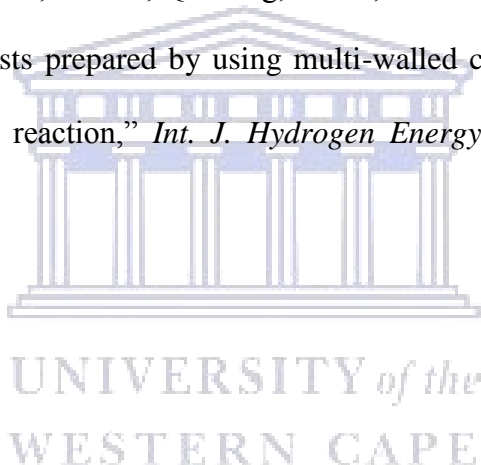
- [41] J. Bao, M. Dou, H. Liu, F. Wang, J. Liu, Z. Li, and J. Ji, "Composition-Dependent Electrocatalytic Activity of Palladium – Iridium Binary Alloy Nanoparticles Supported on the Multiwalled Carbon Nanotubes for the Electro-Oxidation of Formic Acid," *Appl. Mater. Interfaces*, vol. 7, pp. 15223–15229, 2015.
- [42] F. Huang, Z. Wan, Y. Jin, and L. Wen, "The Effects of Cyclic Isothermal Oxidation on Ir / IrO_x pH Electrode and a Method to Correct the Potential Drift of Metal Oxide Electrode," *J. Electrochem. Soc.*, vol. 164, no. 13, pp. 632–640, 2017.
- [43] S. Yao, M. Wang, and M. Madou, "A pH Electrode Based on Melt-Oxidized Iridium Oxide," *J. Electrochem. Soc.*, vol. 4, pp. 29–36, 2001.
- [44] S. Strbac, I. Sreji, and Z. Rakoč, "Electrocatalysis of hydrogen evolution reaction on Au(111) by spontaneously deposited Iridium in Acid," *J. Electrochemical Soc.*, vol. 165, no. 15, pp. 3335–3341, 2018.
- [45] I. Radev, G. Topalov, E. Lefterova, G. Ganske, U. Schnakenberg, G. Tsotridis, and E. Slavcheva, "Optimization of platinum/iridium ratio in thin sputtered films for PEMFC cathodes," *Int. J. Hydrogen Energy*, vol. 37, no. 9, pp. 7730–7735, 2012.
- [46] J. Chen, Y. Li, Z. Gao, G. Wang, J. Tian, C. Jiang, S. Zhu, and R. Wang, "Ultrahigh activity of Pd decorated Ir / C catalyst for formic acid electro-oxidation," *Electrochem. commun.*, vol. 37, pp. 24–27, 2013.
- [47] A. O. Neto, S. G. Silva, and G. S. Buzzo, "Ethanol electrooxidation on PdIr / C electrocatalysts in alkaline media : electrochemical and fuel cell studies," *Ionics (Kiel)*, vol. 21, pp. 487–495, 2015.

- [48] J. S. S. R. activity of Pd nanoparticles supported on the surface of carbon nanotubes pretreated via a sonochemical process for formic acid electro-oxidation Chen, Y. Li, S. Liu, G. Wang, J. Tian, C. Jiang, S. Zhu, and R. Wang, "Remarkable activity of PdIr nanoparticles supported on the surface of carbon nanotubes pretreated via a sonochemical process for formic acid electro-oxidation," *Appl. Surf. Sci.*, vol. 287, pp. 457–460, 2013.
- [49] X. Wang, "Dendritic defect-rich palladium-copper-cobalt nanoalloys as robust multifunctional non-platinum electrocatalysts for fuel cells," *Nat. Commun.*, pp. 1–9, 2018.
- [50] J. Chen, J. Zhang, Y. Jiang, L. Yang, J. Zhong, G. Wang, and R. Wang, "Enhanced formic acid electro-oxidation reaction on ternary Pd-Ir-Cu / C catalyst," *Appl. Surf. Sci.*, vol. 357, pp. 994–999, 2015.
- [51] K. E. Michaux and R. W. Murray, "Formation of Iridium (IV) Oxide (IrO₄) films by electroflocculation," *Langmuir*, vol. 29, no. 4, pp. 12254–12258, 2013.
- [52] A. Papaderakis, N. Pliatsikas, P. Patsalas, D. Tsiplakides, S. Balomenou, and A. Touni, "Hydrogen evolution at Ir-Ni bimetallic deposits prepared by galvanic replacement," *J. Electroanal. Chem.*, vol. 808, no. November 2017, pp. 21–27, 2018.
- [53] R. M. A. Hameed, "Facile preparation of Pd-metal oxide / C electrocatalysts and their application in the electrocatalytic oxidation of ethanol," *Appl. Surf. Sci.*, vol. 411, pp. 91–104, 2017.
- [54] O. Sahin, H. Kivrak, M. Karaman, and D. Atbas, "The Effect of Iridium Addition to Platinum on the Alcohol Electrooxidation Activity," *Am. J. Mater. Sci. Eng.*, vol. 3, no. 1, pp. 15–20, 2015.

- [55] K. A. Anna Zalineeva, Alexey Serov, Monica Padilla, Ulises Martinez and and P. B. A. Stève Baranton, Christophe Coutanceau, “Self-Supported PdxBi Catalysts for the Electrooxidation of Glycerol in Alkaline Media,” *J. Am. Chem. Soc.*, vol. 136, pp. 3937–3945, 2014.
- [56] Y. Wang, S. Zou, and W. Cai, “Recent Advances on Electro-Oxidation of Ethanol on Pt- and Pd-Based Catalysts: From Reaction Mechanisms to Catalytic Materials,” *Catalysts*, Vol. 5 pp. 1507–1534, 2015.
- [57] C. Wang, K. Zhang, H. Xu, Y. Du, and M. C. Goh, “Anchoring gold nanoparticles on poly(3,4-ethylenedioxythiophene) (PEDOT) nanonet as three-dimensional electrocatalysts toward ethanol and 2-propanol oxidation,” *J. Colloid Interface Sci.*, vol. 541, pp. 258–268, 2019.
- [58] Z. X. Liang, T. S. Zhao, J. B. Xu, and L. D. Zhu, “Mechanism study of the ethanol oxidation reaction on palladium in alkaline media,” *Electrochim. Acta*, vol. 54, pp. 2203–2208, 2009.
- [59] T. Ramulifho, K. I. Ozoemena, R. M. Modibedi, C. J. Jafta, and M. K. Mathe, “Electrocatalytic oxidation of ethylene glycol at palladium-bimetallic nanocatalysts (PdSn and PdNi) supported on sulfonate-functionalised multi-walled carbon nanotubes,” *J. Electroanal. Che*, vol. 692, pp. 26–30, 2013.
- [60] H. Xu, B. Yan, K. Zhang, J. Wang, S. Li, C. Wang, Y. Shiraishi, Y. Du, and P. Yang, “Synthesis and characterization of core-shell PdAu convex nanospheres with enhanced electrocatalytic activity for ethylene glycol oxidation,” *J. Alloys Compd.*, vol. 723, pp. 36–42, 2017.



- [61] Y. Chen, M. Cui, S. Li, J. Zhao, Y. Zhang, B. Wei, and K. Ding, “The Influence of Potential Scanning Rate on the Electrocatalytic Activity of Pyrolysis-treated PdO / Graphene for Ethanol Oxidation Reaction (EOR),” *Int. J. Electrochem. Sci.*, vol. 11, pp. 3285–3295, 2016.
- [62] N. Matinise, F. R. Ajayi, C. O. Ikpo, N. Njomo, and N. Ross, “Investigation of the electrocatalytic properties of spherical palladium nanoparticles and palladium (100) iridium bimetallic nanocomposites towards ammonia electrooxidation on Pt electrodes,” *Int. J. Electrochem. Sci.*, vol. 10, pp. 8531–8548, 2015.
- [63] K. Ding, Y. Zhao, L. Liu, Y. Cao, Q. Wang, H. Gu, X. Yan, and Z. Guo, “Pt-Ni bimetallic composite nanocatalysts prepared by using multi-walled carbon nanotubes as reductants for ethanol oxidation reaction,” *Int. J. Hydrogen Energy*, vol. 39, no. 31, pp. 17622–17633, 2014.



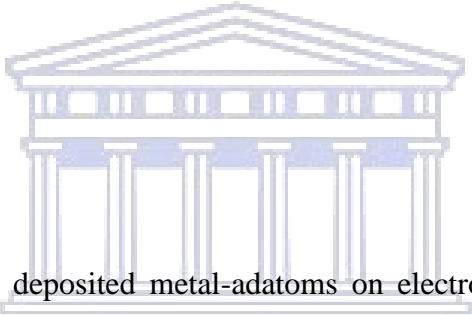
Chapter 5

5.0 Electroformation of mono metallic Pd, bimetallic CuPd, BiPd and trimetallic CuBiPd nanostructured thin film electrocatalysts using E-ALD

Summary

This chapter reports the modification of Au and Pd by alternated underpotential deposition (UPD) of double metal (Bi, and Cu) foreign adatoms using electrochemical atomic layer deposition (E-ALD). Pd thin film was formed using E-ALD cycles involving execution of Cu-UPD and SLRR at OCP.

5.1 Introduction



The effect of underpotential deposited metal-adatoms on electrochemical reactions; including anodic electro-oxidation of alcohols on PGMs-based thin films have been the subject during the last couple of decades. These UPD foreign adatoms possibly serve as a design of a unique bi-metallic surface in terms of kinetic of deposition, morphology, structure and catalytic activity. A number of Pd alloy and Pd-surface modified (Pd-M, (M = Cu, Bi-adatoms, Pb-adatoms [1] Sb-adatoms [2] catalysts have been developed for electrocatalysis of organic fuels [3] and aliphatic alcohol, including ethanol and formic acid. The increase in electrochemical activity of Pd-modified surface as compared to monometallic Pd or Pt electrocatalyst counterparts has been ascribed to effect of foreign adatoms through various mechanisms. These mechanism comprised of “third body” effect [4], electronic effect and bifunctional mechanism for oxidation of small organic molecules (SOMs) [3]. Kokkinidis and co-workers have been frequently reported Pt/ Pd modification using foreign adatoms of heavy metal such as Bi, Pb, Sb to name the few for

electrocatalysis reaction, including EOR and ORR [1]. However there are few reports on Pd-dual modified surface with dual modifier promoter elements.

In this study, we electroform bimetallic (CuPd, BiPd) and trimetallic CuBiPd thin films through Pd modification by alternated electrodeposition of Bi-UPD and Cu-UPD adatoms using E-ALD technique. The electrochemistry (UPD) of Bi³⁺ and Cu²⁺ acid electrolyte solution on Au and Pd-covered Au was determined using cyclic voltammetry for optimal depositing potential. The thin film thin films deposited via repetitive SLRR cycle of Cu-UPD followed by excursion of reductive Bi and Cu adlayer. The structure and morphology acquired thin films characterized using spectroscopic and microscopic characterization techniques. Furthermore, the redox behavior of the thin film electrocatalysts and activity towards EOR was investigated and tested using electrochemical characterization.

5.2.1 Electrochemical characterization of Bi on Au: CV profile

Underpotential deposition (UPD) of electrolyte solution of metal precursor is very crucial prior E-ALD cycle program. The UPD of the desired depositing metal was obtained from CV of the depositing metal on a substrate of interest. Generally UPD values are identified and used for the initial deposition cycle [5]. The CV profile of Au and Pd-covered Au in metal precursors are depicted in **Table 5.1**.

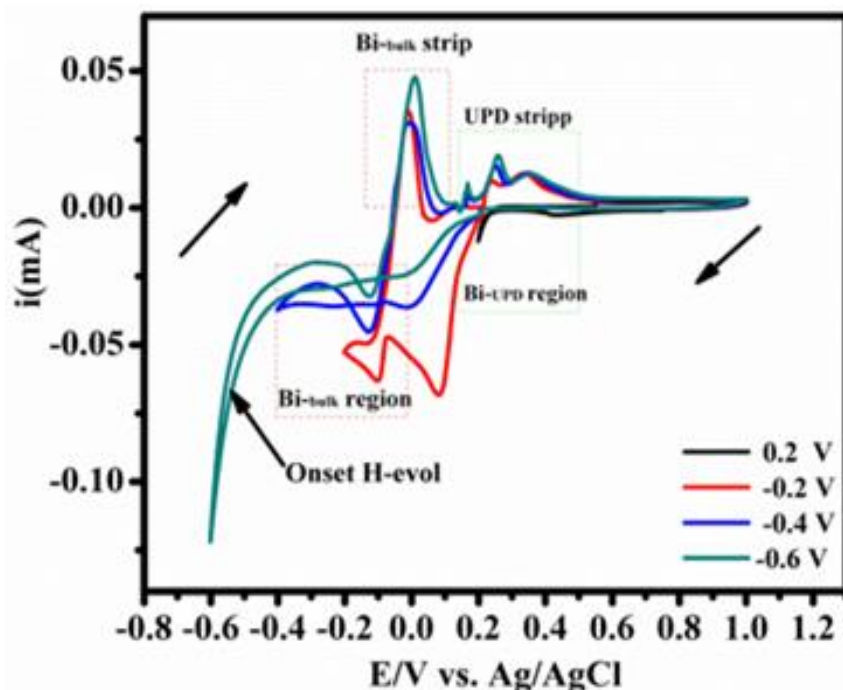


Figure 5.1: CVs of (a) Au in 0.2 mM Bi₂O₃ + 0.1 M HClO₄ at 10 mVs⁻¹.

The formal deposition potential of Bismuth in acid electrolyte can be expressed as shown in **Equation 5.1**. In the case underpotential deposition of bismuth on Au is proposed as the following expression, **Equation 5. 2**;



Figure 5. 1 shows CV of naked Au and in Bi³⁺ solution, cycled to various cathodic potential limit from 1.0 to +0.1 V, -0.1 V, -0.2 V, -0.4 V and -0.6 V. During anodic scanning a small peak appeared, which correspond to the onset Bi-_{UPD} and the peak at +0.18 V, with corresponding Bi-_{UPD} stripping at +0.35 V during anodic scan. When the scan precedes up to -0.4 V, the Bi-bulk begins and onsets hydrogen evolution emerges at -0.250 V. During anodic scan at around -0.099 to 0.001 V the peak is ascribed to bulk stripping with its peak height increases as scanning to high negative potential; Bi-bulk oxidative stripping was observed. The shape and peak assignment is consistent with previous work in literature [6], [7].

5.2.2 Electrochemical characterization of Bi on palladium (Pd) surface

Figure 5. 2 (a), depicts the CVs of Pd in a electrolyte solution of 0.2 mM Bi_2O_3 + 0.1 M HClO_4 . For comparison purpose CVs bare Au and Pd-covered Au are overlaid. It is evident that Bi^{3+} electrolyte solution occurs in a full covered Pd surface as compared to its bare Au counterparts. Pd-covered Au exhibit a stronger Bi-UPD1 and Bi-bulk stripping peak compared to its counterpart, Au. Bi-UPD1 also shows a positive potential (0.04 V) shift. This corresponds to a stronger Bi interaction with Pd than the Au. The peak developed at +0.6 V during cathodic potential and its corresponding peak at +0.85 V are attributed to reduction of Pd-O to Pd and Pd-O formation respectively. Bi-UPDs peaks are not definite in Pd-covered Au because of lack of non-faradaic (double layer) region of Pd compared to Au could be the reason to mask the Bi-UPD peaks.

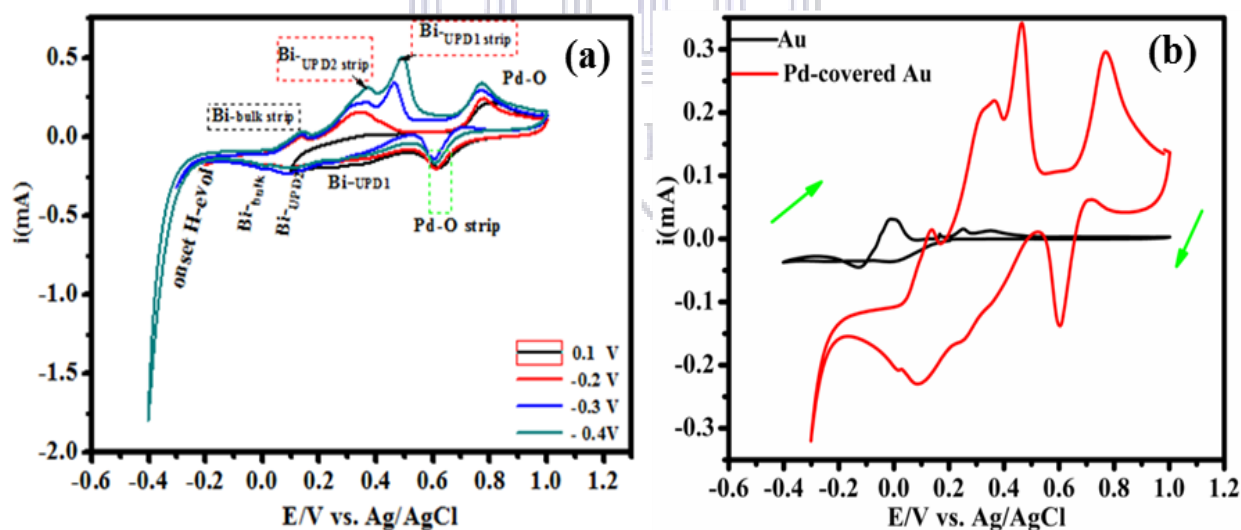
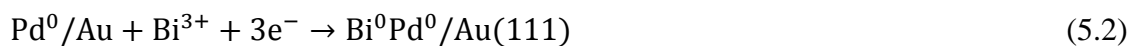


Figure 5.2: CV of Pd thin film in various cathodic limits potential (a), overlaid Au and Pd-covered Au (b) in solution of 0.2 mM Bi_2O_3 + 0.1 M HClO_4 at 10 mVs^{-1} .



5.3 Electrochemical characterization of Cu on Pd electrode: CV profile

Figure 5.3 shows reductive and stripping of a Cu-bulk and UPD on Pd electrode obtained from various cathodic potential limit. There is no prominent shift on UPD around 0.32 V regions during cathodic scanning due to the lack of double layer region in Pd inconstant to Au counterparts. However there is somehow shift in the UPD stripping peak, this should attribute to slight interaction between Pd and Cu-UPD which makes Cu-UPD reduction to occur in more positive as compared to the counterparts (bare Au). Based on CV profile identified, the optimal Cu-UPD = 0.189 V potential was used. The Pd-O peak around 0.5 V is attributed to Pd-O stripping peak, which confirm that Cu²⁺ solution occurred at Pd surface with no Au remnant. The Cu-UPD parameters on Au and Pd-covered Au are listed in **Table 5.1**. Cu-UPD potential will be then used form E-ALD cycle to electrodeposit on Pd surface via reductive Cu-UPD as depicted in **Equation 5.3**.

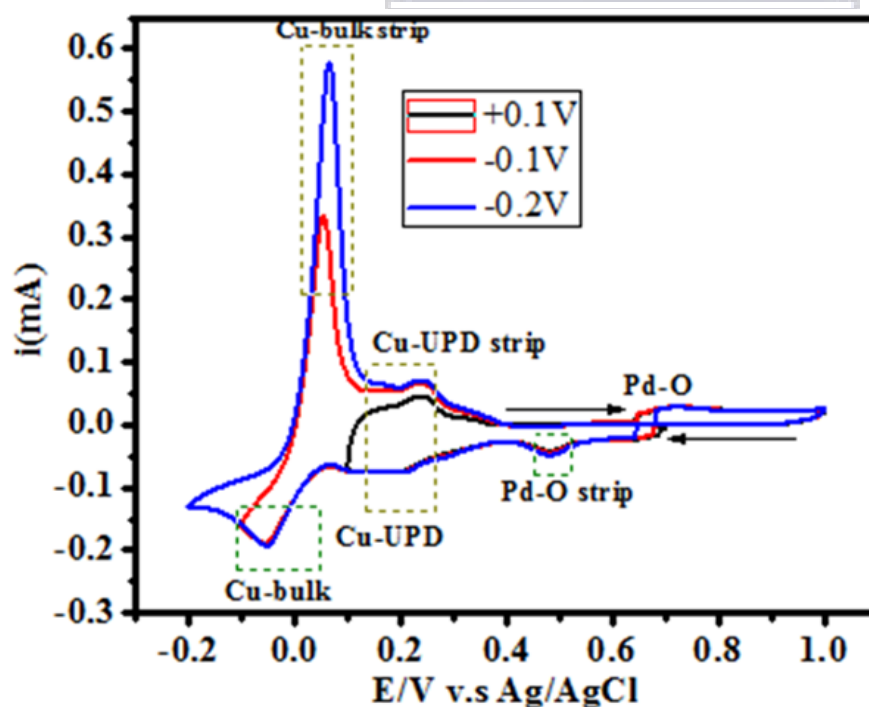
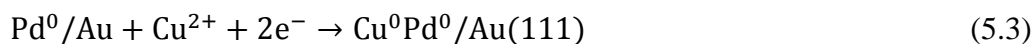


Figure 5.3: CVs of Pd thin film in 0.1 mM CuSO₄ + 0.1 M HClO₄ at 10 mVs⁻¹.



5.2.3 Electrochemical characterization of Pd-based electrodes in Bi^{3+} solution: CV profile

In **Figure 5.4 (a)** CV of Pd and CuPd electrodes in Bi^{3+} electrolyte solution are illustrated the, scanning from 1.0 to -0.4 at 10 mVs^{-1} . It can be observed that Bi^{3+} is occurring on the Pd-based electrode, which is evidenced by early features during cathodic scan that are assigned to Pd-O ox reduction peak around 0.6 V. In the proceeding scan, the Bi-UPD begins at 0.2V to 0.0 V and at higher negative potential, the hydrogen tail (H-absorption feature) occurs at -0.4 V. In a subsequent anodic scan, the corresponding stripping peaks which start with Bi-bulk stripping followed by Bi-UPD stripping peak. At higher positive potential, the intense peak is associated with Pd-O formation. For comparison purposes, various electrode surfaces (such as Au, Pd and CuPd) were exposed in Bi^{3+} solution to probe the electrode-electrolyte electron interaction relationship as displayed in **Figure 5.4 (b)**. The prominent PdO oxide positive shift around 0.6 V for CuBiPd indicates the strong Bi electron interaction with CuPd rather than more than Pd counterparts. This finding may suggest that Pd is fully covered by Cu monolayer. At this region (0.6 V), no features associated with bare Au. The interaction is also consonance by intense and positive shift of Bi-UPD strip and Pd-O ox positive shift. The CV profile data of all electrodes studied in electrolyte solutions are summarized in **Table 5.1**.

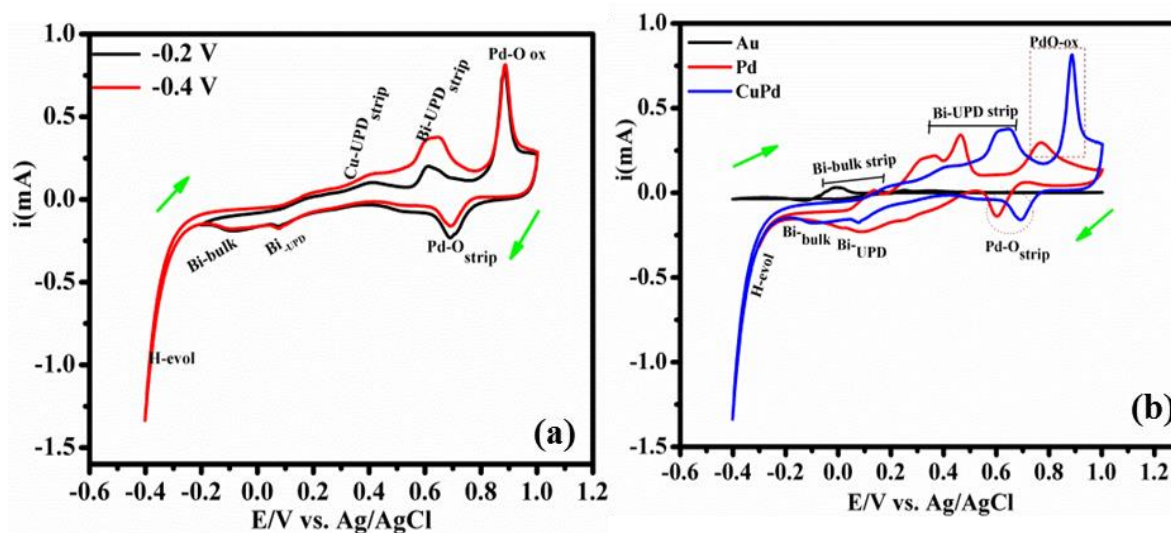


Figure 5.4: CVs of CuPd-covered Au (a), bare Au, and Pd-covered Au in 0.2 mM Bi_2O_3 + 0.1 M HClO_4 at 10 mVs^{-1} scan rate.

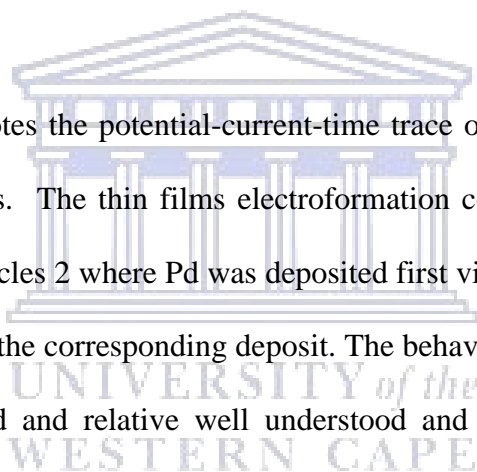
Table 5.1: Electrolyte precursor and deposition parameters

Reaction chamber/System	Species and conc.	UPD potential (mV vs. Ag/AgCl)	UPD strip potential (mV vs. Ag/AgCl)
Au in Cu^{2+}	1 mM Cu^{2+}	180	280
Au in Bi^{3+}	0.5 Mm Bi^{3+}	180-150	400
Pd in Cu^{2+}	1 mM Cu^{2+}	189 to 150	350
Pd in Bi^{3+}	0.2 mM Bi^{3+}	200 to 150	250
CuPd in Bi^{3+}	0.2 mM Bi^{3+}	200 to 0.0	450

5.2.4 E-ALD cycles of Pd modifications with foreign adatoms

In this section E-ALD cycles for the formation of Pd-covered Au and its modification using alternated deposition of foreign adatoms are elucidated. Pd-covered Au was formed through repetitive execution cycles of Cu-UPD followed by Pd SLRR at OCP to exchange Cu-UPD for Pd on Au substrate as described in literature [8],[9],[10], [11], [12]. Modification of Pd-covered Au was prepared through the two sequential steps; (i) Pd SLRR of Cu-UPD and subsequently (ii) alternated electrodeposition of reductive UPD of Bi and Cu and to form the respectively corresponding deposits Pd, BiPd, CuPd and CuBiPd deposits as described in [13] with a slight deviations.

Figure 5.5 (a) and (b) denotes the potential-current-time trace of BiPd, and CuPd respectively showing the first two cycles. The thin films electroformation consists of two sequential steps expressed as cycles 1 and cycles 2 where Pd was deposited first via SLRR of Cu-UPD followed by reductive Cu and Bi-UPD for the corresponding deposit. The behaviour of Cu-UPD sacrificial metal had been frequently studied and relative well understood and has been used before for the deposition of noble Ag, Pt and Pd metals on Au. During the set of potential at UPD = 0.18 V the current response -1000 μA was observed indicating formation of Cu-adatoms. There is a potential drift from 0.250 to 0.420 V (stop potential) during Pd fill at OCP step. The "pre-designated" stop potential (0.420 V) was set in the program (sequencer 4) to trigger the OCP during the BE flow step. Although the potential was set, there was a shift to more positive potential up to 0.586 V which is the formation of the Pd-O layer. The results are in strong agreement with literature [14] and in accordance to CV (Figure 5.2 (c)). The assignment and shape of CVs are comparable and consistent to literature [10], [15], [16]. CuPd was deposited through the repetitive alternation of Cu OCP and its reductive-UPD (0.1896 V) on Pd-covered



Au. The introduction of Cu at OCP was to avoid the Cu-_{UPD} formation of island at the ingress, which could compromise the conformity and trigger nucleation and growth process. The potential shift up to 0.38 to 0.43 V was observed during an insertion of Cu at OCP which may likely attributes to Cu-_{UPD} stripping or CuO formation on the Pd-covered Au surface. The dual promoter nanostructured thin film (CuBiPd) catalyst system was deposited by Pd SLRR of Cu-_{UPD} followed alternated repetitive Cu and Bi-_{UPD} cycles on Pd covered Au. The potential and time trace was adapted from that of BiPd and CuPd E-ALD cycle program. There was no much difference observed on OCP and current response upon set potential during alternation of Bi and Cu for corresponding CuBiPd deposition in the first 1-3 cycles (not shown here).

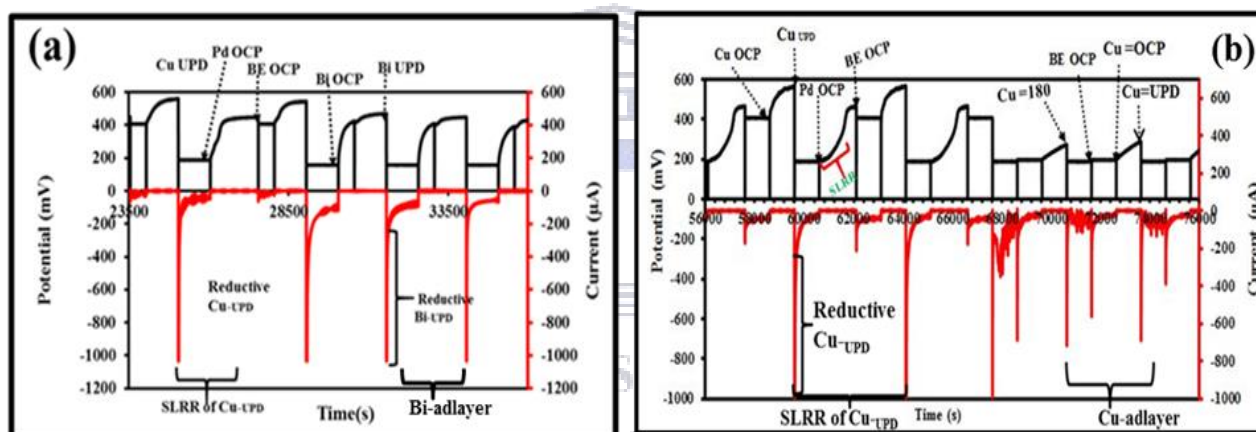


Figure 5.5: Potential-time-current trace of (a) CuBi and (b) CuPd recorded for two deposition cycles.

The surface limited redox replacement of Cu-_{UPD} to exchange for Pd on Au substrate can be expressed as in **Equation 4.5**, as articulated in previous work [17], [18], [19]. The subsequent reductive Cu-_{UPD} on palladium covered Au is represented in **Equation 5.3** and this deposition process was performed to modify the Pd-covered Au surface with Cu adatoms. The CVs obtained from modified Pd surface by Cu adatoms are in strong agreement with previous work by Kumar and Buttry [20]. CV features are not clearly identified due to lack of double layer

region (where no faradaic process takes place) of Palladium. As results of that Cu-UPD occurs simultaneous with Pd-O stripping peak. During the cathodic sweeping direction, and also Cu-bulk is obscured by hydrogen adsorption/absorption potential region as discussed in previous work [21]. During anodic scanning direction, Cu-UPD redox features were occurred around 0.336 V immediately after hydrogen dissolution. The peak assignment is consistent with literature [20], [21].

5.3.1 Characterization of the Pd-M thin film, M= Cu and Bi in 0.1 M HClO₄

Figure 5.6 illustrates all deposited thin films immersed in 0.1 M HClO₄ through flushing the solution into the thin flow cell and cycled between 1.0 and -0.2 V potential to observe the redox features. All Pd-based thin films exhibit a well-known Pd polycrystalline characteristic features such as hydrogen absorption/adsorption-desorption in (-0.198 to -0.2 V) region, Pd-O formation and its corresponding stripping (reduction) at potential around +0.6 V and 0.48 respectively and the CV peaks assignment is similar to that of literature [15], [22],[24]. However, there is an additional feature of pronounced peak around +0.33 V on CuPd in anodic sweeping, which is ascribed to stripping of Cu-UPD as discussed in previous work herein reference [81]. Pd-O reduction peak current of the thin film has the following trend: CuBiPd > CuPd > BiPd > Pd. The increase in Pd-O formation and Pd-O stripping peak which attributes to more Pd particles are dispersed on the Au surface as reported in [25], [26]. Interestingly hydrogen adsorption-desorption is limited for CuBiPd as compared to Pd, which may due to strong interaction between Pd with adatoms as well as negative shifting of H-desorption peak, weakened Pd-H bond due to low binding to the d-band center as discussed by [27]. The CV shapes of the thin film similar and consistent with literature [18], [24], [28], [29], [30], [31], [32].

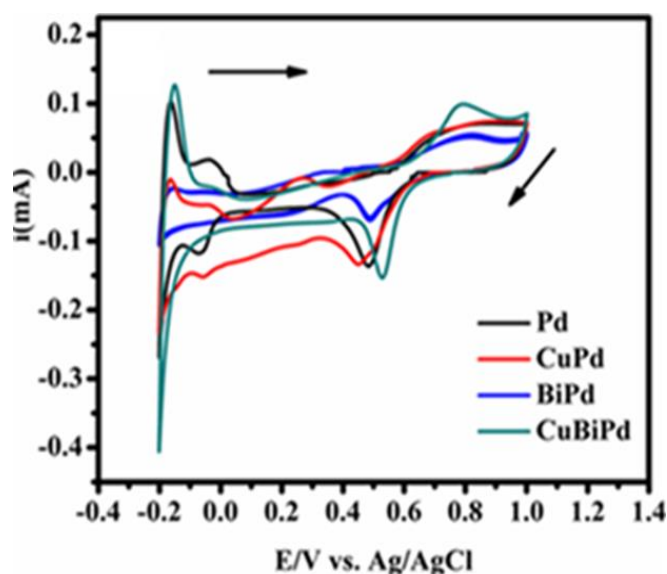


Figure 5.6: CV of Pd-M based thin film in 0.1 M HClO₄ at 30 mVs⁻¹ scan rate.

5.3.2 Effect of potential and scan rate study of CuBiPd thin film in 0.1 M HClO₄

The most behaving nanostructured such as trimetallic (CuBiPd) thin film has been scrutinized in 0.1 M HClO₄ at various potential window (+1.0 V; 1.2V; 1.4V) **Figure 5.7 (a)** and scan rates (40, 30, 25, 20,10) mVs⁻¹ **Figure 5.7 (b)** to provide an insight to its stability. The results are displayed in **Figure 5.7 (c)** with the Randles-Sevcick plot to check the linearity of peak current as a function of scan rates. It can be seen during anodic and cathodic scanning direction that the Pd-Ox formation and the corresponding Pd-Ox reduction is increasing as potential window increasing to a higher positive potential. It is apparent that Pd-Ox reduction peaks increases and subsequently show a negative ($\Delta E = -0.6$ V) shift potential as potential window increases, the results are in good agreement in literature [15], [20]. The Au surface coverage is function of the potential window, AuOx reduction is found at 0.9 V therefore by the window opening up to 1.4, the peak would have occurred. The disappearance of Au-oxide reduction around +0.9 V from Au and the emerging of Pd-O reduction around + 0.48 V as displayed by overlaid Au and Pd-based thin film verifies that Au is fully covered by Pd thin film. This finding indicates the complete surface coverage of Au, which may suggest the homogeneous distribution of CuBiPd on Au with

no surface defects. Scan rates effect study shows linearly peak current increases with an increase in scan rate. This proportionality is also confirmed by the correlation coefficient (0.984 \sim 1) observed with Randles-Sevcik plots (**Figure 5.6 (c)**) which suggest that CuBiPd thin film in 0.1 M HClO₄ possess diffusion-controlled electrocatalyst (electrode) features as explained in literature [33].

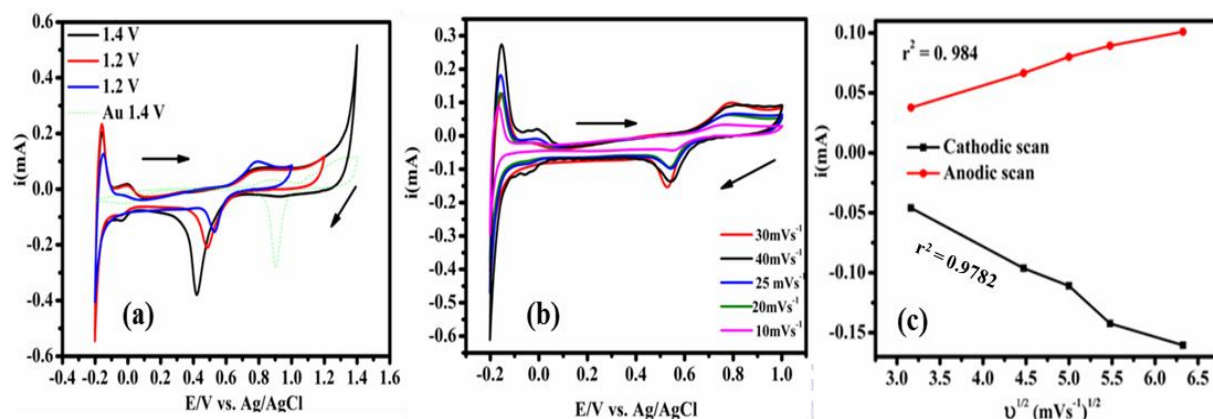


Figure 5.7: CuBiPd in 0.1 M HClO₄ at various potential window (a), scan rates (10, 20, 25, 30 and 40) mVs⁻¹, and Randles-Sevcik plot (c).

The thin film (CuBiPd) possesses the requirements of a quasi-irreversible system, based on a slight difference in peak position (ΔE) between (E_a) of PdO reduction and its corresponding PdO oxidation current and the ratio of anodic and cathodic (I_{pc}/I_{pa}) peak current is almost unit. Using Randles-Sevcik equation, (**Equation 5. 4**) to study the kinetics of electrode-electrolyte reaction process, **Figure 5.7 (b, c)** implies that the electrochemical reactions rate is quite fast and the reduction of Pd-Ox on CuBiPd electrode.

$$I_p = 0.4463 nFA(RTnF)^{1/2}D^{1/2}v^{1/2}C_0 \quad (5.4)$$

5.4.1 X-ray diffraction of Pd-M based thin film

Figure 5. 8 shows XRD pattern of bare Au and as-prepared Pd-based thin films. The XRD patterns reveal four main Bragg's diffraction angles around 38.5°, 56°, 66°, 72.86° and 79. 88.6°

corresponding to the (111), (200), (220), (311) planes of face-centered cubic (fcc) of metallic Pd phase characteristic features in accordance to standard certification (JCPDS card no. 89-4897) and similar to literature [33],[34],[35],[36],[37]. Au bare exhibits polycrystalline phase as elucidated in previous studies [18], [38]. For a clear observation, (111) was magnified as shown in **Figure 5.8**: insert. CuPd shifted to a higher 2θ , indicating an alloy formation, and insertion of Cu adatoms into Pd crystal lattice [39], replacing some Pd atoms resulting to reduction/contraction of Pd (fcc) because Cu has smaller atomic radii as similar observation by [29], [40], [41], [42]. There was no obvious diffraction peak observed for elemental Cu, implying the single-phase PdCu alloy as discussed in the literature [43]. Interesting CuBiPd shows a shift to a lower 2θ angle respectively to Au, and Pd at (111) and (220) planes which are likely to attribute electron interaction between Cu and Bi on the surface of Pd. Bi adatom is also evident at low $2\theta = 20^\circ, 18^\circ$ and 10° region attributed to (110, 100 and 102) planes respectively, and the assignment of peaks is consistent with previous work [44], [45], [46], [47]. BiPd also showed a significant shift to higher 2θ value respective to Pd and Au, which may indicate some alloy formation and too strong electron interaction of Bi-adatoms with Pd surface, and are in good agreement with CV data(see **Figure 5.6**), whereby Bi inhibited hydrogen absorption due to Bi insertion into Pd crystal lattice. In addition, all deposits were preferred orientation of Pd/Au (111) plane. The additional peaks at lower 2θ may indicate the elemental Bi for the corresponding deposits. Conclusively, the addition of adatoms tailored the structure of Pd similar to the literature [48] and in accordance to CV results (**Figure 5. 6**).

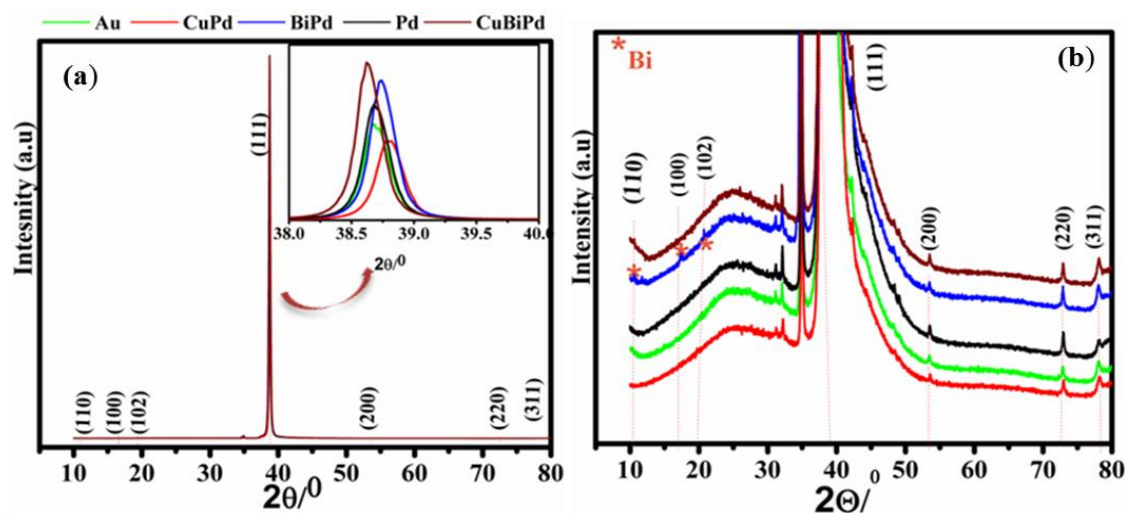


Figure 5.8. (a) Whole XRD pattern of Au, Pd, BiPd, CuPd, and CuBiPd, magnified (111) plane: insert and (b) Magnified whole XRD pattern.

5.4.2 Scanning electron microscope (SEM) analysis of Pd-M based thin films

Figure 5.9 (a-d) displays SEM images results at low magnification and with insert high magnification of as Pd-based thin films. All the SEM micrographs of the nanostructured thin film in **Figure 5.9** indicated flat particles that are in nano-size, dominating homogenous particle dispersion. Pd (**Figure 5.9 (a)**) shows uniformly closely packed nanoparticle, almost not visible with the naked eye. This finding is ascribed to Pd atomic deposition via SLRR of Cu-UPD, which indicates epitaxial growth along Au crystalline surface. It can be seen in **Figure 5.9 (b)** CuPd showed a well distinct particles with conformal distribution of Pd nanoparticles, which is more clear in high magnification (**Figure 5.9 (b):** insert) and small (scattered back spots like particles) which likely ascribed to the corresponding Cu-adatoms and its oxide respectively (due to air contact). In **Figure 5.9 (c)** BiPd exhibit flat uniform quasi-spherical small particles that formed a layer, covering the Pd surface. This may attribute to some 2D growth and the hetero-epitaxial relationship between Bi and Pd surface. It is obvious that the particles are attributed to Bi-adatoms, two potholes like surface, exposing the Pd particle underneath Bi-adlayer, this evidence Pd -modified by Bi adlayer. The spherical Bi particles begin to form an island (agglomeration) as

manifested at low magnification (see **Figure 5.9 (c)**: insert). In **Figure 5.9 (d)**, CuBiPd micrograph displays two phases, i.e., a knife-edge shaped/nanobelts) like a particle at high magnification (**Figure 5.9 (d)** insert)) 1, and small spherical particle on Pd surface. These findings are likely due to Cu-adatoms on the BiPd surface and Bi-adatoms on the Pd surface respectively. Interestingly in CuBiPd exhibited scattered nanoribbons (nanobelts) are clearly observed and are at low magnification as displayed in **Figure 5.9 (d)**. Conclusively, the finding evidence the modification of the Pd surface with foreign adatoms deviated and distorted the Pd morphology, which is in agreement discussion articulated in electrochemical (CV) characterization (see **Figure 5.6**).

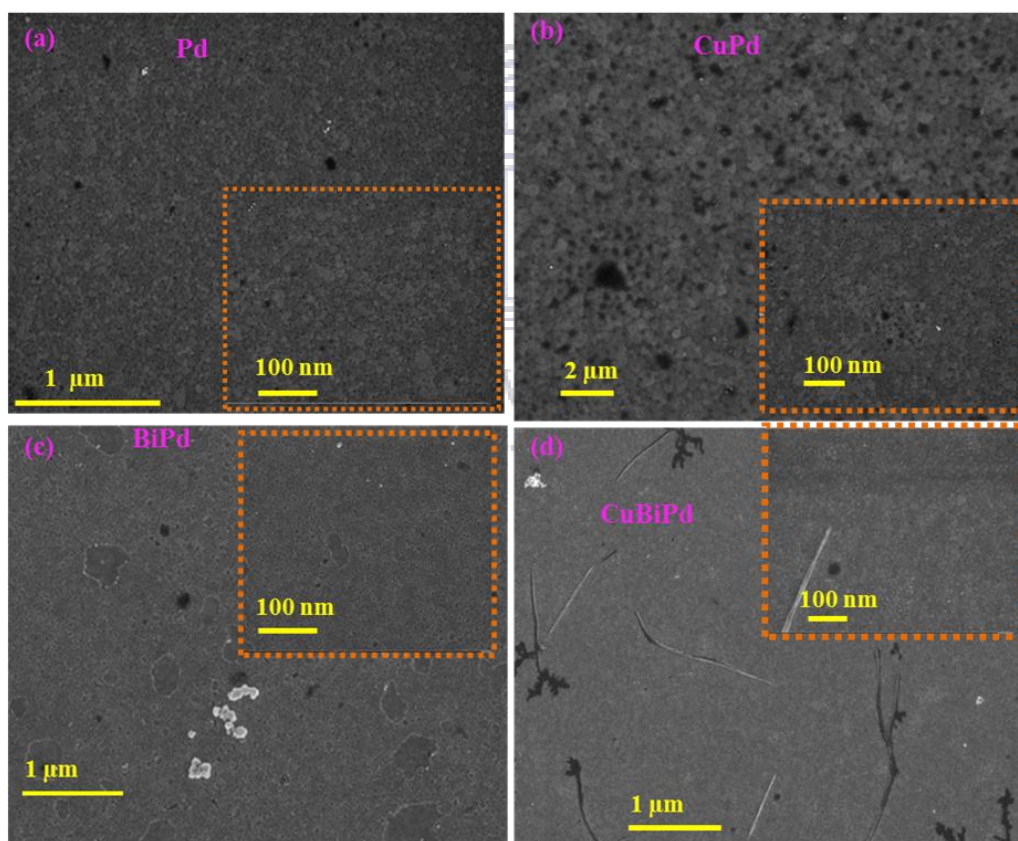


Figure 5.9: Illustrates the low magnification SEM micrographs of Pd (a), CuPd (b), BiPd (c) and CuBiPd (d) and their corresponding high magnification: (inserts).

5.4.2 Energy dispersive X-ray analysis and elemental distribution of Pd-M based thin films

The EDS pattern (**Figure 5.10 (a: insert)**) confirms the existence of elemental Pd, Cu, and Bi for their respective corresponding deposits (Pd, CuPd, BiPd, and CuBiPd) on Au. Elemental mapping (**Figure 5.10 (a: insert)**) (in of monometallic Pd shows the dominant distribution of elemental Pd across the Au substrate and reveals no Cu detected, denoting the exchange of Cu-_{UPD} for Pd during SLRR at OCP. Elemental mapping of BiPd shows uniform distribution of Bi and Pd which corroborate with SEM image, with Bi conformal/homogenously distributed throughout the Pd surface which indicates the modification of Pd by Bi-adatoms. The conformal distribution of elements across the substrate may likely be attribute to 2D growth according to literature. In addition, the homogenously distributed Bi suggests the 2D growth on the palladium surface, which is consistent to layer by layer formation. Composition distribution for CuPd and CuBiPd reveals the distribution of corresponding elements on the whole substrate, with Pd dominating the surface. Conclusively SEM-EDX and elemental mapping evidence the existence of constituents' component of Pd and modifiers (Cu, Bi) and subsequently confirming the electrodeposition of Pd and its modification by foreign adatoms.

UNIVERSITY of the
WESTERN CAPE

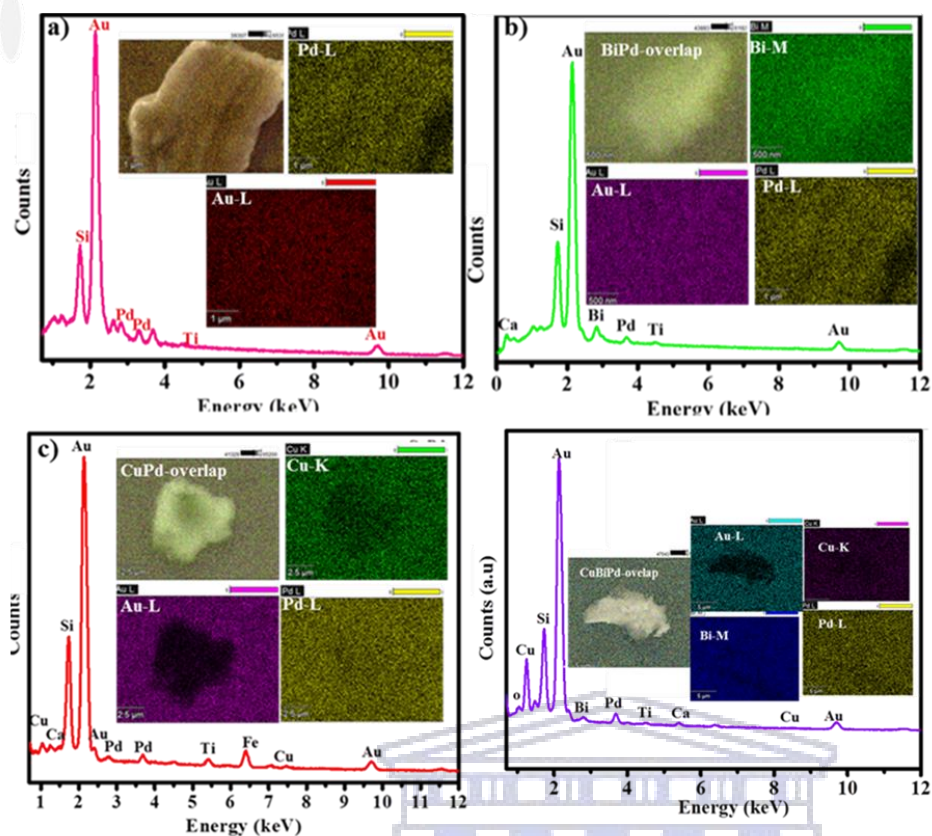
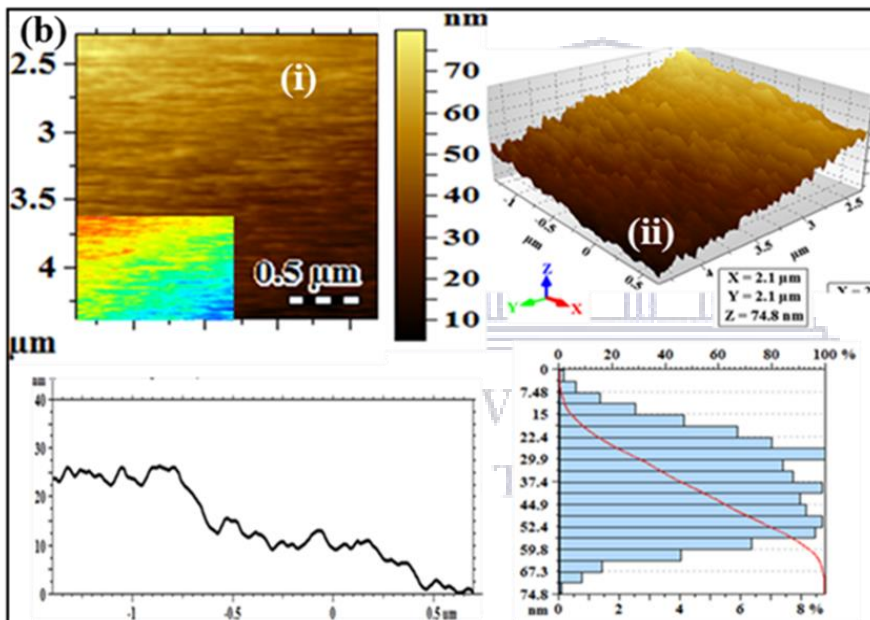
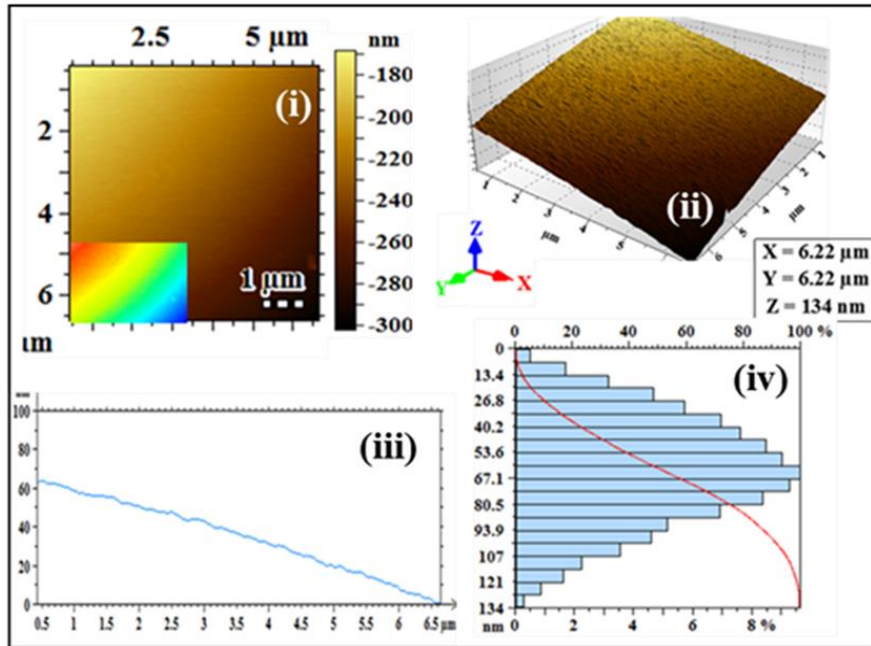


Figure 5. 10: The illustrate elemental of EDS and corresponding elemental mapping (insert) of (a) Pd, (b) BiPd and (c) CuPd, (d) CuBiPd.

5.4.5 Atomic force microscopy (AFM) analysis bimetallic CuPd, BiPd, and CuBiPd

AFM was used to probe the surface morphology, surface texture the technique also attain microscopic and topographic information on the surface topographic of thin films. Thus AFM micrographs quantify average roughness (Ra) and root mean square roughness (Rq)/ (r.m.q) from AFM data. **Figure 5.11** depicts AFM topographic micrographs of Pd, BiPd, CuPd, and CuBiPd, side, zoomed image (insert), the 3D view, and their corresponding texture profiles. It can be observed that 2D and 3d micrographs of Pd has a flat surface, which could be due growth of Pd (**Figure 5.11 (a)**) along Au nanostructure orientation. CuPd (**Figure 5.11 (c)**) 2D and 3D images and mapping (insert) indicate the honeycomb structure formation and also the texture profile (east-west cross-section) is consistent with the images. The 3D of CuPd micrographs reveals core

(Pd particles) and a shell (Cu-UPD adlayer) is well pronounced. BiPd (**Figure 5.11 (b)**) showed coalesced Bi grains which result to nucleation and growth (3D) growth process of Bi microstructure covering the Pd surface. The 2D micrographs of CuBiPd reveal evenly distribution of distinct grain size. These particles form an island which may signify that Cu is deposited on Bi neighboring nanostructures on Pd-covered Au. The thin film clearly distinguishes each other with the calculated roughness trend as follows: CuBiPd = (Sa= 43.0 nm, Sq= 55.0 nm) > CuPd= (Sa= 53.0 nm, Sq= 62.7 nm) > BiPd (Sa= 24.6 nm, Sq= 30.1nm) Pd (Sa= 21.6 nm, Sq= 26.4 nm). The high roughness corresponds to an increase in crystalline texture upon the addition of adatoms on Pd-covered Au. The cross-section analysis of AFM image reveals that most particles obtain the heights of (30-60 nm) for all bimetallic nanostructures which suggest the layer-by-layer 2D growth. Incontrast to bimetallic compounds, the trimetallic (CuBiPd) compound shows additional islands with height ranging from 90-100 nm, suggesting continuous 3D growth process upon the addition of the third metal. In the case of BiPd thin films a define grains formation, islands and inhomogeneity surface are shown. The texture profile of CuPd aligns with 2D (honey-comb structure). The histogram shows that the nanostructures of the BiPd and CuPd thin films are conformal-distributed (50-163 nm and up to 88 %) for, and agglomerated-distributed for BiPd (16 nm -72 nm up to 88 %).



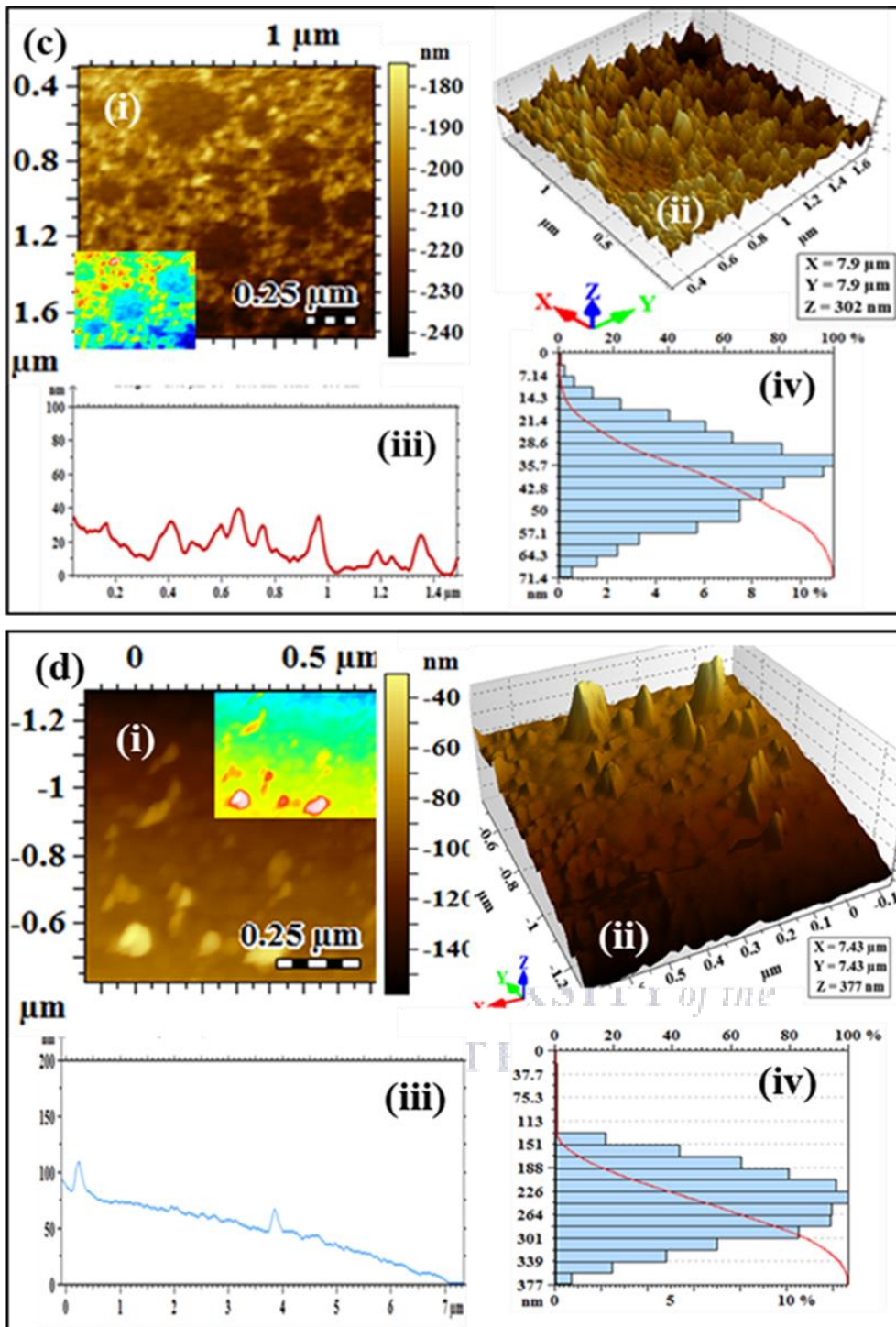


Figure 5.11: Reveals details of Atomic force microscopy (AFM) analysis for (a) Pd, (b) BiPd, (c) CuPd, and (d) CuBiPd.

5.5. Electrochemical characterization Palladium-based thin film: Activity towards ethanol oxidation in alkaline media

5.5.1 Activity of Pd-M based thin film electrocatalysts towards ethanol oxidation in alkaline media: Cyclic voltammetry (CV)

A series of cyclic voltammetry (CV) was used to probe the electrocatalytic activity of the thin films. The Pd based thin films investigated were monometallic Pd on Au, bimetallic CuPd, BiPd, and CuBiPd. In this experiment, an electrolyte solution of 0.1 M EtOH + 0.5 M KOH was prepared with ultrapure water $18.2 \mu\text{S cm}^{-1}$ and it was deaerated for 1 hour before use, during the experiment N_2 gas was allowed to flow over the solution. The ethanol oxidation reaction, showing the rate-determining step is as described in literature [49], [50],[51],[52],[53],[54].

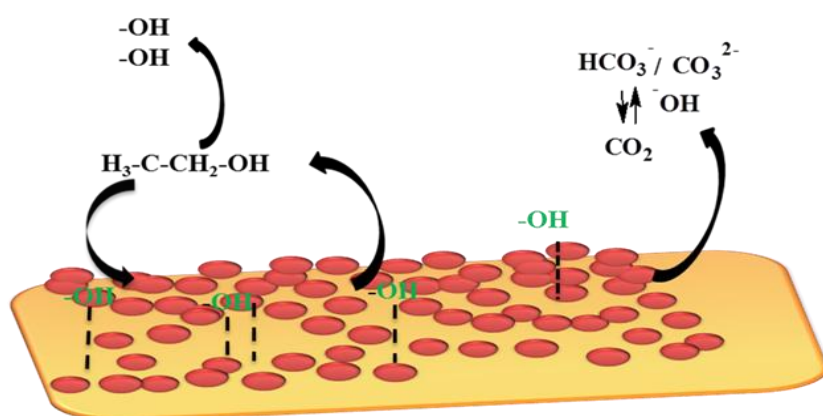
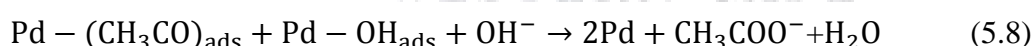
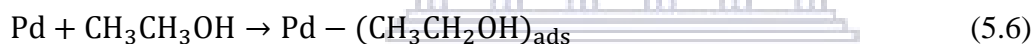


Figure 5.12: Illustration of reaction mechanisms of EtOH oxidation on Pd-based nano-structured thin film surface, as adopted from [52].

As illustrated in **Figure 5.12** and **Equations 5.6-5.7**, EOR intermediate undergoes adsorbed acetyl on Pd-surface which can possibly block Pd-active sites. Therefore it means, EOR on the Pd-M adatoms modified surface may be explained as a bifunctional mechanism as generalized in the rate-determining step in **Equation 5.8**. This fact may indicate that the adsorbed EtOH reaction intermediates formed during EOR may be stripped off the Pd surface by oxygen-containing species adsorbed. In this case (study), the incorporation of the electrocatalyst promoter species such as Bi and Cu adatoms in Pd aids the activation of H₂O dissociation to form hydroxyl (OH) on the Pd surface which may further oxidize CO intermediates and relatively enhances electrocatalytic activity.

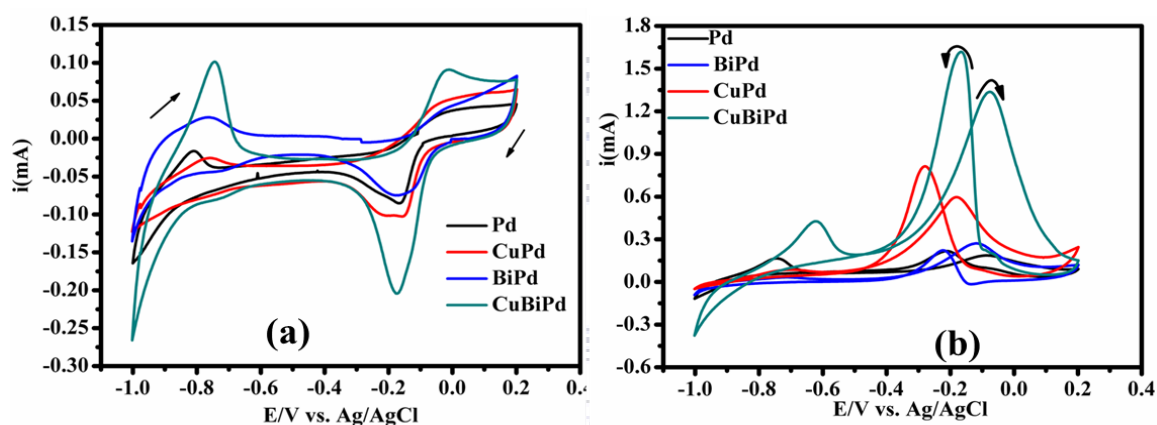


Figure 5.13 : CV of Pd, CuPd and BiPd and CuBiPd in 0.5 M KOH (a) and in 0.5 M KOH+ 0.1 M EtOH (b) at 30 mVs⁻¹.

Table 5. 2: Summary of electro-oxidation activity of Pd based electrocatalyst towards ethanol in alkaline media

Thin films	Forward peak current; I_f (mA)	Reverse peak current, I_b (mA)	Onset (V)	I_f/I_b ratio	ECSA (cm ²)
Pd	0.18696	0.2170	-0.35	0.86	0.367
CuPd	0.587	0.808	-0.45	0.744	0.523
BiPd	0.275	0.220	-0.384	1.244	0.407
CuBiPd	1.35	1.60	-0.482	0.84	0.773

Figure 5.13 (a) depicts CVs of Pd, BiPd, CuPd, and CuBiPd on Au in 0.5 M potassium hydroxide (KOH) solution. All Pd nanostructured thin film shows a typical Pd voltammetric features in KOH and ethanol. During anodic scanning direction all Pd thin film exhibited well-pronounced peaks of Pd-O/Pd-OH formation around 0 to 0.199 V and its corresponding stripping to metallic Pd at -0.1 to -0.2 V in the negative sweeping, agreeing with the literature [33], [35], [36],[51]. Hydrogen adsorption-desorption is manifested at high negative potential region around -0.95 to -0.1 V. Hydrogen adsorption-desorption is manifested at high negative potential region around -0.95 to -0.1 V. Furthermore, trimetallic CuBiPd and bimetallic (BiPd, CuPd) compounds shows a prominent and broad Pd-O reduction which indicates that Bi and Cu adatoms occupies high coverage of Pd-covered Au surface and there is a strong interaction between Pd and adatoms which is consistent with previous work by Zalineeva et al [25]. The distinct Pd-O formation and stripping potential on Pd and modified-Pd imply the deviation in electronic structure as articulated in literature [55] upon the modification of Pd by adatoms. The interaction also consonance with XRD results, whereby CuBiPd showed an obvious shift to a low 2θ value, signifying insertion of Bi into the Pd crystal lattice resulting in some alloy

formation which aligns with previous work by Cai et al [34]. The proportionality of current is associated with Pd-O stripping peak charge which is expressed in **Equation 5. 9**;

$$\text{ECSA (Pd)} = \frac{Q_{\text{PdO}}(\mu\text{C})}{405\mu\text{C} \cdot \text{cm}^{-2}} \quad (5.9)$$

Where ECSA is an electrochemical active surface area, Q_{PdO} charge calculated by integration of the area under CV Pd-O reduction peak, charge value of $405 \mu\text{Ccm}^{-2}$ is estimated for reduction of Pd-O monolayer, m_{Pd} represents loading of Pd on the working electrode. The ECSA is strongly related to intrinsic activity [56], CuBiPd denotes the highest Pd-O stripping charge followed by CuPd. The ECSA of Pd-M thin film electrocatalyst has the following trend: CuBiPd (0.773 cm^2) CuPd (0.523 cm^2) BiPd (0.407 cm^2) Pd (0.367 cm^2). These results show a directly proportional to intrinsic activity induced by intra-atomic charge transfer between Pd and adatoms.

The electrochemical activity of as-prepared nanostructured thin films for EOR was explored in 0.5 M KOH containing 0.1 M ethanol (EtOH) solution using CV, in **Figure 5.13 (b)**. All Pd-thin films showed two typical well-distinct ethanol oxidation peaks, that is oxidation of ethanol during forward scan (i_f , E_a), and re-oxidation or removal of carbonaceous species during backward scan (i_b , E_c) as described in literature [49], [57], [58], [59], [60], [61] At high negative potential, hydrogen adsorption-desorption is suppressed by adsorbed ethanol ethoxy $(\text{CH}_3\text{CO})_{\text{ads}}$ species on the thin film surface [37], [51], [55] (**Equation 5. 8**). The as-prepared nanostructured thin films showed a distinct trend of catalytic activity features, such as onset potential, forward peak current (i_f) response and backward peak current (i_b) response. The Onset potential of the thin films has the following order: CuBiPd (-0.482 V) > CuPd (-0.45 V) > BiPd (-0.384 V) > Pd (-0.35 V). This finding suggests that both bimetallic (mono modified-Pd) CuPd and trimetallic (dual modified-Pd) CuBiPd compounds respectively require the least activation energy to oxidize ethanol as discussed in the literature [52], [62], [65], [68]. The highest peak current was

obtained with CuBiPd (1.35mA) respective to CuPd (1.35 mA, BiPd (0.275 mA) and Pd (0.186 mA). This may suggest an enhanced electron shuttle (diffusion) for CuBiPd as compared to its counterparts. The high electron diffusion is related to high electron cloud [59], which is attributed to dual promoter (CuBi) species on the Pd-modified surface. Although BiPd shows the lowest peak current and positive onset potential among bimetallic, it also displays an improved current response as compared to the Pd, owing to the addition of Bi adatoms. In addition, BiPd showed the highest poison-tolerance (i_f/i_r ratio= 1.233) > CuBiPd (i_f/i_r ratio = 0.94) > CuPd (0.745) signifying the interaction of Bi adatoms with Pd [24],[70]. The highest i_f/i_r ratio of BiPd and CuBiPd is likely due to anti- poisoning ability of Bi [44], whereas CuBiPd compound may attribute to increasing oxygen affinity by dual (CuBi) adatoms on Pd which may completely strip off carbonaceous species through electronic effect, and bifunctional mechanism as described in [8],[36]. Interestingly, CuBiPd show a steeper reverse current as compared to BiPd, this finding may possibly due to the developed oxides on Pd surface. However, the details on adsorbed species on catalyst surface must be careful interpreted by considering in situ CV-Fourier transform infrared spectroscopy (FTIR) as recommended by literature [52], [62]. Given the fact that during the forward scan, Pd(II)-oxides possibly develops as also shown by **Equation 5.8**, then the reduction of the Pd(II) oxide may give high reactivation (reverse) current, then the reduction of the Pd(II) oxide may give high reactivation (reverse) current [54]. The more negative onset binary compounds incorporated by Bi and Cu are ascribed to their oxophilicity character, they tend to form M(OH)_x moiety at a lower potential which lowers the onset potential corroborating with observations in the literature [63], [41]. The oxygen-containing species promotes the bifunctional mechanism during EOR because they increase the concentration of hydroxyl on the catalyst surface to lower the onset and subsequently increase the tolerance of catalyst to poisoning by EtOH intermediates as described in literature [64],[65]. The ‘dual promoter’ electrocatalyst (CuBiPd) system is evidenced by higher current response compared to

single promoters (BiPd and CuPd) as shown in **Figure 5.13 (b)**. The electro-oxidation activity of Pd-M based electrocatalyst towards ethanol in alkaline media is summarized in **Table 5.2**

5.5.2 Scan rate dependence studies of CuBiPd catalyst.

The electro-oxidation of ethanol in KOH occurred effectively and high when using trimetallic CuBiPd thin film. Therefore it is of great interest to scrutinize or interrogate the electrochemical behaviours of trimetallic CuBiPd thin film in both 0.5 M KOH (**Figure 5.14 (a-b)**) and 0.5 M +0.1 M EtOH (**Figure 5.14 (c-d)**). The CV features were recorded at various scan rates (10, 20, 25, 30, 40) mVs^{-1} to study the stability of CuBiPd during ethanol oxidation. It can be observed that the peak current increases with an increase in scan rate in both KOH and KOH containing EtOH. These findings suggest both electrochemical reactions are a diffusion-controlled process. This linearity (proportionality) is supported and confirmed by the Randles-Sevcik plot by plotting peak current as a function of the square root of the scan rate (v), which showed a linear regress with a correlation coefficient of $r^2 = 0.9941$ (see **Figure 5.14 (b)**). These results also provide the evidence that the CuBiPd thin film is stable and electroactive in 0.5 KOH and 0.5 M KOH containing 0.1 M ethanol solution. However, this electrochemical reaction system showed irreversibility process, with the fact that the calculated forwards (anodic) and reverse (cathodic) peak current ratio (i_f/i_r) is not equivalent to unity ($\neq 1$) and the $\Delta E = 159 \text{ mV}$ for KOH which is greater than 59 mV ($\Delta E > 59 \text{ mV}$).

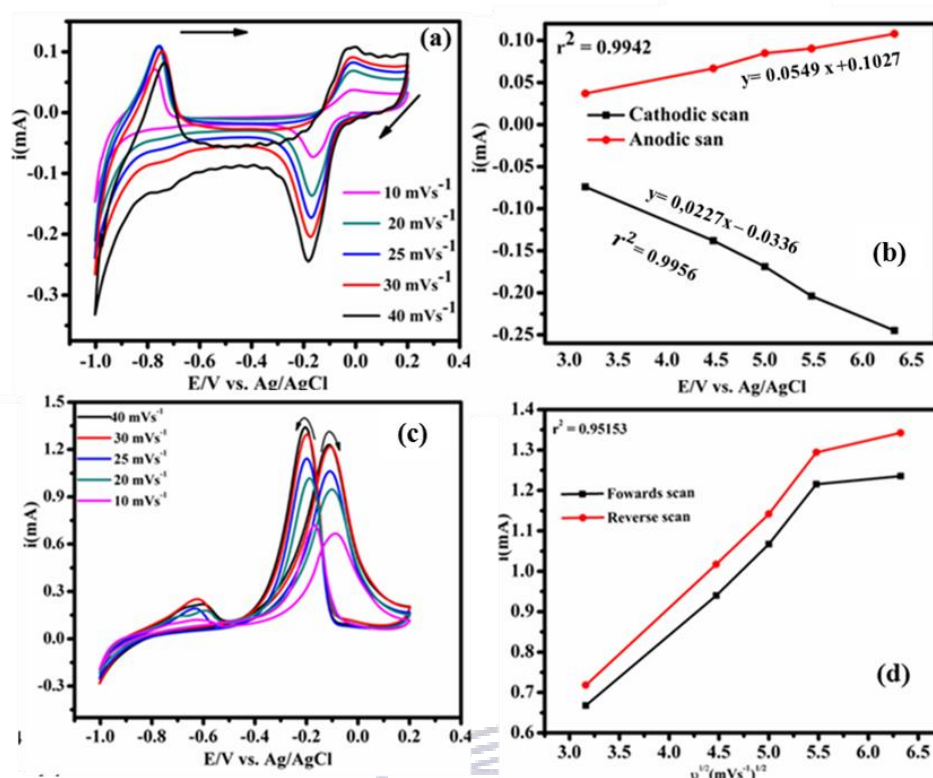


Figure 5.14: CVs and corresponding Randles-Sevcik plot of CuBiPd thin film in (a-b) 0.5 M KOH and (c-d) 0.5 KOH+ 0.1 M EtOH at various scan rates (10, 20, 25, 30, 40) mVs⁻¹.

Randles-Sevcik equation, (**Equation 5.10**) was employed to study the kinetics of electrode process, **Figure 5.14** implies that the electrochemical reactions rate is quite fast and the reduction of Pd-Ox on CuBiPd electrode (**Figure 5.14 (a-b)**) as well as EtOH oxidation (**Figure 5.14 (c-d)**) is a typical diffusion controlled-process.

$$I_p = (2.69 \times 10^5) n^{2/3} A C D^{1/2} \nu^{1/2} \quad (5.10)$$

5.5.3 Chronoamperometric (CA) analysis of Pd-M based thin film in 0.5 KOH + 0.1M EtOH

Chronoamperometry was used to investigate the stability of as-prepared nanostructured thin film in 0.5 M + 0.1 M EtOH at the fixed potential of -0.2 V, and effect of adatoms into the stability of

ethanol oxidation (**Figure 5.15**). The initial high current observed is ascribed to double-layer charging or available active site of Pd nanostructured thin films as explained in previous studies [66]. The quick current decay during the first few minutes presumably due to the gradual accumulation of strongly adsorbed carbonaceous (EtOH intermediates) species [52], [62] to the active site of electrocatalysts which is consistent with previous work [55]. Subsequently, the current response gradual decreases till it reaches a pseudo-steady-state, at this state CuBiPd (0.05 mA) continued to have the highest peak current followed by BiPd (0.05 mA) for up to 100s where BiPd coincide Pd. All the bimetallic compounds show a higher current response compared to monometallic Pd, indicating that the addition of adatoms on the Pd surface enhances activity and stability. The activity and stability of compounds are in accordance with the obtained CV results (**Figure 5.13 (b)**).

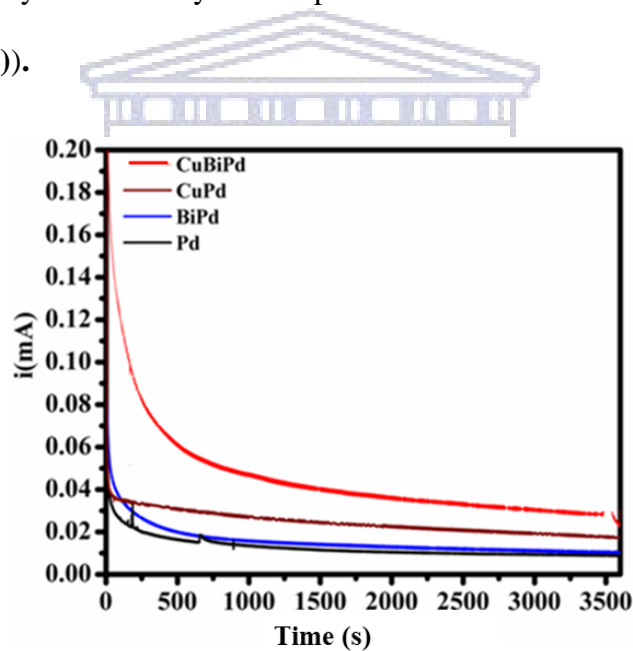


Figure 5.15: CA of Pd (black), BiPd (blue), CuPd (red), CuBiPd (dark green) and zoomed: insert in 0.5 KOH+ 0.1 M EtOH at fixed -0.2 V potential for an hour (3600s) duration.

5.5.4 Electrochemical impedance spectroscopy of Pd-M based thin film towards EtOH oxidation

EIS analysis was used to investigate the interfacial properties of the four thin films; Pd, BiPd, CuPd, and CuBiPd electrodes. Nyquist and Bode Plot were used in **Figure 5.16. (a)** and **(b)** in 0.5M + 0.1M EtOH solution at -0.2 V applied potential. The small semicircle in the Nyquist plot in the high-frequency region is due to double layer-capacitance between electrode interface and electrolyte denoted as R_s (resistance). Electrochemical impedimetric parameters are summarized in **Table 2**.

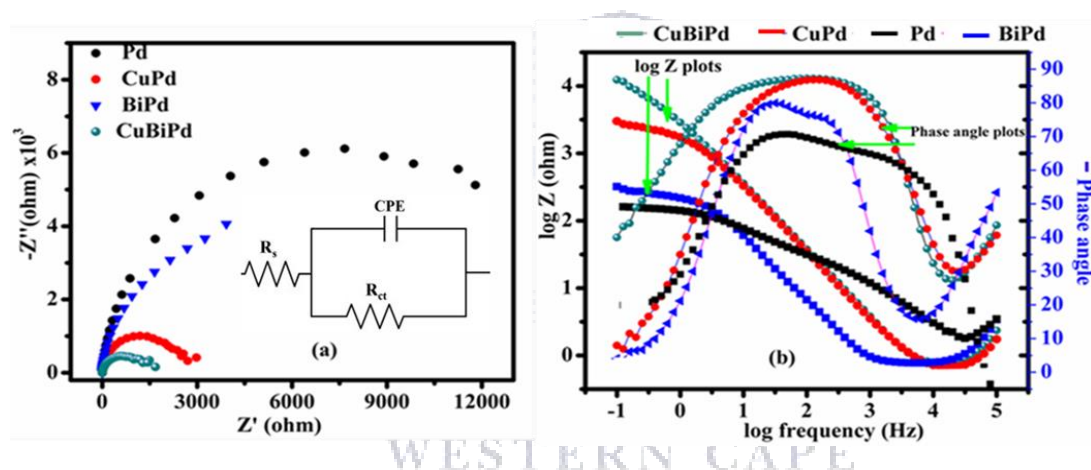


Figure 5.16: (a) Nyquist plot and (b) the corresponding bode plot of Pd (black), CuPd (red), BiPd (blue), CuBiPd (dark green), insert (a): Randle Sevcic circuit.

Table 5. 3: Impedimetric parameters of nanostructured thin films.

Thin films	R_s (k Ω)	R_{ct} (k Ω)	n	10^{-2} CPE(F)	ϕ ($^\circ$)
Pd	7.33	14.9	0.87	40.8	74
CuPd	7.53	2.98	0.7813	4.43	87.33
BiPd	0.99	3.97	0.8102	5.55	84.41
CuBiPd	6.36	2.29	0.892	5.0	88.65

To interpret the impedance results, the Randles Sevcik equivalent circuit [R_s (R_{ct} , CPE)] (**Figure 5. 16 (a)**; insert), was used to fit and simulate the electrochemical parameters, where R_s is solution resistance of electrolyte, R_{ct} is a charge transfer and CPE a constant phase element [67]. R_{ct} is related to reaction kinetics. CuBiPd show smallest arc ($R_{ct} = 2.29 \text{ k}\Omega$) relative to both CuPd ($R_{ct} = 2.98 \text{ k}\Omega$), and BiPd ($R_{ct} = 3.9 \text{ k}\Omega$). The R_{ct} values indicate that CuBiPd has higher electron transfer kinetic relative to CuPd, Bi and Pd during EOR. Higher polarization resistance of CuBi and BiPd, indicates fast charge transfer and increased conductivity induced addition of second metal (Cu) and third metal (Bi) on which they act as "third body" effect on Pd surface. Using the electric circuit fit diagram, the exchange current and time constant values were calculated using **Equation 5. 11**;

$$i_0 = R_t \frac{RT}{nFR_{ct}} \quad (5. 11(a))$$

$$\tau = R_{ct} \times CPE \quad (5. 11) (b))$$

Where i_0 = exchange current, n is a number of electrons transferred, τ is a time constant value [68]. Pd thin film electrocatalyst gave the exchange current with the following trend CuBiPd > CuPd > BiPd > Pd, while the time constant value shows Vis versa. In the case of exchange current value, CuBiPd reveals the highest value followed by CuPd. Furthermore, the rate of electron transfer (ket) during ethanol oxidation on Pd, the surface is slow compared to that of bimetallic (mono-modified (CuPd, BiPd)) and trimetallic (dual modified- (CuBiPd)).

The corresponding Bode plot evidence the electric properties of the nanostructured thin films and the results corroborate with the corresponding Nyquist plot. The phase angles obtained from bode plot for CuBiPd = -88.65° , CuPd = -87.41° , BiPd = -81° . CuPd showed the highest electron conductivity as expected based on phase angle value and since Cu possesses electric conducted properties. Interestingly dual adatoms (CuBi) enhanced conductivity to make CuBiPd a metallic conductor (phase angle = 84° close to 90°), in accordance to 90° phase angle for ideal conducting-

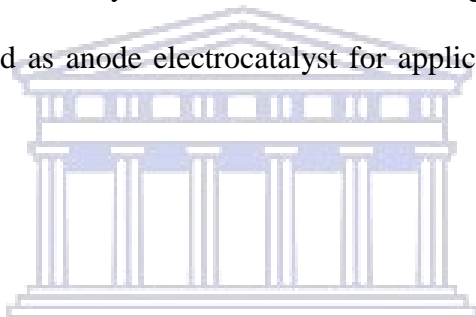
pure metal [69], [70],[71]. BiPd shows a lower phase angle compared to other bimetallic compounds, however, it exhibits a higher phase angle than Pd. In addition, the incorporation of Cu and Bi on the Pd electrode reduces the electron resistance of the Pd electrode.

The total impedance value in Bode plot confirms the conductivity properties of as-prepared thin films with the following trend: CuBiPd, $\log F=0$, ($\log Z = 4.1$) > CuPd, $\log F= 0$, ($\log Z =3.475$) > BiPd, $\log F=0$, ($\log Z= 2.5356$) > Pd, $\log F= 0$, ($\log Z = 2.221$). Furthermore, CuBiPd showed high total impedance of max phase angle at high frequency ($f = 0.9 \text{ Hz}$) (f negatively shifted) which means that CuBiPd has a least resistive behaviour relative to the as-synthesized bimetallic (CuPd, $f = 1.04 \text{ Hz}$; BiPd, $f = 1.4$) compounds and monometallic (Pd, $f = 152 \text{ Hz}$). This signifies the inductive behaviour of CuBi than Cu and Bi adatoms, which promote the complete removal of carbonaceous species, due to an increase in OH concentration and decrease in adsorptive sites for carbonaceous intermediates [63] in good agreement with CV to (Figure 5.13 (b)). Decisively, based on Nyquist and bode plot, the addition of foreign adatoms enhances the electron conductivity of the Pd surface and subsequently increases kinetic reaction for EOR in alkaline electrolyte.

5.5.6 Sub conclusion

Trimetallic (dual modified-Pd) CuBiPd and bimetallic BiPd, CuPd thin films were successfully deposited using E-ALD. Trimetallic compounds displayed higher electrocatalytic activity towards EOR relative to its bimetallic and monometallic counterparts. CuBiPd showed an increased peak current towards EOR by 3.5 folds relative to Pd. Also, an enhanced conductivity, electron kinetic transfer, and stability performance compared to Pd. SEM micrographs and elemental distribution showed well-dispersed particles which suggest that the SLRR cycles used promoted 2D growth. Furthermore, the SEM of these results was coherent with structure analysis from XRD, which shows some existence of layer-by-layer formation (epitaxial) relationship. To

our knowledge, there are rare reports on Pd-based forming nanoribbon structures using E-ALD. AFM showed uniform grain distribution, suggesting the 2D formation by the surface-limited reaction. However, BiPd revealed an even distribution with an island which may translate to a nucleation cluster forming 3D growth. CuBiPd showed an outstanding activity compared to monometallic Pd, which translates to relative higher oxophilic character and electronic effect and synergistic effect possessed by Cu and Bi on Pd. In addition, CuBiPd showed the smallest diameter on impedance arc (R_{ct}) indicating the smallest transfer resistance, which makes it a better electrocatalyst. The observed fascinating properties of the thin film formed by a low number (few minutes) of SLRR cycles protocol, makes E-ALD a futuristic methodology to electro-formed thin film electrocatalyst. These results encourage the use of bimetallic CuPd, BiPd, and trimetallic CuBiPd as anode electrocatalyst for application in alkaline direct ethanol fuel cells (ADLFCs).



References

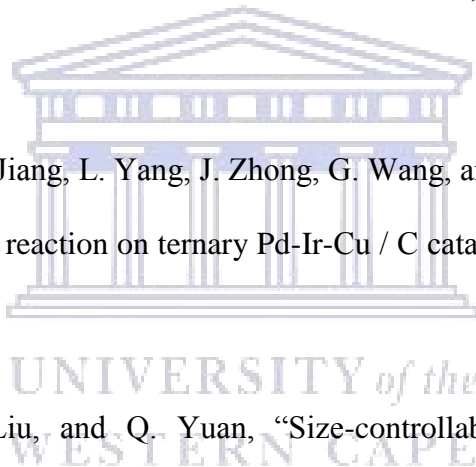
- [1] G. Kokkinidis and G. Papanastasiou, "Some specific features of the catalytic role of UPD foreign metal adatoms and water on the anodic oxidation of absolute methanol on Pt," *J. Electroanal. Chem.*, vol. 221, pp. 175–186, 1987.
- [2] L. Wang, X. Cao, Y. Wang, and Q. Li, "Sb Surface Modification of Pd by Mimetic Underpotential Deposition for Formic Acid Oxidation," *Catalyst*, vol. 5, pp. 1388–1398, 2015.
- [3] I. G. Casella and M. Contursi, "Characterization of bismuth adatom-modified palladium electrodes The electrocatalytic oxidation of aliphatic aldehydes in alkaline solutions," *Electr. Acta*, vol. 52, pp. 649–657, 2006.

- [4] R. R. A. and A. R. D. M.D. Spasojevic, "Electroanalysis on surface modified by foreign metal adatoms: oxidation of formaldehyde on platinum," *J. Electroanal. Chem.*, vol. 109, pp. 261–269, 1980.
- [5] V. Venkatasamy, N. Jayaraju, S. M. Cox, C. Thambidurai, M. Mathe, and J. L. Stickney, "Deposition of HgTe by electrochemical atomic layer epitaxy (EC-ALE)," *J. Electroanal. Chem.*, vol. 589, pp. 195–202, 2006.
- [6] T. Solomun and W. Kautek, "Electrodeposition of bismuth and silver phases in nanometer-sized zero-dimensional STM-formed cavities on gold (111)," *Electr. Acta*, vol. 4686, no. July, pp. 679–687, 2018.
- [7] W. Zhu, J. Y. Yang, J. Hou, X. H. Gao, S. Q. Bao, and X. A. Fan, "Optimization of the formation of bismuth telluride thin film by using ECALE," *J. Electroanal. Chem.*, vol. 585, pp. 83–88, 2005.
- [8] R. M. Modibedi, M. K. Mathe, R. G. Motsoeneng, L. E. Khotseng, K. I. Ozoemena, and E. K. Louw, "Electro-deposition of Pd on Carbon paper and Ni foam via surface limited redox-replacement reaction for oxygen reduction reaction," *Electrochim. Acta*, vol. 128, no. May, pp. 406–411, 2014.
- [9] T. S. Mkwizu, M. K. Mathe, and I. Cukrowski, "Electrodeposition of multilayered bimetallic nanoclusters of ruthenium and platinum via surface-limited redox-replacement reactions for electrocatalytic applications," *Langmuir*, vol. 26, no. 1, pp. 570–580, 2010.
- [10] L. B. Sheridan, J. Czerwiniski, N. Jayaraju, D. K. Gebregziabiher, J. L. Stickney, D. B. Robinson, and M. P. Soriaga, "Electrochemical Atomic Layer Deposition (E-ALD) of

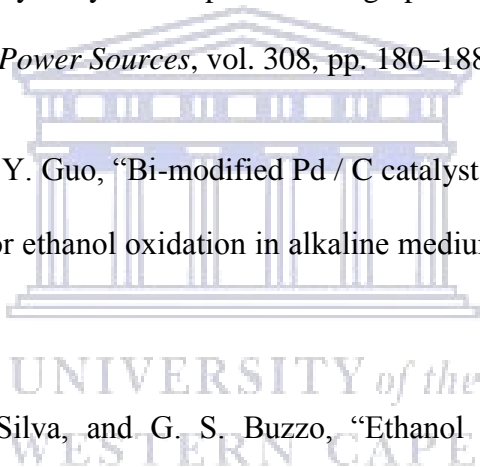
- Palladium Nanofilms by Surface Limited Redox Replacement (SLRR), with EDTA Complexation,” *Electrocatalysis*, vol. 3, no. 2, pp. 96–107, 2012.
- [11] M. Fayette, Y. Liu, D. Bertrand, J. Nutariya, N. Vasiljevic, and N. Dimitrov, “From Au to Pt via Surface Limited Redox Replacement of Pb UPD in One-Cell Configuration,” *Langmuir*, vol. 27, pp. 5650–5658, 2011.
- [12] I. Achari and S. Ambrozik, “Palladium Ultrathin Film Growth by Surface-Limited Redox Replacement of Cu and H UPD Monolayers: Approaches, Pros, Cons, and Comparison,” *Electrochem. Soc. Interface*, pp. 65–69, 2018.
- [13] B. Q. Yuan, A. Tripathi, M. Slavkovic, and S. R. Brankovic, “Lead Underpotential Deposition on Pt-submonolayer Modified Au (111),” *J. Phys. Chem.*, vol. 226, pp. 965–977, 2012.
- [14] L. B. Sheridan, V. M. Yates, D. M. Benson, J. L. Stickney, and D. B. Robinson, “Hydrogen sorption properties of bare and Rh-modified Pd nanofilms grown via surface limited redox replacement reactions,” *Electrochim. Acta*, vol. 128, pp. 400–405, 2014.
- [15] L. B. Sheridan, Y. Kim, B. R. Perdue, K. Jagannathan, J. L. Stickney, and D. B. Robinson, “Hydrogen Adsorption, Absorption, and Desorption at Palladium Nano films formed on Au(111) by Electrochemical Atomic Layer Deposition (E-ALD): Studies using Voltammetry and In Situ Scanning Tunneling Microscopy,” *J. Phys. Chem. C*, vol. 117, no. 111, pp. 15728–15740, 2013.
- [16] L. B. Sheridan, D. K. Gebregziabihier, J. L. Stickney, and D. B. Robinson, “Formation of palladium nanofilms using electrochemical atomic layer deposition (E-ALD) with chloride complexation,” *Langmuir*, vol. 29, no. 5, pp. 1592–1600, 2013.

- [17] S. R. Brankovic, J. X. Wang, and R. R. Adzic, "Metal monolayer deposition by replacement of metal adlayers on electrode surfaces," *Surf. Sci*, vol. 474, pp. 73–79, 2001.
- [18] T. S. Mkwizu and I. Cukrowski, "Physico-chemical modelling of adlayer phase formation via surface-limited reactions of copper in relation to sequential electrodeposition of multilayered platinum on crystalline gold," *Electrochim. Acta*, vol. 147, pp. 432–441, 2014.
- [19] T. S. Mkwizu, M. K. Mathe, and I. Cukrowski, "Multilayered Nanoclusters of Platinum and Gold : Insights on Electrodeposition Pathways , Electrocatalysis , Surface and Bulk Compositional Properties Multilayered Nanoclusters of Platinum and Gold : Insights on Electrodeposition Pathways , Electrocatalys," *J. Electrochem. Soc.*, vol. 160, no. February 2016, pp. 529–546, 2013.
- [20] A. Kumar and D. A. Buttry, "Size-Dependent Underpotential Deposition of Copper on Palladium Nanoparticles," *J. Phys. Chem. C*, vol. 119, pp. 16927–16933, 2015.
- [21] T. Chierchie, "Voltammetric study of the underpotential deposition on polycrystalline and single crystal palladium surfaces," *Electr. Acta*, vol. 33, pp. 341–345, 1988.
- [22] D. M. Benson, C. F. Tsang, J. D. Sugar, K. Jagannathan, D. B. Robinson, F. El Gabaly, P. J. Cappillino, and J. L. Stickney, "Enhanced Kinetics of Electrochemical Hydrogen Uptake and Release 2 on Palladium Powders Modified by Electrochemical Atomic Layer Deposition," *Appl. Mater. Interfaces*, 2017.
- [23] M. B. and D. M. Kolb, "A hydrogen adsorption and absorption study with ultrathin Pd overlayers on Au(111) AND Au (100)," *Electr. Acta*, vol. 38, no. 15, pp. 2145–2153, 1993.

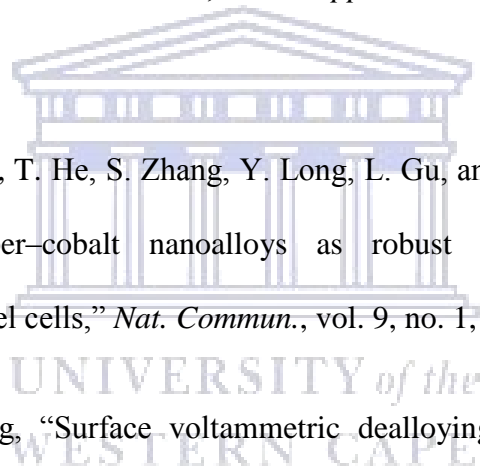
- [24] L. A. Kibler, "Influence of steps on the electrochemical oxidation of CO adlayers on Pd (111) and on Pd films electrodeposited onto Au (111)," *J. Electroanalytical Chem.*, vol. 534, pp. 107–114, 2002.
- [25] K. A. Anna Zalineeva, Alexey Serov,‡ Monica Padilla, Ulises Martinez and and P. B. A. Stève Baranton, Christophe Coutanceau, "Self-Supported Pd_xBi Catalysts for the Electrooxidation of Glycerol in Alkaline Media," *J. Am. Chem. Soc.*, vol. 136, pp. 3937–3945, 2014.
- [26] N. Xaba and R. M. Modibedi, "Pd , PdSn , PdBi , and PdBiSn Nanostructured Thin Films for the Electro-Oxidation of Ethanol in Alkaline Media," *Electrocatalysis*, pp. 11–16, 2019.
- [27] J. Chen, J. Zhang, Y. Jiang, L. Yang, J. Zhong, G. Wang, and R. Wang, "Enhanced formic acid electro-oxidation reaction on ternary Pd-Ir-Cu / C catalyst," *Appl. Surf. Sci.*, vol. 357, pp. 994–999, 2015.
- [28] T. Ma, C. Li, T. Liu, and Q. Yuan, "Size-controllable synthesis of dendritic Pd nanocrystals as improved electrocatalysts for formic acid fuel cells ' application," *J. Saudi Chem. Soc.*, vol. 22, no. 7, pp. 846–854, 2018.
- [29] Q. Dong, W. Zeng, H. Wan, S. Yu, C. Guo, and M. Huang, "Highly Effective PdCu Electrocatalysts Supported on Polyelectrolyte Functionalized Titanium Dioxide for Direct Formic Acid Fuel Cells," *Int. J. Electrochem. Sci.*, vol. 12, pp. 1389–1400, 2017.
- [30] R. N. Singh, "Pd1 % Ni Composite Electrodes for Electrooxidation of Phenol in Acid Solution Pd-1 % Ni Composite Electrodes for Electrooxidation of Phenol in Acid Solution," *Int. J. Electrochem. Sci.*, vol. 4, no. November, pp. 1638–1649, 2015.



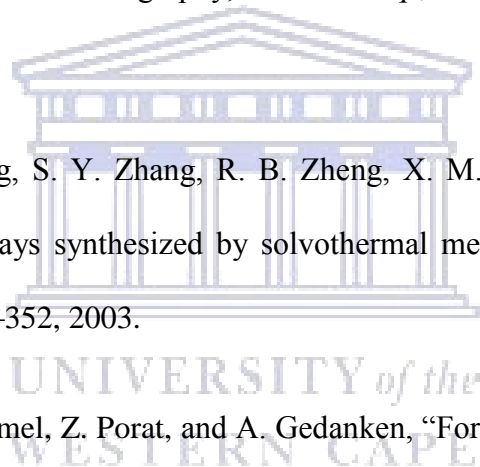
- [31] S. Garbarino and L.D. Burke, "The Surface Active Site Model for Formic Acid Electrooxidation at Palladium in Aqueous Acid Solution," *Int. J. Electrochem. Sci.*, vol. 5, no. May, 2014.
- [32] D.M.Benson, "Modification of palladium surface by electrochemical atomic layer deposition (E-ALD) and atomic layer electroless deposition (ALED) for enhanced hydrogen transfer reaction," PhD thesis, University of Georgia, December, 2015.
- [33] M. S. Ahmed, D. Park, and S. Jeon, "Ultrasmall PdMn_{1-m}O_x binary alloyed nanoparticles on graphene catalysts for ethanol oxidation in alkaline media Ultrasmall Pd m Mn 1 À m O x binary alloyed nanoparticles on graphene catalysts for ethanol oxidation in alkaline media," *J. Power Sources*, vol. 308, pp. 180–188, 2016.
- [34] J. Cai, Y. Huang, and Y. Guo, "Bi-modified Pd / C catalyst via irreversible adsorption and its catalytic activity for ethanol oxidation in alkaline medium," *Electrochim. Acta*, vol. 99, pp. 22–29, 2013.
- [35] A. O. Neto, S. G. Silva, and G. S. Buzzo, "Ethanol electrooxidation on PdIr / C electrocatalysts in alkaline media : electrochemical and fuel cell studies," *Ionics (Kiel)*, vol. 21, pp. 487–495, 2015.
- [36] R. Jana, S. Dhiman, and S. C. Peter, "Facile solvothermal synthesis of highly active and direct ethanol fuel cell applications Facile solvothermal synthesis of highly active and robust Pd_{1.87}Cu_{0.11}Sn electrocatalyst towards direct ethanol fuel cell applications," *Mater. Res. Express*, vol. 3, no. 8, pp. 1–9, 2016.



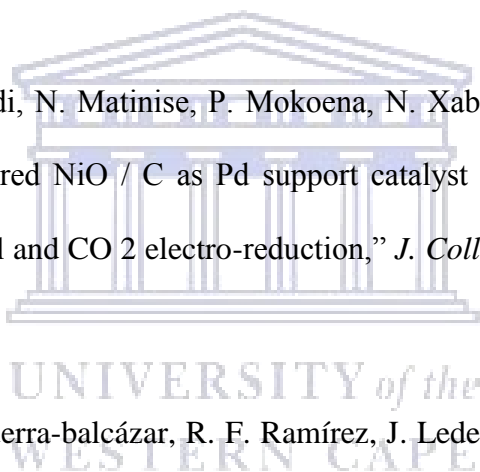
- [37] R. M. Modibedi, T. Masombuka, and M. K. Mathe, “Carbon supported Pd-Sn and Pd-Ru-Sn Snanocatalysts for ethanol electro-oxidation in alkaline medium,” *Int. J. Hydrogen Energy*, vol. 6, pp. 1–9, 2011.
- [38] D. O. Banga, R. Vaidyanathan, and L. Xuehai, “Electrochimica Acta Formation of PbTe nanofilms by electrochemical atomic layer deposition (ALD),” *Electr. Acta*, vol. 53, pp. 6988–6994, 2008.
- [39] V. S. Marakatti, S. C. Sarma, B. Joseph, D. Banerjee, and S. C. Peter, “Synthetically Tuned Atomic Ordering in PdCu Nanoparticles with Enhanced Catalytic Activity toward Solvent-Free Benzylamine Oxidation,” *ACS Appl. Mater. Interfaces*, vol. 9, pp. 3602–3615, 2017.
- [40] C. Li, Q. Yuan, B. Ni, T. He, S. Zhang, Y. Long, L. Gu, and X. Wang, “Dendritic defect-rich palladium–copper–cobalt nanoalloys as robust multifunctional non-platinum electrocatalysts for fuel cells,” *Nat. Commun.*, vol. 9, no. 1, pp. 1–9, 2018.
- [41] C. Zhu and Y. Yang, “Surface voltammetric dealloying investigation on PdCu / C electrocatalysts toward ethanol oxidation in alkaline media,” *J Nanopart Res*, vol. 20, p. 314, 2018.
- [42] S. Roy and P. Mukherjee, “Palladium and palladium e copper alloy nano particles as superior catalyst for electrochemical oxidation of methanol for fuel cell applications,” *Int. J. Hydrogen Energy*, vol. 41, pp. 17072–17083, 2016.
- [43] J. Xue, G. Han, W. Ye, Y. Sang, H. Li, P. Guo, and X. S. Zhao, “Structural Regulation of PdCu₂ Nanoparticles and Their Electrocatalytic Performance for Ethanol Oxidation Structural Regulation of PdCu₂ Nanoparticles and Their Electrocatalytic Performance for



- Ethanol Oxidation,” *Appl. Mater. Interfaces*, vol. 8, no. November, pp. 34497–34505, 2016.
- [44] W. Giurlani, A. Giaccherini, E. Salvietti, M. Passaponti, A. Comparini, V. Morandi, F. Liscio, and M. Cavallini, “Selective Electrodeposition-Based Atomic Layer Deposition (SEBALD) of Bismuth underpotential morphology control,” *Electrochem. Soc. Interface*, pp. 77–81, 2018.
- [45] S. Dadashi, R. Poursalehi, and H. Delavari, “Optical and structural properties of oxidation resistant colloidal bismuth/gold nanocomposite: An efficient nanoparticles based contrast agent for X-ray computed tomography,” *J. Mol. Liq.*, vol. 254, no. January, pp. 12–19, 2018.
- [46] X. Y. Liu, J. H. Zeng, S. Y. Zhang, R. B. Zheng, X. M. Liu, and Y. T. Qian, “Novel bismuth nanotube arrays synthesized by solvothermal method,” *Chem. Phys. Lett.*, vol. 374, no. 3–4, pp. 348–352, 2003.
- [47] V. B. Kumar, G. Kimmel, Z. Porat, and A. Gedanken, “Formation of particles of bismuth-based binary alloys and intermetallic compounds by ultrasonic cavitation,” *New J. Chem.*, vol. 39, no. 7, pp. 5374–5381, 2015.
- [48] Y. C. Wei, T. Y. Chen, C. W. Liu, T. S. Chan, J. F. Lee, C. H. Lee, T. L. Lin, and K. W. Wang, “The structure modification and activity improvement of Pd-Co/C electrocatalysts by the addition of Au for the oxygen reduction reaction,” *Catal. Sci. Technol.*, vol. 2, no. 8, pp. 1654–1664, 2012.



- [49] C. Jun Yin, Mei Shan Ng, Lefu Yang, Derrick Mott, Weiqin Fang, Ning Kang, Jin Luo, and Zhong, “Catalytic and Electrocatalytic Oxidation of Ethanol over Palladium- Based Nanoalloy Catalysts,” *Langmuir*, vol. 29, pp. 9249–9258, 2013.
- [50] L. Zhang, Q. Chang, H. Chen, and M. Shao, “Nano Energy Recent advances in palladium-based electrocatalysts for fuel cell reactions and hydrogen evolution reaction,” *Nano Energy*, vol. 29, pp. 198–219, 2016.
- [51] Z. X. Liang, T. S. Zhao, J. B. Xu, and L. D. Zhu, “Mechanism study of the ethanol oxidation reaction on palladium in alkaline media,” *Electrochim. Acta*, vol. 54, pp. 2203–2208, 2009.
- [52] X. Fuku, M. Modibedi, N. Matinise, P. Mokoena, N. Xaba, and M. Mathe, “Single step synthesis of bio-inspired NiO / C as Pd support catalyst for dual application : Alkaline direct ethanol fuel cell and CO 2 electro-reduction,” *J. Colloid Interface Sci.*, vol. 545, pp. 138–152, 2019.
- [53] R. C. Cerritos, M. Guerra-balcázar, R. F. Ramírez, J. Ledesma-garcía, and L. G. Arriaga, “Morphological Effect of Pd Catalyst on Ethanol Electro-Oxidation Reaction,” *Materials (Basel)*, vol. 5, pp. 1686–1697, 2012.
- [54] K. Ding, Y. Zhao, L. Liu, Y. Li, L. Liu, Y. Wang, H. Gu, H. Wei, and Z. Guo, “Multi-walled carbon nanotubes supported Pd composite nanoparticles hydrothermally produced from technical grade PdO precursor,” *Electrochim. Acta*, vol. 176, pp. 1256–1265, 2015.
- [55] W. Du, K. E. Mackenzie, D. F. Milano, N. A. Deskins, D. Su, and X. Teng, “Palladium – Tin Alloyed Catalysts for the Ethanol Oxidation Reaction in an Alkaline Medium,” *ACS Catal.*, vol. 2, pp. 287–297, 2012.



- [56] R. F. Savinell and R. L. Zeller, "Electrochemically Active Surface Area: Voltammetric Charge Correlations for Ruthenium and Iridium Dioxide Electrodes," *J. Electrochem. Soc.*, vol. 137, no. 2, pp. 489–494, 1990.
- [57] M. D. Obradović, Z. M. Stančić, U. Lačnjevac, V. V. Radmilović, A. Gavrilović-Wohlmuther, V. R. Radmilović, and S. L. Gojković, "Electrochemical oxidation of ethanol on palladium-nickel nanocatalyst in alkaline media," *Appl. Catal. B Environ.*, vol. 189, pp. 110–118, 2016.
- [58] H. Chen, Z. Xing, S. Zhu, L. Zhang, Q. Chang, J. Huang, W. Cai, N. Kang, C. Zhong, and M. Shao, "Palladium modified gold nanoparticles as electrocatalysts for ethanol electrooxidation," *J. Power Sources*, vol. 321, pp. 264–269, 2016.
- [59] A. K. Ipadeola, R. Barik, S. C. Ray, and K. I. Ozoemena, "Bimetallic Pd / SnO₂ Nanoparticles on Metal Organic Framework (MOF) -Derived Carbon as Electrocatalysts for Ethanol Oxidation," *Electrocatalysis*, 2019.
- [60] Y. Wang, Q. He, K. Ding, H. Wei, J. Guo, Q. Wang, R. O. Connor, X. Huang, Z. Luo, T. D. Shen, S. Wei, and Z. Guo, "Multiwalled Carbon Nanotubes Composit ed with Palladium Nanocatalysts for Highly Efficient Ethanol Oxidation," *J. Electrochemical Soc.*, vol. 162, no. 7, pp. 51–54, 2015.
- [61] A. S. Douk, H. Saravani, and M. Noroozifar, "Preparation and Electrocatalytic Characteristics of PdW/C Catalyst for Ethanol Oxidation," *Int. J. Hydrogen Energy*, vol. 42, no. 22, pp. 15149–15159, 2017.

- [62] R. A. Gonçalves, M. R. Baldan, E. G. Ciapina, and O. M. Berengue, "Nanostructured Pd / Sb 2 O 3 : A new and promising fuel cell electrocatalyst and non-enzymatic amperometric sensor for ethanol," *Appl. Surf. Sci.*, vol. 491, no. February, pp. 9–15, 2019.
- [63] D. Y. Chung, K. Lee, and Y. Sung, "Methanol Electro-Oxidation on the Pt Surface: Revisiting the Cyclic Voltammetry Interpretation," *J. Phys. Chem. C*, vol. 120, pp. 9028–9035, 2016.
- [64] J. Carlos, C. Gómez, R. Moliner, and M. J. Lázaro, "Palladium-Based Catalysts as Electrodes for Direct Methanol Fuel Cells : A Last Ten Years Review," *Catalysts*, vol. 6, pp. 1–20, 2016.
- [65] B. Liu, Z. Chia, C. Cheng, and J. Lee, "Promotional Effects of Ir Addition in Carbon-Supported Pt 5 Rh Electrocatalysts for the Electrooxidation of Ethanol at Room Temperature," *Energy Fuels*, vol. 25, pp. 3135–3141, 2011.
- [66] R. M. Modibedi, T. Masombuka, and M. K. Mathe, "Carbon supported Pd-Sn and Pd-Ru-Sn nanocatalysts for ethanol electro-oxidation in alkaline medium," *Int. J. Hydrogen Energy*, vol. 36, no. 8, pp. 4664–4672, 2011.
- [67] A. Chen, D. J. La Russa, and B. Miller, "Effect of the Iridium Oxide Thin Film on the Electrochemical Activity of Platinum Nanoparticles," *Langmuir*, vol. 20, no. 24, pp. 9695–9702, 2004.
- [68] T. Ramulifho, K. I. Ozoemena, R. M. Modibedi, C. J. Jafta, and M. K. Mathe, "Electrocatalytic oxidation of ethylene glycol at palladium-bimetallic nanocatalysts (PdSn and PdNi) supported on sulfonate-functionalised multi-walled carbon nanotubes," *J. Electroanal. Che*, vol. 692, pp. 26–30, 2013.

- [69] X. Fuku, B. Singh, R. F. Ajayi, A. N. Jijana, P. Baker, E. Dempsey, and E. Iwuoha, “A gallium telluride quantum dots bioelectrode system for human epidermal growth factor,” *Anal. Methods*, pp. 32–37, 2015.
- [70] A. C. Mkhohlakali, X. Fuku, R. M. Modibedi, L. E. Khotseng, S. C. Ray, and M. K. Mathe, “Electrosynthesis and characterization of PdIr using electrochemical atomic layer deposition for ethanol oxidation in alkaline electrolyte,” *Appl. Surf. Sci.*, vol. 502, pp. 144–158, 2019.
- [71] N. Mayedwa, N. Mongwaketsi, S. Khamlich, K. Kaviyarasu, N. Matinise, and M. Maaza, “Green Synthesis of Nickel Oxide , Palladium and Palladium Oxide Synthesized,” *Appl. Surf. Sci.*, pp 1-7, 2017. <https://doi.org/10.1016/j.apsusc.2017.12.116>



Chapter 6

6.1 Electro-formation of nanostructured Te-based thin film (Te-M, where M= Pd, BiPd)

Summary

This section reports the rare or rather the first time oxidative underpotential deposition of tellurium on the Pd-based electrode surface for the oxidation of ethanol in alkaline media to be applied in the ADEFC.

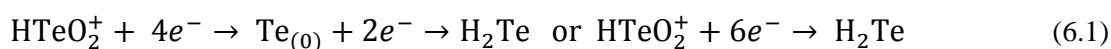
6.2.0 Results and discussion

6.2.1 Identification of oxidative Te underpotential deposition (oxTe-_{UPD}) on Au, Pd, BiPd and CuPd: CV profiles

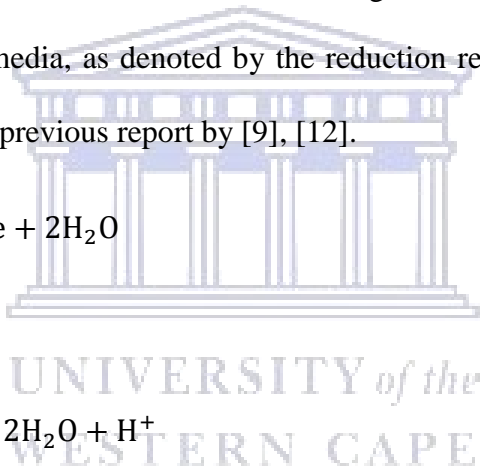
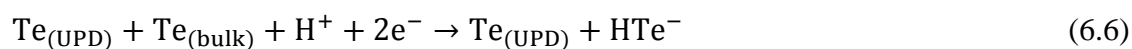
Before any electro-formation (E-ALD cycle) of Te on Au, it is imperative to investigate the UPDs (CV profile) to single out the oxTe-_{UPD} region which is the potential of interest. Generally, UPD values are identified and used for the initial deposition cycle [1]. The CV profile was investigated by using the cathodic window procedure to find the optimal ox-Te-_{UPD} value. The CV identification is illustrated in **Figure 6.1 (a)** and **Table 6.1**.

6.2.2 Electrochemical characterization of Te on Au

The electrochemical stable species of Te is established by the Pourbaix diagram (see **Figure 2.16, (Chapter 2: section 2.5.6)**) to give tellurous acid (HTeO₂⁺) species at low pH (1-2) at initial potential [2]. In addition, Te shows poor solubility at high pH range (4-7) and also yields a poor adhering in alkaline media. Te deposition from tellurous species occurs in multiple steps until telluride (H₂Te) is formed, which is known as the soluble species. In summary, this redox couple can be expressed as follows;



In this study, the electrochemical behavior of acidic Te species on Au was determined using acid bath of HTeO_2^+ in 0.1M HClO_4 pH 1.5 at 10 mVs^{-1} , successfully scanned from 1.0 V to various cathodic potential limits (-0.2,-0.4, -0.6, -0.7, -0.8 V) to fully identify all the redox couples of $\text{Te}_{\text{-UPD}}$ and bulk (OPD) potential as displayed in **Figure 6.1 (a)**. The CV displayed two reductive peaks at +0.33 V and -0.188 V associated with $\text{Te}_{\text{-UPD}}$. These small peaks and wide difference between its stripping potential suggest the slow experimental kinetics for $\text{Te}_{\text{-UPD}}$ and the CVs curves are comparable to those reported in the previous study for Te deposition on Au in acid electrolyte [3], [4], [5], [6], [7], [8]. During the anodic sweeping direction, the peaks around +0.5 and 0.8 V correspond to the stripping of the bulk and $\text{Te}_{\text{-UPD}}$ stripping respectively as described in the literature [5], [9], [10]. The redox features are in agreement with the reaction of tellurium electrodeposition in acidic media, as denoted by the reduction reaction mechanism below [11]. CV curves are similar to the previous report by [9], [12].



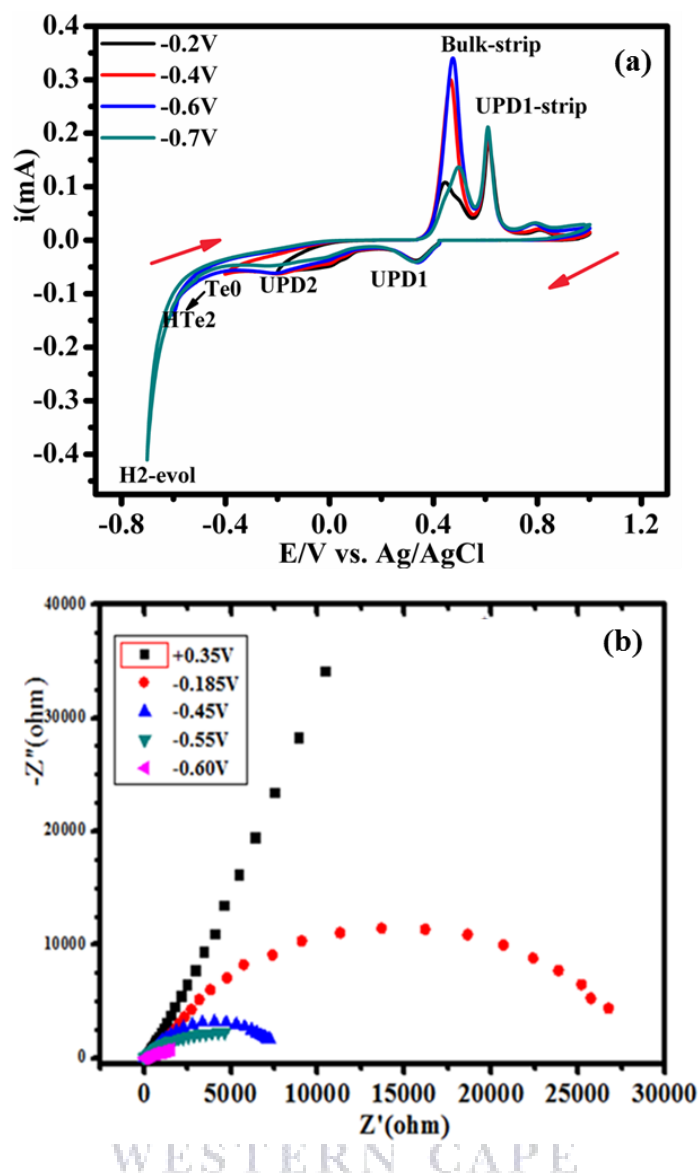


Figure 6.1: (a) CV of Au in 0.5nm HTeO_2^+ + 0.1 M HClO_4 at 10 mVs^{-1} and (b) Nyquist plot at various bias cathodic limit potential.

Figure 6.1 (b) shows EIS (Nyquist plot). This experiment aimed to investigate and evaluate the experimental reaction kinetics of Au in HTeO_2^+ at various selected cathodic limit potential using the new approach to prove the literature study and CV. It was indeed found that the OPD potential region shows a fast reaction kinetic, due to a small semicircle observed at -0.6, followed by -0.45 V which may be attributed to fast electron charge transfer on the electrode surface. The larger semi-circle observed for UPD potentials such as +0.35 V and -0.18 V, indicates the high charge transfer resistance on the Au surface. This could be due to slow

electron charge transfer, which corroborates CV results in **Figure 6.1 (a)**. Due to the slow electron kinetic transfer of Te-UPDs, the Te-OPD triggered the massive Te electro formation along with Te-UPD at (-0.5 to -0.6 V) potential, followed by re-reduction of Te-bulk at more negative potential to form a soluble tellurite (HTe^-) species as denoted in **Equation 6.5**, leaving the Te-adlayer on the surface which is coherent with literature [3], [13]. The process is referred to as oxidative underpotential deposition (OX-UPD). OX-UPD has been studied for I Halide (I atom to I^-) [59], S to S^- and Te (0) to Te^{2-} or Te^{4+} to Te^{2-} on metallic electrodes such as Ag [17], Au [13], [15] Pt [16], and GC [17], [18], [25] substrate.

6.3 Electro formation and characterization of Oxidative Te- underpotential deposition on Au: Te thin film

Figure: 6.2 (a) illustrate the potential-current-time trace of Te on Au, it can be seen that during the Te flow at OCP, current showed no response, and reductive OPD (-500 mV) potential set, the reductive current response was observed which is ascribed to the formation of the Te (bulk) as represented by the time-potential-current graph (**Figure. 6.2 (a)**) and **Equation. 6.1**. During the BE flush at -600 mV, the oxidative current spike can be observed that some amount Te(0) bulk stripping was observed leaving Te-adlayer. The current response changes indicate the re-reduction of Te(0) (bulk) formed previously. This steps consonance with **Equation. 6.6** which explains the redox couple for oxidative Te-UPD and re-reduction of bulk Te(0) and that time, the combination of bulk and soluble tellurite (H_2Te) species is formed leaving the Te UPD-adlayer. The CVs of Te-covered Au in 0.1M HClO_4 using window opening procedure, showed the typical Te CV signatures in acid as displayed in **Figure 6.2 (b)**. The CVs are similar to CVs of Au in **Figure 6.1(a)**, there is the distinct current response, Te-covered Au showed high charge as compared to Au in Te^{4+} solution. During the negative scan, the oxidative stripping peak denoted as III' increases indicating the more oxidative $\text{Te}_{(0)}$ bulk stripping especially around -600 mV and

also suggests the surface limited reaction. This result evidence Te atomic layer deposition and the potential corroborate with selected potential from CVs (**Figure 6.1 (a)**). The potential beyond -600 mV (-700 mV) shows drastically drop of peak III' which may be ascribed to simultaneous occurrence of hydrogen evolution and soluble telluride (H_2Te) species

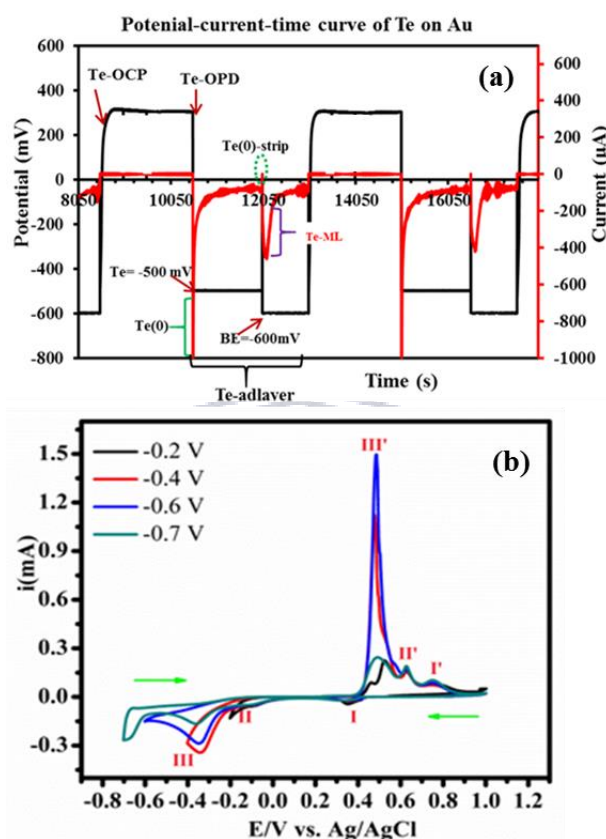


Figure 6.2: Potential-current-time trace of Te-Au for 3 cycles (a) and CV in 0.1 M HClO_4 at 10 mVs^{-1} (b).

6.3.1 Identification of oxidative Te- underpotential deposition on Pd-covered Au:

CV profile

Figure 6.3 (a) shows CV of Pd on Au in 0.5 mM HTeO_2^+ at various cathodic limit (-0.2; -0.4 and -0.6 V) potential. For comparison purposes, Pd and bare Au were overlaid as shown insee **Figure 6.3 (b)**. It can be seen that HTeO_2^+ aliquot occurs on the Pd interface; due to strong Te-UPD_2 and

strong Te-bulk stripping peak compared to bare Au counterparts. Te-_{UPD1} and Pd-O reduction almost occurred simultaneously as described in the literature [19] during cathodic scanning direction. However, there is a slight positive (0.13 V) shift in Te-_{UPD1} respective to bare Au, which is attributed to Te stronger interaction with Pd and some opened remnant Au active sites [20]. On Pd thin film a weaker and positive shift Te-_{UPD} stripping peak was also observed as compared to bare Au counterparts during anodic scanning. Therefore it can be concluded that Te-_{UPD} potential is almost the same for deposition on a bare and Pd-covered Au. The redox features are in agreement with the reaction of tellurium electrodeposition in acidic media, as denoted by the following mechanism for reduction reaction [11].

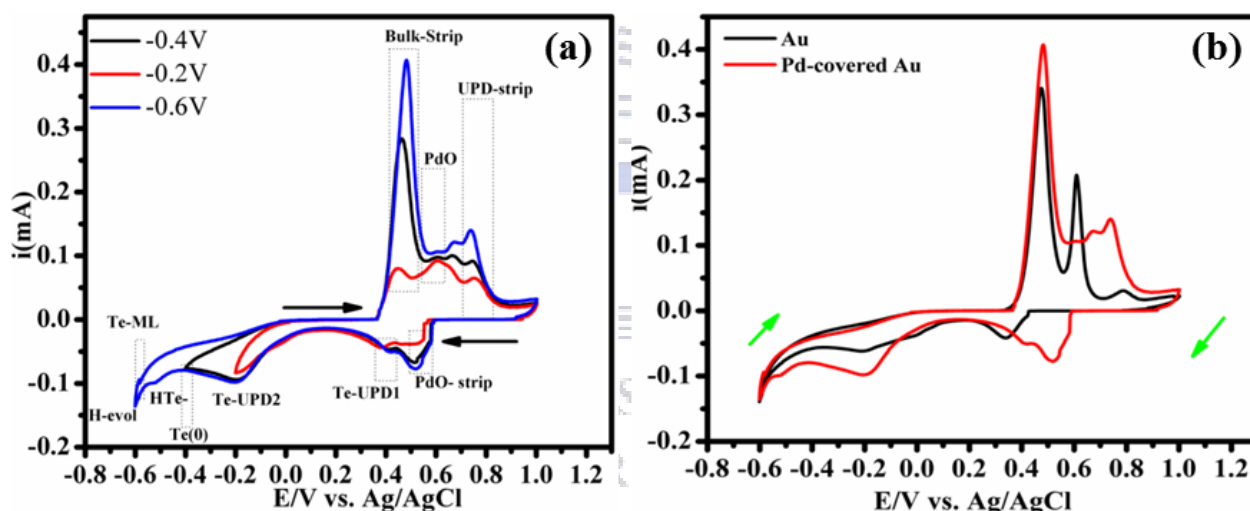


Figure 6.3: CV of Pd-covered Au at various cathodic limit potential (a), overlaid Pd-covered Au and bare Au (b) in a solution of 0.5 mM HTeO_2^+ at 10 mVs^{-1} .

As for TePd formation on Au, the following equation is proposed as adopted from the equation (Equation 6.7) described in the literature [4], [12] for the deposition of CdTe on Au.



Reduction

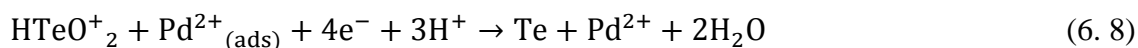


Table 6.1: Electrolyte precursor and deposition parameters

Reaction chamber/System	Species and conc.	UPD potential (mV vs. Ag/AgCl)	UPD strip potential (mV vs. Ag/AgCl)
Au in Te ⁴⁺	0.5 m HTeO ₂ ⁺	-500 to -600	695
Pd in Te ⁴⁺	0.5 mM Te ⁴⁺	189 to 150	350
PdBi-covered-Au	0.5 mM Te ⁴⁺	-450 to -550	450

6.3.2 Electrochemical characterization of TePd on Au: CV profile in 0.1 M HClO₄

Figure 6.4 (a) represents the time-potential-current trace of TePd deposition for three cycles. It was observed that during Te-flow for 10s at OCP and there was no current (zero) response, the OCP value increases as a number of cycles increases. This could suggest that Te flow occurs in a distinguished electrode surface (Te is covering the exposed Pd surface). During the set potential step at Te (OPD) = -0.5V, the reductive current response was observed to be -1100 μA which may confirm the formation of bulk Te(0). The excess Te was re-reduced at a high negative potential of -0.6 V and reductive as well as oxidative current peaks were observed which evidence the stripping of some bulk Te leaving an atomic layer on the surface and this step is referred to as oxidative underpotential deposition as discussed in the literature [4], [21].

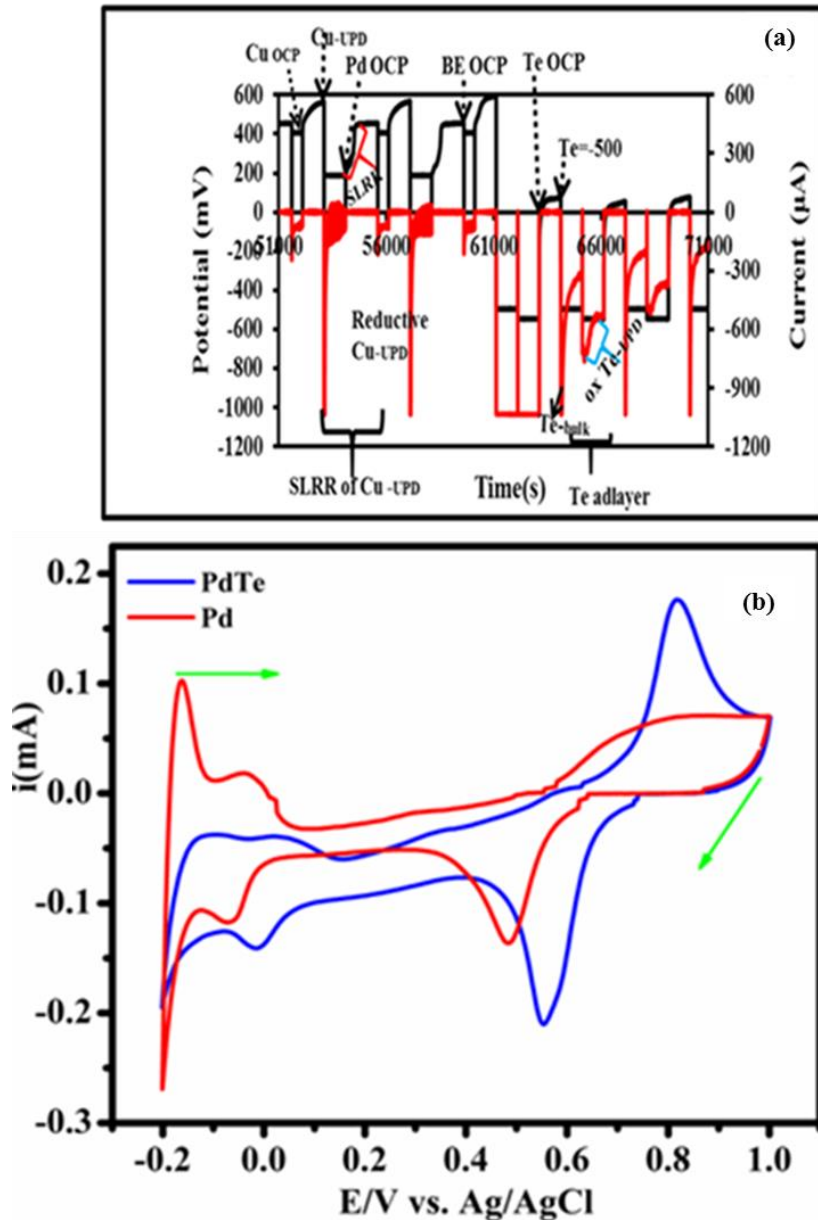


Figure 6.4: (a) Potential-current-time trace of TePd recorded for 2 cycles and (b) overlaid CVs of Pd and TePd in 0.1 M HClO_4 at 30 mVs^{-1} .

Shortly after the E-ALD cycles, PdTe thin film was immersed in 0.1 M HClO_4 solution flowing into the thin flow cell and cycled between 1.0 and -0.2V potential to observe the redox features. For comparison purposes, CVs of Pd and PdTe were overlaid. Both CVs of the acquired thin films exhibit the well-known Pd characteristic features, consistent with the literature [22], [23] [24], [25]. Distinct current response and potential shift at Pd-O region (+0.6 and 0.48 V) and

hydrogen absorption- adsorption (-0.198 to -0.2 V) potential regions were observed. TePd showed inhibitory hydrogen-adsorption and prominent Pd-O formation which is likely due to strong Pd-Te bond electron interaction which weakens Pd-hydride and also due to the simultaneous formation of Te-UPD stripping and Pd-O and this is consistent with the literature [26], [27], [28], [29]. On the Pd-O formation (anodic scan) and Pd-O reduction current (cathodic scan) the thin films (Pd and TePd) showed that: TePd > Pd, which suggest more Pd particles are dispersed on the Au upon the addition of Te oxygen species as delineated by [41], [30],[31]. The positive shift of hydrogen deposition and Pd-O peak potential respectively possibly ascribe to the weakened Pd-H bond (low binding energy) [32], [33], [34],[35]. The more positive onset for Pd-O reduction on TePd indicates that less activation energy is required to reduce the Pd-O as described in the literature [36]. In addition, this distinct Pd-O formation and corresponding stripping potential on Pd and TePd imply the deviation in electronic structure as articulated in literature [37] is due to the insertion of Te into the Pd lattice causing an electron interaction relationship. The shape of the CVs for the thin films is similar and consistent with the literature [22],[25],[38],[39],[40].

6.3.3 Electrochemical characterization of Te on BiPd in 0.1 M HClO₄

Figure 6.5 represents the CVs of BiTePd and TePd in 0.1 M HClO₄ at 30 mVs⁻¹. The CV curves are overlaid with their Pd, BiPd counterparts to contrast the incorporation of Te. It can be seen that during the cathodic scan and anodic scan from +1.0 V to -0.2 V, all thin films exhibit a well-known polycrystalline Pd redox feature, the redox feature is explained in this chapter, see **section 6.3.2**. However, the thin films manifest a distinct hydrogen absorption-desorption and Pd-O reduction potential and current response. It can be observed that TePd has the highest Pd-O reduction peak which signifies the exposure of Pd on solution electrolyte and enhances the surface area and well dispersion of particle upon the incorporation of Te adatoms in accordance

to [31]. This may also be related to strong electron interaction of Te and Pd, and strong affinity of Pd for oxygen-containing species such as Te. BiTePd exhibit the smaller charge for Pd-O in contrast to Pd and TePd, which implies the less exposure of Pd character than its Pd and TePd counterparts. This later finding correlate with elemental map results (see **Figure 6.8 (b)**) and SEM micrographs (see **Figure 6.7 (c-d)**, where the mapping shows the highly density distribution of elemental Bi and Te with minute deposits of Pd. Moreover, the SEM displays the complete covered surface by BiTe, with traces of Pd defects. At higher negative potential BiTePd showed the smallest, almost zero current response for hydrogen absorption (α Pd-hydride) as compared to its counterparts, however, it exhibits the remarkable high adsorption (β Pd-hydride). Interesting to note, this could be due to a combination of thermoelectric and Pd-lattice (hydrogen storage) properties of BiTe and Pd respectively. There is a high electron interaction between BiTe and Pd atom which favors the hydrogen adsorption rather than absorption.

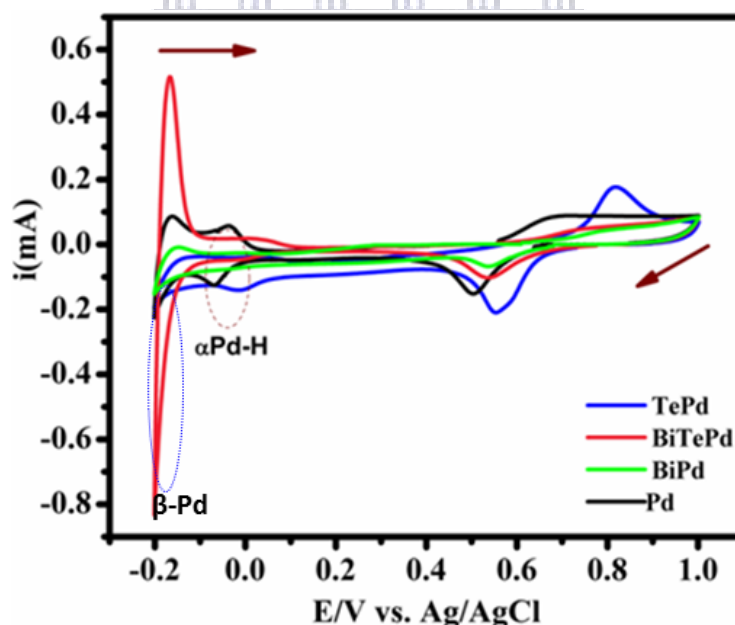


Figure 6.5: Overlaid CVs of Te, TeBiPd, and corresponding Pd, BiPd derivatives in 0.1 M HClO_4 at 30 mVs^{-1} .

6.4 X-ray diffraction of Te-M based nanostructured thin films, M = Pd, and BiPd electrodes

Figure 6.6 depicts the XRD pattern of bare Au and as-prepared Te-M-based thin films. For comparison, in each electrode modified with Te-adlayer is overlaid with unmodified one to investigate the effect of Te in the structure. For instance, Pd (unmodified) is overlaid with TePd (Pd modified) and as for BiPd (unmodified electrode) with BiTePd (modified electrode). All the thin films exhibits the XRD patterns that reveal four main Bragg's diffraction angles around 38.5° , 56° , 66° , 72.86° and $79.88.6^\circ$ corresponding to the (111), (200), (220), (311) planes of face-centered cubic (fcc) of metallic Pd phase characteristic features in accordance to standard certification (JCPDS card no. 89-4897) and similar to literature [12], [41], [42],[44], [45],[73]. Au bare exhibits polycrystalline phase as delineated in previous studies [46]. All deposits were preferred orientation of the Pd/Au (111) plane. For a clear observation, the XRD pattern was zoomed (**Figure 6.6**), with (111) planes further magnified. There is an apparent positive 2θ shift (at (111 and (220) plane) in TePd (**Figure 6.6 (a)**) respective to Pd planes which imply the insertion of Te atoms in Pd lattice structure forming some alloy and strong electron interaction. This resulted in weakened Pd-hydride bond upon Te insertion to Pd crystal lattice structure which is in strong agreement with CV (see **Figure 6.4 (a)**). The elemental Te adatoms are also evident at low $2\theta = 25^\circ$, 16° and 10° region attributed to (110, 100 and 102) planes respectively, and the assignment of peaks is coherent with previous work [8], [47], [48]. The elemental Te diffraction peaks are so intense Te(110) and Te (102) peaks are parallel to Pd/Au(111) planes which indicate layer-by-layer (epitaxial) growth of Te on Pd/Au surface electrode [49],[50], [51]. It can be observed in **Figure 6.6 (b)** that BiTePd showed a shift to high 2θ values as compared to BiPd. These results could be ascribed to single-phase alloy formation, which is evidenced by the absence of elemental Bi at low 2θ . The elemental peak ($2\theta = 29^\circ$) may suggest that Te deposited

in remnants Pd-active sites. **Figure 6.6 (d)** displays the overlaid ternary Te-M based and its counterpart (bimetallic (TePd, and BiPd)) electrodes. It can be seen that the as-synthesized bimetallic compounds shifted to higher 2θ , which could be due to the stronger electron interaction of between Bi and Te adatoms more than to Pd surface in trimetallic Te-M based thin films counterparts.

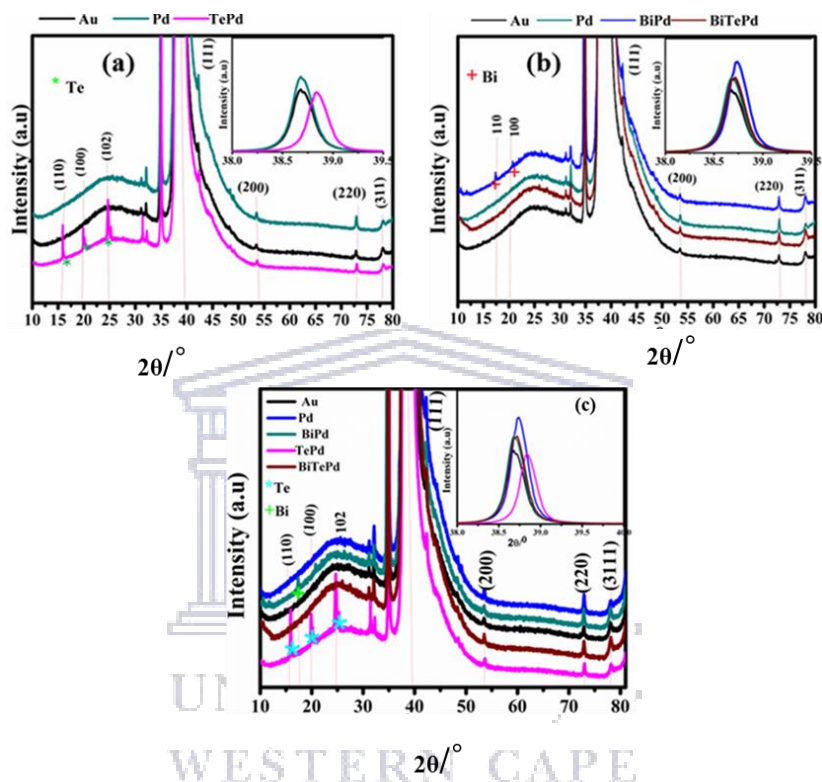


Figure 6.6: XRD pattern of Au, Pd, TePd (a) and Te-M (b-c) thin films, insert: Magnified (111) planes

6.5 Scanning electron microscope (SEM)-energy dispersive x-ray (EDX) and elemental distribution of Te-M based thin films

Figure 6.7 reveals SEM micrographs of the as-synthesized; Pd, CuPd, and TePd and BiTePd thin films at low magnification and high magnification of as TeM-based thin films. For comparison purposes, Pd and BiPd were included in **Figure 6.8** to see changes in morphology

upon the addition of Te. It can be seen that Pd forms conformal quasi-spherical particles deposited across the Au substrate as discussed in **section 5.4.2 (Figure 5.9)**. TePd forms dendritic structures that are conformal across the surface as displayed in **Figure 6.7 (a)**. Very interesting to note, the dendrites outgrow from the center (nuclei) to various directions with observed branches of distinct dimensions. This deposits consonance with electrodeposited Te-feather shaped particles as described by [52], **Figure. 6.7 (a-b)**. The enlarged branches formed dominated trunks that grew randomly, crossing each other forming 45° - 55° . The sub-branches end forms cauliflower-shaped particles with distinct layers which attribute to layer-by-layer Te-deposition growing on branches (see **Figure 6. 7 (b)**). Te-covered electrode surface has a tendency of controlling the morphology via surface directing diffusion process, similar to the observation in literature by [53]. BiTePd displayed a very conformal flat deposit which may indicate the layer-by-layer deposition of elements. The deposits showed homogenous nanometer-sized deposits, however, the small white Te-dendritic lumps can be observed. In this image (**Figure 6.7 (c-d)**) Pd trace are not definite, which attributes to complete coverage of Pd by Bi and Te adlayer. Bi-adlayer almost obscured the Te-adlayer, this finding corroborates with elemental mapping results (**Figure 6.8 (b): insert**), where Bi is highly dense across the substrate.

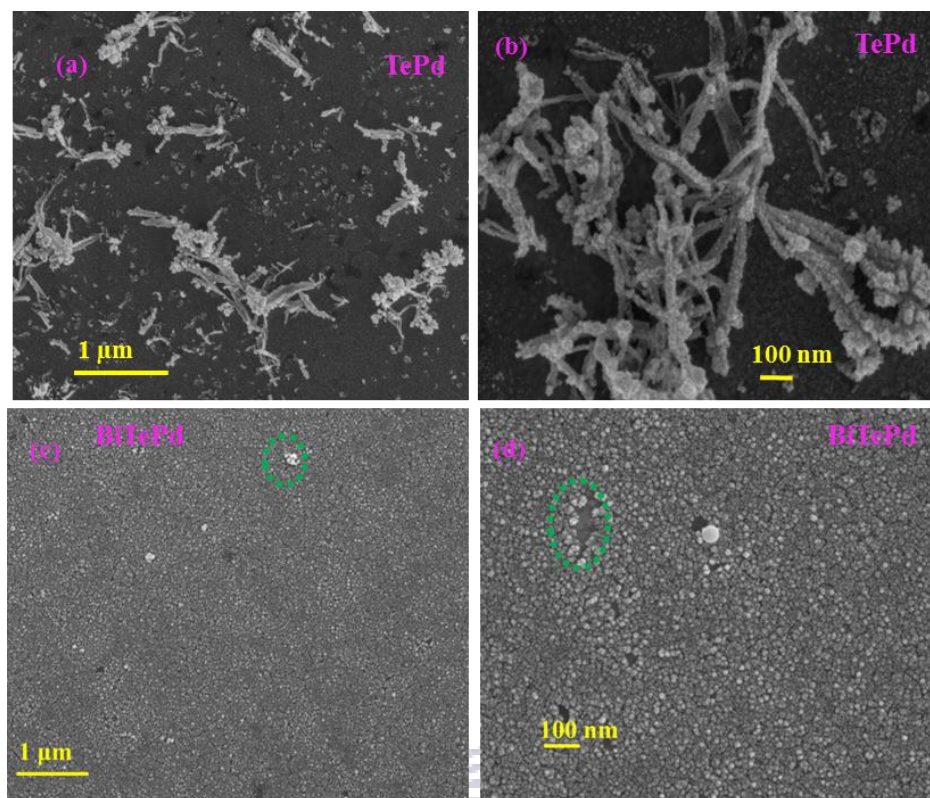


Figure 6.7. Scanning electron microscope (SEM) analysis for TePd (a-b) and BiTePd (c-d) on Au.

EDS pattern and elemental mapping in **Figure 6.8** displays the existence of elemental Te, Cu, Bi and Pd for their respective corresponding deposits, such as TePd, and BiTePd. The Elemental mapping (**Figure 6.8**: inserts) is coherent with EDX results. It can be seen that Te-Pd and BiTePd, have a highly dense Te across the thin film which may imply the conformal deposition, alloy phase formation and epitaxial elemental Te deposition. The finding is in coherent with the XRD pattern (see **Figure 6.6 (a-b)**), where the deposits displayed shifts to the 2θ value (at (111; seen inserts) and (200) planes and the emergence of intense peaks at low 2θ (15° - 25°) value.

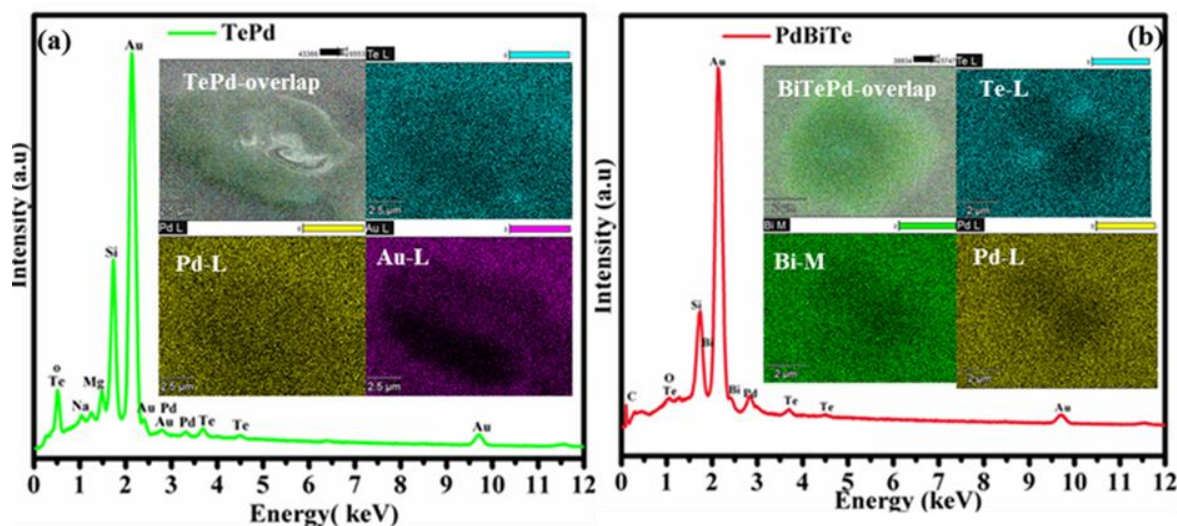


Figure 6.8: Illustrates the EDX and corresponding elemental mapping (inserts) of (a) PdTe, (b) and BiTePd

6.6 Atomic force microscopy (AFM) of Te-M thin-film analogous

AFM was used to probe the surface morphology, surface texture the technique also attain microscopic and topographic information on the surface topographic of thin films. Thus AFM micrographs quantify average roughness (Ra) and root mean square roughness (Sq)/ (r.m.q).

Figure 6.9 depicts AFM topographic 2D micrographs of (a) TePd, and (b) BiTePd, and their corresponding 3D view, and texture profiles. The 2D TePd micrographs exhibit the high conformity and well-dispersed grain distribution, the grain distribution is also clearly seen and corroborate with mapping (insert) and 3D view (**Figure 6.9 (a (iii))**). This finding is associated with the layer-by-layer formation of Te on Pd-covered Au. 2D images of BiTe reveals the flat grain distribution, which forms cone like-island, clearly observed with a 3D view. **Figure 6.10 (b)** depicts the 2D topographic micrographs of BiTePd, which shows a flat and conformal dispersion of grains. The BiTePd AFM results corroborate with SEM images in **Figure 6.7**. All the AFM micrographs have exhibited a distinct average surface (Sa) and root mean square (RMS) in nano-meter size with this order: BiTePd (Sa= 49.2 nm; Sq = 58.1 nm > TePd (Sa=

45.4 nm; $S_q = 54.6$ nm). The cross sectional (east to west) analysis exhibits the spikes attaining height ranging from 100-202 nm. These spikes may indicate the random distribution of Bi on TePd and active Pd remnants (Pd-covered Au) during the desposition of trimetallic BiTePd compound).

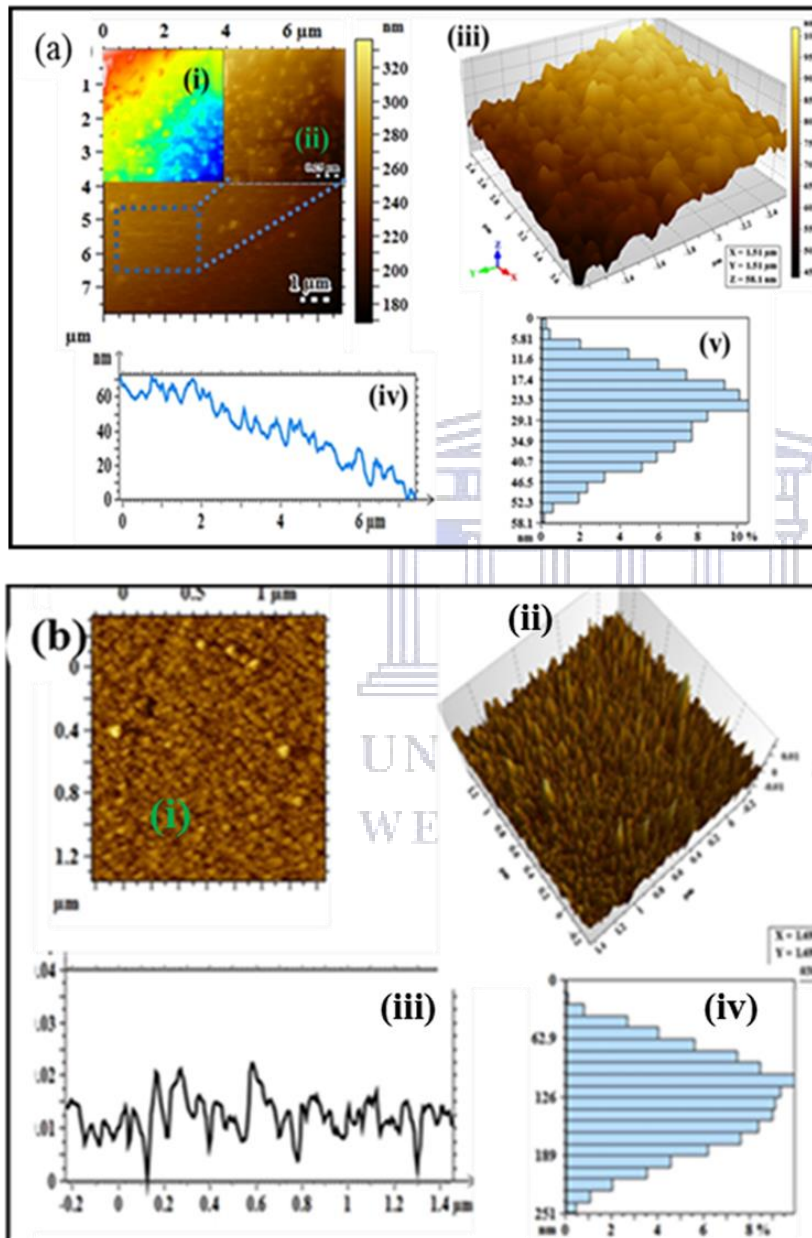


Figure 6.9: AFM topography (2D (i) and 3D (ii)) micrographs revealing details of Atomic Force Microscopy (AFM) analysis for (a) TePd, (b) BiTePd thin films and corresponding height profile (iii) and Histogram (iv).

6.7 Electrochemical characterization Palladium-based thin film: Activity towards ethanol oxidation in alkaline media

Figure 6.10 (a-c) illustrates cyclic voltammogram curves for Te-M analogous thin films in a 0.5 M KOH solution. The CV illustrated herein, the thin films reported includes Pd, BiPd, TePd, and BiTePd and are displayed in **Figure 6.10**. All Pd nanostructured thin films were cycled between -1V to +0.2 V potential window, and the redox feature showed a typical Pd voltammetric signatures, with distinct peak current, for Pd-O ox formation and its corresponding Pd-O reduction. This feature includes well-pronounced peaks of Pd-O/Pd-OH formation around -0.1 to 0.19 V and its corresponding Pd-Ox reduction at 0.1 V to -0.35V respectively as described by literature [42], [43], [44], [54]. Hydrogen adsorption-desorption is manifested at the high negative potential region around -0.98 to -0.1V. However, these features showed a diverse/distinct current response and onset potential. This variation may signify that the electrolyte solution occurs in various electrode compositions. The peak current for Pd-Ox formation and its corresponding Pd-Ox reduction observed of BiTePd thin film derivatives in **Figure 6.10** has this order: BiTePd > TePd > BiPd > Pd. This finding indicates that upon the incorporation of Te on each electrode increases the oxide on the Pd-based electrode surface, signifying the high affinity of Pd-electrodes for oxides when oxygenated Te is added. The highest peak current obtained with trimetallic BiTePd thin film is possibly assigned to dual oxygenated BiTe species on Pd-surface modified. **Figure 6.10** shows higher Pd-Ox formation peak current for BiTePd thin films electrocatalyst as compared to its counterparts, possessing the following trend: BiTePd > TePd > BiPd >, which indicates the strong electron interaction of BiTe and modified Pd-surface. In **Figure 6.11**, it can be observed that the trimetallic have a high charge for Pd-O in contrast to monometallic and bimetallic counterparts, this could be interpreted to well-dispersed Bi and Te particles on Pd surfaces and possibly high electrochemically active

surface area. Conclusively, Te and BiTe increase the concentration of OH due to oxophilic properties. The increased concentration may assist to free the active sites Pd thin film and subsequently promote the thin films electrocatalytic bifunctional mechanism.

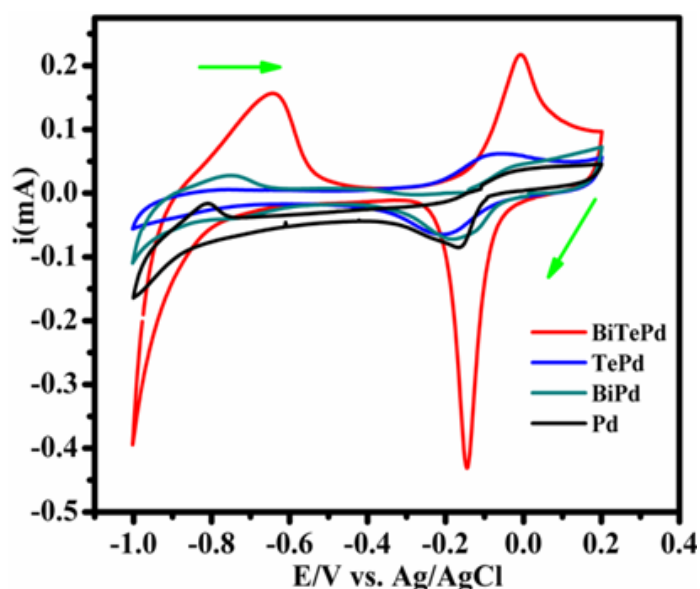


Figure 6.10: CV of BiTePd thin film and its analogous in 0.5 M KOH at 30 mVs^{-1} scan rate.

Figure 6.11 (a-c) shows the CV of Te-M derivatives in 0.1 M EtOH + 0.5 M KOH. All Pd-thin films showed two typical well-distinct ethanol oxidation peaks, that is oxidation of ethanol during forward scan (i_f , $E_{p,f}$), and reduction of Pd(II) oxide formed during forward scan or removal of carbonaceous species during backward scan (i_b , $E_{p,b}$) as described in literature [55], [56],[57],[58],[59],[60]. For comparison purposes and to investigate the effect of Te incorporation on each thin film electrode, the CVs were overlaid. It can be seen that the incorporation of Te on Pd (**Figure 6.11(a)**), and on BiPd (b) thin film electrodes negatively shifted the onset potential and increased the oxidation (forward) current for EOR. This finding signifies the least activation energy and high electron diffusion respectively upon addition of Te on Pd. The more negative onset binary compounds incorporated by Te is due to oxophilic character, they tend to form $M(\text{OH})_x$ moiety at a lower potential which lowers the onset potential [61]. Te is an oxygen species that may assist to strip off carbonaceous (by-products) species due

to its electronic effect and bifunctional mechanism as described in [62]. The steep reverse peak current observed on BiTePd (i_f/i_r ratio= 0.89) as compared to BiPd (i_f/i_r ratio= 0.99) (**Figure 6.11 (b)**), bring us about the exceptional explanation, which may pinpoint the higher Pd (II)-oxide formation may occur at higher potential (during forward scan) as indicated by **Equation 5.8** (see **Chapter 5, section 5.6**), then the reduction of the Pd (II)-oxide may form higher reverse peak. To be certain about reaction (EOR) by-product adsorbed on these two thin film electrocatalysts and tolerance, the in-situ CV-FTIR is highly recommended by literature [63]–[65]. The summary of the selected electrocatalytic indices of Te-M thin film electrocatalysts towards EOR is summarized in **Table 6.2**.

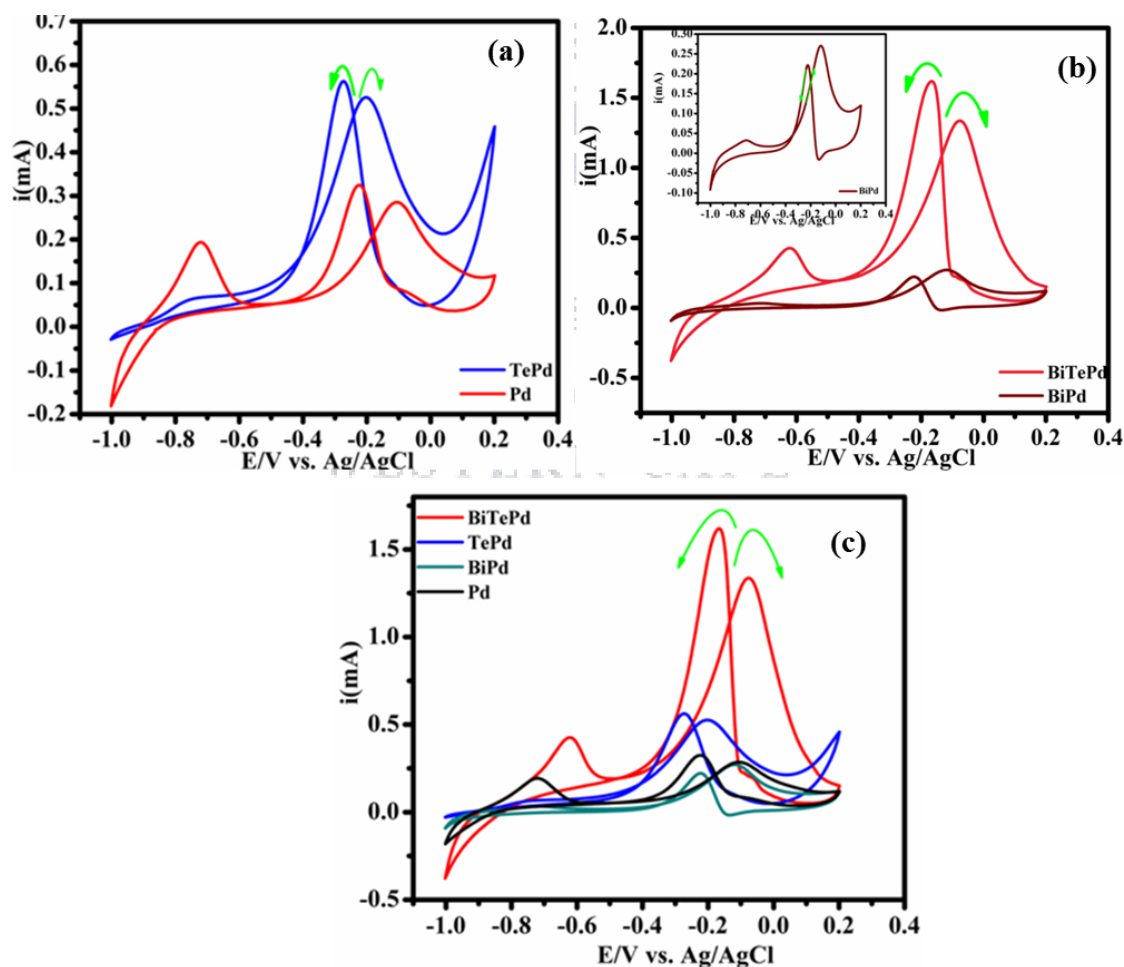


Figure 6.11: CV of Pd, Te-M based thin films in 0.5 M KOH+ 0.1 M EtOH at 30 mVs⁻¹ scan rate.

Table 6.2: Summary of electro-oxidation activity of Pd based electrocatalyst towards ethanol in alkaline media at 30 mVs⁻¹ scan rate.

Thin films	Forward peak current; I_f (mA)	Reverse peak current, I_b (mA)	Onset (V)	I_f/I_b ratio
Pd	0.13	0.15	-0.39	0.94
TePd	0.527	0.559	-0.535	0.94
BiPd	0.24	0.18	-0.4	1.33
BiTePd	1.26	1.53	-0.55	0.82

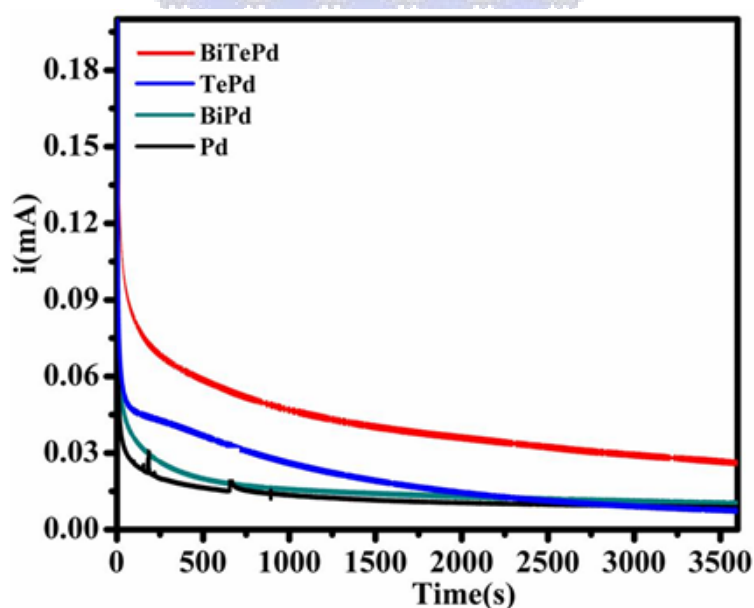


Figure 6.12: CA of BiTePd based thin films in 0.5 M KOH + 0.1 M EtOH for 1hour (3600s).

To investigate the electrochemical stability of as-prepared Te-M based thin films in 0.5 M + 0.1 M EtOH, and effect of Te adatoms into a stable current response in 1-hour duration (3600s) polarization experiment towards EOR (**Figure 6.12**). The current density-time plots test of

nanostructured Te-M based thin film electrocatalysts analogues ranging from Pd, TePd, BiPd, and BiTePd thin films in at fixed potential of -0.2 V selected (from CVs, **Figure 6.11**) was used. The initial high current value observed presumably associated with charging/discharging of a double layer or implies to the present active site of Pd nanostructured thin films as described in the literature [50], [64], [66]. The rapid current decay during the first few minutes is presumably due to the gradual accumulation of adsorbed poisonous carbonaceous (EtOH intermediates) species [66] at the active site of electrocatalysts which is consistent with previous work [37]. Subsequently, the current response gradually decreases until it reaches a steady-current. At this stage, BiTePd showed the highest steady-current followed by TePd and BiPd. This finding demonstrates that BiTePd thin film electrocatalyst decay is slower than the others, implying BiTePd is the most stable, which is constant with previous studies by [67]. The ternary compounds showed higher current response throughout in contrast to bimetallic compounds. The results correlate with CV results in (**Figure 6.11 (d)**).

6.8 Scan rate dependence study of BiTePd in 0.5 M KOH + 0.1 EtOH

Figure 6. 13 (a, c) depicts CVs of BiTePd thin film electrocatalyst displaying the electrode current response in **(a)** 0.5 M KOH and in **(c)** 0.5 M KOH + 0. 1 M EtOH. Due to the high electrochemical activity of BiTePd thin film among Te-M thin film electrocatalysts, it was then further scrutinized by observing a change in anodic and cathodic peak currents as a function of the square root of various (10, 15, 20, 25 and 40) mVs^{-1} scan rates. The forward (oxidation) peak current showed an increase with scan rate and the potential shift was also observed. Increasing the scan rate resulted in a significant increase in the current response, with a linearity correlation coefficient ($r^2 = 0.997$) shown by the Randles-Sevcik plot (**Figure 6.13 (b, d)**) in both 0.5 M KOH and 0.1 M EtOH solution. This result shows the stability of the electrode and electrode-ethanol interface (electrocatalyst) reveals the diffusion-controlled electrocatalytic process.

Nonetheless, electrochemical reaction system showed reversibility process, with the fact that the calculated forwards (anodic) and reverse (cathodic) peak current ratio (i_f/i_r) is almost 1 and the difference with peak potential $\Delta E = 159$ mV for KOH with EtOH and without EtOH which is greater than 59 mV ($\Delta E > 59$ mV). The increase in the peak current with the increase in the scan rate is ascribed to the excitation signal caused during the charging of the interface capacitance by the charge transfer process.

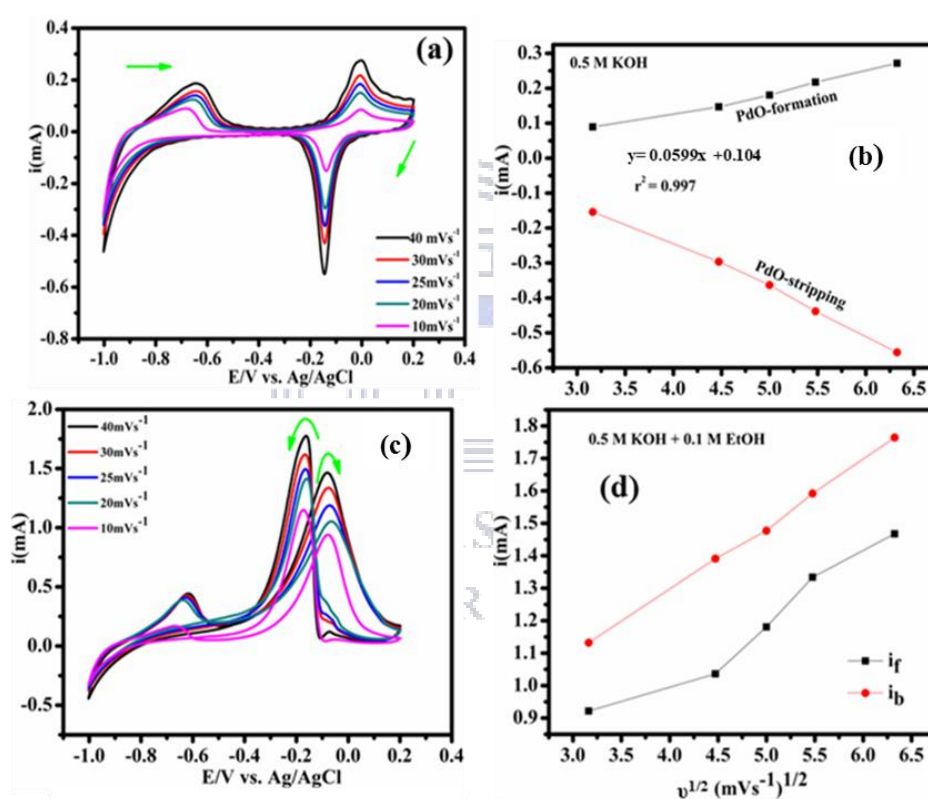


Figure 6. 13: BiTePd thin film in 0.5 M KOH (a) and 0.5 M KOH + 0.1 M EtOH (c) at various scan rates (10, 20, 25, 30 and 40) mVs^{-1} and corresponding Randles-Sevcik plot (b,d).

To substantiate the electrons mobility in the system, the diffusion coefficient (D) and surface coverage (Γ) were calculated with the equations as follows; For reversible systems Randles-Sevcik equation (**Equation 6.10**) and Laviron equation, (**Equation 6.11**) were employed to study

the kinetics of the electrode process. **Figure 6.13** shows a proportionality of the current response versus scan rate, and the results indicate that the electrochemical reaction rate is quite fast and the reduction of Pd-Ox on the BiTePd electrode in **Figure 6.13** 0.5 M KOH (**a,b**) as well as in EtOH oxidation (c). (**Figure 6.13 (c, d)**) is a typical diffusion controlled-process in all electrolyte solutions.

$$I_p = 2.69 \times 10^5 n^3 A D^{\frac{1}{2}} v^{\frac{1}{2}} C \quad (6.10)$$

$$\frac{I_p}{v} = \frac{n^2 F^2 A \Gamma}{4RT} \quad (6.11)$$

The value of slope from I_p vs. $v^{1/2}$ for PdOr peak is used to explain the nature of the process influencing the electrochemistry of surface-limited species and was obtained to be ($\Gamma = 3.6 \times 10^{-3} \text{s}^{-1}$). The calculated diffusion coefficient using aforementioned **Equation (6.10)** for KOH on Pd is obtained as $1.96 \times 10^{-5} \text{ cm}^2 \cdot \text{s}^{-1}$. The later finding may attribute that the electrochemical reaction occurs on a BiTePd monolayer.

6.9 Electrochemical Impedance Spectroscopy of Te-M nanostructured thin films

Figure 6.14 displays the Nyquist plot of Te-M analogous thin film materials in 0.5 M KOH containing 0.1 M EtOH solutions at selected -0.2 V from CV results (**from Figure 6.10**). It can be seen that the materials exhibit a diverse diameter semi-circle which indicates the electron transfer kinetics of the thin film-electrolyte interface. The Randles-Sevcik equivalent circuit (**Figure 6.14**): insert) has been used to simulate the semi-circles to obtain the values of the corresponding important EIS parameters possessing important elements such as ($R_s(R_{ct}CPE)$) and all the associated error obtained was less than 4 % [68] as indicated in **Table 6.3**, which makes it a suitable fit. Where R_s is solution resistance of electrode-electrolyte interface, R_{ct} is a charge transfer resistance and is correlated to reaction kinetic while CPE a constant phase element is a distributive element that models a double layer capacitance (Cdl) [69]. Generally,

the size of the semi-circle estimates the charge transfer resistance value [67], with a small semi-circle representing an enhanced charge transfer, while a large semi-circle indicating high electron charges transfer resistance. The R_{ct} of the materials possesses the following trend: Pd > BiPd > TePd > BiTePd. This implies that trimetallic (BiTePd) thin films electrocatalyst is the most conductive relative to its counterparts, and has the fastest electron kinetic transfer. In addition, Pd-surface modification by Te and Bi adatoms possibly remove CO intermediate and further promote dehydrogenation and subsequent increase in electrocatalytic activity towards the EOR. The results corroborate with CA and CV results, BiTePd exhibit the highest electrochemical activity as compared to bimetallic (TePd, BiPd) counterparts.

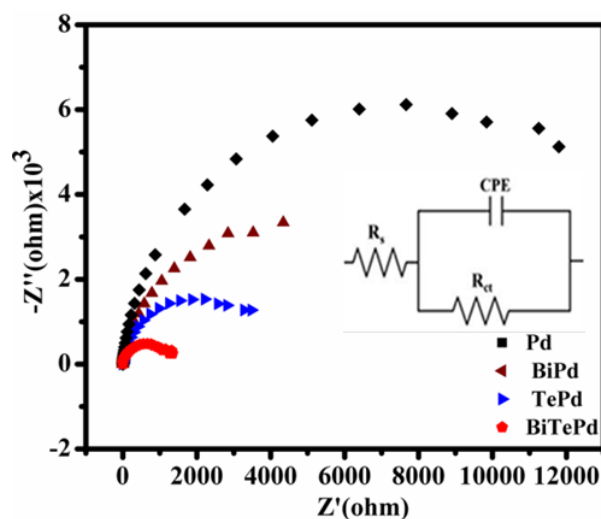


Figure: 6.14: Nyquist plot of Te-M analogues in 0.5 KOH + 0.1M EtOH at a constant potential of -0.2 V at 1×10^4 to 0.1 Hz frequency range, Randles-Sevcik circuit: insert.

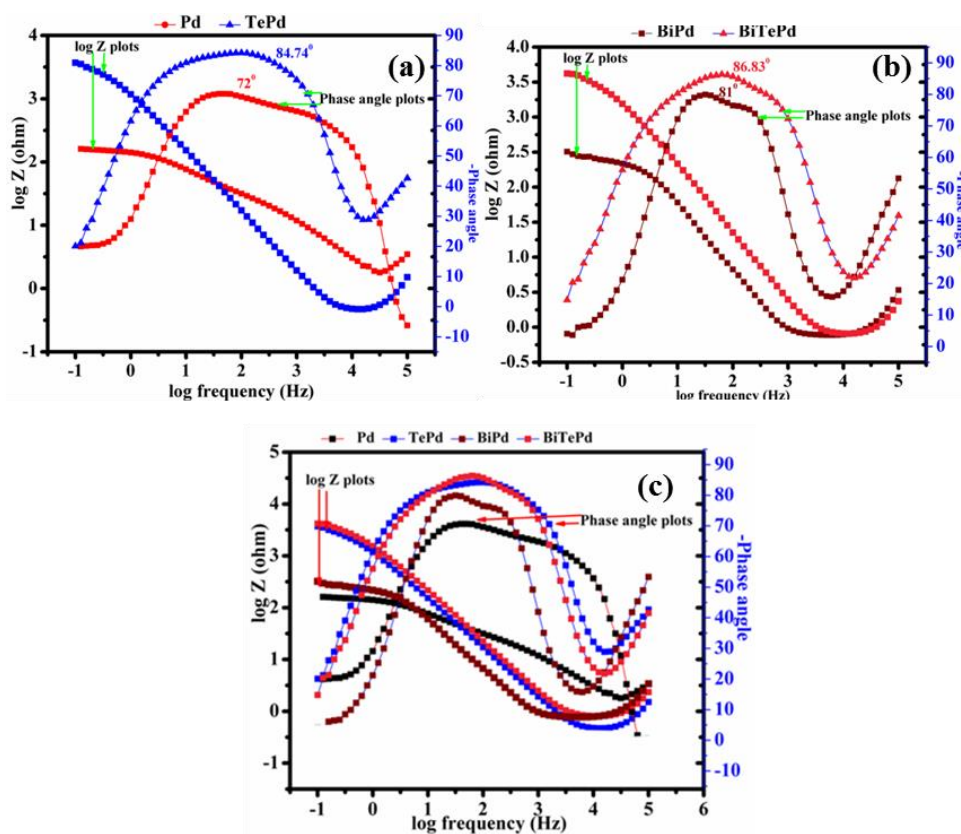


Figure 6.15: Bode plot of Te-M analogues in 0.5 KOH + 0.1M EtOH at a constant potential of -0.2 V.

In **Figure 6.15** depicts the Bode plot of Te-M derivative thin film, bimetallic ranging from Te-Pd **(a)**, BiPd **(b)** and the corresponding ternary compounds BiTePd **(c)** and its analogues in 0.5 KOH + 0.1 EtOH. In **Figure 6.15 (a)** for comparison purposes, Pd and TePd were overlaid, it can be observed that phase angle max ($-\theta_{\max}$) increased from 74° to 84.7° upon the addition of Te signifying an enhanced conductivity and electrocatalytic activity according to the literature [71]. The transformation from resistive behavior at low frequency to capacitive behavior at high frequency was observed, because of increased concentration of hydroxyl that further attack carbonyl as explained by [64] species promoting bifunctional mechanism. The findings demonstrate the higher electrocatalytic properties of TePd towards EOR, which corroborates with results from CV (**Figure 6.11 (a)**) and Nyquist plot (**Figure 6.14**). The change of symmetric peak on BiPd upon addition of Te to produce BiTePd, as displayed in **Figure 6.15 (b)**

indicates that EOR occurs in a varied composition of the working electrode as described by [72]. Generally, the symmetric peak is associated with the relaxation process of the electrode-electrolyte interface [65], [67]. According to the maximum phase ($-\theta_{\max}$), the increase upon the incorporation of Te on BiPd, from 81° to 86.63° for BiPd and BiTePd respectively signifies that BiTePd is more conducting than BiPd which is consistent with CVs in **Figure 6.11 (b)**. BiTePd exhibits a larger impedance than BiPd, which may be ascribed to the existence Pd(II)-oxides as explained in literature [67]. The presence of Pd(II)-oxides is in agreement with CV results as explained in **section 6.7 (Figure 6.11)**, and are evidenced by the steep reverse peak (shown in **Figure 6.11 (b)**) as described by literature [65]. **Figure 6.15 (c)** illustrates an overlaid Bode plots of all as-prepared thin film electrocatalysts, it can be seen that both bimetallic and ternary compounds have almost the same maximum phase angle ($-\theta_{\max}$) with semi-metallic character and slight maximum frequency ($\max \log f$) shift and exposed in the same electrolyte solution. This finding may confirm that all nanostructures are deposited on a Pd/Au substrate.

Table 6.3: Summary of some impedimetric parameter of Te-M based thin film in 0.5 KOH + 0.1 EtOH

Thin films	R_s (Ω)	R_{ct} (k Ω)	n	CPE(F)	% error	φ ($^\circ$)
Pd	7.33E3	14.9	0.87	40.8	0.126	74
TePd	0.99	2.4205	0.81	5.55	0.22	84.41
BiTePd	0.82	2.01	0.74	4.95	0.89	86.83
BiPd	0.99	3.97	0.892	5.55	1.1	84.41

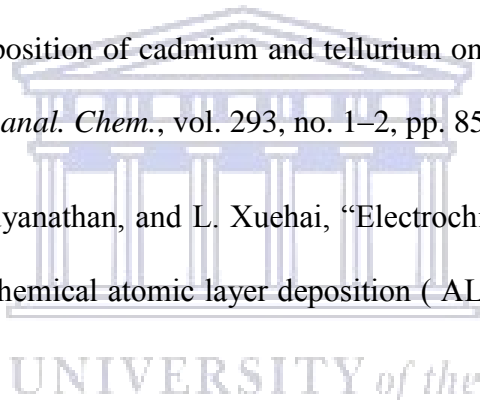
Sub conclusion

Electrodeposition of monometallic Pd, bimetallic metallic (TePd, and BiPd) compounds, and trimetallic (BiTePd) compounds have been electroformed successfully using E-ALD technique. The E-ALD cycles formed through repetitive execution of SLRR of Cu-UPD followed by oxidative Te-UPD. Incorporation of Te adatoms in various electrodes, including Pd, BiPd enhanced the electrochemical activity towards EOR respective to its monometallic counterparts. EDX and elemental mapping, exhibit the existence, conformal and dense Te and Bi on TePd and BiTePd respectively, which is coherent with alloy phase formation and the epitaxial relationship between the substrate and Te. The atomic layer-by-layer Te deposits and the alloy was also confirmed with XRD, showing Pd/Au (111) preferred orientation. These are the first PGMs-based chalcogenides dendritic structures using E-ALD. AFM showed well-dispersed TePd grains, where's BiTePd exhibited evenly grain distribution with increased surface roughness. In the case of CuTePd, the most turbulent grain distribution which formed some island, which may correlate to nucleation and growth (3D). Moreover, TePd and BiTePd showed the small diameter of the semi-circle (R_{ct}) indicating the smallest electron transit resistance, which makes it a better electrocatalyst. Te plays a pivotal role in fine-tuning the morphology/structure as well as the electrochemical activity of Pd-based thin films. The results are in strong agreement with CV, CA and XRD. This E-ALD cycle approach makes E-ALD technique futuristic methods to form PGMs-based p-nictogens and chalcognides electrocatalysts for DEFCs.

References

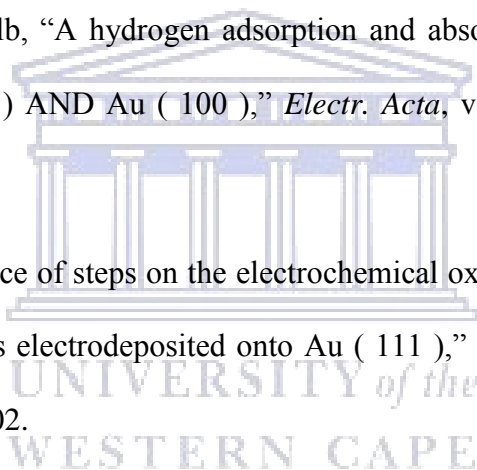
- [1] V. Venkatasamy, N. Jayaraju, S. M. Cox, C. Thambidurai, M. Mathe, and J. L. Stickney, "Deposition of HgTe by electrochemical atomic layer epitaxy (EC-ALE)," *J. Electroanal. Chem.*, vol. 589, pp. 195–202, 2006.
- [2] E. P. B. Rudnik, "Electrochemical behavior of tellurium in acidic nitrate solutions in acidic nitrate solutions," *Matallurgy Foundry Eng.*, vol. 40, no. October, pp. 15–32, 2014.
- [3] T. A. Sorenson, K. Varazo, D. W. Suggs, and J. L. Stickney, "Formation of and phase transitions in electrodeposited tellurium atomic layers on Au (1 1 1)," *Surf. Sci.*, vol. 470, pp. 197–214, 2001.
- [4] F. Forni, M. Innocenti, G. Pezzatini, and M. L. Foresti, "Electrochemical aspects of CdTe growth on the face (111) of silver by ECALE," *Electrochim. Acta*, vol. 45, no. 20, pp. 3225–3231, 2000.
- [5] W. Zhu, J. Y. Yang, D. X. Zhou, S. Q. Bao, X. A. Fan, and X. K. Duan, "Electrochemical characterization of the underpotential deposition of tellurium on Au electrode," *Electrochim. Acta*, vol. 52, pp. 3660–3666, 2007.
- [6] Y. Kim, N. Jayaraju, D. Vairavapandian, Y. G. Kim, D. Banga, and J. L. Stickney, "Electrochemical Atomic Layer Deposition (E- ALD) of Pt Nanofilms Using SLRR Cycles Electrochemical Atomic Layer Deposition (E-ALD) of Pt Nanofilms," *J. Electrochem. Soc.*, vol. 10, no. January 2012, pp. 16–22, 2014.
- [7] D. Banga, Y.-G. Kim, and J. Stickney, "PbSe/PbTe Superlattice Formation via E-ALD," *J. Electrochem. Soc.*, vol. 158, no. 2, p. D99, 2011.
- [8] K. Varazo, M. D. Lay, T. A. Sorenson, and J. L. Stickney, "Formation of the first monolayers of CdTe on Au(111) by electrochemical atomic layer epitaxy (EC-ALE):

- Studied by LEED, Auger, XPS, and in-situ STM,” *J. Electroanal. Chem.*, vol. 522, no. 1, pp. 104–114, 2002.
- [9] D. O. Banga, R. Vaidyanathan, L. Xuehai, J. L. Stickney, S. Cox, and U. Happeck, “Formation of PbTe nanofilms by electrochemical atomic layer deposition (ALD),” *Electrochim. Acta*, vol. 53, pp. 6988–6994, 2008.
- [10] L. P. Colletti and B. H. Flowers, “Lisa P. Colletti,* Billy H. Flowers, Jr., and John L. Stickney** Department of Chemistry, University of Georgia, Athens, Georgia 30602, USA,” no. May, 1998.
- [11] B. W. Gregory, M. L. Norton, and J. L. Stickney, “Thin-layer electrochemical studies of the underpotential deposition of cadmium and tellurium on polycrystalline Au, Pt and Cu electrodes,” *J. Electroanal. Chem.*, vol. 293, no. 1–2, pp. 85–101, 1990.
- [12] D. O. Banga, R. Vaidyanathan, and L. Xuehai, “Electrochimica Acta Formation of PbTe nanofilms by electrochemical atomic layer deposition (ALD),” *Electr. Acta*, vol. 53, pp. 6988–6994, 2008.
- [13] E. Mori, C. K. Baker, J. R. Reynolds, and K. Rajeshwar, “Aqueous electrochemistry and gold of tellurium at glassy carbon A combined voltammetry-oscillating microgravimetry study quartz crystal,” *Journal Electroanal. Chem.*, vol. 252, pp. 441–451, 1988.
- [14] B. C. Bravo, S. L. Michelhaugh, and M. P. Soriaga, “Anodic Underpotential Deposition and Cathodic Stripping of Iodine at Polycrystalline and Single-Crystal Gold. Studies by LEED, AES, XPS, and Electrochemistry,” *J. Phys. Chem.*, vol. 95, no. 11, pp. 5245–5249, 1991.

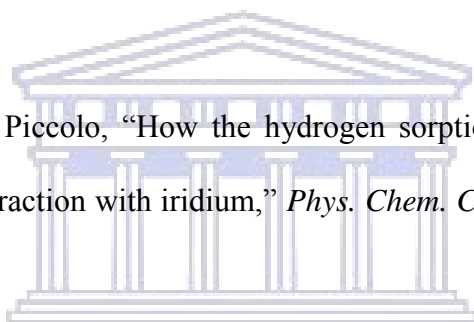


- [15] T. A. Sorenson, K. Varazo, D. W. Suggs, and J. L. Stickney, "Formation of and phase transitions in electrodeposited tellurium atomic layers on Au (1 1 1)," *Surf. Sci.*, vol. 470, pp. 197–214, 2001.
- [16] L. P. Colletti and J. L. Stickney, "Thin-layer electrochemical studies of the oxidative underpotential deposition of sulfur and its application to the electrochemical atomic layer epitaxy deposition of CdS," *J. Electroanal. Chem.*, vol. 369, pp. 145–152, 1994.
- [17] E. Mori, C. K. Baker, J. R. Reynolds, and K. Rajeshwar, "Aqueous electrochemistry of tellurium at glassy carbon and gold. A combined voltammetry-oscillating quartz crystal microgravimetry study," *J. Electroanal. Chem.*, vol. 252, no. 2, pp. 441–451, 1988.
- [18] D. W. Suggs and J. L. Stickney, "Characterization of atomic layers of tellurium electrodeposited on the low-index planes of gold," *J. Phys. Chem.*, vol. 95, no. 5, pp. 10056–10064, 1991.
- [19] F. Haidar, M. Maas, A. Piarristeguy, A. Pradel, S. Cavaliere, and M. Record, "Ultra-Thin Platinum Deposits by Surface-Limited Redox Replacement of Tellurium," *nanomaterials*, vol. 8, no. 1–12, 2018.
- [20] W. Zhu, J. Y. Yang, X. H. Gao, S. Q. Bao, X. A. Fan, T. J. Zhang, and K. Cui, "Effect of potential on bismuth telluride thin film growth by electrochemical atomic layer epitaxy," vol. 50, pp. 4041–4047, 2005.
- [21] J. L. A. B.M. Huang, L.P. Colletti, B.W. Gregory, J.L. Stickney, "Preliminary Studies of the Use of an Automated Flow-Cell Electrodeposition System for the Formation of CdTe Thin Films by Electrochemical Atomic Layer Epitaxy," *J. Electrochem. Soc.*, vol. 142, no. 9, 1995.

- [22] D. M. Benson, C. F. Tsang, J. D. Sugar, K. Jagannathan, D. B. Robinson, F. El Gabaly, P. J. Cappillino, and J. L. Stickney, "Enhanced Kinetics of Electrochemical Hydrogen Uptake and Release on Palladium Powders Modified by Electrochemical Atomic Layer Deposition," *Appl. Mater. Interfaces*, vol. 8, 2017.
- [23] L. B. Sheridan, Y. Kim, B. R. Perdue, K. Jagannathan, J. L. Stickney, and D. B. Robinson, "Hydrogen Adsorption, Absorption, and Desorption at Palladium Nanofilms formed on Au(111) by Electrochemical Atomic Layer Deposition (E-ALD): Studies using Voltammetry and In Situ Scanning Tunneling Microscopy," *J. Phys. Chem. C*, vol. 117, no. 111, pp. 15728–15740, 2013.
- [24] M. B. and D. M. Kolb, "A hydrogen adsorption and absorption study with ultrathin Pd overlayers on Au(111) AND Au (100)," *Electr. Acta*, vol. 38, no. 15, pp. 2145–2153, 1993.
- [25] L. A. Kibler, "Influence of steps on the electrochemical oxidation of CO adlayers on Pd (111) and on Pd films electrodeposited onto Au (111)," *J. Electroanalytical Chem.*, vol. 534, pp. 107–114, 2002.
- [26] J. Cai, Y. Huang, and Y. Guo, "PdTex/C nanocatalysts with high catalytic activity for ethanol electro-oxidation in alkaline medium," *Appl. Catal. B Environ.*, vol. 150–151, pp. 230–237, 2014.
- [27] J. . S. B.M. Huang, L.P. Colletti, B.W. Gregory, J.L. Anderson, "Preliminary Studies of the use of an Automated Flow-Cell Electrochemical System for the Formation of CdTe Thin Film by Electrochemical Atomic Layer Epitaxy." pp. 3007–3016, 1995.
- [28] R. Wang, S. Liao, H. Liu, and H. Meng, "Synthesis and characterization of Pt – Se / C electrocatalyst for oxygen reduction and its tolerance to methanol," vol. 171, pp. 471–476, 2007.



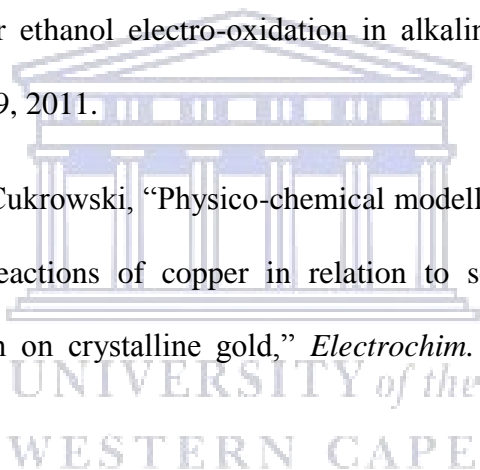
- [29] F. Haidar, M. Maas, A. Piarristeguy, A. Pradel, S. Cavaliere, and M. Record, "Ultra-Thin Platinum Deposits by Surface-Limited Redox Replacement of Tellurium," *nanomaterials*, vol. 8, pp. 1–12, 2018.
- [30] N. Xaba and R. M. Modibedi, "Pd , PdSn , PdBi , and PdBiSn Nanostructured Thin Films for the Electro-Oxidation of Ethanol in Alkaline Media," *Electrocatalysis*, pp. 11–16, 2019.
- [31] K. A. Anna Zalineeva, Alexey Serov, Monica Padilla, Ulises Martinez and and P. B. A. Stève Baranton, Christophe Coutanceau, "Self-Supported PdxBi Catalysts for the Electrooxidation of Glycerol in Alkaline Media," *J. Am. Chem. Soc.*, vol. 136, pp. 3937–3945, 2014.
- [32] C. Goyhenex and L. Piccolo, "How the hydrogen sorption properties of palladium are modified through interaction with iridium," *Phys. Chem. Chem. Phys.*, vol. 19, no. 48, pp. 32451–32458, 2017.
- [33] C. Zlotea, F. Morfin, T. S. Nguyen, N. T. Nguyen, J. Nelayah, C. Ricolleau, M. Latroche, and L. Piccolo, "Nanoalloying bulk-immiscible iridium and palladium inhibits hydride formation and promotes catalytic performances," *Nanoscale*, vol. 6, no. 17, pp. 9955–9959, 2014.
- [34] B. F. A. Lewis and D. Ph, "The Hydrides of Palladium and Palladium Alloys," no. 4, pp. 132–137, 1960.
- [35] C. Busó-Rogero, J. Solla-Gullón, F. J. Vidal-Iglesias, E. Herrero, and J. M. Feliu, "Adatom modified shape-controlled platinum nanoparticles towards ethanol oxidation," *Electrochim. Acta*, vol. 196, pp. 270–279, 2016.



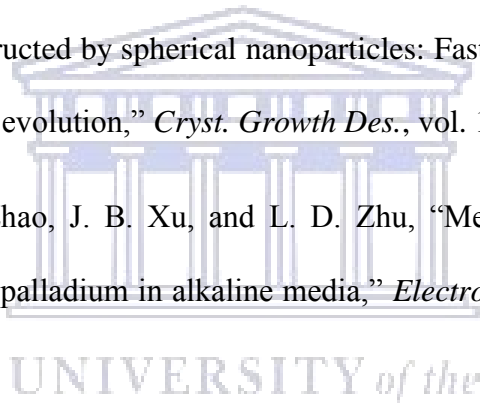
UNIVERSITY OF
WESTERN CAPE

- [36] L. B. Sheridan, D. K. Gebregziabih, J. L. Stickney, and D. B. Robinson, "Formation of Palladium Nanofilms Using Electrochemical Atomic Layer Deposition (E-ALD) with Chloride Complexation," *Langmuir*, vol. 29, pp. 1592–1600, 2013.
- [37] W. Du, K. E. Mackenzie, D. F. Milano, N. A. Deskins, D. Su, and X. Teng, "Palladium – Tin Alloyed Catalysts for the Ethanol Oxidation Reaction in an Alkaline Medium," *ACS Catal.*, vol. 2, pp. 287–297, 2012.
- [38] R. N. Singh, "Pd1 % Ni Composite Electrodes for Electrooxidation of Phenol in Acid Solution Pd-1 % Ni Composite Electrodes for Electrooxidation of Phenol in Acid Solution," *Int. J. Electrochem. Sci.*, vol. 4, no. November, pp. 1638–1649, 2015.
- [39] S. Garbarino and L.D. Burke, "The Surface Active Site Model for Formic Acid Electrooxidation at Palladium in Aqueous Acid Solution," *Int. J. Electrochem. Sci.*, vol. 5, no. May, 2014.
- [40] T. S. Mkwizu and I. Cukrowski, "Physico – chemical Modelling of Adlayer Phase Formation via Surface – limited Reactions of Copper in Relation to Sequential Electrodeposition of Multilayered Platinum on Crystalline Gold," *Electr. Acta*, vol. 147, pp. 432–441, 2014.
- [41] J. Cai, Y. Huang, and Y. Guo, "Bi-modified Pd / C catalyst via irreversible adsorption and its catalytic activity for ethanol oxidation in alkaline medium," *Electrochim. Acta*, vol. 99, pp. 22–29, 2013.
- [42] A. O. Neto, S. G. Silva, and G. S. Buzzo, "Ethanol electrooxidation on PdIr / C electrocatalysts in alkaline media : electrochemical and fuel cell studies," *Ionics (Kiel)*, vol. 21, pp. 487–495, 2015.

- [43] R. Jana, S. Dhiman, and S. C. Peter, "Facile solvothermal synthesis of highly active and direct ethanol fuel cell applications Facile solvothermal synthesis of highly active and robust Pd_{1.87}Cu_{0.11}Sn electrocatalyst towards direct ethanol fuel cell applications," *Mater. Res. Express*, vol. 3, no. 8, pp. 1–9, 2016.
- [44] M. S. Ahmed, D. Park, and S. Jeon, "Ultrasmall Pd_mMn_{1-m}O_x binary alloyed nanoparticles on graphene catalysts for ethanol oxidation in alkaline media Ultrasmall Pd_mMn_{1-À}mO_x binary alloyed nanoparticles on graphene catalysts for ethanol oxidation in alkaline media," *J. Power Sources*, vol. 308, pp. 180–188, 2016.
- [45] R. M. Modibedi, T. Masombuka, and M. K. Mathe, "Carbon supported Pd-Sn and Pd-Ru-Sn Snanocatalysts for ethanol electro-oxidation in alkaline medium," *Int. J. Hydrogen Energy*, vol. 6, pp. 1–9, 2011.
- [46] T. S. Mkwizu and I. Cukrowski, "Physico-chemical modelling of adlayer phase formation via surface-limited reactions of copper in relation to sequential electrodeposition of multilayered platinum on crystalline gold," *Electrochim. Acta*, vol. 147, pp. 432–441, 2014.
- [47] H. Suh, J. Noh, J. Lee, S. Lee, N. V Myung, K. Hong, and J. Kim, "Morphological Evolution of Te and Bi₂Te₃ Microstructures during Galvanic Displacement of Electrodeposited Co Thin Films," *Electrochim. Acta*, vol. 255, pp. 1–8, 2017.
- [48] I. WitoNSKA, M. Frajtek, and S. Karski, "Selective oxidation of glucose to gluconic acid over Pd – Te supported catalysts," *Appl. Catal. A Gen.*, vol. 401, pp. 73–82, 2011.
- [49] B. Perdue, J. Czerniawski, J. Anthony, and J. Stickney, "Optimization of Te Solution Chemistry in the Electrochemical Atomic Layer Deposition Growth of CdTe," *J. Electrochemical Soc.*, vol. 161, no. 7, pp. 3087–3092, 2014.



- [50] A. C. Mkhohlakali, X. Fuku, R. M. Modibedi, L. E. Khotseng, S. C. Ray, and M. K. Mathe, "Electrosynthesis and characterization of PdIr using electrochemical atomic layer deposition for ethanol oxidation in alkaline electrolyte," *Appl. Surf. Sci.*, vol. 502, pp. 144–158, 2019.
- [51] X. Huang, J. Guan, Z. Lin, B. Liu, S. Xing, W. Wang, and J. Guo, "Epitaxial Growth and Band Structure of Te Film on Graphene," *Nano Lett.*, vol. 17, no. 8, pp. 4619–4623, 2017.
- [52] S. Bae, H. Kim, and H. S. Lee, "Formation mechanism of PbTe dendritic nanostructures grown by electrodeposition," *Mater. Chem. Phys.*, vol. 187, pp. 82–87, 2017.
- [53] Y. Zhang, Y. Ni, X. Wang, J. Xia, and J. Hong, "Polycrystalline Cu₇Te₄ dendritic microstructures constructed by spherical nanoparticles: Fast electrodeposition, influencing factors, and the shape evolution," *Cryst. Growth Des.*, vol. 11, pp. 4368–4377, 2011.
- [54] Z. X. Liang, T. S. Zhao, J. B. Xu, and L. D. Zhu, "Mechanism study of the ethanol oxidation reaction on palladium in alkaline media," *Electrochim. Acta*, vol. 54, pp. 2203–2208, 2009.
- [55] C. Jun Yin, Mei Shan Ng, Lefu Yang, Derrick Mott, Weiqin Fang, Ning Kang, Jin Luo, and Zhong, "Catalytic and Electrocatalytic Oxidation of Ethanol over Palladium- Based Nanoalloy Catalysts," *Langmuir*, vol. 29, pp. 9249–9258, 2013.
- [56] M. D. Obradović, Z. M. Stančić, U. Lačnjevac, V. V. Radmilović, A. Gavrilović-Wohlmuther, V. R. Radmilović, and S. L. Gojković, "Electrochemical oxidation of ethanol on palladium-nickel nanocatalyst in alkaline media," *Appl. Catal. B Environ.*, vol. 189, pp. 110–118, 2016.



- [57] H. Chen, Z. Xing, S. Zhu, L. Zhang, Q. Chang, J. Huang, W. Cai, N. Kang, C. Zhong, and M. Shao, "Palladium modified gold nanoparticles as electrocatalysts for ethanol electrooxidation," *J. Power Sources*, vol. 321, pp. 264–269, 2016.
- [58] A. K. Ipadeola, R. Barik, S. C. Ray, and K. I. Ozoemena, "Bimetallic Pd / SnO₂ Nanoparticles on Metal Organic Framework (MOF) -Derived Carbon as Electrocatalysts for Ethanol Oxidation," *Electrocatalysis*, 2019.
- [59] Y. Wang, Q. He, K. Ding, H. Wei, J. Guo, Q. Wang, R. O. Connor, X. Huang, Z. Luo, T. D. Shen, S. Wei, and Z. Guo, "Multiwalled Carbon Nanotubes Compositated with Palladium Nanocatalysts for Highly Efficient Ethanol Oxidation," *J. Electrochemical Soc.*, vol. 162, no. 7, pp. 51–54, 2015.
- [60] A. S. Douk, H. Saravani, and M. Noroozifar, "Preparation and Electrocatalytic Characteristics of PdW/C Catalyst for Ethanol Oxidation," *Int. J. Hydrogen Energy*, vol. 42, no. 22, pp. 15149–15159, 2017.
- [61] C. Zhu and Y. Yang, "Surface voltammetric dealloying investigation on PdCu / C electrocatalysts toward ethanol oxidation in alkaline media," *J Nanopart Res*, vol. 20, p. 314, 2018.
- [62] M. Huang, F. Wang, L. Li, and Y. Guo, "Short communication A novel binary Pt₃Te_x / C nanocatalyst for ethanol electro-oxidation," *J. Power*, vol. 178, pp. 48–52, 2008.
- [63] P. Oc, J. Torrero, M. Montiel, M. A. Pe, and S. Rojas, "Insights on the electrooxidation of ethanol with Pd- based catalysts in alkaline electrolyte," *Int. J. Hydrogen Energy*, no. xxxx, 2019. <https://doi.org/10.1016/j.ijhydene.2019.10.124>

- [64] X. Fuku, M. Modibedi, N. Matinise, P. Mokoena, N. Xaba, and M. Mathe, "Single step synthesis of bio-inspired NiO / C as Pd support catalyst for dual application : Alkaline direct ethanol fuel cell and CO₂ electro-reduction," *J. Colloid Interface Sci.*, vol. 545, pp. 138–152, 2019.
- [65] R. A. Gonçalves, M. R. Baldan, E. G. Ciapina, and O. M. Berengue, "Nanostructured Pd / Sb₂O₃: A new and promising fuel cell electrocatalyst and non-enzymatic amperometric sensor for ethanol," *Appl. Surf. Sci.*, vol. 491, no. February, pp. 9–15, 2019.
- [66] R. M. Modibedi, T. Masombuka, and M. K. Mathe, "Carbon supported Pd-Sn and Pd-Ru-Sn nanocatalysts for ethanol electro-oxidation in alkaline medium," *Int. J. Hydrogen Energy*, vol. 36, pp. 4664–4672, 2011.
- [67] K. Ding, Y. Zhao, L. Liu, Y. Li, L. Liu, Y. Wang, H. Gu, H. Wei, and Z. Guo, "Multi-walled carbon nanotubes supported Pd composite nanoparticles hydrothermally produced from technical grade PdO precursor," *Electrochim. Acta*, vol. 176, pp. 1256–1265, 2015.
- [68] A. Chen, D. J. La Russa, and B. Miller, "Effect of the Iridium Oxide Thin Film on the Electrochemical Activity of Platinum Nanoparticles," *Langmuir*, vol. 20, pp. 9695–9702, 2004.
- [69] T. Ramulifho, K. I. Ozoemena, R. M. Modibedi, C. J. Jafta, and M. K. Mathe, "Electrocatalytic oxidation of ethylene glycol at palladium-bimetallic nanocatalysts (PdSn and PdNi) supported on sulfonate-functionalised multi-walled carbon nanotubes," *J. Electroanal. Chem.*, vol. 692, pp. 26–30, 2013.
- [70] W. Xu, S. Zhu, Z. Li, Z. Cui, and X. Yang, "Preparation of Nanoporous Pd / CuO by Dealloying and Their Electrocatalysis for Methanol in Alkaline Condition Preparation of Nanoporous Pd / CuO by Dealloying and Their Electrocatalysis for Methanol in Alkaline Condition," *J. Electrochem. Soc.*, vol. 161, pp. 1474–1480, 2014.

- [71] N. Mayedwa, N. Mongwaketsi, S. Khamlich, K. Kaviyarasu, N. Matinise, and M. Maaza, “Green Synthesis of Nickel Oxide, Palladium and Palladium Oxide Synthesized,” *Appl. Surf. Sci.*, 2017. <https://doi.org/10.1016/j.apsusc.2017.12.116>
- [72] R. M. A. Hameed, “Facile preparation of Pd-metal oxide / C electrocatalysts and their application in the electrocatalytic oxidation of ethanol,” *Appl. Surf. Sci.*, vol. 411, pp. 91–104, 2017



Chapter 7

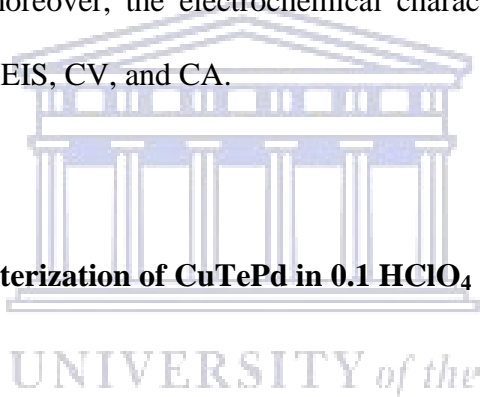
Summary

This section discusses the ternary CuTePd compound and briefly reports its corresponding monometallic (Pd), bimetallic analogous (CuPd, TePd). This study investigates the incorporation of Te on CuPd electrode surface. Prior to the electro-formation of CuTePd, oxidative underpotential deposition of Te will be investigated through immersion of CuPd thin film in a HTeO_4^+ aliquot. The electroformed CuTePd is characterized using microscopic and spectroscopic techniques; moreover, the electrochemical characterization and electrochemical activity were obtained using EIS, CV, and CA.

7.0 Results and discussion

7.1 Electrochemical characterization of CuTePd in 0.1 HClO_4

Cyclic voltammetry displayed in **Figure 7.1 (a)** was used to investigate the possible formation and optimal potential (UPD) to set an initial E-ALD cycle for the deposition of CuTePd. It was done through immersion of CuPd thin film (reported in **Chapter 5**) in electrolyte solution of 0.5 mM HTeO_2^+ + 0.1 M HClO_4 as depicted in **Figure 7.1 (a)**.



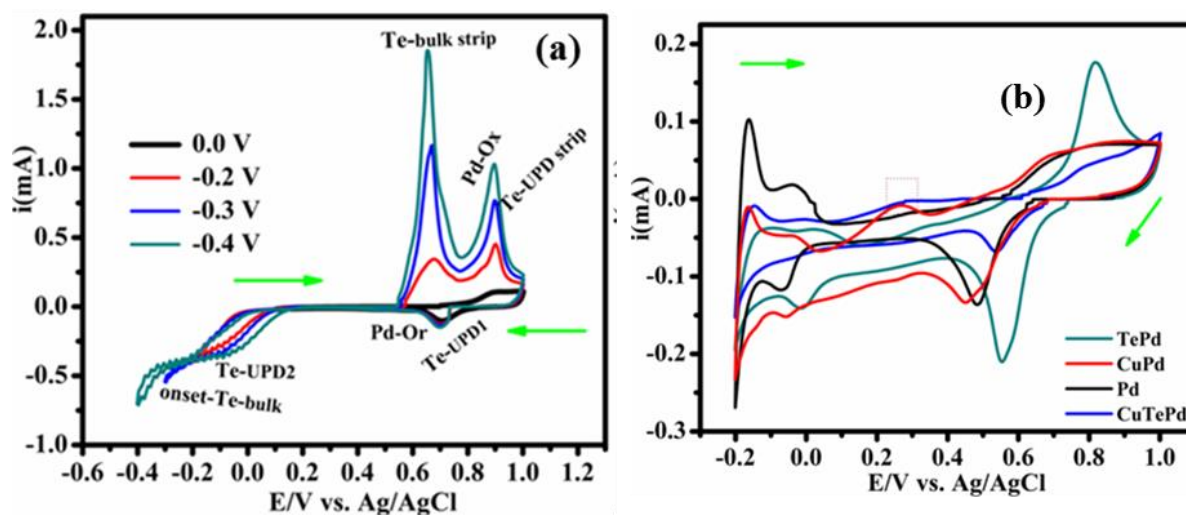


Figure 7.1: CV of CuPd in 0.5 mM HTeO₂⁺ at 10 mVs⁻¹ in various cathodic limits (a) and CuTePd thin films derivative in 0.1 M HClO₄ at 30 mVs⁻¹ scan rate (b).

The acquired CuTePd thin film was characterized by immersion in 0.1M HClO₄. **Figure 7.1 (b)** represents the overlaid CuPd and CuTePd and aims to investigate the effect of Te on CuPd. CuTePd thin film in 0.1M HClO₄ cycled from 1.0 to -0.2 V potential, and Pd characteristic features were observed as described in literature [1], [2],[3],[4],[5]. During the cathodic scan, Pd-O reduction and formation show a positive potential shift for CuTePd respective to CuPd counterpart, which indicates the electron interaction and structure deviation of CuPd upon the Te addition. Interestingly, CuTePd exhibit the lower Pd-O reduction (cathodic scan) and Pd oxidation (anodic scan) current response which may indicate the stronger electron interaction between Te and Cu than Pd. This is also confirmed by the enhanced peak current of Cu-UPD stripping peak which occurred simultaneously with onset Te-bulk stripping peak as denoting by the box. As cathodic scanning proceeds to a more negative potential, hydrogen adsorption/desorption is suppressed which may indicate the presence of dual modifier (CuTe) species for CuTePd as compared to a single modifier (Cu) on CuPd counterparts. The apparent small charge for Pd-O formation and its corresponding stripping may also be due to less

exposure of Pd to the electrolyte (HClO_4) because of blocked or hinder Pd active sites by islands formed which is evidence by AFM micrographs (**Figure 6.10 (b)**).

7.2 X-ray diffraction of CuTePd and its analogues Pd, TePd and CuPd nanostructured thin films.

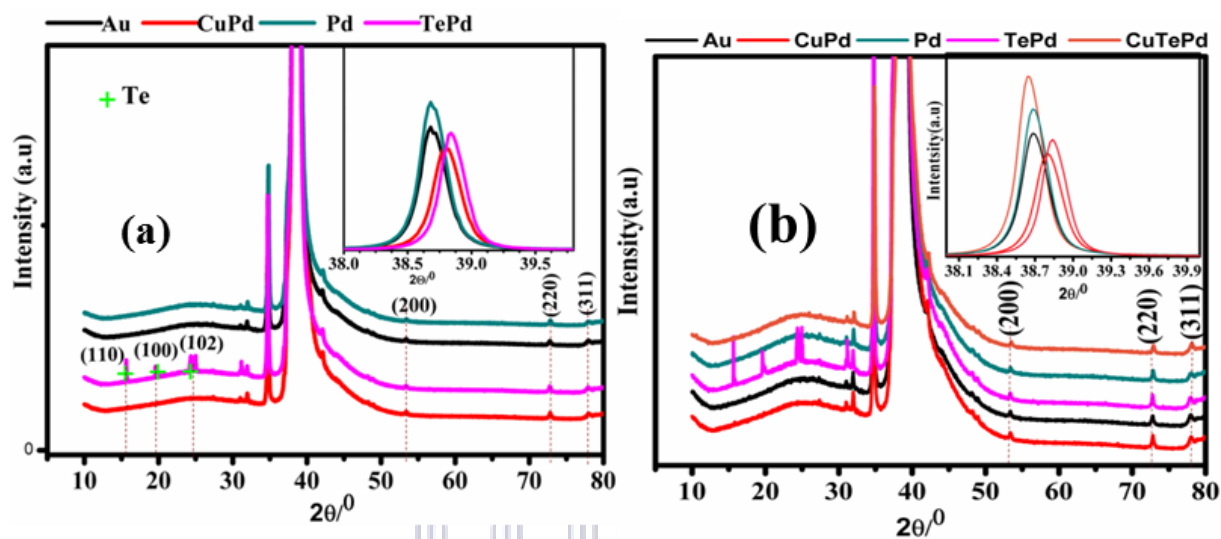


Figure 7.2: XRD pattern of Au, Pd, CuPd TePd thin films (a) and CuTePd and its derivatives thin films, insert: Magnified (111) planes.

Figure 6.7 depicts the XRD pattern of bare Au and as-prepared CuTePd and its derivative thin films such as Pd, TePd, and CuPd. For comparison, in each electrode modified with Te-adlayer is overlaid with unmodified one to investigate the incorporation of Te in the structure. All the thin films exhibit the XRD patterns that exhibit four main Bragg's diffraction angles around 38.5° , 56° , 66° , 72.86° and $79.88.6^\circ$ corresponding to the (111), (200), (220), (311) planes of face-centered cubic (fcc) of Pd phase characteristic features in accordance to standard certification (JCPDS card no. 89-4897) [6], [7], [8].

Meanwhile, the higher intensity observed for CuTePd (**Figure 7.2 (b)**) in comparison to its counterpart CuPd; suggests the increase in crystallinity upon Te incorporation. CuTePd shows

two phases of the alloy phase due to shifting to lower 2θ . The elemental peak ($2\theta = 29^\circ$) may suggest that Te deposited in remnants Pd-active sites. **Figure 7.1 (b)** displays the ternary CuTePd based and its counterpart (binary (Pd, TePd, and CuPd) electrodes. It can be seen that the electro-formed binary shifted to higher 2θ , which could corroborate the stronger electron interaction among adatoms more than to Pd surface in ternary Te-M based thin film counterparts. The Higher intensity of CuTePd as compared to other thin films may suggest the increased crystallinity.

7.3 Energy dispersive x-ray (EDX) and elemental distribution of Te-M based thin films

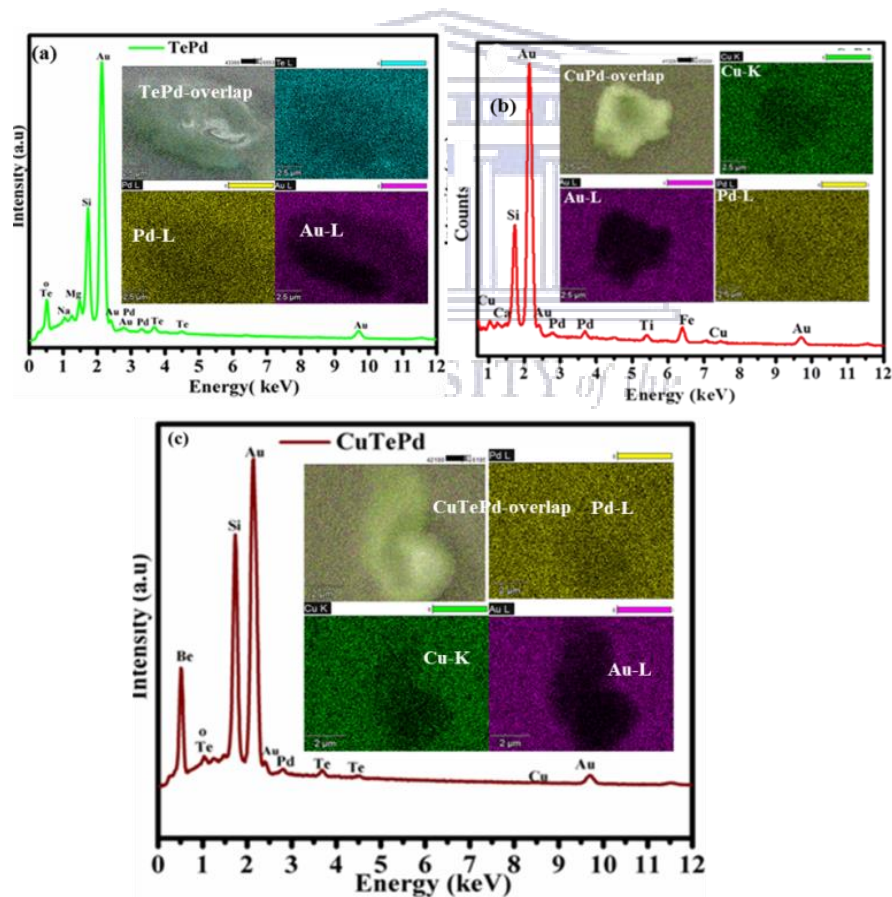


Figure 7.3: Illustrates the EDX and corresponding elemental mapping (inserts) of (a) PdTe and CuTePd (b).

EDS pattern and elemental mapping in **Figure 6.9** evidence of the existence of elemental Te, Cu, and Pd for their respective corresponding deposits, such as CuPd, TePd, CuTePd. CuPd and TePd thin films are displayed in this figure to contrast the incorporation of Te in CuPd and are as discussed in **section 6.7 Chapter 6**. The Elemental mapping (**Figure 6.9**: inserts)) is coherent with EDX results. It can CuTePd, shows no clear evidence of elemental Te in both EDS and elemental mapping results, which may be submerged by large Cu molecules, which was the last deposition step during the E-ALD cycle. This is also corroborated with the XRD pattern, where Te patterns were invisible in regions where it was expected, around 2θ (15° - 35°) (see **Figure 7.4 (c)**).

7.4 Scanning electron microscope (SEM)

Figure 7.4 reveals SEM micrographs of the as-synthesized; TePd and CuTePd thin films at low magnification and high magnification of Te-M based thin films. CuPd is as discussed in **Chapter 5** (see **section 5.4.2, Figure 5.9 (b)**). CuTePd structure exhibits the Te-nanostructure (white particles) deposited throughout the surface and nanoribbon shaped particles than may attribute Cu-nanostructure (**Figure 7.4 (c-d)**). Very fascinating, these features show an apparent network of flower-like- nano dendritic and nanoribbon microstructures of Te and Cu respectively. Te-covered electrode surface tend to control the morphology via surface directing diffusion process, similar to the observation in literature by [9].

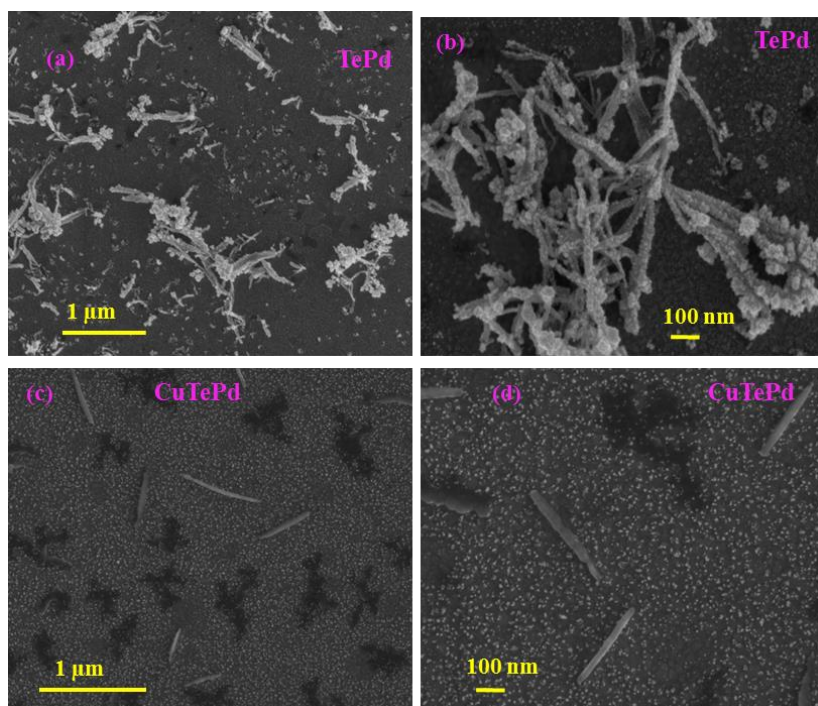
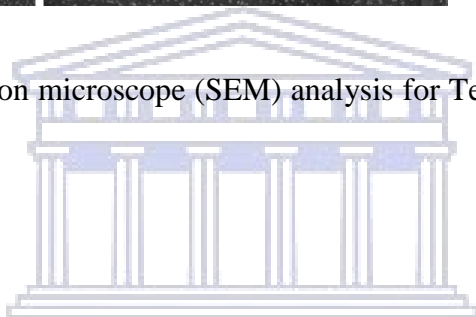


Figure 7.4: Scanning electron microscope (SEM) analysis for TePd (a-b)) and CuTePd (c-d) on Au.



7.5 Atomic force microscopy (AFM) of Te-M thin film analogs

Figure 7.5 represents the AFM topographic 2D micrographs of (a) TePd, and (b) CuTePd, their corresponding 3D view, and texture profiles. The 2D TePd micrographs exhibit the high conformity and well-dispersed grain distribution, the grain distribution is also clearly seen and corroborate with mapping (insert) and 3D view (**Figure 7.5 (a (iii))**). This finding is associated with the layer-by-layer formation of Te on Pd –covered Au. 2D images of CuTe reveals an even grain distribution, which forms cone like-island clearly observed with 3D view. The islands are manifested on a texture profile (**Figure 7.5 (b (iv))**). The texture profile results indicate the inhomogeneity and turbulent grain distribution with varied phases, which may signify the formation of a ternary compound. CuTePd exhibit the higher surface roughness ($S_a = 51.1$ nm,

$S_q = 60.7$ nm) as compared to its analogues TePd ($S_a = 48.5$ nm; $S_q = 57.5$ nm). The cross-section (east to west) analysis of the whole TePd and CuTePd AFM micrograph shows that some grains of trimetallic CuTePd developed a needle like islands with height from 50-100 nm and displayed in **Figure 7.5** (b (iii-iv)). This suggests some 3D growth process for trimetallic CuTePd.

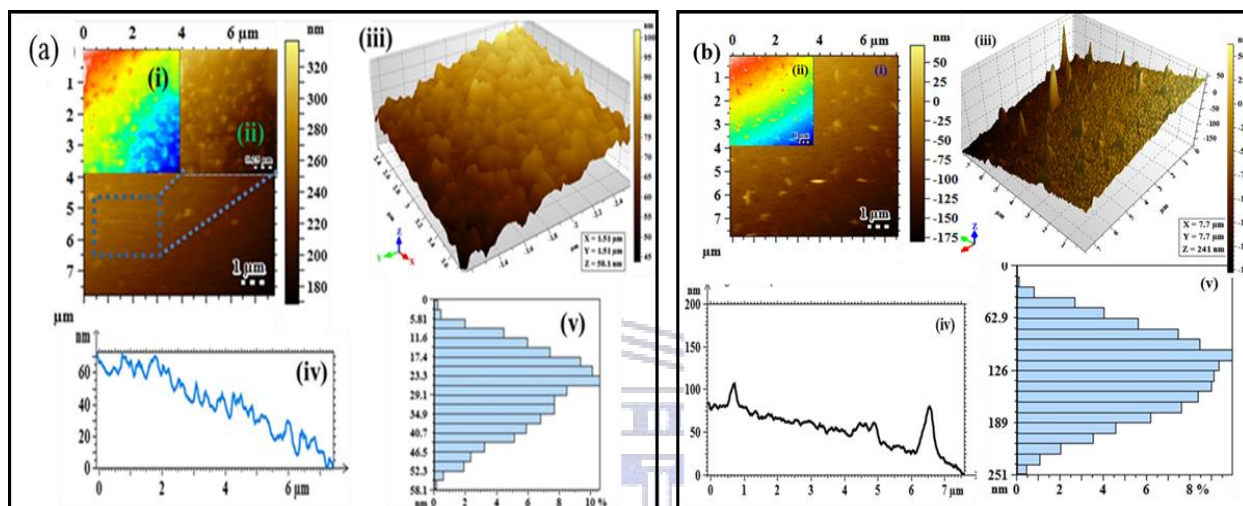


Figure 7.5: AFM topography (2D (i) and 3D (ii)) micrographs revealing details of Atomic Force Microscopy (AFM) analysis for (a) TePd, (b) CuTePd thin films and corresponding height profile (iii) and Histogram (iv).

7.6 Electrochemical characterization Palladium-based thin film: Activity towards ethanol oxidation in alkaline media

Figure 7.6 (a-b) illustrates cyclic voltammogram curves for CuTePd thin film and its analogues such as Pd, CuPd, and TePd. All Pd based thin films were cycled from -1V to +0.2V potential in 0.5 M KOH. **Figure 7.6 (a)** shows higher Pd-Ox formation peak current for CuTePd thin films electrocatalyst in contrast to its analogues, possessing the following trend: CuTePd > TePd > CuPd which indicates the strong electron interaction of CuTe and Pd-surface modified. It can be

seen that trimetallic have a high charge for Pd-O in contrast to monometallic and bimetallic counterparts, this could correspond to the high electrochemically active surface area. Conclusively, Te, and CuTe increase the oxide formation because Te is an oxyanion species. This finding may assist to create the active sites Pd thin film and subsequently promote the bifunctional mechanism during oxidation of ethanol.

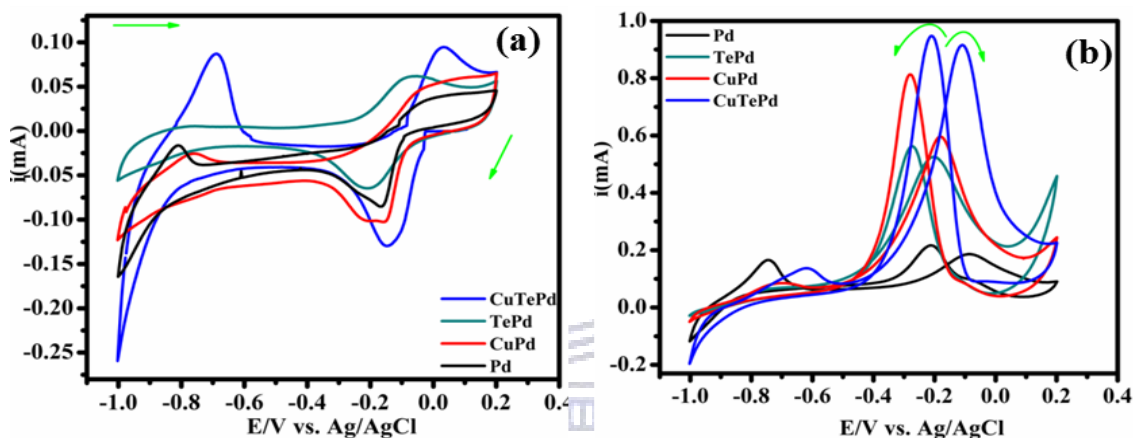


Figure 7.6: CV of CuTePd, CuPd, TePd and Pd in 0.5 M KOH (a) and 0.5 M KOH+ 0.1 M EtOH at 30 mVs^{-1} scan rate.

The electrochemical activity of as-prepared CuTePd and its derivatives thin films for EOR was investigated in 0.5 M KOH containing 0.1 M ethanol (EtOH) solution using CV, in **Figure 7.6 (b)**. All Pd-thin films showed two typical well-distinct ethanol oxidation peaks, that is oxidation of ethanol during forward scan (i_f , E_a), and re-oxidation or removal of carbonaceous species during backward scan (i_b , E_c) as explained in previous studies [10], [11], [12], [13]. During the anodic scan, CuTePd showed a high forward current response, followed by CuPd, TePd, and Pd respectively. These findings may indicate the higher catalytic activity for CuTePd thin film electrocatalyst as compared to its counterparts. During the subsequent reverse scan, CuTePd exhibits the highest i_f/i_r ratio in contrast to TePd, CuPd and Pd, which could be ascribed to high protection of Pd by CuTe from poisonous EtOH reaction intermediates as explained in literature [14], [15]. Interestingly, CuTePd shows the late (positive) onset potential, which implies the

slow reaction kinetic for CuTePd as compared to the bimetallic TePd and CuPd respectively. This is due to excess oxides on Pd-active sites which inhibit the EtOH attack by Pd. The protection of Pd by CuTe moiety was also confirmed in **Figure 7.1 (b)**. The results are summarized in **Table 7.1** This finding suggests that trimetallic (dual modified-Pd) CuTePd thin film electrocatalyst require more activation energy to oxidize ethanol as discussed in the literature [16], [17].

Table 7.1: Summary of electro-oxidation activity of Pd based electrocatalyst towards ethanol in alkaline media

Thin films	Forward peak current; I_f (mA)	Reverse peak current, I_b (mA)	Onset (V)	I_f/I_b ratio
Pd	0.13	0.15	-0.39	0.938
CuPd	0.587	0.811	-0.45	0.75
TePd	0.527	0.559	-0.535	0.94
CuTePd	0.9089	0.942	-0.432	0.964

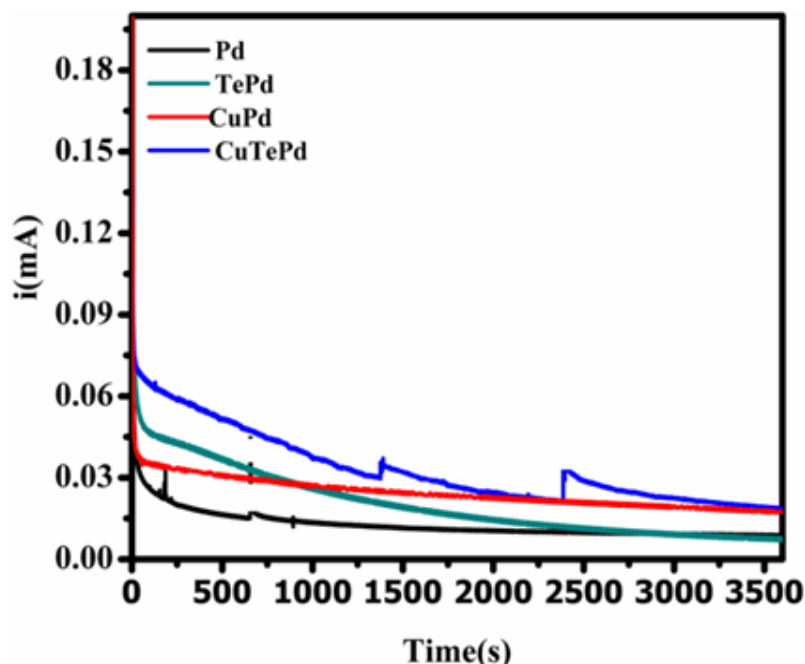


Figure 7.7: CA of CuTePd based thin films in 0.5 M KOH +0.1 M EtOH for 1 hour (3600s).

Figure 7.7 depicts the chronoamperometric study of as-prepared CuTePd based thin films electrocatalyst in 0.5 M + 0.1 M EtOH. CuTePd thin film was overlaid with Pd, TePd, CuPd to spot the difference respective to its analogous. The electrochemical stability was done for 1 hour duration (3600s) towards EOR. The current density-time plots test of nanostructured CuTePd based thin film electrocatalysts analogues ranging from Pd, TePd, CuPd, and CuTePd thin films in at fixed potential of -0.2 V selected (from CVs, **Figure 7.6 (b)**) was used. The initial high current value observed presumably associated with the double layer or indicates the present active site of Pd nanostructured thin films as described in the literature [2], [16], [18]. The rapid current decay during the first few minutes is presumably due to the gradual accumulation of adsorbed poisonous carbonaceous (EtOH intermediates) species [18] at the active site of electrocatalysts which is consistent with previous work [19]. The results consonance with CV results in **Figure 7.6 (b)**. However, CuPd exhibit a low current decay as compared to other catalysts almost 30 % current decay as among others. This possible implies that, the low if/if ratio and the steeper reverse peak of CuPd as compared to other electrocatalysts might not be due

to the effect of by-product but rather high developed Pd(II)-oxide as discussed in the literature [14],[17]. According to the literature [16],[17],[20], in situ FTIR-CV is highly recommended to strongly confirm the adsorbed species on the electrocatalytic surface. Subsequently, the current response gradually decreases till it reaches a constant current; CuTePd remained to have the highest steady-current followed by CuPd and Te respectively. This finding indicates that CuTePd thin film electrocatalyst is well protected by CuTe species and implying that CuTePd is the most stable in accordance to the literature [21]. The notable electron jump in CuTePd CA curves could be due to the inhomogeneity (agglomeration) and rugged surface, or the electrolyte solution occurs on various electrode compositions.

7.7 Electrochemical Impedance Spectroscopy of CuTePd nanostructured thin films and its derivatives

Figure 7.8 displays the Nyquist plot of CuTePd and its analogous thin film materials in 0.5 M KOH containing 0.1 M EtOH solutions at selected -0.2 V from CV results (**from Figure 7.6**). It can be seen that the materials exhibit a diverse diameter semi-circle which indicates the electron transfer kinetics of the thin film-electrolyte interface. The Randles-Sevcik equivalent circuit (**Figure 7.8**): insert) has been used to simulate the semi-circles to obtain the values of the corresponding important EIS parameters possessing important elements such as ($R_s(R_{ct}CPE)$). Interestingly, CuPd exhibits the small semi-circle as compare to CuTePd which implies that CuPd has a higher electron kinetic transfer for ethanol oxidation reaction (EOR) as compared to CuTePd. The findings correlate with CV, onset potential results obtained in **Figure 7.6 (b)** which is possibly attributed to the protection of Pd active sites by CuTe moiety. This might indicate the slow scissoring of the C-C bond during the EOR. This finding might also be assigned to 3D dimension formation structure as indicated by AFM for CuTePd (**see Figure 7.5 (b)**) which may hinder the active sites of Pd. The less accessible Pd active site by EtOH may possibly result to

larger R_{ct} , and subsequently, lower electron kinetic transfer. The relative increase Pd-O upon the incorporation of dual oxygenated (CuTe) species may hinder the charge transfer, because of protected Pd-active site which is consistent with previous studies by [54],[68]. Another advantage for CuPd and TePd over CuTePd, is it indicates the conformal flat (2D) surface with well-dispersed particle and probable increased ECSA (see Pd-O reduction peak, in **Figure 7.1 (b)**), Furthermore TePd exhibited dendritic structures (see **Figure 7.5 (a-b)**) in which dendritic-ends are associated to active sites and bifunctional mechanism.

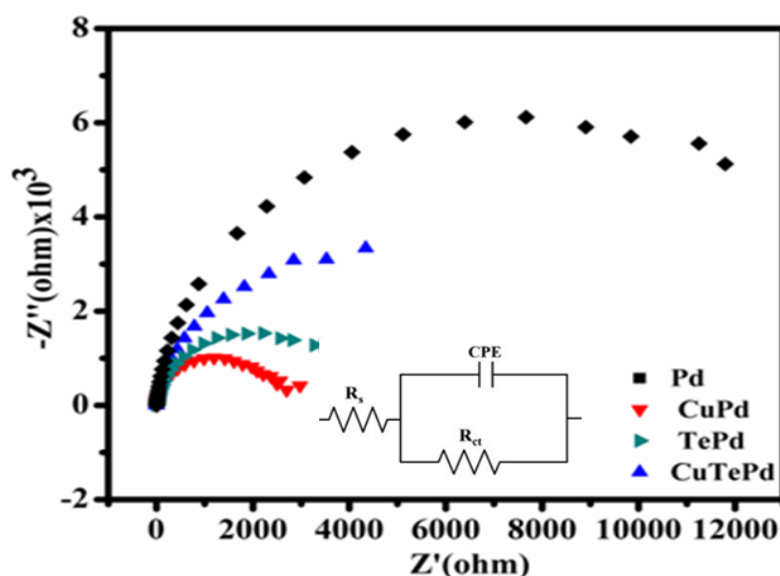


Figure 7.8: Nyquist plot of CuTePd and its analogous in 0.5 KOH + 0.1M EtOH at a constant potential of -0.2 V at 1×10^4 to 0.1 Hz frequency range, Randles-Sevcik circuit: insert.

Figure 7.9 (a) illustrates CuPd, CuTePd and CuTePd analogues **(b)** in 0.5 KOH + 0.1M EtOH. It can be seen that CuPd and CuTePd show a higher phase angle as compared to its analogues with almost the same 86.34° and 86.10° phase angle maximum ($-\theta_{max}$) respectively. The high phase angle for CuPd than CuTePd could be attributed to the higher electron conductivity, which is subsequently correlated with fast electron kinetic transfer for EOR. The slight difference in phase angle might be due to Cu and Te occurs on the common Pd/Au substrate. CuTePd exhibits a

varied electrode composition as evidenced by the symmetric peak occurs at low frequency. The high Pd-oxides are evidenced by large impedance value gradual decrease which might be resulted by dual (CuTe) oxygenated species on a Pd which may inhibit the Pd active sites to access by 0.5 M KOH+ 0.1 M EtOH. This possibly inhibits the charge transfer, and promotes the resistive behavior, and has a strong agreement with the Nyquist plot which indicates a larger semi-circle as compared to CuPd. These findings are also having a strong agreement with CV (**Figure 7.6 (b)**) where CuTePd showed later-onset potential during forwards scan as compared to CuPd counterparts, which indicates the slow electron kinetic transfer induced by lack of Pd active site. This may be delineated by AFM micrographs (clearly seen on 3D images) (see **Figure 7.5 (b)**), where CuTePd depicts some islands of microstructure which presumably coherent with less Pd access by an electrolyte.

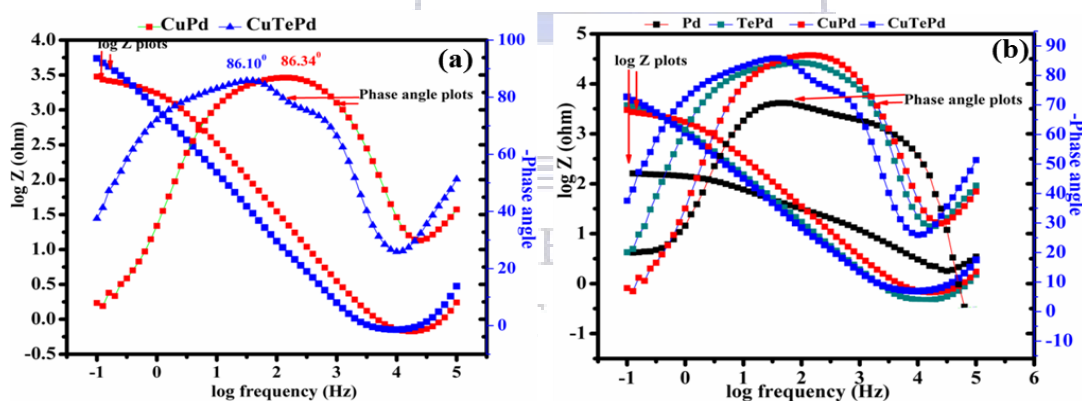


Figure 7.9: Bode plot of CuTePd and its analogues in 0.5 KOH + 0.1M EtOH at a constant potential of -0.2 V.

Table 7.2: Summary of some impedimetric parameter of CuTePd based thin film in 0.5 KOH + 0.1 EtOH

Thin films	R_s (Ω)	R_{ct} (k Ω)	n	CPE(F)	%error	φ ($^\circ$)
Pd	7.33E3	14.9	0.87	40.8	1.26	74

TePd	0.99	2.4205	0.81	5.55	2.2	84.41
CuTePd	5.2E3	5.5	0.833	9.45	1.5	86.10
CuPd	7.53	2.314	0.7813	4.43	3.2	86.34

Sub-conclusion

Electroformation of monometallic Pd, bimetallic metallic (TePd, and CuPd) compounds, and trimetallic (CuTePd) compound has been electro synthesized successfully using E-ALD technique. The E-ALD cycles formed through alternating execution of SLRR of Cu-_{UPD} followed by oxidative Te-_{UPD}. The trimetallic CuTePd suffered a sluggish electron kinetic transfer and late-onset potential towards EOR, however, this compound is still surpassed its analogues (TePd, CuPd) thin films by electrochemical stability, poisoning tolerance and current response. Interestingly SEM images show that CuTePd exhibits the network of dendritic shaped particles and nano-ribbon nanostructures. The electrochemical surface limited reaction approach for electrosynthesis of CuTePd and properties observed makes an E-ALD a convenient technique. However, the optimization of E-ALD cycles for CuTePd formation should be considered to avoid the islands that could possibly inhibit electron kinetic transfer during EOR

References

- [1] H. Hattori, "Electrocatalysis by Pb adatoms of HCOOH oxidation at Pf(111) in acidic solution," *Electrochim. Acta*, vol. 41, no. 10, pp. 1619–1628, 1996.
- [2] A. C. Mkhohlakali, X. Fuku, R. M. Modibedi, L. E. Khotseng, S. C. Ray, and M. K. Mathe, "Electrosynthesis and characterization of PdIr using electrochemical atomic layer deposition for ethanol oxidation in alkaline electrolyte," *Appl. Surf. Sci.*, vol. 502, no. August 2019, pp. 144–158, 2019.
- [3] I. Achari, S. Ambrozik, and N. Dimitrov, "Electrochemical Atomic Layer Deposition of Pd Ultrathin Films by Surface Limited Redox Replacement of Underpotentially Deposited H in a Single Cell," *J. Phys. Chem. C*, vol. 121, pp. 4404–4411, 2017.
- [4] D. M. Benson, C. F. Tsang, J. D. Sugar, K. Jagannathan, D. B. Robinson, F. El Gabaly, P. J. Cappillino, and J. L. Stickney, "Enhanced Kinetics of Electrochemical Hydrogen Uptake and Release 2 on Palladium Powders Modified by Electrochemical Atomic Layer 3 Deposition," *Appl. Mater. Interfaces*, 2017.
- [5] A. Kumar and D. A. Buttry, "Size-Dependent Underpotential Deposition of Copper on Palladium Nanoparticles," *J. Phys. Chem. C*, vol. 119, pp. 16927–16933, 2015.
- [6] R. Jana, S. Dhiman, and S. C. Peter, "Facile solvothermal synthesis of highly active and direct ethanol fuel cell applications Facile solvothermal synthesis of highly active and robust Pd_{1.87}Cu_{0.11}Sn electrocatalyst towards direct ethanol fuel cell applications," *Mater. Res. Express*, vol. 3, no. 8, pp. 1–9, 2016.
- [7] M. S. Ahmed, D. Park, and S. Jeon, "Ultrasmall PdMn_{1-m}O_x binary alloyed nanoparticles on graphene catalysts for ethanol oxidation in alkaline media Ultrasmall Pd

- m Mn₁-mOx binary alloyed nanoparticles on graphene catalysts for ethanol oxidation in alkaline media,” *J. Power Sources*, vol. 308, pp. 180–188, 2016.
- [8] R. M. Modibedi, T. Masombuka, and M. K. Mathe, “Carbon supported Pd-Sn and Pd-Ru-Sn Nanocatalysts for ethanol electro-oxidation in alkaline medium,” *Int. J. Hydrogen Energy*, vol. 6, pp. 1–9, 2011.
- [9] Y. Zhang, Y. Ni, X. Wang, J. Xia, and J. Hong, “Polycrystalline Cu₇Te₄ dendritic microstructures constructed by spherical nanoparticles: Fast electrodeposition, influencing factors, and the shape evolution,” *Cryst. Growth Des.*, vol. 11, no. 10, pp. 4368–4377, 2011.
- [10] C. Jun Yin, Mei Shan Ng, Lefu Yang, Derrick Mott, Weiqin Fang, Ning Kang, Jin Luo, and Zhong, “Catalytic and Electrocatalytic Oxidation of Ethanol over Palladium- Based Nanoalloy Catalysts,” *Langmuir*, vol. 29, pp. 9249–9258, 2013.
- [11] A. K. Ipadeola, R. Barik, S. C. Ray, and K. I. Ozoemena, “Bimetallic Pd / SnO₂ Nanoparticles on Metal Organic Framework (MOF) -Derived Carbon as Electrocatalysts for Ethanol Oxidation,” *Electrocatalysis*, 2019.
- [12] Y. Wang, Q. He, K. Ding, H. Wei, J. Guo, Q. Wang, R. O. Connor, X. Huang, Z. Luo, T. D. Shen, S. Wei, and Z. Guo, “Multiwalled Carbon Nanotubes Compositated with Palladium Nanocatalysts for Highly Efficient Ethanol Oxidation,” *J. Electrochemical Soc.*, vol. 162, no. 7, pp. 51–54, 2015.
- [13] A. S. Douk, H. Saravani, and M. Noroozifar, “Preparation and Electrocatalytic Characteristics of PdW/C Catalyst for Ethanol Oxidation,” *Int. J. Hydrogen Energy*, vol. 42, no. 22, pp. 15149–15159, 2017.

- [14] W. Xu, S. Zhu, Z. Li, Z. Cui, and X. Yang, "Preparation of Nanoporous Pd / CuO by Dealloying and Their Electrocatalysis for Methanol in Alkaline Condition Preparation of Nanoporous Pd / CuO by Dealloying and Their Electrocatalysis for Methanol in Alkaline Condition," *J. Electrochem. Soc.*, vol. 161, no. October 2014, pp. 1474–1480, 2014.
- [15] Z. X. Liang, T. S. Zhao, J. B. Xu, and L. D. Zhu, "Mechanism study of the ethanol oxidation reaction on palladium in alkaline media," *Electrochim. Acta*, vol. 54, pp. 2203–2208, 2009.
- [16] X. Fuku, M. Modibedi, N. Matinise, P. Mokoena, N. Xaba, and M. Mathe, "Single step synthesis of bio-inspired NiO / C as Pd support catalyst for dual application : Alkaline direct ethanol fuel cell and CO₂ electro-reduction," *J. Colloid Interface Sci.*, vol. 545, pp. 138–152, 2019.
- [17] R. A. Gonçalves, M. R. Baldan, E. G. Ciapina, and O. M. Berengue, "Nanostructured Pd / Sb₂O₃ : A new and promising fuel cell electrocatalyst and non-enzymatic amperometric sensor for ethanol," *Appl. Surf. Sci.*, vol. 491, no. February, pp. 9–15, 2019.
- [18] R. M. Modibedi, T. Masombuka, and M. K. Mathe, "Carbon supported Pd-Sn and Pd-Ru-Sn nanocatalysts for ethanol electro-oxidation in alkaline medium," *Int. J. Hydrogen Energy*, vol. 36, no. 8, pp. 4664–4672, 2011.
- [19] W. Du, K. E. Mackenzie, D. F. Milano, N. A. Deskins, D. Su, and X. Teng, "Palladium Tin Alloyed Catalysts for the Ethanol Oxidation Reaction in an Alkaline Medium," *ACS Catal.*, vol. 2, pp. 287–297, 2012.

- [20] P. Oc, J. Torrero, M. Montiel, M. A. Pe, and S. Rojas, “Insights on the electrooxidation of ethanol with Pd- based catalysts in alkaline electrolyte,” *Int. J. Hydrogen Energy*, no. xxxx, 2019.
- [21] K. Ding, Y. Zhao, L. Liu, Y. Li, L. Liu, Y. Wang, H. Gu, H. Wei, and Z. Guo, “Multi-walled carbon nanotubes supported Pd composite nanoparticles hydrothermally produced from technical grade PdO precursor,” *Electrochim. Acta*, vol. 176, pp. 1256–1265, 2015.



UNIVERSITY *of the*
WESTERN CAPE

Chapter 8

8.1 Conclusion

Electrochemical atomic layer deposition was successfully used to deposit monometallic (Te, Pd), bimetallic (PdIr, CuPd, BiPd, TePd) and trimetallic (CuBiPd, BiTePd and CuTePd) nanostructured thin film electrocatalysts. The thin films were successfully electrodeposited on Au via SLRR of Cu-UPD followed by SLRR for Pd and Ir. CuPd and BiPd Pd deposits formed through alternated Pd SLRR of Cu-UPD followed by reductive Cu-UPD and Bi-UPD for the corresponding deposits. In contrast to bimetallic TePd, which was formed via SLRR of Cu-UPD followed by oxidative Te underpotential deposition (ox-Te-UPD). The trimetallic nanostructured thin films were electro-formed through the combination of SLRR of Cu-UPD and alternated execution of Bi-UPD, Cu-UPD (for CuBiPd) and ox-Te-UPD (for BiTePd and CuTePd). All the E-ALD cycles for electroformation of nanostructured thin films were studied and monitored using CV and potential-current-time curves.

The acquired thin films (PdIr, CuPd, BiPd, TePd) and trimetallic (CuBiPd, BiTePd, and CuTePd) were characterized using CV in alkaline media (0.5 M KOH) and acidic media (0.1 M HClO₄) to determine the CV signature (redox features). All the Pd-based nanostructured thin films: deposits exhibited typical Pd voltammogram features, with distinct current response profiles at the Pd-O region (0.46 V v.s Ag/AgCl). The structure and morphology of these thin films were further characterized using XRD, XPS, SEM-EDX, and AFM. The bimetallic and trimetallic Pd based thin films showed an alloy formation phase and other thin films displayed some epitaxial relationship with preferred Au/Pd (111) substrate orientation using XRD.

PdIr showed a more negative onset potential and higher current (-0.423 V; 0.664 mA) than Pd (-0.402 V; 0.494 mA) thin film, indicating that the bimetallic PdIr is more active than monometallic Pd. The Electrochemical impedance spectroscopy (EIS) showed smaller $R_{ct} = 0.23 \text{ k}\Omega$ for PdIr than that of Pd; $R_{ct} = 14.8 \text{ k}\Omega$, when subjected to a fixed potential of -0.2 V. PdIr, showed a higher i_f/i_b ratio of 1.094 than Pd ($i_f/i_b = 0.94$) indicating higher tolerance to poisoning by ethanol oxidation intermediates species than Pd. Moreover, chronoamperometry (CA) results confirmed that the addition of Ir to Pd improved the stability of the nanostructured PdIr film.

The modification of Pd with metal adatoms such as OX-Te-UPD , Cu-UPD , and Bi-UPD adlayers as catalytic promoters improved the electrochemical activity and fast electron kinetic transfer. The trimetallic CuBiPd, BiTePd, CuTePd compounds exhibited the remarkable activity and stability towards ethanol oxidation reaction (EOR) than monometallic Pd. The onset potential has the follows trend: BiTePd (-0.55 V) > CuBiPd (-0.482 V) > TePd (-0.535V) > CuPd (-0.45V) > **CuTePd** (-0.432) > PdIr ((-0.423V) > BiPd (-0.384 V) > Pd (-0.35 V). The ternary CuTePd showed the positive onset potential, low conductivity and low electron kinetic transfer as compared to TePd and CuPd, and this is believed to be related to the structural formation (or 3D growth) during E-ALD cycles, which it will be worth to further optimize its E-ALD cycle.

The fascinating properties and electrochemical activity and stability of bimetallic (PdIr CuPd, BiPd, TePd) and trimetallic (CuBiPd, BiTePd, and CuTePd) formed few number of cycles (15 cycles) makes E-ALD a reliable and futuristic method for nanostructured thin film. E-ALD electroformed a quality of on nanostructured thin films at a low number of cycles, within a few minutes. This makes, E-ALD the potential technique for electroformation of nanostructured thin film electrocatalysts. The Pd-based chalcogenides exhibited higher electrocatalytic activity and rarely interesting structures. The high activity and kinetics of bimetallic and trimetallic thin film electrocatalyst towards ethanol fuel cells make them a potential candidate for Direct liquid fuel cell (DLFCs), specifically for the direct ethanol fuel cell. Due to the fact that ethanol oxidation

reaction (EOR) was performed at room temperature, DEFCs is promising environmentally friendly technology.

8.2 Recommendations

Modeling of structural formation of various PGM-based chalcogenides should be mandatory to strengthen the synthesis of electrocatalysts. Further work can be done to determine the thickness of the nanostructured thin films using the ellipsometry spectroscopy technique. Te-M nanostructured thin films exhibited high electrochemical activity and interesting surface morphology (nano dendrimers) which is believed to control by surface diffusion process using a 15:15 ratio, it will be worth to explore the varied Te ratio against Pd. The incorporation of Te on the high performing PdIr electrocatalyst could enhance more activity towards EOR. The future work following this trend is the consideration of a 'giant' quaternary compounds which can be comprised of PdIr-BiTe. Lastly due to the properties revealed by the electroformed nanostructured thin films should be tested in other electrocatalytic reactions such as oxygen reduction reaction and oxygen evolution reaction in acidic solutions, as well as for glycerol oxidation in alkaline media as glycerol is one of the attractive fuels in the direct liquid fuel cells. The substrate used for electroformation of thin film, is the well-known gold (Au), which opens the 'gates' to explore other flexible substrates for other applications.

